A NUMERICAL INVESTIGATION OF THERMAL-HYDRAULIC CHARACTERISTICS IN THREE DIMENSIONAL PLATE AND WAVY FIN-TUBE HEAT EXCHANGERS FOR LAMINAR AND TRASITIONAL FLOW REGIMES

by

Satchit Pradip Panse

A thesis submitted in partial fulfillment
of the requirements for the degree

of

Master of Science

in

Mechanical Engineering

MONTANA STATE UNIVERSITY
Bozeman, Montana

May, 2005

APPROVAL

of a thesis submitted by

Satchit Pradip Panse

This thesis has been read by each member of the thesis committee and has been found to be satisfactory regarding content, English usage, format, citations, bibliographic style, and consistency, and is ready for submission to the College of Graduate Studies.

Dr. M. Ruhul Amin

Approved for the Department of Mechanical and Industrial Engineering

Dr. Jay Conant

Approved for the College of Graduate Studies

Dr. Bruce McLeod

STATEMENT OF PERMISSION TO USE

Satchit Pradip Panse

May, 2005

ACKNOWLEDGEMENTS

I would like to thank Dr. Ruhul Amin for his guidance in my research and thesis work. I would like to express my appreciation to Dr. Alan George and Dr. William Martindale for their work as committee members.

I am profoundly grateful to Dr. Douglas Cairns for his continued support and enthusiasm throughout my research work. I would also like to thank Dr. V. Cundy and Dr. J. Conant for their encouragement for the present thesis work.

I would like to express my gratitude to the Ansys Inc. for the computational fluid dynamics code CFX-5.5.1 used in this study.

I gratefully acknowledge the Department of Mechanical and Industrial Engineering and my parents for their financial assistance without which this work would not have been possible.

Finally, I would like to appreciate the continued support I received from the staff members of the Department of Mechanical and Industrial Engineering and the fellow graduate students.

TABLE OF CONTENTS

TABLE OF CONTENTS – continued

TABLE OF CONTENTS – continued

LIST OF TABLES

Table Page

LIST OF TABLES - continued

LIST OF FIGURES

LIST OF FIGURES - continued

Figure Page

LIST OF FIGURES - continued

Figure Page

LIST OF FIGURES - continued

Figure Page

LIST OF FIGURES - continued

Figure Page

LIST OF FIGURES - continued

Figure Page

LIST OF FIGURES - continued

Figure Page

NOMENCLATURE

Symbol	Description
A_a	Heat transfer area
A_c	Minimum flow area
Cp	Local pressure coefficient
$\overline{Cp}$	Average pressure coefficient
C_ε	*k*-ε turbulence model constant
$C_{\varepsilon RNG}$	RNG *k*-ε turbulence model constant
C_μ	*k*-ε turbulence model viscosity constant
C_ω	*k*-ω turbulence model constant
c	Specific heat at constant pressure
D	Tube Diameter
D_h	Hydraulic Diameter
Fp	Fin pitch
Ft	Fin thickness
F_U	Momentum flux
f	friction factor
f_η	RNG *k*-ε turbulence model coefficient
f_μ	Zero equation turbulence model constant
H	Fin spacing

NOMENCLATURE - continued

h	Local heat transfer coefficient
$\bar{h}$	Average heat transfer coefficient
h_e	Specific enthalpy
h_{tot}	Specific total enthalpy
j	Colburn factor
j/f	Efficiency index
K	Von Karmon constant
k	Turbulence kinetic energy
L	Flow length
Ll	Longitudinal tube pitch
Lt	Transverse tube pitch
$LMTD$	Log mean temperature difference
l_t	Turbulence length scale
m	Mass flow rate
Nu	Local Nusselt number
$\overline{Nu}$	Average Nusselt number
P	Local dimensionless pressure
P_{in}	Inlet pressure
P_k	Shear production of turbulence
Pr	Prandtl number

NOMENCLATURE - continued

Q	Average heat flux
q''	Heat flux
Re	Reynolds number based on hydraulic diameter, D_h
Re_D	Reynolds number based on tube diameter, D
Re_H	Reynolds number based on fin spacing, H
$\underline{\underline{S}}:$	Strain rate tensor
S_E	Energy source
S_M	Momentum source
St	Stanton number
T	Temperature
T_b	Bulk mean temperature
T_{in}	Inlet temperature
T_w	Wall temperature
U	Dimensionless velocity vector
u	Velocity component in x-coordinate direction
V_{in}	Inlet (frontal) velocity
v	Velocity component in y-coordinate direction
Wa	Wavy angle
Wh	Wavy height
w	Velocity component in z-coordinate direction

NOMENCLATURE - continued

α	k-ω turbulence model constant
β	k-ω turbulence model constant
Γ	Diffusivity
Γ_{eff}	Effective diffusivity
Γ_t	Turbulent diffusivity
Γ_Φ	Dynamic diffusivity of an additional variable
δ	The identity matrix or Kronecker delta function
ε	Turbulence dissipation rate
ν	Kinematic viscosity
λ	Thermal conductivity
μ	Dynamic viscosity
μ_{eff}	Effective viscosity
μ_t	Turbulent viscosity
ξ	Bulk viscosity
ρ	Fluid density
σ	Stress tensor including pressure
σ_k	k-ε turbulence model constant
σ_ε	k-ε turbulence model constant
σ_{kRNG}	RNG k-ε turbulence model constant

NOMENCLATURE - continued

$\sigma_{\varepsilon RNG}$	RNG k-ε turbulence model constant
σ_{ω}	k-ω turbulence model constant
σ_{Φ}	Stress tensor for an additional variable
τ	Shear stress
τ_{ω}	Wall shear stress
$\underline{\underline{\tau}}$	Reynolds stress tensor
Φ	Additional variable (non-reacting scalar)
ϕ	General scalar variable
ω	Turbulence frequency
Θ	Dimensionless temperature
Θ_b	Dimensionless bulk mean temperature

ABSTRACT

The plate fin-and-tube heat exchangers are used in wide variety of industrial applications, particularly in the heating, air-conditioning and refrigeration industries. In most cases the working fluid is liquid on the tube side exchanging heat with a gas, usually air. The current study is focused on two fin configurations, the plain plate-fin and the wavy-fin. These two fin configurations are numerically investigated in both staggered and in-lined tube layouts. The present investigation ranges from laminar flow regime into the sub-critical or transitional flow regime. The suitability of the eddy viscosity turbulence models for the flow representation in the transitional flow regime is discussed in this study.

This study reveals that the flow distinction between plain and wavy fin has a profound influence on the heat transfer and flow friction performance of these configurations when compared on the basis of tube layouts. The obtained results also indicate that the number of tube rows plays an important part for the overall heat exchanger performance and an optimum choice for the number of tube rows must be made in order to achieve the critical balance between high heat transfer performance and low pressure drop. It was observed that for an optimum number of tube rows, increasing the longitudinal or transverse tube pitch causes a decrease in the thermal and hydraulic performance of the heat exchanger. For the transitional flow regime, the k-ω turbulence model was found to be more suitable than the k-ε based turbulence models. This suitability of the k-ω turbulence model was linked to the better near wall treatment by this model as compared to the k-ε based models. The results for the fin pitch study indicated that the decrease in the fin pitch causes a decrease in both heat transfer and flow friction characteristics for the transitional flow regime. The results also suggested that for the transitional flow regime, for an equal wavy height, the thermal and hydraulic performance is increased as the wavy angle is increased. On the other hand, for an equal wavy angle, it is decreased as the wavy height is increased.

CHAPTER 1

INTRODUCTION

Plate fin-and-tube heat exchangers are employed in a wide variety of engineering applications such as air-conditioning equipment, process gas heaters, and coolers. Generally, the heat exchangers consists of a plurality of equally spaced parallel tubes through which a heat transfer medium such as water, oil, or refrigerant is forced to flow while a second heat transfer medium such as air is directed across the tubes in a block of parallel fins. In such types of heat exchangers, continuous and plain or specially configured fins are used on the outside of the array of the round tubes of staggered or in-lined arrangement passing perpendicularly through the plates to improve the heat transfer coefficient on the gas side. The heat transfer between the gas, fins and the tube surfaces is determined by the flow structure which is in most cases three-dimensional. In practical applications, the dominant resistance is usually on the air side which may be 10 times larger than that of the tube side. Hence to improve the overall heat transfer performance, the use of enhanced surfaces is very popular in air-cooled heat exchangers, although a continuous plain fin is still a commonly used configuration where low pressure drop characteristics are desired. Common types of specially configured fin types used in these heat exchangers are wavy or corrugated fin, louvered fin, offset strip fin and perforated fin. Wavy or corrugated fins are one of the very popular fin patterns that are developed to improve the heat transfer performance. The wavy surface can lengthen the flow path of the air flow and cause better airflow mixing. Therefore, higher heat transfer performance is expected compared to the plain plate fin surface. However, the higher heat transfer

performance of the wavy fin surface is accompanied by the higher pressure drop as compared to the plain plate fin type.

Background

Plain-Fin Configuration:

In case of plain plate fin-and-tube heat exchangers, a liquid flows through the tubes and a gas (usually air) flows through the channels formed by the neighboring, parallely placed fins around the tube banks. Figure 1 shows the three-dimensional view of a plain plate fin-and-tube heat exchanger. The tubes are placed in either staggered or in-lined layout. Figure 2 shows the top and the front view of a plain plate fin-and-tube heat exchanger with staggered tube layout. Figure 3 shows the top and the front view of a plain plate fin-and-tube heat exchanger with in-lined tube layout.

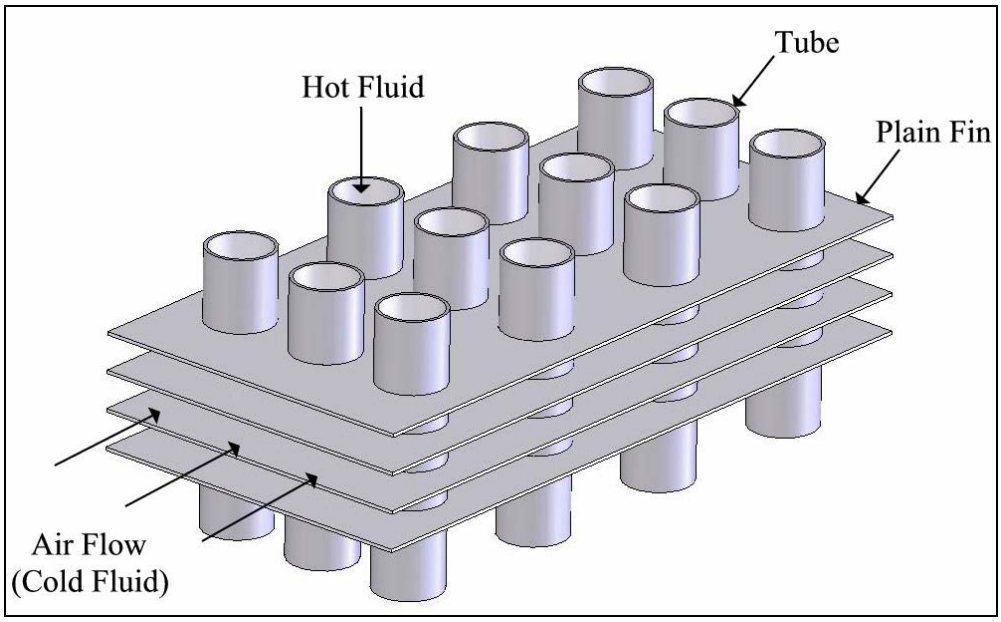

Figure 1. Plain plate fin-and-tube heat exchanger

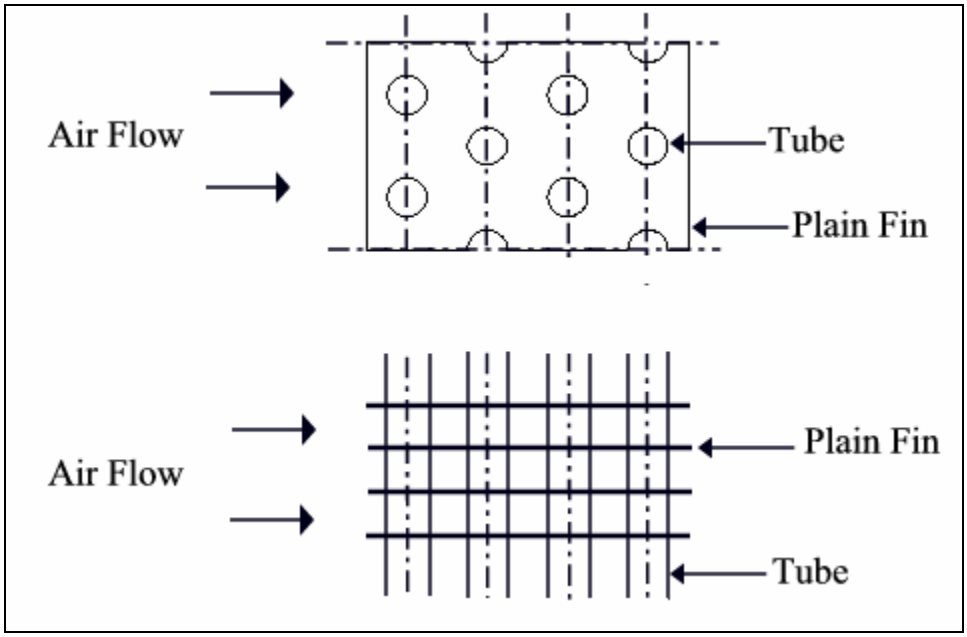

Figure 2. Plain plate fin-and-tube heat exchanger with staggered tube layout

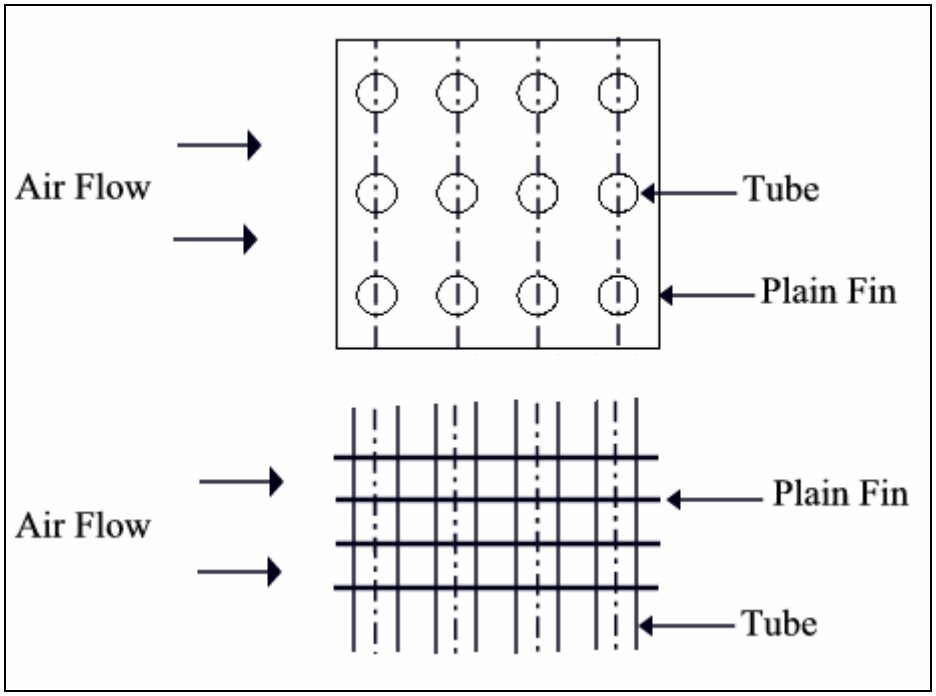

Figure 3. Plain plate fin-and-tube heat exchanger with in-lined tube layout

An extensive number of experimental studies have been reported in the literature on the thermal and hydraulic characteristics of the plain-fin patterns. Following literature review briefly summarizes a selected number of articles for the plain fin-and-tube heat exchanger configurations.

Plate fin-and-tube heat exchangers of plain fin pattern are employed in a wide variety of engineering applications such as air-conditioning apparatus, process gas heaters and coolers. The plain fin-and-tube heat exchangers usually consist of mechanically or hydraulically expanded round tubes in a block of parallel continuous fins and, depending on the application, the heat exchangers can be produced with one or more rows. The plain plate fin configuration is still the most popular fin pattern, owing to its simplicity, durability and versatility in application.

During the past few decades many efforts have been devoted to heat transfer and friction characteristics of plate fin-and-tube heat exchangers. Rich (1973 and 1975) a total of 14 configurations, in which tube size was 13.34 mm and the longitudinal and transverse tube pitches were 27.5 and 31.75 mm, respectively. He investigated the effects of fin-pitch and number of tube row for these 14 staggered plate fin-and-tube heat exchangers. He concluded that the heat transfer coefficient was essentially independent of fin spacing and the pressure drop per row is independent of number of tube rows. Based on the test results for five heat exchangers, McQuiston (1978) proposed the first correlation for the finning friction factor. His correlation shows correlation shows a strong direct dependence of heat transfer performance with the finning friction factor. For the friction factor correlation McQuiston (1978) claimed the accuracy is $\pm 35\%$. Saboya

and Sparrow (1974 and 1976) used the naphthalene mass transfer method to measure the local coefficients for one-row, two-row and three-row plate-fin and tube heat exchangers. They obtained higher values of local heat and mass transfer coefficients on the forward part of the fin due to the presence of developing boundary layers. Kayansayan (1993) proposed correlations for the Colburn factor (j), based on the experimental data for 10 fin coils. However, the heat exchangers tested by Kayansayan (1993) were all four tube row and no frictional data were reported. Furthermore, the experimental data of Kayansayan (1993) were considerably lower than those reported by Rich (1973 and 1975). Wang et al. (1996) pointed out that some of the data of Kayansayan (1993) showed a scattering inconsistency, which may imply some inaccuracies of the test results. The effect of the number of tube rows on the heat transfer performance for the plain-fins is also studied by Rosman et al. (1984). These authors found higher fin efficiency for the two-row tube configuration compared to the single-row tube configuration in the range of $200 \leq \mathrm{Re} \leq 1700$. Based on the database of five investigations Gray and Webb (1986) proposed correlations for Colburn factor (j) and friction factor (f) for plain fin geometry. These correlations by Gray and Webb (1986) gave reasonably predictive ability for the plain fin heat exchangers having larger tube diameter, larger longitudinal and transverse tube pitch, when compared with the data of McQuiston (1978). A significant improvement of the Gray and Webb (1986) correlation is their friction factor correlation, which is superior to McQuiston's (1978) correlation. Seshimo and Fujii (1991) provided test results for a total of 35 samples. This study by Seshimo and Fujii (1991) investigated the effect of fin spacing, fin length along with the tube row number on the heat transfer

and friction performance of plain fin heat exchangers in the range of $300 \le \mathrm{Re} \le 2000$. Kundu et al. (1992) measured the heat transfer coefficient and pressure drop over an eight tube row in-lined tube array placed between two parallel plates using two different aspect ratios (ratio of tube spacing to tube diameter) in the range of $220 \le \mathrm{Re} \le 2800$. Eckels and Rabas (1987) studied plain fin-and-tube heat exchangers with a fin spacing from approximately 2.0 to 3.2 mm under wet conditions. An enhanced heat transfer was observed under the wet conditions. An increase in the pressure drop was also observed under the wet conditions; however, this effect diminished at high Reynolds numbers. Wang et al. (1996) reported airside performance for 15 samples of plain fin-and-tube heat exchangers. They examined the effects of several geometrical parameters, including the number of tube rows, fin spacing and fin thickness. Wang et al. (1996) argued that the occurrence of "maximum phenomenon" for the Colburn j factors at a large number of tube rows and small fin spacing may not be associated with the experimental uncertainties as commented by Gray and Webb (1986). They also proposed a heat transfer and friction correlation to describe their own data set. This experimental data by Wang et al. (1996) also reported that the Gray and Webb correlations (1986) may significantly underpredict the heat transfer performance. Recently, Kim et al. (1999) and Wang et al. (2000) proposed correlations for heat transfer and friction characteristics for several geometric parameters on the thermal and hydraulic performance of a number of plain-fin heat exchangers. Kim and Song (2002) studied the effect of distance between the plates for a single tube row in the range $114 \le \mathrm{Re} \le 2660$ and found high heat and

mass transfer coefficients in the front of the tube due to the existence of a horseshoe vortex observed in case of a plain-fin.

There are also a number of numerical studies for plate fin-and-tube heat exchangers in the literature. Most of the earlier researchers used two-dimensional (2-D) and laminar flow conditions in their numerical calculations. For 2-D numerical simulations, Launder and Massey (1978) and Fujii et al. (1984) used the hybrid polar Cartesian grid system for a staggered and an in-line tube bank, respectively. Wung and Chen (1989) employed the boundary fitted coordinate system to study the flow field and heat transfer for both staggered and in-lined tube arrays. Kundu (1991) reported 2-D numerical results along with experimental data for the influence of fin spacing on the heat transfer and pressure drop over a four-row in-line cylinder between two parallel plates for $50 \le \mathrm{Re} \le 500$. These authors observed three different separation patterns depending on the spacing between cylinders and plates. These authors also noted that 2-D flow field studies cannot sufficiently predict heat transfer between the fluid and the fin; hence their simulations have limited application. Zdravistch et al. (1994) performed 2-D simulations for heat transfer predictions in a tube bank without fins. He used Dirchlet and Nuemann boundary conditions at the inlet and outlet boundaries, respectively, for each computational element. The calculated outlet values are used as inlet boundary conditions for the next computational element deeper into the tube bank. He also reported the importance of the necessity for 3-D simulations when side wall effects are important, as in tube banks with fins.

Owing to the complicated flow structure between the fins the three-dimensional (3-D) numerical studies tend to be difficult. Few researchers have reported 3-D modeling for plain-fin configuration in their numerical studies. For convenience of calculation, Yamashita et al. (1986) used a fundamental model, consisting of a pair of parallel plates and a square cylinder passing perpendicularly through the plates, which simulate plate-fins and a tube. Bastini et al. (1991) employed one circular tube as the computation domain and assumed that the flow was fully developed with periodic boundary condition to simulate the heat and flow field of in-lined tube arrays. Mendez et al. (2000) investigated both experimentally and numerically the effect of fin spacing on the convection of heat and on the hydrodynamics over a 3-D single-row plate-fin configuration in the range $260 \leq \mathrm{Re} \leq 1460$, using both dye visualization technique and a general purpose fluid flow solver.

Recently Jang et al. (1996) performed numerical studies over a 3-D multi-row plate-fin heat exchanger. They obtained 15-27% higher average heat transfer coefficient and 20-25% higher pressure drop for the staggered arrangement compared to the in-lined arrangement. This study, for the first time provided numerical solutions using a realistic geometry and the inlet-outlet conditions for the actual multi-row (1-6 rows) plate fin-and-tube heat exchangers. In this study, the whole computational domain (1-6 rows) from fluid inlet to outlet was solved directly. Even though a three-dimensional simulation is performed for the actual multi-row plate-fin heat exchanger, this study however was limited to the laminar flow range, where the flow was studied in the range $60 \leq \mathrm{Re} \leq 900$.

Tutar and Akkoca (2004) recently reported a 3-D transient numerical study which investigates the time-dependent modeling of the unsteady laminar flow and the heat transfer over multi-row (1-5 rows) of plate fin-and-tube heat exchanger. In this study the authors transiently investigate the flow field featuring a horseshoe vortex around the tube. The time-dependent evolution of the horseshoe vortex on the forward part of the tube and its journey to the rear of the tube is studied in detail. These authors conclude that the local flow structure including formation and evolution of the vortex system and singular point interactions correlates strongly with the heat transfer characteristics. But again the flow range of the study was laminar $400 \leq \mathrm{Re} \leq 1200$.

Tutar et al. (2001) reported a three-dimensional numerical investigation which studies the effect of fin spacing and Reynolds number over a single row tube domain for a Reynolds number range of $1200 \leq \mathrm{Re} \leq 2000$. This investigation is undertaken by using both time and space averaged turbulence models such as standard k-ε model, nonlinear RNG k-ε model and Large Eddy Simulation (LES) model. The average Nusselt number, pressure coefficients and vorticity distributions are determined for the various fin spacing conditions for all turbulence models and the values of these governing parameters are compared with each other. This study, even though undertakes a 3-D turbulent range analysis for the plate-fin flow, the domain used in this study (single tube row) is not realistic. In the practical applications, 1-6 tube row domains are usually used. Also, this study does not attempt to compare the numerical results obtained using different turbulence models with the experimental data. Therefore the suitability of any particular

turbulence model for the practical applications of the plate-fin heat exchanger is not answered.

Wavy-Fin Configuration:

Wavy fins are one of the most popular heat exchanger surfaces since it can lengthen the airflow inside the heat exchanger and improve mixing of the airflow. Hence, wavy fin-and-tube heat exchangers are extensively employed in various industrial applications. They are quite compact and characterized by a relatively low cost fabrication.

In case of wavy plate fin-and-tube heat exchangers, a liquid flows through the tubes and a gas (usually air) flows through the channels formed by the neighboring, parallely placed wavy fins around the tube banks. Figure 4 shows the three-dimensional view of a wavy plate fin-and-tube heat exchanger. The tubes are placed in either staggered or in-lined layout. Figure 5 shows the top and the front view of a wavy plate fin-and-tube heat exchanger with staggered tube layout. Figure 6 shows the top and the front view of a wavy plate fin-and-tube heat exchanger with in-lined tube layout.

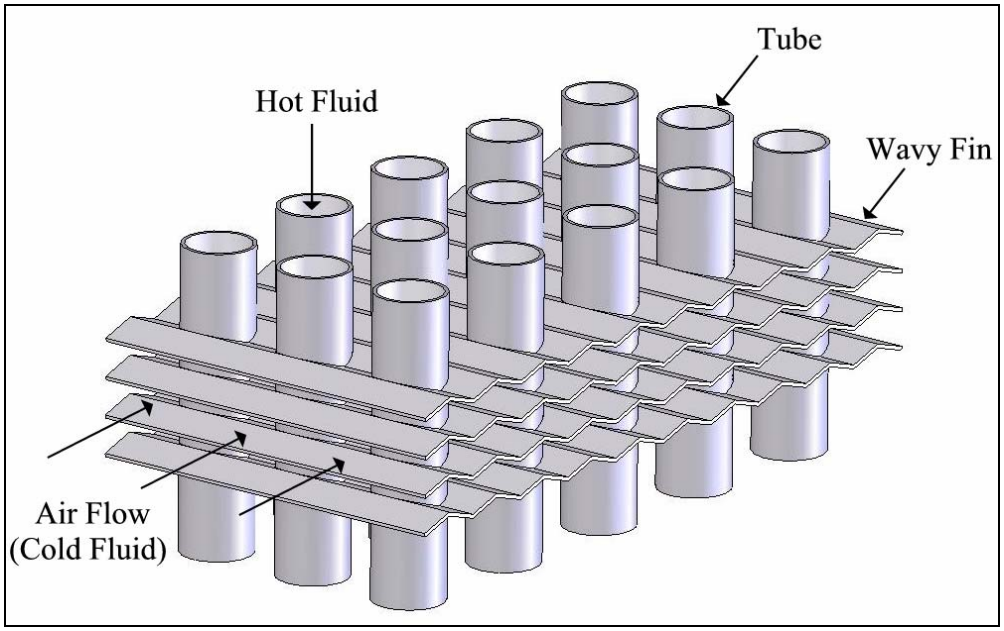

Figure 4. Wavy plate fin-and-tube heat exchanger

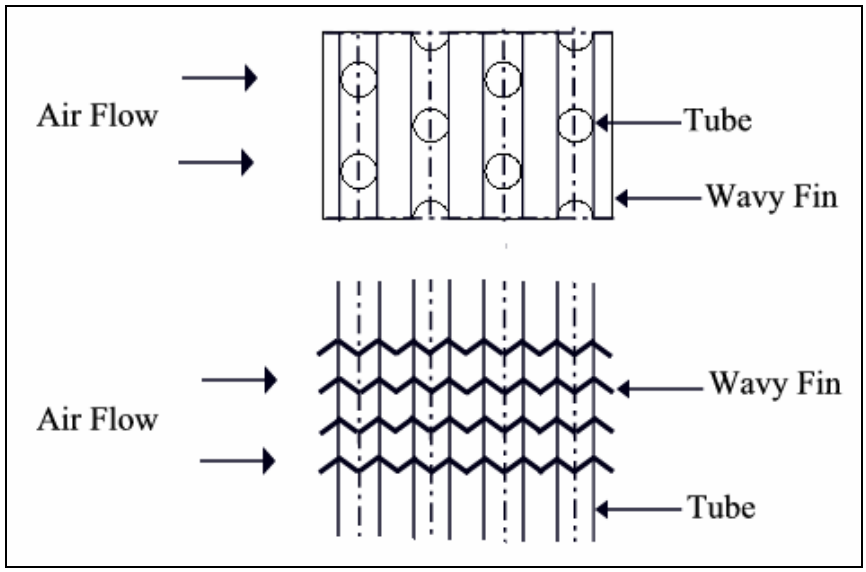

Figure 5. Wavy plate fin-and-tube heat exchanger with staggered tube layout

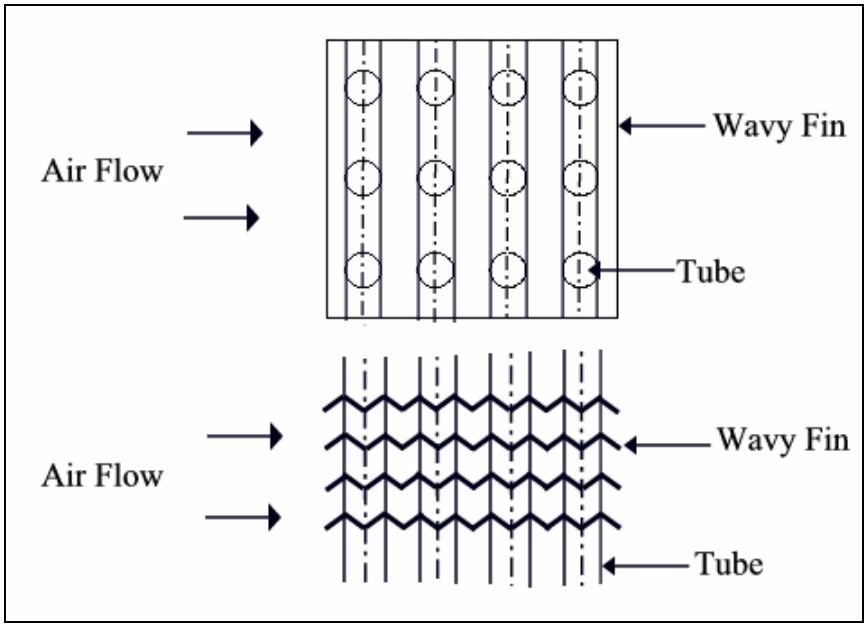

Figure 6. Wavy plate fin-and-tube heat exchanger with in-lined tube layout

As per the plain plate-fins, a vast amount of experimental work has been reported for the wavy-fin configurations. A brief summary of the available literature is presented here.

The first comprehensive study related to the wavy fin pattern was done by Beecher and Fagan (1987). They presented test results for 21 wavy fin-and-tube heat exchangers. All heat exchangers were arranged in a triple row staggered layout. This study by Beecher and Fagan (1987) measured the effect of air velocity and fin pattern on the air-side heat transfer in wavy fin-and-tube heat exchangers using single channel experimental test models. Data were presented in terms of Nusselt number based on arithmetic mean temperature difference vs. Graetz number. Their fins were electrically heated, and thermocouples were embedded in the plates to determine the plate surface temperature. Kim et al. (1996) proposed correlations for predicting the Colburn factor (j) and the friction factor (f) based on the Beecher and Fagan (1987) test data. Goldstein and

Sparrow (1977) used the naphthalene sublimation technique to determine the local and average heat transfer characteristics for flow in a two-dimensional corrugated wall channel. The effect of rounding of protruding edges of a two-dimensional corrugated wall duct was investigated by Sparrow and Hossfeld (1984). It was found that given a Reynolds number, the rounding of the corrugation peaks brought about a decrease in the Nusselt number and the friction factor decreased even more than did the Nusselt number. Ali and Ramdhyani (1992) experimentally studied the convective heat transfer in the entrance region of two-dimensional corrugated channels. The Nusselt number in the corrugated channels exceeded those in the parallel-plate channels by approximately 140-240%, the corresponding increases in friction factor being 130-280%. Snyder et al. (1993) investigated forced convection heat transfer rates and pressure drops in the thermally fully developed region of a two-dimensional serpentine channel. On an equal Reynolds number basis, the heated surface of the serpentine channel outperformed the baseline parallel plate channel by about a factor of 9 in air and 14 in water. Yoshii (1972) presented dry-surface Nusselt number data for two eight-row coil (one with in-line and one with staggered layout) with a wavy pattern. Later Yoshii et al. (1973) reported wet and dry surface data for two wavy finned cooling coils. One coil had a two-row in-lined tube arrangement and the other had a two-row staggered tube arrangement. They showed that a 20-40% increase in the heat transfer coefficient and a 50-100% increase in the pressure drop, for a wavy-finned cooling coil operating under wet-surface conditions. Webb (1990) used multiple regression technique to provide correlations for heat transfer and flow friction data. The Webb (1990) correlations can predict 88% of the wavy-fin

data within $\pm 5\%$ and 96% of the data within $\pm 10\%$. An experimental study was conducted by Mirth and Ramadhyani (1994) to determine the Nusselt number and friction factor on the air side of wavy-finned, chilled water cooling coil. In this study, general correlations of the dry and wet surfaces were presented. Recently, Wang et al. (1995 and 1997) made extensive experiments on the heat transfer and pressure drop characteristics of wavy-fin and tube heat exchangers. Wang et al. (1997) performed wind tunnel tests to determine the heat transfer and pressure drop characteristics of 18 samples of wavy fin-and-tube heat exchangers. Several geometrical parameters including number of tube rows, fin pitch, and flow arrangement were considered. This study by Wang et al. (1997) reported that the fin pitch has negligible effect on the Colburn factor (j), and the effect of number of tube rows on the friction factor (f) is negligible. Wang et al. (1998) tested 14 fin-and-tube heat exchangers 7 of them having wavy fin geometry. The geometrical parameters were considered including number of tube rows and fin pitch. Wang et al. (1999) examined the effects of number of tube rows, fin pitch, tube diameter and edge corrugation for 22 wavy fin-and tube heat exchangers. They also gave correlations for use in describing the Colburn factor and friction factor. The term of fin thickness was included in the correlation of the Colburn factor however the effect of fin thickness on the air-side performance was not described. Yan and Sheen (2000) examined 36 fin-and-tube heat exchangers (12 plain fin, 12 wavy fin and 12 louver fin geometries). The effects of number of tube rows and fin pitch on the air side performance were examined. The air-side performance of plain, wavy, and louver fin and-tube heat exchangers were compared. Recently, Wang et al. (2002) proposed the most updated heat transfer

coefficient and friction factor correlations obtained by including the previous data and new test results of wavy fin-and-tube heat exchangers. A total of 61 samples containing approximately 570 data points were used to derive the correlations.

Few researchers have presented numerical studies on the thermal and hydraulic characteristics for a wavy corrugated channel flow. Since wavy fin heat exchangers are widely used in the industry, the ability of numerical codes to predict the thermal/hydraulic performance of these surfaces is of considerable interest. Wavy fin-and-tube heat exchanger consists of equally spaced parallel wavy plates and an array of regularly arranged circular tubes normal to the fins. This results in a problem, which must be carried out using a three-dimensional model, and which should include both the fin and the tube. Most of earlier numerical studies are two-dimensional in nature and assume laminar flow for the wavy channel. Asako and Faghri (1987) numerically predicted the heat transfer coefficient, friction factor and streamline for periodically developed flow in a two-dimensional (2D) corrugated duct. The calculations were carried out using a laminar flow model for Reynolds numbers ranging from 100 to 1500. As expected their predicted pressure drop results were higher than the corresponding values for a straight duct. Amano (1985) conducted a numerical study of laminar and turbulent heat transfer in a 2D corrugated wall channel for Reynolds numbers between 10 and 25000. He illustrated the flow patterns in the perpendicular corrugated wall channel. Nishimura et al. (1987) used a finite element method to study a two-dimensional pulsatile flow in a wavy channel with periodically converging-diverging cross-sections. Xin and Tao (1988) numerically analyzed the laminar fluid flow and heat transfer in two-dimensional wavy

channels of uniform cross sectional area. The laminar boundary layer flows over a wavy wall have been numerically investigated by Patel et al. (1991). Rutledge and Sleicher (1994) numerically studied the possibility of improving the heat transfer rates by incorporating small corrugations into a two-dimensional channel. Yang et al. (1997) performed numerical prediction of a transitional flow in a periodic fully developed corrugated duct (2D). The calculations used the Lam-Bremhorst low Reynolds number turbulence model for a Reynolds number range of 100 to 2500. They predicted results for two corrugation angles and for three channel spacings. They found that the predicted transitional Reynolds number is lower than the value for a parallel plate duct, and it decreases with increase in corrugation angle. Ergin et al. (1996) numerically investigated the effect of channel spacing on the periodic fully developed turbulent flow in a 2D corrugated duct using k-ε turbulence model for Reynolds number between 500 and 7000. They reported that, at low Reynolds number, the friction factor increases with increase in channel spacing, reaches a maximum value, and then decreases. McNab et al. (1998) used the commercial software code Star-CD to model heat transfer and fluid flow in an automotive radiator. Although, the calculations were carried out in three-dimensions, no tube was included in the computational domain. In the laminar regime at a Reynolds number of 260, the difference between computation and measurement are 33% for the friction factor (f) and 54% for the Colburn factor (j). In the turbulent regime, the computed friction factors (f) and Colburn factors (j) were within 17% of the measurements.

Recently Jang and Chen (1997) have reported a three-dimensional numerical investigation for the multi-row (1-4 tube row) wavy fin-and-tube heat exchangers. The whole computational domain from fluid inlet to outlet is solved directly. The effects of different geometrical parameters, including tube row numbers, wavy angles and wavy heights are investigated in this study. This investigation however, was restricted to the laminar flow range $400 \le \mathrm{Re} \le 1200$.

Motivation for Present Research

The forgoing literature review shows that even though few researchers have reported three-dimensional numerical investigations for the thermal and hydraulic performance of the plain and wavy fin configurations, most of these studies are limited to the laminar flow range $(400 \le \mathrm{Re}_H \le 1200)$. The experimental studies by Wang et al. (1996) have shown that the flow range for the plain-fin configurations extends from laminar $(400 \le \mathrm{Re}_H \le 1200)$ to the transitional $(1300 \le \mathrm{Re}_H \le 2000)$ and even into the turbulent zones. While the flow range for the wavy fin configurations lies in the laminar and the transitional regions for most of the practical applications. Tutar et al. (2001) have reported numerical study which investigates applicability of three turbulence models (*k*-ε model, Renormalization Group or RNG *k*-ε model and Large Eddy Simulation or LES model) for the plain-fin transitional flow region. These authors have compared the thermal-hydraulic numerical results of these three models with each other, but no comparison with experimental data has been reported. Hence the suitability of any particular turbulence model for simulating the transitional region flow for such fin configurations remains unanswered. Also a number of numerical studies have reported

the investigations for the use of turbulence models for the louvered fin configurations, however, no such studies have been reported for the wavy-fin configuration. The current numerical study investigates the heat transfer and flow friction characteristics in the transitional flow region $(1300 \le \mathrm{Re}_H \le 2000)$, for plain-fin and wavy-fin configurations using three eddy viscosity based turbulence models namely *k*-ε model, RNG *k*-ε model and *k*-ω model. The numerical results for the thermal and hydraulic characteristics using these three models are compared with each other as well as the experimental data, from the point of view of the suitability of these models for simulating the transitional flow range $(1300 \le \mathrm{Re}_H \le 2000)$ for most of the practical applications.

The experimental studies by Wang et al. (1996) and Jang et al. (1996) have investigated the effect of the number of tube rows for the plain-fin multi row (1-6 tube rows) heat exchanger. These studies have reported that from the point of view of optimization of the heat exchanger, i.e. in order to achieve the critical balance between the high heat transfer performance and low pressure drop, a four tube row configuration is the best choice for the plain-fin configuration. Similar experimental studies by Wang et al. (1997) and numerical studies by Jang et al. (1997) for the wavy-fin configuration have reported that the tube row effect is less important for the wavy-fin as compared to the plain-fin counterpart. The present numerical investigation explores in detail the effect of the tube row number on the heat transfer and flow friction characteristics for the wavy-fin configuration using six different multi-row models (1-6 tube rows) from the point of view of the heat exchanger optimization. The thermal and hydraulic performance for these six multi-row wavy-fin models have been analyzed thoroughly to estimate the optimal

number of tube rows for achieving the balance between the high thermal performance against the low pressure drop.

As stated earlier, most of the experimental and the numerical studies have reported that a four tube row configuration is the most optimum choice for the plain-fin configuration and the effect of the number of tube rows is less important for the wavy-fin configuration. No studies have been reported which investigates the effect of the longitudinal and transverse tube pitches for these optimum four tube row domains of these fins. The current numerical investigation explores the effect of the longitudinal (Ll) and the transverse (Lt) tube pitches on the heat transfer and the flow friction performance for these optimum four tube row domains of the plain and the wavy fin configurations.

A number of experimental studies by Elmahdy and Biggs (1979), McQuiston and Tree (1971) and Wang et al. (1996 and 1997) have explored the effects of fin pitch (Fp) on the thermal and hydraulic performance of the plain and wavy-fin configurations. The experimental study by Elmahdy and Biggs (1979) has shown increase in the heat transfer coefficient with the increase in the fin pitch (Fp). On the other hand the experimental work of McQuiston and Tree (1971) has shown opposite trend, i.e. decrease in heat transfer coefficient with the increase in the fin pitch (Fp) for the plain-fin configuration. While the experimental studies by Wang et al. (1996 and 1997) for the plain and wavy fin configurations have shown no significant effect of the change in fin pitch (Fp) over the thermal performance of these configurations. Numerical investigation by Jang et al. (1996) for the plain-fin configurations shows increase in the heat transfer and pressure drop with the increase in the fin pitch. While numerical investigation by Jang et al.

(1997) for the wavy-fin configurations have shown decrease in the thermal and hydraulic characteristics with the increase in the fin pitch. However, these numerical investigations by Jang et al. (1996 and 1997) for plain and wavy fin configurations have been performed for the laminar flow range $(400 \le \mathrm{Re}_H \le 1200)$. One of the objectives of this study is to investigate in detail the effects of the fin pitch (Fp) on the thermal and hydraulic characteristics for the plain and the wavy-fin configurations for the transitional flow range $(1300 \le \mathrm{Re}_H \le 2000)$.

Wavy angle (Wa) and wavy height (Wh) are the important factors which determine the heat transfer and pressure drop characteristics for the wavy-fin configuration. However, very limited experimental data is available which explores the effects of these geometrical parameters on the thermal and hydraulic performance of the wavy-fin configuration. The numerical study by Jang et al. (1997) explores the effect of these parameters on the performance of the wavy-fin configuration. Jang et al. (1997) reports that for equal wavy height, both the Nusselt number and pressure drop coefficient are increased as the wavy angle is increased; while for the equal wavy angle, they are decreased as the wavy height is increased. Again the numerical study by Jang et al. (1997) for wavy-fin configuration is reported for the laminar flow range. Another objective of this study is to investigate in detail the effects of the wavy angle (Wa) and wavy height (Wh) on the thermal and hydraulic characteristics of the wavy-fin configuration for the transitional flow range $(1300 \le \mathrm{Re}_H \le 2000)$.

In his numerical investigation for the plain-fin configuration Jang et al. (1996) has compared the effects of staggered and in-lined tube arrangements on the thermal and

hydraulic characteristics of the heat exchanger. He reports that the average heat transfer coefficient of the staggered configuration is 15-27% higher than the in-lined arrangement, while the pressure drop of the staggered configuration is 20-25% higher than that of the in-lined arrangement for the plain-fin configuration. His investigations for the plain-fin staggered configuration and the plain-fin in-lined configuration were based on the same geometrical parameters for both of these arrangements. The experimental studies by Wang et al. (1997) have reported thermal and hydraulic characteristics for the wavy-fin staggered and the wavy-fin in-lined configurations. The experimental data by Wang et al. (1997) for the wavy-fin staggered configuration and the wavy-fin in-lined configuration is not based on the same geometrical parameters for of these arrangements. The longitudinal and the transverse tube pitches for example, used by Wang et al. (1997) for the staggered and in-lined wavy-fin configurations are quite different. Therefore there is a lack of data (experimental or numerical) for comparative analysis of the wavy-fin configurations based on the tube layouts for the same geometrical parameters. One cannot use the analogy from the plain-fin configurations to the wavy-fins, since the flow structures for these two fin configurations are fairly different. The flow structure for the plain-fin configurations is pretty straightforward, since the flow gets obstructed only by the tubes. But the flow structure for the wavy-fin is rather complicated, since flow is guided by the wavy corrugations and the flow structure gets re-oriented every time the flow passes over a wavy corrugation. This difference between plain and wavy-fins definitely play role in the difference between the thermal and hydraulic characteristics for the staggered and in-lined tube layouts of these fin configurations based on the same

geometrical parameters. The current study explores in detail, the flow structure for the plain and wavy-fins in the staggered and in-lined tube layouts and the effect of this flow structure difference on the thermal and hydraulic performance of these two fins in the staggered and in-lined layouts based on the same geometrical parameters.

CHAPTER 2

PLATE-AND-FIN HEAT EXCHANGERS

This chapter briefly discusses enhanced extended surface geometries for plate-and-fin heat exchangers. Normally, at least one of the fluids used in the plate-and-fin heat exchangers is a gas. In forced convection heat transfer between a gas and a liquid, the heat transfer coefficient of the gas is typically 5-20% that of the liquid, as shown by Kays and London (1984). The use of extended surfaces reduces the gas side thermal resistance. However, the resulting gas-side resistance may still exceed that of the liquid. In this case, it is advantageous to use specially configured extended surfaces which provide increased heat transfer coefficients. Such special surface geometries may provide heat transfer coefficients 50-150% higher than those given by plain extended surfaces. For heat transfer between gases, such enhanced surfaces provide a substantial heat exchanger size reduction. There is a trend toward using enhanced surface geometries with liquids for cooling electronic equipment. Data taken for gases may be applied to liquids if Prandtl number dependency is known. Brinkman et al. (1988) provided data for water and a dielectric fluid (FC-77), but they did not provide Prandtl number dependency for their data. In the absence of specific data on Prandtl number dependency, one may assume $St \propto \mathrm{Pr}^{-2/3}$, Kays and London (1984).

The typical extended surfaces used for the plate-and-fin heat exchangers are:

1) Plain Fin
2) Offset Strip Fin
3) Perforated Fin

4) Wavy Fin

5) Louvered Fin

Two basic concepts are extensively used for the heat transfer enhancement for such extended surfaces. These are:

1) Special channel shapes, such as wavy channel, which provide mixing due to the boundary layer separation within the channel.

2) Repeated growth and wake destruction of boundary layers. This concept is employed in the offset strip fin, in louvered fin and, to some extent, in the perforated fin.

Offset Strip Fin

In case of offset strip fin, a boundary layer is developed on the short strip length, followed by its dissipation in the wake region between the strips. Typical strip lengths are 3-6 mm, and the Reynolds number is within the laminar region. As reported by Kays and London (1984), the Colburn factor (j) of the offset strip fin is about 2.5 times higher than that of the plain fin for the comparable geometries. While the friction factor (f) is about 3 times higher than that of the plain fin. Considering the ratio of the Colburn factor (j) and the friction factor (f) as the "efficiency index" ratio, the offset strip fin yields about 150% increased heat transfer coefficient and about 83% increased in the friction as that of plain fin, Kays and London (1984). Greater enhancement will be obtained by using shorter strip lengths.

Louvered Fin

The louvered fin geometry bears a similarity to the offset strip fin. But rather than offsetting the slit strips, the entire slit fin is rotated 20-45 degrees relative to the air flow direction. The louvered surface is the standard geometry for automotive radiators. For the same strip width, the louver-fin geometry provides heat transfer coefficients comparable to those of the offset strip fin. Although louvered surfaces have been in existence since 1950's, it has only been within past 20 years that serious attempts have been made to understand the flow phenomena and performance characteristics of the louvered fin. Until the flow visualization studies of Achaichia and Cowell (1988), it was assumed that the flow is parallel to the louvers. At very low Reynolds numbers, Achaichia and Cowell (1988) observed that the main flow stream did not pass through the louvers. However, at high Reynolds numbers the flow becomes nearly parallel to the louvers. Achaichia and Cowell (1988) speculated that at low air velocities the developing boundary layers on the adjacent louvers became thick enough to effectively block the passage, resulting in nearly axial flow through the array. Thus two types of flow structures exist within the louvered plate-fin array:

1) At low Reynolds numbers, a peculiar flow structure described by Achaichia and Cowell (1988) as "duct flow" is observed, where fluid travels axially through the array, essentially bypassing the louvers.
2) At high Reynolds numbers, a boundary layer flow is observed, where fluid travels parallel to the louvers.

Wavy Fin

The wavy fin extended surfaces are recognized by the peculiar corrugations which enhance the heat transfer performance in comparison to the plain plate surfaces. For a corrugated geometry having constant corrugation angles and sharp wave tips, the key parameters that affect the heat transfer performance are the wavy pitch, the corrugation angle and the fin spacing. In case of wavy fins the boundary layer is repeatedly interrupted as the flow passes over the corrugations, this redeveloping of the boundary layer from the reattachment point of the last wavy corrugation contributes to the heat transfer enhancement. The heat transfer and the flow friction performance of the wavy fin is comparable to that of the offset strip fin, as shown by the experimental studies by Kays and London (1984).

Perforated Fin

The perforated fin is manufactured by punching a pattern of spaced holes in the fin material before it is folded to form the U-shaped flow channels. If the porosity of the resulting surface is sufficiently high, heat transfer enhancement can occur due to the boundary layer dissipation in the wake region formed by the holes. The experimental studies by Kays and London (1984) show that the performance of the perforated fin is less than that of a good offset strip fin and thus the perforated fin is rarely used today. Furthermore, the perforated fin represents a wasteful way of making enhanced surface, since the material removed in making the perforated hole is relegated to the scrap.

Plain Fin

Plain fin represents simplest geometry of all the extended fin surfaces. Even though lower heat transfer performance is observed for plain fins as compared to the specially configured fin surfaces, these fin types are still widely used where low pressure drop characteristics are desired. In case of plain fin either rectangular or triangular flow channels are used. In the case of a plain fin, for a turbulent flow, standard equations of turbulent flow in circular tubes may be used to calculate Colburn factor (j) and friction factor (f). If the Reynolds number based on the hydraulic diameter is less than 2000, one may use theoretical laminar flow solutions for j and f, Kays and London (1984). The experimental studies by Kays and London (1984) provide an extensive data for the plain fin geometries. Theoretical solutions for the laminar flow have also been developed for many plain fin channel shapes. The cross sectional geometry of the plain fin channel can have very significant effect on the heat transfer and flow friction performance as shown by Kays and London (1984).

In the summary, it can be concluded that in case of a plate-and-fin heat exchanger, the fin geometry has become as increasingly important factor in the design. The high-performance offset strip, wavy and louver fins provide quite high heat transfer coefficients for gases and two-phase applications. It offers significant advantages over the traditional fin-and-round tube geometry. Key advantages are (a) lower gas pressure drop than circular tube designs and (b) the ability to have the fins normal to the gas flow over the full gas flow depth.

Early variants of the extended plate-and-fin heat exchangers were applied to gas-to-gas applications. It is now used for gases, liquids, or two-phase fluids on either side. Designs using extruded aluminum tubes with internal membranes allow quite high tube-side design pressure (e.g. 150 atm). Further innovative designs, additional applications, and advanced fin geometries are expected. The plate-and-fin heat exchangers are currently made using aluminum, steel and even ceramics.

CHAPTER 3

PROBLEM FORMULATION

Governing Equations

In this section, the laws governing the problem are explained in detail. The governing equations are subjected to the boundary conditions of the problem to formulate a solution. These expressions would then be discretized using the finite volume method to estimate the solution. The present problem involved thermal transport with convective heat transfer. Working fluid used is air with Prandtl number set to 0.736.

Assumptions about the fluid and the analysis are as follows:

1. The fluid is Newtonian, incompressible with constant physical properties.
2. The flow is assumed to be three-dimensional and steady state.
3. Viscous dissipation and viscous work are neglected.
4. No body forces.

Based on above assumptions, the problem is defined by the laws of mass, momentum and energy which are stated in the following sections. The presented study stretches from the laminar range flow $(400 \le \mathrm{Re}_H \le 1200)$ to the transitional range flow $(1300 \le \mathrm{Re}_H \le 2000)$. Equations that govern the problem are that of a laminar model for the flow in the laminar range. While for the solution of the flow in the transitional range turbulence models are used, and the equations that govern the problem in the transitional range are that of the turbulence models. The applicability of the turbulence models for the transitional range flow is explained in detail in the results section of this

thesis. Three different turbulence models were tested in the present study for the flow in the transitional range namely, *k*-ε model, RNG *k*-ε model and Baseline (BSL) *k*-ω model. The commercial CFD code CFX-5 was used to carry out the computations.

Laminar Model

The flow in the laminar range $(400 \le \mathrm{Re}_H \le 1200)$ was described by the conservation laws for mass (continuity), momentum (Navier-Stokes), and by the energy equation. The basic equations describing the three-dimensional flow are as follows:

The Continuity Equation:

$$\frac{\partial u}{\partial x} + \frac{\partial v}{\partial y} + \frac{\partial w}{\partial z} = 0 \tag{1}$$

The Momentum Equation:

x-Component:

$$\rho\left(u\frac{\partial}{\partial x}u + v\frac{\partial}{\partial y}u + w\frac{\partial}{\partial z}u\right) = -\frac{\partial p}{\partial x} + \mu\left(\frac{\partial^2 u}{\partial x^2} + \frac{\partial^2 u}{\partial y^2} + \frac{\partial^2 u}{\partial z^2}\right) \tag{2}$$

y-Component:

$$\rho\left(u\frac{\partial}{\partial x}v + v\frac{\partial}{\partial y}v + w\frac{\partial}{\partial z}v\right) = -\frac{\partial p}{\partial y} + \mu\left(\frac{\partial^2 v}{\partial x^2} + \frac{\partial^2 v}{\partial y^2} + \frac{\partial^2 v}{\partial z^2}\right) \tag{3}$$

z-Component:

$$\rho\left(u\frac{\partial}{\partial x}w + v\frac{\partial}{\partial y}w + w\frac{\partial}{\partial z}w\right) = -\frac{\partial p}{\partial z} + \mu\left(\frac{\partial^2 w}{\partial x^2} + \frac{\partial^2 w}{\partial y^2} + \frac{\partial^2 w}{\partial z^2}\right) \tag{4}$$

The Energy Equation:

$$\rho C_p\left(u\frac{\partial}{\partial x}T + v\frac{\partial}{\partial y}T + w\frac{\partial}{\partial z}T\right) = \lambda\left(\frac{\partial^2 T}{\partial x^2} + \frac{\partial^2 T}{\partial y^2} + \frac{\partial^2 T}{\partial z^2}\right) \tag{5}$$

Turbulence Models

This section briefly describes basic concepts and classification of different turbulence models. The three turbulence models tested in this study were k-ε model, RNG k-ε model and Baseline (BSL) k-ω model. The fluid flow was governed by the equations described in the following sections named after the above three turbulence models for transitional range flow $(1300 \leq \mathrm{Re}_H \leq 2000)$.

Turbulence consists of small scale fluctuations in the flow characteristics over time. It is a complex process, mainly because it is three dimensional, unsteady and chaotic, and it can have a significant effect on the characteristics of the flow. Turbulence occurs when the inertia forces in the fluid become significant compared to viscous forces, and is characterized by a high Reynolds Number.

In principle, the Navier-Stokes equations describe both laminar and turbulent flows without the need for additional information. However, turbulent flows at realistic Reynolds numbers span a large range of turbulent length and time scales and would generally involve length scales much smaller than the smallest finite volume mesh which can be practically used in a numerical analysis. The Direct Numerical Simulation (DNS) of these flows would require computing power which is many orders of magnitude higher than available in the foreseeable future.

To enable the effects of turbulence to be predicted, a large volume of CFD research has concentrated on methods which make use of turbulence models. Turbulence models have been specifically developed to account for the effects of turbulence without recourse to a prohibitively fine mesh and Direct Numerical Simulation.

Statistical Turbulence Models and the Closure Problem

When looking at time scales much larger than the time scales of turbulent fluctuations, turbulent flow could be said to exhibit average characteristics, with an additional time-varying, fluctuating component. For example, a velocity component may be divided into an average component, and a time varying component.

In general, turbulence models seek to modify the original unsteady Navier-Stokes equations by the introduction of averaged and fluctuating quantities to produce the Reynolds Averaged Navier-Stokes (RANS) equations. These equations represent the mean flow quantities only while still modeling turbulence effects, without a need for the resolution of the turbulent fluctuations. All scales of the turbulence field are being modeled. Turbulence models based on the RANS equations are known as Statistical Turbulence Models due to the statistical averaging procedure employed to obtain the equations.

Simulation of the RANS equations greatly reduces the computational effort compared to a Direct Numerical Simulation and is generally adopted for practical engineering calculations. However, the averaging procedure introduces additional unknown terms containing products of the fluctuating quantities, which act like viscous stresses in the fluid. These terms, called ‘turbulent’ or ‘Reynolds’ stresses, are difficult to determine directly and so become further unknowns.

The Reynolds (turbulent) stresses need to be modeled by additional equations of known quantities in order to achieve “closure”. Closure implies that there is a sufficient number of equations for all the unknowns, including the Reynolds-Stress tensor resulting

from the averaging procedure. The equations used to close the system define the type of turbulence model.

Reynolds Averaged Navier Stokes (RANS) Equations

As described above, turbulence models seek to solve a modified set of transport equations by introducing averaged and fluctuating components. For example, a velocity U may be divided into an average component, $\overline{U}$ and a time varying component u.

$$U = \overline{U} + u \tag{6}$$

The averaged component is given by,

$$\overline{U} = \frac{1}{\Delta t} \int_{t}^{t+\Delta t} U \cdot dt \tag{7}$$

where Δt is a time scale that is large relative to the turbulent fluctuations, but small relative to the time scale to which the equations are solved. Substituting the time averaged quantities into the original transport equations, results in the Reynolds-averaged equations for unsteady flow.

The momentum and scalar transport equations contain turbulent flux terms additional to the molecular diffusive fluxes. These are the Reynolds stress, and the Reynolds flux. These terms arise from the non-linear convective term in the un-averaged equations, not the linear diffusive one. They reflect the fact that convective transport due to turbulent velocity fluctuations will act to enhance mixing over and above that caused by thermal fluctuations at the molecular level. At high Reynolds numbers, turbulent velocity fluctuations occur over a length scale much larger than the mean free path of thermal fluctuations, so that the turbulent fluxes are much larger than the molecular fluxes.

Turbulence models close the Reynolds-averaged equations by providing models for the computation of the Reynolds stresses and Reynolds fluxes. The turbulence models can be broadly divided into two classes: eddy viscosity models and Reynolds stress models.

Eddy Viscosity Models

One proposal suggests that turbulence consists of small eddies which are continuously forming and dissipating, and in which the Reynolds stresses are assumed to be proportional to mean velocity gradients. This defines an 'eddy viscosity model'. The eddy viscosity hypothesis assumes that the Reynolds stresses can be related to the mean velocity gradients and Eddy (turbulent) Viscosity by the gradient diffusion hypothesis, in a manner analogous to the relationship between the stress and strain tensors in laminar Newtonian flow.

Analogous to the eddy viscosity hypothesis is the eddy diffusivity hypothesis, which states that the Reynolds fluxes of a scalar are linearly related to the mean scalar gradient. This formulation expresses the turbulent fluctuation terms as functions of the mean variables if the turbulent viscosity, μ_t, is known. Both the k-ε and k-ω two-equation turbulence models provide this variable.

Subject to these hypotheses, the effective viscosity μ_{eff}, and the effective diffusivity Γ_{eff} are defined for the eddy viscosity model as,

$$\mu_{eff} = \mu + \mu_t \tag{8}$$

$$\Gamma_{eff} = \Gamma + \Gamma_t \tag{9}$$

where, μ_t, is the turbulent or eddy viscosity and Γ_t is the turbulent or eddy diffusivity.

Eddy viscosity models are distinguished by the manner in which they prescribe the eddy viscosity and eddy diffusivity.

The Zero Equation Model:

Very simple eddy viscosity models compute a global value for μ_t from the mean velocity and a geometric length scale using an empirical formula. Because no additional transport equations are solved, these models are termed 'zero equation'.

The Zero Equation model is simple to implement and use, can produce approximate results very quickly, and provides a good initial guess for simulations using more advanced turbulence models. A constant turbulent eddy viscosity is calculated for the entire flow domain. The zero equation model uses an algebraic equation to calculate the viscous contribution from turbulent eddies.

The turbulence viscosity is modeled as the product of a turbulent velocity scale μ_t, and a turbulence length scale l_t, as proposed by Prandtl and Kolmogorov,

$$\mu_t = \rho f_\mu U_t l_t \tag{10}$$

Where f_μ is a proportionality constant. The velocity scale is taken to be the maximum velocity in the fluid domain. The length scale is derived as,

$$l_t = \frac{V_D^{\frac{1}{3}}}{7} \tag{11}$$

Where V_D is the fluid domain volume.

Two Equation Turbulence Models:

Two-equation models are much more sophisticated than the zero equation models. Both the velocity and length scale are solved using separate transport equations (hence the term 'two-equation').

Two-equation turbulence models are very widely used, as they offer a good compromise between numerical effort and computational accuracy. The k-ε and k-ω two-equation models have been built into most general purpose computational fluid dynamic software packages.

These models use the gradient diffusion hypothesis to relate the Reynolds stresses to the mean velocity gradients and the turbulent viscosity. The turbulent viscosity is modeled as the product of a turbulent velocity and turbulent length scale.

In two-equation models the turbulence velocity scale is computed from the turbulent kinetic energy, which is provided from the solution of its transport equation. The turbulent length scale is estimated from two properties of the turbulence field, usually the turbulent kinetic energy and its dissipation rate. The dissipation rate of the turbulent kinetic energy is provided from the solution of its transport equation.

The k-ε Model:

The k-ε (k-epsilon) model is the industry standard two-equation turbulence model. k is the turbulence kinetic energy and is defined as the variance of the fluctuations in velocity. It has dimensions of (L^2T^{-2}), e.g. m^2/s^2. ε is the turbulence eddy dissipation (the rate at

which the velocity fluctuations dissipate) and has dimensions of k per unit time (L^2T^{-3}), e.g. m^2/s^3.

The k-ε model introduces two new variables into the system of equations. The governing equations based on the assumptions for the study are as follows:

The Continuity Equation:

$$\frac{\partial u}{\partial x}+\frac{\partial v}{\partial y}+\frac{\partial w}{\partial z}=0 \tag{12}$$

The Momentum Equation:

x-Component:

$$\rho\left(\frac{\partial u}{\partial t}+u\frac{\partial}{\partial x}u+v\frac{\partial}{\partial y}u+w\frac{\partial}{\partial z}u\right)=-\frac{\partial p'}{\partial x}+\mu_{eff}\left(\frac{\partial^2 u}{\partial x^2}+\frac{\partial^2 u}{\partial y^2}+\frac{\partial^2 u}{\partial z^2}\right) \tag{13}$$

y-Component:

$$\rho\left(\frac{\partial v}{\partial t}+u\frac{\partial}{\partial x}v+v\frac{\partial}{\partial y}v+w\frac{\partial}{\partial z}v\right)=-\frac{\partial p'}{\partial y}+\mu_{eff}\left(\frac{\partial^2 v}{\partial x^2}+\frac{\partial^2 v}{\partial y^2}+\frac{\partial^2 v}{\partial z^2}\right) \tag{14}$$

z-Component:

$$\rho\left(\frac{\partial v}{\partial t}+u\frac{\partial}{\partial x}w+v\frac{\partial}{\partial y}w+w\frac{\partial}{\partial z}w\right)=-\frac{\partial p'}{\partial z}+\mu_{eff}\left(\frac{\partial^2 w}{\partial x^2}+\frac{\partial^2 w}{\partial y^2}+\frac{\partial^2 w}{\partial z^2}\right) \tag{15}$$

where p' is the modified pressure given by,

$$p'=p+\frac{2}{3}\rho k \tag{16}$$

The k-ε model, like the zero equation model, based on the eddy viscosity concept, so that,

$$\mu_{eff}=\mu+\mu_t \tag{17}$$

where μ_t is the turbulence viscosity. The *k*-ε model assumes that the turbulence viscosity is linked to the turbulence kinetic energy and dissipation via relation

$$\mu_t = C_\mu \rho \frac{k^2}{\varepsilon} \tag{18}$$

where C_μ is a constant.

The Energy Equation:

The energy equation for the turbulent heat transfer given by Thomas (1980) is as follows,

$$\rho C_p \left(\frac{\partial}{\partial t} T + u \frac{\partial}{\partial x} T + v \frac{\partial}{\partial y} T + w \frac{\partial}{\partial z} T \right) = \lambda_{eff} \left(\frac{\partial^2 T}{\partial x^2} + \frac{\partial^2 T}{\partial y^2} + \frac{\partial^2 T}{\partial z^2} \right) \tag{19}$$

where λ_{eff} is the effective thermal conductivity given by,

$$\lambda_{eff} = \lambda + \lambda_t \tag{20}$$

where λ_t is the eddy thermal conductivity given by,

$$\lambda_t = \frac{C_p \mu_t}{\mathrm{Pr}_t} \tag{21}$$

where Pr_t is the turbulent Prandtl number which is assumed to be constant in the present analysis with a value 0.9, Yuan (2000).

The values of *k* and ε come directly from the differential transport equations for the turbulence kinetic energy and turbulence dissipation rate:

$$\rho \left[\frac{\partial k}{\partial t} + \left(u \frac{\partial k}{\partial x} + v \frac{\partial k}{\partial y} + w \frac{\partial k}{\partial z} \right) \right] - \frac{\mu_{eff}}{\sigma_k} \left(\frac{\partial^2 k}{\partial x^2} + \frac{\partial^2 k}{\partial y^2} + \frac{\partial^2 k}{\partial z^2} \right) = P_k - \rho \varepsilon \tag{22}$$

$$\rho\left[\frac{\partial\varepsilon}{\partial t}+\left(u\frac{\partial\varepsilon}{\partial x}+v\frac{\partial\varepsilon}{\partial y}+w\frac{\partial\varepsilon}{\partial z}\right)\right]-\frac{\mu_{eff}}{\sigma_{\varepsilon}}\left(\frac{\partial^2\varepsilon}{\partial x^2}+\frac{\partial^2\varepsilon}{\partial y^2}+\frac{\partial^2\varepsilon}{\partial z^2}\right)=\frac{\varepsilon}{k}\left(C_{\varepsilon 1}P_k-C_{\varepsilon 2}\rho\varepsilon\right) \tag{23}$$

Where $C_{\varepsilon 1}$, $C_{\varepsilon 2}$, σ_k and σ_{ε} are constants which are given as $C_{\varepsilon 1}=1.44$, $C_{\varepsilon 2}=1.92$, $\sigma_k=1.0$ and $\sigma_{\varepsilon}=1.3$.

P_k is the shear production due to turbulence, which for incompressible flow is given by Equation (22). Here U^T is the transpose of velocity vector matrix:

$$P_k=\mu_t\left[\frac{\partial^2 U}{\partial x^2}+\frac{\partial^2 U}{\partial y^2}+\frac{\partial^2 U}{\partial z^2}+\frac{\partial U}{\partial x}\left(\frac{\partial U^T}{\partial x}\right)+\frac{\partial U}{\partial y}\left(\frac{\partial U^T}{\partial y}\right)+\frac{\partial U}{\partial z}\left(\frac{\partial U^T}{\partial z}\right)\right]$$
$$-\frac{2}{3}\left\{\left(\frac{\partial U}{\partial x}+\frac{\partial U}{\partial y}+\frac{\partial U}{\partial z}\right)\left[\mu_t\left(\frac{\partial U}{\partial x}+\frac{\partial U}{\partial y}+\frac{\partial U}{\partial z}\right)+\rho k\right]\right\} \tag{24}$$

<u>The RNG *k*-ε Model:</u>

The RNG *k*-ε model is an alternative to the standard *k*-ε model. It is based on renormalization group analysis of the Navier-Stokes equations. The transport equations for turbulence generation and dissipation are the same as those for the standard *k*-ε model, but the model constants differ, and the constant $C_{\varepsilon 1}$ is replaced by the function $C_{\varepsilon 1 RNG}$.

The transport equation for turbulence dissipation becomes:

$$\rho\left[\frac{\partial\varepsilon}{\partial t}+\left(u\frac{\partial\varepsilon}{\partial x}+v\frac{\partial\varepsilon}{\partial y}+w\frac{\partial\varepsilon}{\partial z}\right)\right]-\frac{\mu_{eff}}{\sigma_{\varepsilon RNG}}\left(\frac{\partial^2\varepsilon}{\partial x^2}+\frac{\partial^2\varepsilon}{\partial y^2}+\frac{\partial^2\varepsilon}{\partial z^2}\right)=\frac{\varepsilon}{k}\left(C_{\varepsilon 1 RNG}P_k-C_{\varepsilon 2 RNG}\rho\varepsilon\right) \tag{25}$$

where,

$$C_{\varepsilon 1RNG} = 1.42 - f_{\eta} \tag{26}$$

where f_{η} is the RNG k-ε turbulence model coefficient and is given by,

$$f_{\eta} = \frac{\eta\left(1 - \frac{\eta}{4.38}\right)}{\left(1 + \beta_{RNG}\eta^{3}\right)} \tag{27}$$

$$\eta = \sqrt{\frac{P_k}{\rho C_{\mu RNG}\varepsilon}} \tag{28}$$

The constants for the model are given as $C_{\varepsilon 1RNG} = 1.42 - f_{\eta}$, $C_{\varepsilon 2RNG} = 1.68$, $\sigma_{kRNG} = 0.7179$, $\sigma_{\varepsilon RNG} = 0.7179$, $\beta_{RNG} = 0.012$ and $C_{\mu RNG} = 0.085$.

The k-ω Model:

One of the main problems in turbulence modeling is the accurate prediction of flow separation from a smooth surface. This is an important phenomenon in many technical applications. Particularly for airplane aerodynamics, the stall characteristic of a plane is controlled by the flow separation on the wing. For this reason, the aerodynamic community has developed a number of advanced turbulence models for this application. In general, standard turbulence models based on the ε-equation predict the onset of separation too late and underpredict the amount of separation later on. This is problematic, as this behavior gives an overly optimistic performance characteristic for an airfoil. The prediction is therefore not on the conservative side from an engineering stand-point. The new models developed to solve this problem have shown a significantly

more accurate prediction of separation in a number of test cases and in industrial applications.

Currently, the most prominent two-equation models in this area are the *k*-ω based models of Menter (1994). One of the advantages of the *k*-ω formulation is the near wall treatment for low-Reynolds number computations. The model does not involve the complex non-linear damping functions required for the *k*-ε model and is therefore more accurate and more robust. A low-Reynolds number grid would require a near wall grid resolution of at least $y^+ < 2$, where y^+ is the non-dimensional near wall spacing given by Equation (43). This condition cannot be guaranteed in most applications and for this reason, a new near wall treatment was developed for the *k*-ω model. It allows for smooth shift from a low-Reynolds number form to a wall function formulation.

The Wilcox *k*-ωModel:

The starting point of the present formulation is the *k*-ω model developed by Wilcox (1986). It solves two transport equations, one for the turbulent kinetic energy, *k*, and one for the turbulent frequency, ω. The stress tensor is computed from the eddy-viscosity concept.

k-equation:

$$\rho\left[\frac{\partial k}{\partial t}+\left(u\frac{\partial k}{\partial x}+v\frac{\partial k}{\partial y}+w\frac{\partial k}{\partial z}\right)\right]=P_k-\beta'\rho k\omega+\left(\mu+\frac{\mu_t}{\sigma_k}\right)\left(\frac{\partial^2 k}{\partial x^2}+\frac{\partial^2 k}{\partial y^2}+\frac{\partial^2 k}{\partial z^2}\right) \tag{29}$$

ω-equation:

$$\rho\left[\frac{\partial\omega}{\partial t}+\left(u\frac{\partial\omega}{\partial x}+v\frac{\partial\omega}{\partial y}+w\frac{\partial\omega}{\partial z}\right)\right]=\alpha\frac{\omega}{k}P_k-\beta\rho\omega^2+\left(\mu+\frac{\mu_t}{\sigma_\omega}\right)\left(\frac{\partial^2\omega}{\partial x^2}+\frac{\partial^2\omega}{\partial y^2}+\frac{\partial^2\omega}{\partial z^2}\right) \tag{30}$$

In addition to the independent variables, the density, ρ, and the velocity vector, ***U***, are treated as known quantities from the Navier-Stokes method. *Pk* is the production rate of turbulence:

$$P_k=\mu_t 2\underline{\underline{S}}:\nabla U \tag{31}$$

with the strain rate tensor, $\underline{\underline{S}}$: given by,

$$\underline{\underline{S}}:=\frac{1}{2}\left[\left(\frac{\partial U}{\partial x}n_x+\frac{\partial U}{\partial y}n_y+\frac{\partial U}{\partial z}n_z\right)+\left(\frac{\partial U^T}{\partial x}n_x+\frac{\partial U^T}{\partial y}n_y+\frac{\partial U^T}{\partial z}n_z\right)\right] \tag{32}$$

where, n_x, n_y and n_z are unit vectors in x, y and z direction, respectively.

The model constants are given as $\beta'=0.09$, $\alpha=\frac{5}{9}$, $\beta=\frac{3}{40}$, $\sigma_k=2$ and $\sigma_\omega=2$

The unknown Reynolds stress tensor $\underline{\underline{\tau}}$, is calculated from:

$$\underline{\underline{\tau}}=\mu_t 2\underline{\underline{S}}-\rho\frac{2}{3}\delta k \tag{33}$$

In order to avoid the build-up of turbulent kinetic energy in stagnation regions, a limiter to the production term is introduced into the equations according to Menter (1994):

$$\overline{P}_k=\min\left(P_k,C_{\lim}\varepsilon\right) \tag{34}$$

with $C_{\lim}=10$

The Baseline (BSL) *k*-ω Model:

The main problem with the Wilcox model is its well known strong sensitivity to freestream conditions. Depending on the value specified for ω at the inlet, a significant variation in the results of the model can be obtained. This is undesirable and in order to solve the problem, a blending between the *k*-ω model near the surface and the *k*-ε model in the outer region was developed by Menter (1994). It consists of a transformation of the *k*-ε model to a *k*-ω formulation and a subsequent addition of the corresponding equations. The Wilcox model is thereby multiplied by a blending function F_1 and the transformed *k*-ε model by a function $1-F_1$. F_1 is equal to one near the surface and switches over to zero inside the boundary layer. At the boundary layer edge and outside the boundary layer, the standard *k*-ε model is therefore recovered.

Wilcox Model:

$$\rho\left[\frac{\partial k}{\partial t}+\left(u\frac{\partial k}{\partial x}+v\frac{\partial k}{\partial y}+w\frac{\partial k}{\partial z}\right)\right]=P_k-\beta'\rho k\omega+\left(\mu+\frac{\mu_t}{\sigma_{k1}}\right)\left(\frac{\partial^2 k}{\partial x^2}+\frac{\partial^2 k}{\partial y^2}+\frac{\partial^2 k}{\partial z^2}\right) \tag{35}$$

$$\rho\left[\frac{\partial \omega}{\partial t}+\left(u\frac{\partial \omega}{\partial x}+v\frac{\partial \omega}{\partial y}+w\frac{\partial \omega}{\partial z}\right)\right]=\alpha_1\frac{\omega}{k}P_k-\beta_1\rho\omega^2+\left(\mu+\frac{\mu_t}{\sigma_{\omega 1}}\right)\left(\frac{\partial^2 \omega}{\partial x^2}+\frac{\partial^2 \omega}{\partial y^2}+\frac{\partial^2 \omega}{\partial z^2}\right) \tag{36}$$

Transformed *k*-ω Model:

$$\rho\left[\frac{\partial k}{\partial t}+\left(u\frac{\partial k}{\partial x}+v\frac{\partial k}{\partial y}+w\frac{\partial k}{\partial z}\right)\right]=P_k-\beta'\rho k\omega+\left(\mu+\frac{\mu_t}{\sigma_{k2}}\right)\left(\frac{\partial^2 k}{\partial x^2}+\frac{\partial^2 k}{\partial y^2}+\frac{\partial^2 k}{\partial z^2}\right) \tag{37}$$

$$\rho\left[\frac{\partial\omega}{\partial t}+\left(u\frac{\partial\omega}{\partial x}+v\frac{\partial\omega}{\partial y}+w\frac{\partial\omega}{\partial z}\right)\right]=\{\ \alpha_2\frac{\omega}{k}P_k-\beta_2\rho\omega^2+\left(\mu+\frac{\mu_t}{\sigma_{\omega 2}}\right)\left(\frac{\partial^2\omega}{\partial x^2}+\frac{\partial^2\omega}{\partial y^2}+\frac{\partial^2\omega}{\partial z^2}\right)$$

$$+2\rho\sigma_{\omega 2}\frac{1}{\omega}\left(\frac{\partial k}{\partial x}n_x+\frac{\partial k}{\partial y}n_y+\frac{\partial k}{\partial z}n_z\right)\left(\frac{\partial\omega}{\partial x}n_x+\frac{\partial\omega}{\partial y}n_y+\frac{\partial\omega}{\partial z}n_z\right)\ \}$$

(38)

Now the equations of the Wilcox model are multiplied by function F_1 and the Transformed k-ω equations by a function 1-F_1 and the corresponding k- and ω- equations are added to give the BSL model:

$$\rho\left[\frac{\partial k}{\partial t}+\left(u\frac{\partial k}{\partial x}+v\frac{\partial k}{\partial y}+w\frac{\partial k}{\partial z}\right)\right]=P_k-\beta'\rho k\omega+\left(\mu+\frac{\mu_t}{\sigma_{k3}}\right)\left(\frac{\partial^2 k}{\partial x^2}+\frac{\partial^2 k}{\partial y^2}+\frac{\partial^2 k}{\partial z^2}\right) \qquad (39)$$

$$\rho\left[\frac{\partial\omega}{\partial t}+\left(u\frac{\partial\omega}{\partial x}+v\frac{\partial\omega}{\partial y}+w\frac{\partial\omega}{\partial z}\right)\right]=\{\ \alpha_3\frac{\omega}{k}P_k-\beta_3\rho\omega^2+\left(\mu+\frac{\mu_t}{\sigma_{\omega 3}}\right)\left(\frac{\partial^2\omega}{\partial x^2}+\frac{\partial^2\omega}{\partial y^2}+\frac{\partial^2\omega}{\partial z^2}\right)$$

$$+(1-F_1)2\rho\sigma_{\omega 3}\frac{1}{\omega}\left(\frac{\partial k}{\partial x}n_x+\frac{\partial k}{\partial y}n_y+\frac{\partial k}{\partial z}n_z\right)\left(\frac{\partial\omega}{\partial x}n_x+\frac{\partial\omega}{\partial y}n_y+\frac{\partial\omega}{\partial z}n_z\right)\ \} \qquad (40)$$

The coefficients of the new model are a linear combination of the corresponding coefficients of the underlying models:

$$\Phi_3=F_1\Phi_1+(1-F_1)\Phi_2 \qquad (41)$$

where the model constants are given as,

$\beta'=0.09$, $\alpha_1=\frac{5}{9}$, $\beta_1=\frac{3}{40}$, $\sigma_{k1}=2$, $\sigma_{\omega 1}=2$, $\alpha_2=0.44$, $\beta_2=0.0828$, $\sigma_{k2}=1$ and $\sigma_{\omega 2}=0.856$.

Reynolds Stress Models (RSM)

These models are based on transport equations for all components of the Reynolds stress tensor and the dissipation rate. They are suitable for strongly anisotropic flows. These models do not use the eddy viscosity hypothesis, but solve an equation for the transport of Reynolds stresses in the fluid.

The Reynolds stress model transport equations are solved for the individual stress components. The Reynolds Stress (or Second Moment Closure (SMC)) models naturally include effects of streamline curvature, sudden changes in the strain rate, secondary flows or buoyancy compared to turbulence models using the eddy-viscosity approximation.

Their general use has been limited because of the increased number of additional transport equations which leads to a reduced numerical stability and requires increased computational effort.

Algebraic Reynolds stress models solve algebraic equations for the Reynolds stresses, whereas differential Reynolds stress models solve differential transport equations individually for each Reynolds stress component.

The exact production term and the inherent modeling of stress anisotropies theoretically make Reynolds Stress models more suited to complex flows, however practice shows that they are often not superior to two-equation models. Reynolds stress models can be suited to flows where the strain fields are complex, and reproduce the anisotropic nature of turbulence itself. They are particularly useful where there is strong streamline curvature or swirl.

Modeling Flow Near the Wall

An important issue in the accurate prediction of industrial turbulent flows is the formulation and the numerical treatment of the equations in regions close to solid walls. The near-wall formulation determines the accuracy of the wall-shear-stress and the wall heat transfer predictions and has an important influence on the development of boundary layers, including the onset of separation.

Near a no-slip wall, there are strong gradients in the dependent variables and viscous effects on the transport processes are large. The representation of these processes within a numerical simulation raises the following problems:

- How to account for viscous effects at the wall.
- How to resolve the rapid variation of flow variables which occurs within the boundary layer region.

Two approaches are commonly used to model the flow in the near-wall region:

- The Wall-Function method.
- The Low-Reynolds-Number method.

In the present study the wall-function method is employed to model the flow in the near-wall region. In the wall-function approach, the viscosity affected sublayer region is bridged by employing empirical formulas to provide near-wall boundary conditions for the mean flow and turbulence transport equations. These formulas connect the wall conditions (e.g. the wall-shear-stress) to the dependent variables at the near-wall grid node which is presumed to lie in the fully-turbulent region of the boundary layer. The

major advantage of the wall-function approach is that it conserves valuable computer resources, and it avoids the need to account for viscous effects in the turbulence model.

An alternative approach to the use of wall-functions is to use a fine-grid analysis in which computations are extended through the viscosity affected sublayer close to the wall. The low-Re approach requires a very fine grid in the near-wall zone. Computer-storage and runtime requirements are usually greater than those of the wall-function approach and care must be taken to ensure good numerical resolution in the near-wall region to capture the rapid variation in variables.

Experiments have shown that the near-wall region can be subdivided into two layers. In the innermost layer, the so-called "viscous sublayer", the flow is almost laminar-like, and the (molecular) viscosity plays a dominant role in momentum and heat transfer. In the outer layer, called the "fully-turbulent layer", turbulence plays a major role. Finally there is a region between the viscous sublayer and the fully turbulent layer where the effects of molecular viscosity and turbulence are of equal importance. This region is called the log-law region.

The wall-function approach is an extension of the method of Launder and Spalding (1974). In the log-law region, the near wall tangential velocity is related to the wall-shear-stress, τ_ω, by means of a logarithmic relation.

Assuming that the logarithmic profile reasonably approximates the velocity distribution near the wall, it provides a means to numerically compute the fluid shear stress as a function of the velocity at a given distance from the wall. This is known as a

'wall function' and the logarithmic nature gives rise to the well known 'log law of the wall'.

Wall functions are still the most popular way to account for wall effects. In the present study Scalable Wall Functions are used for all turbulence models based on the ε-equation. For *k*-ω based models, an automatic near-wall treatment method is applied.

Mathematical Formulation:

The logarithmic relation for the near wall velocity is given by:

$$u^+ = \frac{U_t}{u_\tau} = \frac{1}{K}\ln\left(y^+\right) + C \tag{42}$$

Where:

$$y^+ = \frac{\rho \Delta y u_\tau}{\mu} \tag{43}$$

$$u_\tau = \left(\frac{\tau_\omega}{\rho}\right)^{1/2} \tag{44}$$

u^+ is the near wall velocity, u_τ is the frictional velocity, U_t is the known velocity tangent to the wall at a distance of Δy from the wall, y^+ is the dimensionless distance from the wall, τ_ω is the wall shear stress, *K* is the Von Karman constant and C is a log-layer constant depending on wall roughness.

Scalable Wall-Functions:

Equation (42) has the problem that it becomes singular at separation points where the near wall velocity U_t, approaches zero. In the logarithmic region, an alternative velocity scale, $u*$ can be used instead of u^+:

$$u* = C_\mu^{1/4} k^{1/2} \tag{45}$$

This scale has the useful property that it does not go to zero if U_t goes to zero (in turbulent flow k is never completely zero). Based on this definition, the following explicit equation for the wall-shear-stress is obtained:

$$\tau_\omega = \tau_{visc}\left(\frac{y*}{u^+}\right) \tag{46}$$

Where:

$$\tau_{visc} = (\mu U_t)/(\Delta y) \tag{47}$$

$$y* = (\rho u * \Delta y)/\mu \tag{48}$$

One of the major drawbacks of the wall-function approach is that the predictions depend on the location of the point nearest to the wall and are sensitive to the near-wall meshing; refining the mesh does not necessarily give a unique solution of increasing accuracy [Grotjans and Menter (1998)]. The problem of inconsistencies in the wall-function in the case of fine grids can be overcome with the use of the scalable wall-function formulation developed by the computational fluid dynamics code CFX (version 5.5.1) (2002). It can be applied on arbitrarily fine grids and allows you to perform a consistent grid refinement independent of the Reynolds number of the application.

The basic idea behind the scalable wall-function approach is to assume that the surface coincides with the edge of the viscous sublayer, which is defined to be at $y+ = 11$. This is the intersection between the logarithmic and the linear near wall profile. The computed $y+$ is not allowed to fall below this limit. Therefore, all grid points are outside the viscous sublayer and all fine grid inconsistencies are avoided.

The following equations are required to calculate τ_ω for the k-ε model:

$$u_\tau = \left(\frac{\tau_\omega}{\rho} \right)^{1/2} \tag{49}$$

$$y^+ = y \frac{\rho}{\mu} u^+ \tag{50}$$

<u>Solver Yplus and Yplus:</u>

Two variables related to $y+$ are output to the results file, Yplus and Solver Yplus.

- Yplus is based on the distance from the wall to the first node. This is the usual definition in the CFD community.
- Solver Yplus is the variable used by the CFX-5 Solver; it is based on the distance to the center of the near wall control volume. Since the first control volume off the wall is half the distance to the first node, and the center of the control volume is half of that, Solver Yplus is typically 1/4 of the value of Yplus.

There are thus two definitions for the non-dimensional near-wall spacing $y+$ used in this document. The first definition is the standard definition of $y+$ (YPLUS) as used in the scientific literature. The second definition is the value of $y+$ (SOLVER YPLUS) used inside the CFX-5 Solver for the different variants of the near-wall treatment. The two

definitions are different, as the standard definition is not suitable for separated flows due to the singularity of the logarithmic profile at locations of zero wall shear stress.

The definition of the standard $y+$ is given by the following formulation:

$$y^{+} = \frac{\sqrt{\tau_{\omega} / \rho} \cdot \Delta n}{\mu} \tag{51}$$

Where Δn is the normal distance between the wall and the first grid point off the wall.

The scalable wall function $y+$ is defined as:

$$\hat{y}^{+} = \frac{u^{*} \Delta n / 4}{\mu} \tag{52}$$

<u>Automatic Near-Wall Treatment for k-ω Based Model:</u>

While the wall-functions presented above allow for a consistent grid refinement, they are based on physical assumptions which are problematic, especially in flows at lower Reynolds numbers, as the sublayer portion of the boundary layer is neglected in the mass and momentum balance. For flows at low Reynolds numbers, this can cause an error in the displacement thickness of up to 25%. It is therefore desirable to offer a formulation which will automatically switch from wall-functions to a low-*Re* near wall formulation as the grid is refined. The k-ω model of Wilcox has the advantage that an analytical expression is known for ω in the viscous sublayer, which can be exploited to achieve this goal. The main idea behind the present formulation is to blend the wall value for ω between the logarithmic and the near wall formulation. The flux for the k-equation is

artificially kept to be zero and the flux in the momentum equation is computed from the velocity profile. The equations are as follows:

Flux for the momentum equation:

$$F_U = -\rho u_\tau u^* \tag{53}$$

With:

$$u_\tau = \sqrt{\nu \left| \frac{\Delta U}{\Delta y} \right|} \tag{54}$$

$$u^* = \max\left(\sqrt{a_1 k}, u_\tau\right) \tag{55}$$

Flux for the *k*-equation:

$$F_k = 0 \tag{56}$$

In the ω-equation, an algebraic expression is specified instead of an added flux. It is a blend between the analytical expressions for ω in the logarithmic region:

$$\omega_l = \frac{u^*}{a_1 K y} = \frac{1}{a_1 K \nu} \frac{u^{*2}}{y^+} \tag{57}$$

and the corresponding expression in the sublayer:

$$\omega_s = \frac{6\nu}{\beta(\Delta y)^2} \tag{58}$$

with Δy being the distance between the first and the second grid point. In order to achieve a smooth blending and to avoid cyclic convergence behavior, the following formulation is selected:

$$\omega_\omega = \omega_s \left[1 + \left(\frac{\omega_l}{\omega_s} \right)^2 \right]^{1/2} \tag{59}$$

While in the wall-function formulation, the first point is treated as being outside the edge of the viscous sublayer, the location of the first grid point is now virtually moved down through the viscous sublayer as the grid is refined in the low-*Re* mode. It is to be emphasized, that the physical location of the first grid point is always at the wall ($y = 0$). The error in the wall-function formulation results from this virtual shift, which amounts to a reduction in displacement thickness. This error is always present in the wall-function model, but is reduced to zero as the method shifts to the low-*Re* model. The shift is based on the distance between the first and the second grid point $\Delta y = y_2 - y_1$ with y being the wall normal distance.

CHAPTER 4

NUMERICAL METHOD

The CFD Model

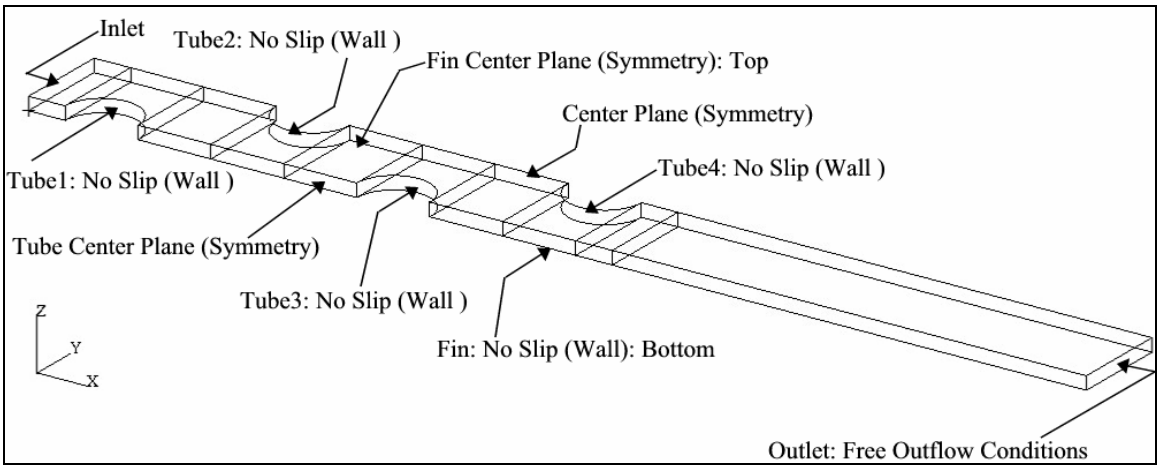

Figure 7. Computational domain and boundary conditions for plain-fin staggered configuration

Figure 7 shows computational domain for plain-fin staggered configuration along with the co-ordinate system and the boundary conditions used. The boundaries of the computational domain include inlet and outlet boundaries, symmetry planes and solid walls. The computational domain extends farther than the heat exchanger to reduce the numerical oscillations. The outlet is located seven times the tube diameter from the last downstream row cylinder.

Figure 8 shows the computational domain along with the co-ordinate system used for the plain-fin in-line, wavy-fin staggered and wavy-fin in-line configurations. The boundary conditions used for the domains in Figure 8 are same as shown in Figure 7 for the plain-fin staggered configuration.

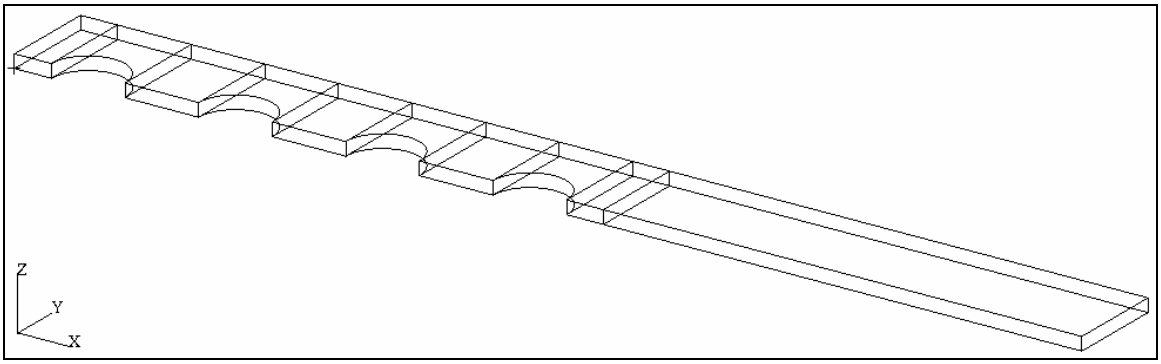

(a)

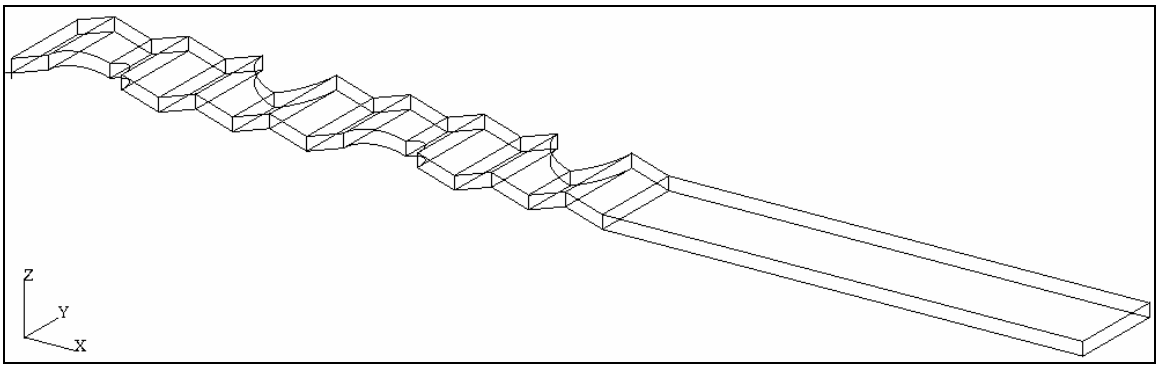

(b)

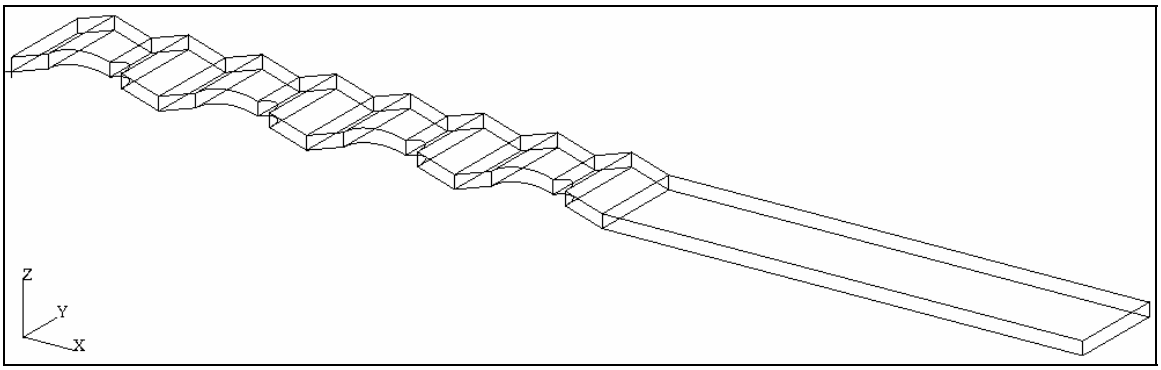

(c)

Figure 8. Computational domain and co-ordinate system used for (a) plain-fin in-lined (b) wavy-fin staggered and (c) wavy-fin in-lined configurations

Nomenclature

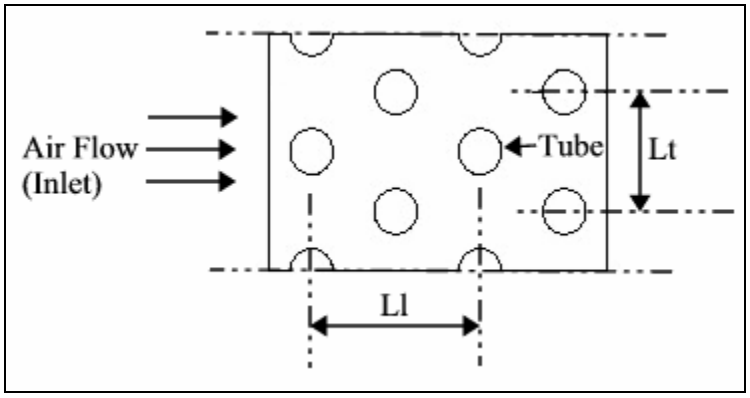

(a)

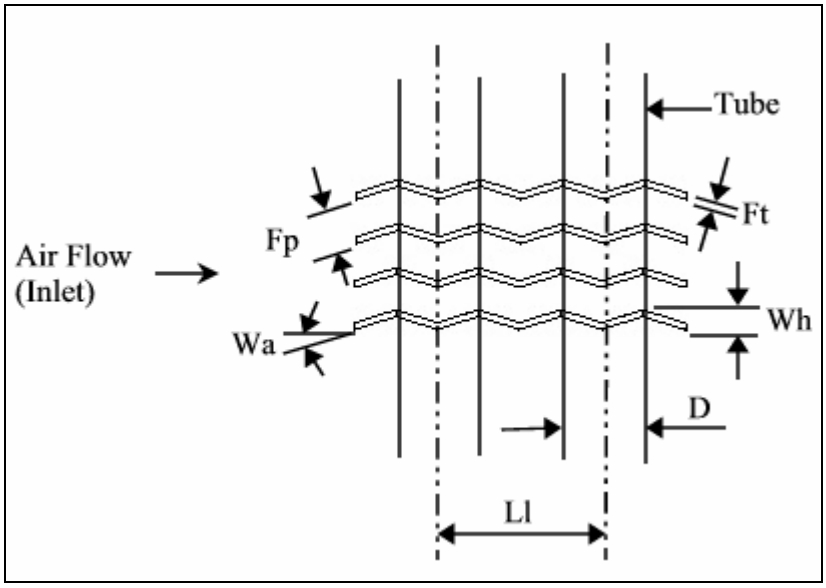

(b)

Figure 9. Nomenclature used with respect to (a) plain-fin staggered and (b) wavy-fin configuration

Figure 9 shows the nomenclature used for the plain-fin and wavy-fin configurations used in the present study. Figure 9 (a) explains the nomenclature with reference to a plain-fin staggered configuration (the tubes are in staggered order) and Figure 9 (b)

explains the nomenclature with reference to a wavy-fin configuration. Note that even though different fin configurations are used in these figures the nomenclature is the same for all four models used in the present study, i.e. plain-fin staggered, plain-fin in-line, wavy fin staggered and wavy-fin in-line configurations.

Figure 9 (a) shows the nomenclature used for longitudinal tube pitch (Ll) and transverse tube pitch (Lt). In the present study three different combinations of longitudinal tube pitches (Ll) and transverse tube pitches (Lt) are investigated for their effects on the heat transfer and pressure drop for the plain and wavy fin configurations.

Figure 9 (b) shows the nomenclature used for fin pitch (Fp), fin thickness (Ft), wavy height (Wh), wavy angle (Wa) and tube diameter (D). In the present study three different combinations of fin pitch (Fp), wavy height (Wh) and Wavy angle (Wa) are investigated for their effects on the heat transfer and pressure drop for the wavy fin configurations. The fin thickness (Ft) and the tube diameter (D) are kept constant in all the simulations.

Boundary Conditions

This section describes boundary conditions used in the present study with reference to Figure 7. Assuming symmetry conditions on the mid-plane between two fins, the bottom and top boundaries simulate the fin and the mid-plane respectively. This symmetry of the problem was used to model only one half of the domain for the computational purposes.

The boundary conditions used are as follows:

1. At the upstream boundary (inlet), uniform flow with constant velocity U_{in} and constant temperature T_{in} are assumed.
2. At the downstream end of the computational domain (outlet), streamwise gradient (Nuemann boundary conditions) for all the variables are set to zero.
3. No-slip boundary condition is used at the fin and tube surfaces. These surfaces are assumed to be solid walls with no slip wall boundary condition ($u = v = w = 0$) and constant wall temperature T_w. The fin and tubes are assumed to be made of aluminum. Since aluminum has a relatively high thermal conductivity material, constant wall temperature boundary condition can be safely assumed over the fin and tube surfaces, Jang (1996 and 1997).
4. Symmetry boundary conditions are prescribed at the center plane, tube center plane and the top symmetry plane (mid-plane between two fins) as shown in Figure 7. At theses planes zero normal velocity and zero normal gradients of all variables are assumed.

The pressure drop is expressed in terms of dimensionless pressure coefficient C_P defined as,

$$C_P = \frac{P - P_{in}}{\frac{1}{2}\rho V_{in}^{\ 2}} \tag{60}$$

Where P_{in} is the pressure at the inlet.

The heat flux Q is given by,

$$Q = mc(T - T_{in}) = \rho U A_c c(T - T_{in}) \tag{61}$$

The logarithmic mean temperature difference $LMTD$ is defined as,

$$LMTD = \frac{(T_{wall} - T) - (T_{wall} - T_{in})}{\ln\left[\frac{(T_{wall} - T)}{(T_{wall} - T_{in})}\right]} \tag{62}$$

The local heat transfer coefficient h is defined in terms of heat flux Q and the logarithmic mean temperature difference $LMTD$ as,

$$h = \frac{Q}{A_a \cdot LMTD} \tag{63}$$

The local heat transfer can be expressed in the dimensionless form by the Nusselt number Nu, defined as,

$$Nu = \frac{h \cdot H}{\lambda} = \left.\frac{\partial\left(\frac{\Theta}{\Theta_b}\right)}{\partial n}\right|_{wall} \tag{64}$$

Where n is the dimensionless unit vector normal to the wall and Θ_b is the local dimensionless bulk mean temperature defined as,

$$\Theta_b = \frac{T_b - T_w}{T_{in} - T_w} \tag{65}$$

The average heat transfer coefficient $\bar{h}$, the average pressure coefficient $\overline{C_P}$ and the average Nusselt number $\overline{Nu}$ can then be obtained by,

$$\bar{h} = \frac{\int h \cdot dA_s}{\int dA_s} \tag{66}$$

$$\overline{C_P} = \frac{\int C_p \cdot dA_s}{\int dA_s} \tag{67}$$

$$\overline{Nu} = \frac{\int Nu \cdot dA_s}{\int dA_s} \tag{68}$$

Where dA_s is the infinitesimal area of the wall surface.

The friction factor *f* and the Colburn factor *j* are defined as,

$$f = \frac{P - P_{in}}{\frac{1}{2}\rho V_{in}^{\ 2}} \times \frac{H}{4L} \tag{69}$$

$$j = \frac{\overline{Nu}}{\mathrm{Re}_H \ \mathrm{Pr}^{1/3}} \tag{70}$$

Non-Dimensionalization of Governing Equations and Associated Boundary Conditions:

For the sake of generality, the governing equations and the boundary conditions used are presented in terms of non-dimensional parameters as follows:

Dimensionless space variables:

$$x^* = \frac{x}{H} \tag{71}$$

$$y^* = \frac{y}{H} \tag{72}$$

$$z^* = \frac{z}{H} \tag{73}$$

Dimensionless velocity components:

$$u^* = \frac{u}{U_{in}} \tag{74}$$

$$v^* = \frac{v}{U_{in}} \tag{75}$$

$$w^* = \frac{w}{U_{in}} \tag{76}$$

Dimensionless pressure:

$$p^* = \frac{p}{\rho U_{in}^{\ 2}} \tag{77}$$

Dimensionless temperature:

$$\Theta = \frac{(T - T_w)}{(T_{in} - T_w)} \tag{78}$$

Dimensionless time:

$$t^* = \frac{tU_{in}}{H} \tag{79}$$

Dimensionless turbulent viscosity:

$$\mu_t^{\ *} = \frac{\mu_t}{\mu} \tag{80}$$

The above dimensionless parameters result in the following governing equations:

Laminar Model:

The Continuity Equation:

$$\frac{\partial u^*}{\partial x^*} + \frac{\partial v^*}{\partial y^*} + \frac{\partial w^*}{\partial z^*} = 0 \tag{81}$$

The Momentum Equation:

x-Component:

$$u^* \frac{\partial}{\partial x^*} u^* + v^* \frac{\partial}{\partial y^*} u^* + w^* \frac{\partial}{\partial z^*} u^* = -\frac{\partial p^*}{\partial x^*} + \frac{1}{\mathrm{Re}_H} \left(\frac{\partial^2 u^*}{\partial x^{*2}} + \frac{\partial^2 u^*}{\partial y^{*2}} + \frac{\partial^2 u^*}{\partial z^{*2}} \right) \tag{82}$$

y-Component:

$$u^* \frac{\partial}{\partial x^*} v^* + v^* \frac{\partial}{\partial y^*} v^* + w^* \frac{\partial}{\partial z^*} v^* = -\frac{\partial p^*}{\partial y^*} + \frac{1}{\mathrm{Re}_H} \left(\frac{\partial^2 v^*}{\partial x^{*2}} + \frac{\partial^2 v^*}{\partial y^{*2}} + \frac{\partial^2 v^*}{\partial z^{*2}} \right) \tag{83}$$

z-Component:

$$u^* \frac{\partial}{\partial x^*} w^* + v^* \frac{\partial}{\partial y^*} w^* + w^* \frac{\partial}{\partial z^*} w^* = -\frac{\partial p^*}{\partial z^*} + \frac{1}{\mathrm{Re}_H} \left(\frac{\partial^2 w^*}{\partial x^{*2}} + \frac{\partial^2 w^*}{\partial y^{*2}} + \frac{\partial^2 w^*}{\partial z^{*2}} \right) \tag{84}$$

The Energy Equation:

$$u^* \frac{\partial}{\partial x^*} \Theta + v^* \frac{\partial}{\partial y^*} \Theta + w^* \frac{\partial}{\partial z^*} \Theta = \frac{1}{\mathrm{Re}_H \, \mathrm{Pr}} \left(\frac{\partial^2 \Theta}{\partial x^{*2}} + \frac{\partial^2 \Theta}{\partial y^{*2}} + \frac{\partial^2 \Theta}{\partial z^{*2}} \right) \tag{85}$$

The non-dimensional parameters appearing in the laminar model governing equations are as follows:

$$\mathrm{Re}_H = \frac{\rho U_{in} H}{\mu} \tag{86}$$

$$\mathrm{Pr} = \frac{\mu C_p}{\lambda} \tag{87}$$

Turbulence Models:

The Continuity Equation:

$$\frac{\partial u^*}{\partial x^*} + \frac{\partial v^*}{\partial y^*} + \frac{\partial w^*}{\partial z^*} = 0 \tag{88}$$

The Momentum Equation:

x-Component:

$$\frac{\partial u^*}{\partial t^*} + u^* \frac{\partial}{\partial x^*} u^* + v^* \frac{\partial}{\partial y^*} u^* + w^* \frac{\partial}{\partial z^*} u^* = -\frac{\partial p'^*}{\partial x^*} + \frac{1}{(\mathrm{Re}_H)_T} \left(\frac{\partial^2 u^*}{\partial x^{*2}} + \frac{\partial^2 u^*}{\partial y^{*2}} + \frac{\partial^2 u^*}{\partial z^{*2}} \right) \tag{89}$$

y-Component:

$$\frac{\partial v^*}{\partial t^*} + u^* \frac{\partial}{\partial x^*} v^* + v^* \frac{\partial}{\partial y^*} v^* + w^* \frac{\partial}{\partial z^*} v^* = -\frac{\partial p'^*}{\partial y^*} + \frac{1}{(\mathrm{Re}_H)_T} \left(\frac{\partial^2 v^*}{\partial x^{*2}} + \frac{\partial^2 v^*}{\partial y^{*2}} + \frac{\partial^2 v^*}{\partial z^{*2}} \right) \tag{90}$$

z-Component:

$$\frac{\partial w^*}{\partial t^*} + u^* \frac{\partial}{\partial x^*} w^* + v^* \frac{\partial}{\partial y^*} w^* + w^* \frac{\partial}{\partial z^*} w^* = -\frac{\partial p'^*}{\partial z^*} + \frac{1}{(\mathrm{Re}_H)_T} \left(\frac{\partial^2 w^*}{\partial x^{*2}} + \frac{\partial^2 w^*}{\partial y^{*2}} + \frac{\partial^2 w^*}{\partial z^{*2}} \right) \tag{91}$$

where p'^* is the modified dimensionless pressure given by,

$$p'^* = \frac{p + \rho k}{\rho U_{in}^{\ 2}} \tag{92}$$

The Energy Equation:

$$\frac{\partial \Theta}{\partial t^*} + u^* \frac{\partial}{\partial x^*} \Theta + v^* \frac{\partial}{\partial y^*} \Theta + w^* \frac{\partial}{\partial z^*} \Theta = \frac{1}{(\mathrm{Re}_H)_T (\mathrm{Pr})_T} \left(\frac{\partial^2 \Theta}{\partial x^{*2}} + \frac{\partial^2 \Theta}{\partial y^{*2}} + \frac{\partial^2 \Theta}{\partial z^{*2}} \right) \tag{93}$$

The non-dimensional parameters appearing in the turbulence model governing equations are as follows:

$$\left(\mathrm{Re}_H\right)_T = \frac{\rho U_{in} H}{\mu_{eff}} \tag{94}$$

$$\left(\mathrm{Pr}\right)_T = \frac{\mu_{eff} C_p}{\lambda_{eff}} \tag{95}$$

Non-Dimensional Boundary Conditions:

Non-dimensional boundary conditions are explained with respect to Figure 7. The non-dimensional boundary conditions used in the present investigation are as follows:

The upstream boundary (Inlet):

$$u^* = 1 \tag{96}$$

$$\Theta = 1 \tag{97}$$

$$v^* = w^* = 0 \tag{98}$$

Fin and tube wall surfaces (no-slip conditions):

$$u^* = v^* = w^* = 0 \tag{99}$$

$$\Theta = 0 \tag{100}$$

The downstream boundary (Outlet):

$$\frac{\partial u^*}{\partial x^*} = \frac{\partial v^*}{\partial x^*} = \frac{\partial w^*}{\partial x^*} = 0 \tag{101}$$

Top symmetry boundary on the X-Y plane:

$$\frac{\partial u^*}{\partial z^*} = \frac{\partial v^*}{\partial z^*} = \frac{\partial \Theta}{\partial z^*} = 0 \tag{102}$$

$$w^* = 0 \tag{103}$$

Side symmetry boundaries on the X-Z plane:

$$\frac{\partial u^*}{\partial y^*} = \frac{\partial w^*}{\partial y^*} = \frac{\partial \Theta}{\partial y^*} = 0 \tag{104}$$

$$v^* = 0 \tag{105}$$

Computation Grid System

The commercial computational fluid dynamics code CFX-5 (2002) was employed to carry out the present numerical investigation. CFX-5 uses Advancing Front and Inflation (AFI) mesher routine to mesh the domain surfaces and domain volume. When definition file is being written AFI first creates a 'front' of triangular mesh elements on the surfaces of the fluid domain using surface mesher routine. Once the surface mesh is created AFI then creates domain volume mesh from the front of the surface mesh. The volume mesh consists of tetrahedral elements.

Figure 10 shows one such tetrahedral element employed by CFX-5 for the domain volume mesh.

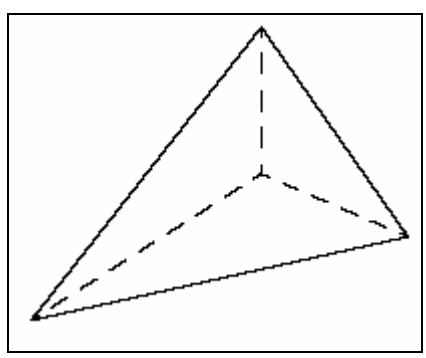

Figure 10. Tetrahedral volume mesh element

Figure 11 shows the surface grid system with triangular mesh elements used for the plain-fin staggered, plain-fin in-line, wavy-fin staggered and wavy-fin in-line

configurations. Note that when using CFX-5 (version 5.5.1) one can only count the total number of node points in the domain volume. But one can not visualize the actual tetrahedral volume mesh. Hence the figure shows only the surface mesh with triangular mesh elements and not the entire fluid domain volume mesh with tetrahedral mesh elements.

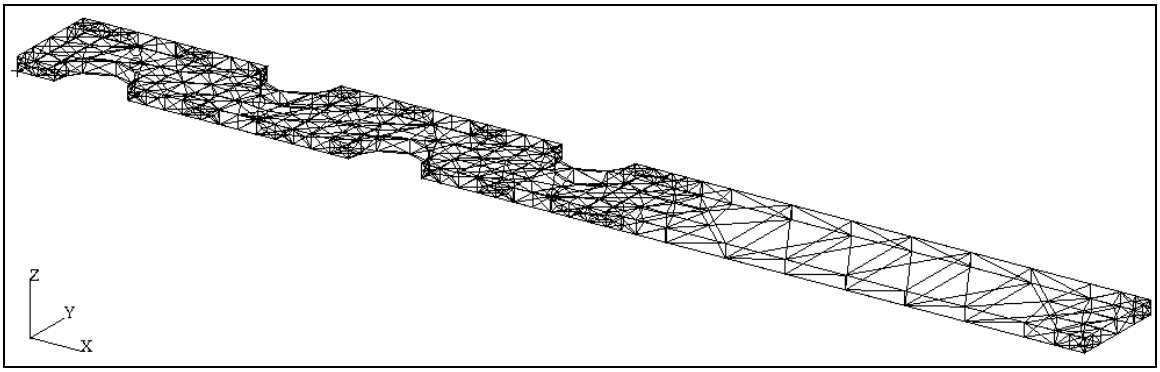

(a)

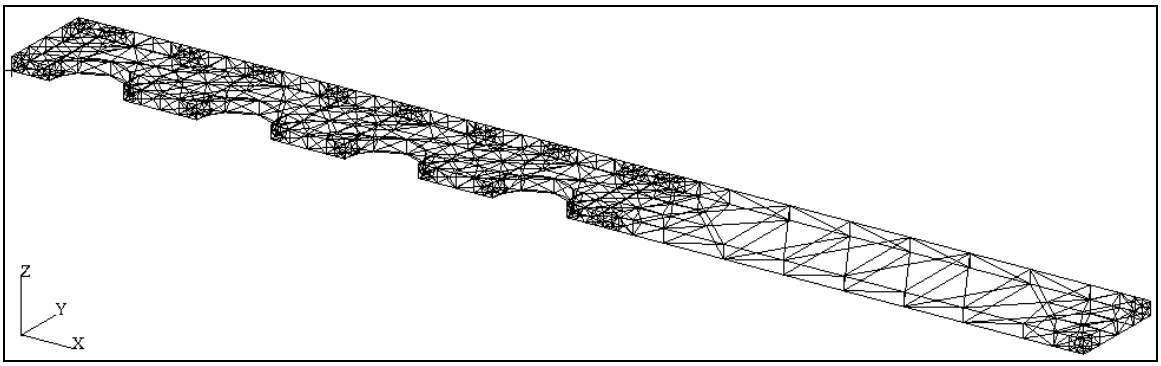

(b)

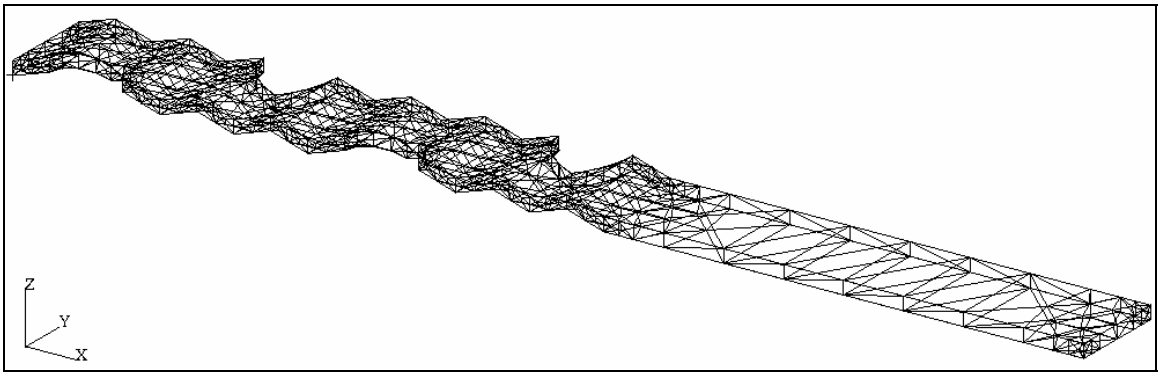

(c)

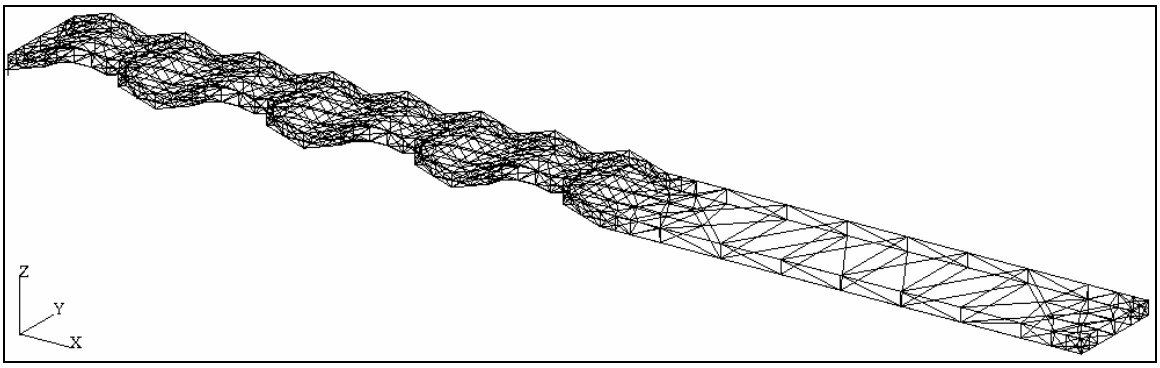

(d)

Figure 11. Surface grid system with triangular mesh elements used for (a) plain-fin staggered (b) plain-fin in-lined (c) wavy-fin staggered and (d) wavy-fin in-lined configurations

Numerical Procedure

The first step of numerical simulation is to discretize the governing equations to reduce the governing partial differential equations to a set of algebraic equations. The computational fluid dynamics (CFD) code CFX-5 uses finite volume method (FVM) in conjunction with an algebraic multi-grid method to solve the resulting scalar system of equations for the dependent variable in each control volume. This approach involves discretizing the spatial domain into finite control volumes using the mesh. The governing

equations are integrated over each control volume, such that relevant quantity (mass, momentum, energy etc.) is conserved in a discrete sense for each control volume. The CFX-5 solver rapidly removes local errors in the solution, and an algebraic multi-grid scheme is used to accelerate the convergence of the solver by computing the corrections on a series of coarse grid levels. In all simulations, the second-order upwind scheme is used for the discretization of the momentum and energy equations.

CFX-5 uses a coupled solver, which solves the hydrodynamic equations (for u, v, w, p) as a single system. This solution approach uses a fully implicit discretisation of the equations at any given time step. For steady state problems the time-step behaves like an 'acceleration parameter', to guide the approximate solutions in a physically based manner to a steady-state solution. This reduces the number of iterations required for convergence to a steady state.

Figure 12 shows a flow chart that illustrates the general solution procedure. The solution of each set of equations shown in the flow chart consists of two numerically intensive operations. For each time-step:

1. The non-linear equations are linearized (coefficient iteration) and assembled into the solution matrix.
2. The linear equations are solved (equation solution iteration) using an algebraic multi-grid method.

The time-step iteration is controlled by the physical time-step (global) or local time-step factor (local) setting to advance the solution in time for a steady state simulation. In this case, there is only one linearization (coefficient) iteration per time-step.

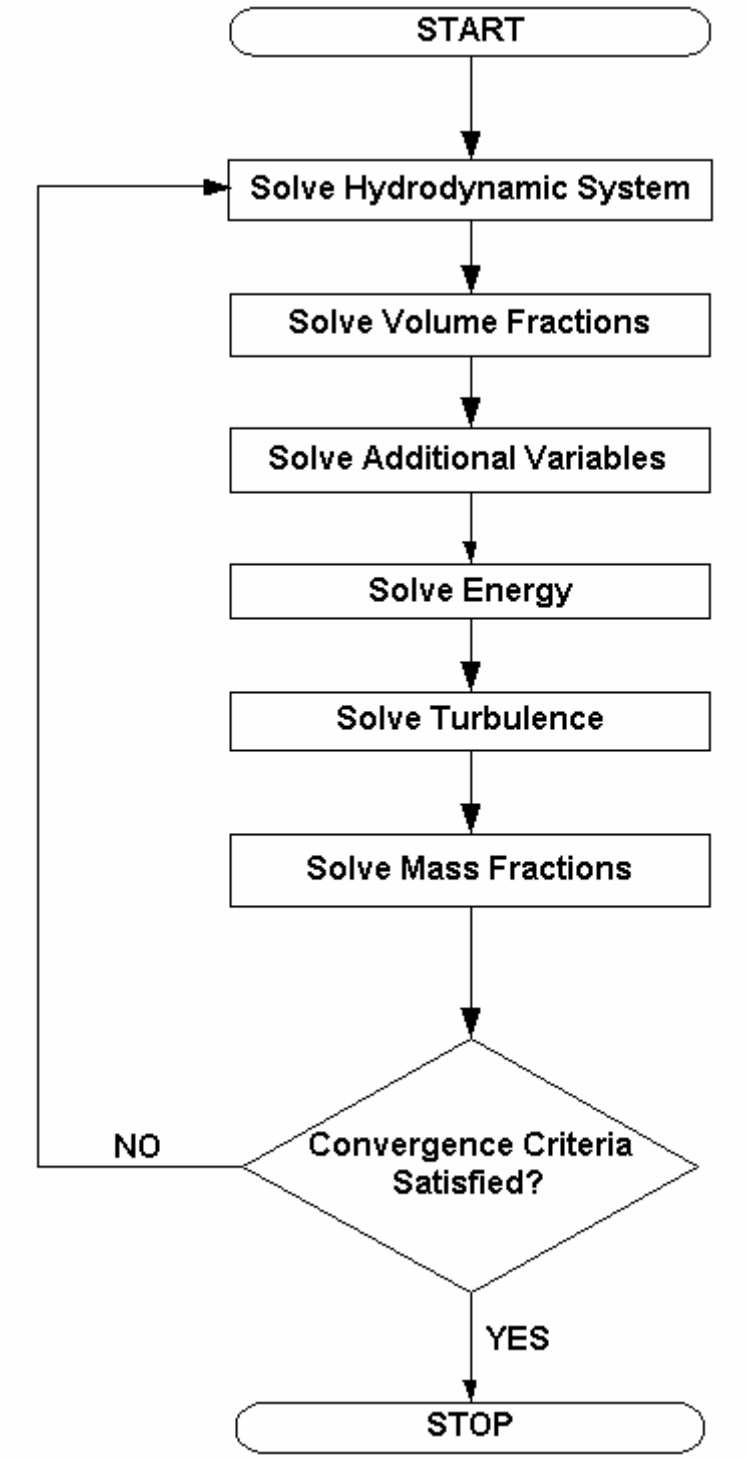

Figure 12. Algorithm incorporated by CFX-5

CHAPTER 5

GRID INDEPENDENCE

In order to minimize the computation time with a desired level of accuracy, the grid independence test is required. The computational time increases with an increase in the number of elements. On the other hand, a coarser grid may give misleading results with steep gradients. The computational mesh was chosen so that accurate results can be obtained and the computational time is minimum. The following is an overview of the mesh refinement test.

Grid was denser in the region of the tubes, because of the high velocity, pressure and temperature gradients produced as the flow passes over the tubes. Grid independence tests with three different grid sizes were conducted to establish the accuracy of the results. The numbers of the nodes in the grid were doubled for each grid size test.

For laminar flow range $(400 \le \mathrm{Re}_H \le 1200)$, grid independence test was carried out for the highest Reynolds number i.e. Re_H = 1200. And for the transitional flow range $(1300 \le \mathrm{Re}_H \le 2000)$, grid independence test was also carried out for the highest Reynolds number i.e. Re_H = 2000. A case with higher process parameters ensured that the grid would be effective for lower values of the process parameters as well. These tests were taken for plain fin staggered configuration and wavy-fin staggered configurations. For plain-fin in-line configuration and wavy-fin in-line configuration same optimal grid sizes were used as obtained from the tests on the staggered configurations, since

geometrical parameters for plain and wavy in-line configurations were same as that of plain and wavy staggered configurations respectively.

The domain system configurations for the grid independence tests are shown in the Table 1. These domain configurations are taken as per the experimental studies by Wang et al. (1996 and 1997).

Table 1. Geometrical Parameters for the fin configurations for the Grid Independence

	Ll (mm)	Lt (mm)	Fp (mm)	Ft (mm)	D (mm)	Wa (Degrees)	Wh (mm)
Plain Fin Staggered Configuration	22	25.4	3.00	0.13	9.5	-	-
Wavy Fin Staggered Configuration	19.05	25.4	3.53	0.12	9.525	17.5	1.5

Laminar Flow Range

As stated earlier, the laminar flow range $(400 \le \mathrm{Re}_H \le 1200)$ was investigated with a laminar flow model, while transitional flow range $(1300 \le \mathrm{Re}_H \le 2000)$ was investigated using three different turbulence models. This section describes grid independence tests taken for plain-staggered and wavy-fin staggered configurations for laminar flow range and using the laminar model. These tests are taken at Re_H=1200. Tables 2 and 3 show different grid resolutions used for plain-fin staggered and wavy-fin staggered configurations for the laminar flow range.

Table 2. Different grid resolutions for the plain-fin staggered configuration for the laminar range flow

Plain-Fin Staggered Configuration (Laminar Model)	Reynolds Number (Re_H)	Number of Nodes
Test 1	1200	5250
Test 2	1200	10500
Test 3	1200	21000

Table 3. Different grid resolutions for the wavy-fin staggered configuration for the laminar range flow

Wavy-Fin Staggered Configuration (Laminar Model)	Reynolds Number (Re_H)	Number of Nodes
Test 1	1200	6300
Test 2	1200	12600
Test 3	1200	25200

Plain-Fin Staggered Configuration:

Grid independence tests with three different grid sizes (5250, 10500 and 21000 nodes) were conducted to establish the accuracy of the results. The variation of the temperature distribution along the domain centerline from inlet to the outlet was investigated to establish the independence of the temperature distribution for a given number of nodes in the computational domain. The results of the grid independence tests are shown in Figure 13.

The maximum temperature difference along the domain centerline between the cases with 5250 and 10500 nodes was 2.93%. While, the maximum temperature difference along the domain centerline between the cases with 10500 and 21000 nodes was 0.74%.

Therefore, the grid with 10500 nodes was chosen for the current investigation to ensure accuracy of the results with minimum computational time.

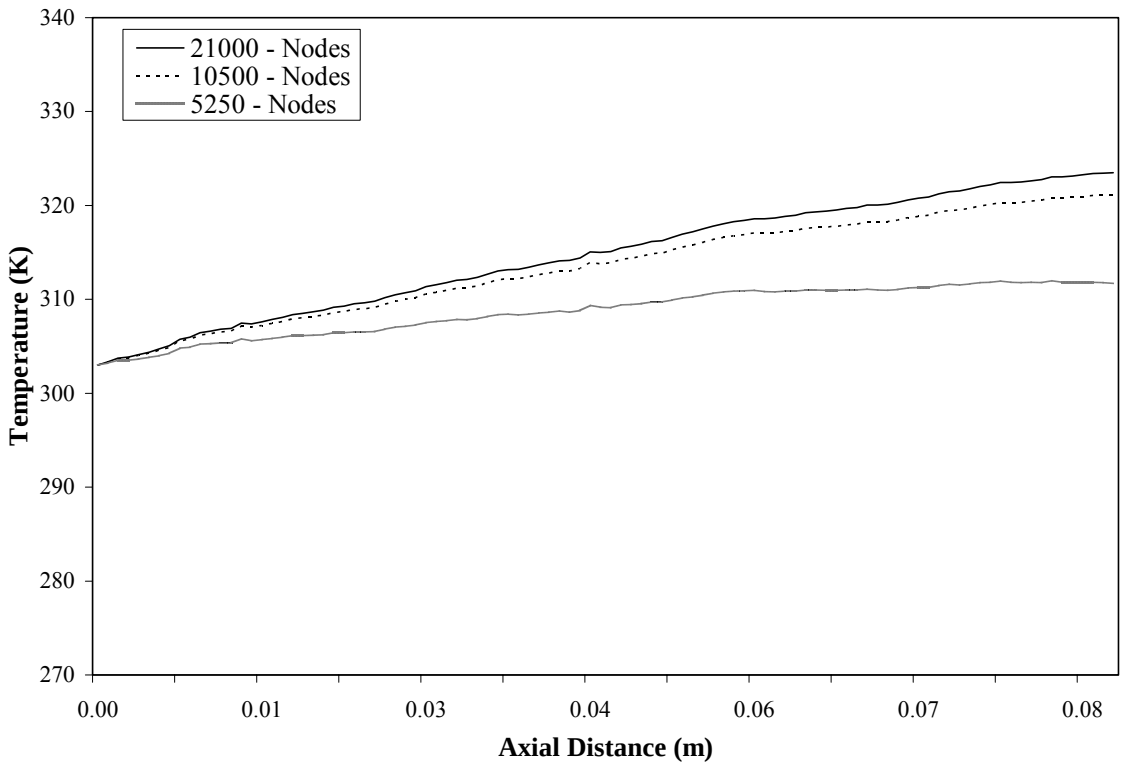

Figure 13. Domain centerline temperature profiles for different grid resolutions for plain-fin staggered configuration for the laminar range flow

Wavy-Fin Staggered Configuration:

Grid independence tests with three different grid sizes (6300, 12600 and 25200 nodes) were conducted to establish the accuracy of the results. Here again, the variation of the temperature distribution along the domain centerline from inlet to the outlet was investigated to establish the independence of the temperature distribution for a given number of nodes in the computational domain. The results of the grid independence tests are shown in Figure 14.

The maximum temperature difference along the domain centerline between the cases with 6300 and 12600 nodes was 2.87%. While, the maximum temperature difference along the domain centerline between the cases with 12600 and 25200 nodes was 0.62%. Therefore, the grid with 12600 nodes was chosen for the current investigation to ensure accuracy of the results with minimum computational time.

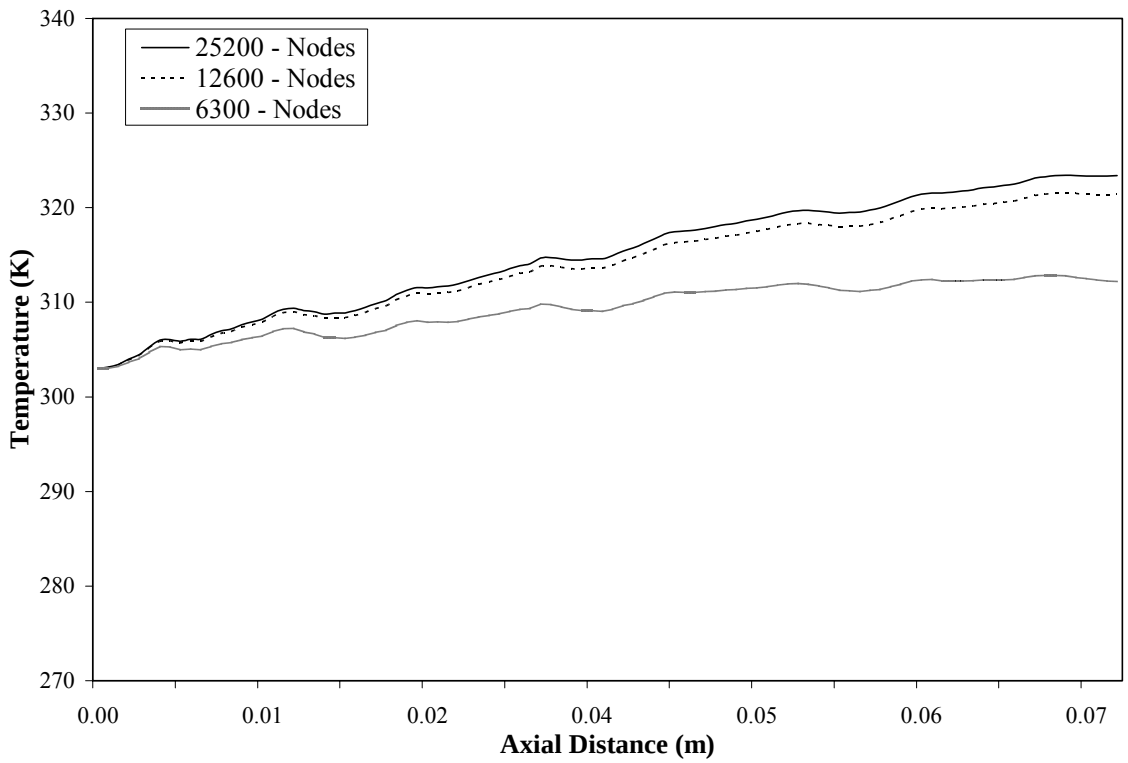

Figure 14. Domain centerline temperature profiles for different grid resolutions for wavy-fin staggered configuration for the laminar range flow

Transitional Flow Range

Transitional flow range $(1300 \le \mathrm{Re}_H \le 2000)$ was investigated using three different turbulence models namely k-ε model, RNG k-ε model and k-ω model. This section describes grid independence tests taken for plain-staggered and wavy-fin staggered

configurations for transitional flow range and using the above mentioned models. These tests are taken at Re_H =2000.

The k-ε Model

This section describes the grid independency tests taken on plain-fin staggered configuration and wavy-fin staggered configuration using the *k*-ε model. Tables 4 and 5 show different grid resolutions used for plain-fin staggered and wavy-fin staggered configurations for the *k*-ε model study.

Table 4. Different grid resolutions for the plain-fin staggered configuration for the transitional range flow (*k*-ε model)

Plain-Fin Staggered Configuration (*k*-ε Model)	Reynolds Number (Re_H)	Number of Nodes
Test 1	2000	11200
Test 2	2000	22400
Test 3	2000	44800

Table 5. Different grid resolutions for the wavy-fin staggered configuration for the transitional range flow (*k*-ε model)

Wavy-Fin Staggered Configuration (*k*-ε Model)	Reynolds Number (Re_H)	Number of Nodes
Test 1	2000	12400
Test 2	2000	24800
Test 3	2000	49600

Plain-Fin Staggered Configuration:

Grid independence tests with three different grid sizes (11200, 22400 and 44800 nodes) were conducted to establish the accuracy of the results for the k-ε model. The variation of the temperature distribution along the domain centerline from inlet to the outlet was investigated to establish the independence of the temperature distribution for a given number of nodes in the computational domain. The results of the grid independence tests are shown in Figure 15.

The maximum temperature difference along the domain centerline between the cases with 11200 and 22400 nodes was 2.36%. While, the maximum temperature difference along the domain centerline between the cases with 22400 and 44800 nodes was 0.65%. Therefore, the grid with 22400 nodes was chosen for the current investigation to ensure accuracy of the results with minimum computational time.

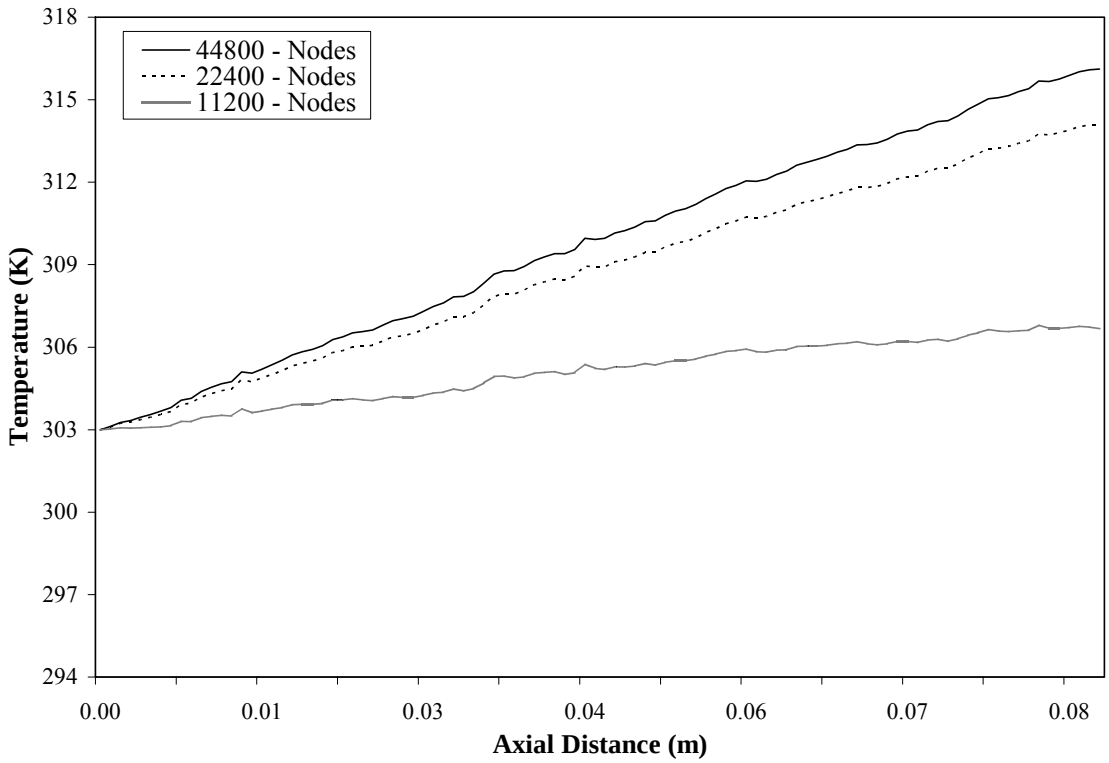

Figure 15. Domain centerline temperature profiles for different grid resolutions for plain-fin staggered configuration for the transitional range flow (k-ε model)

Wavy-Fin Staggered Configuration:

Grid independence tests with three different grid sizes (12400, 24800 and 49600 nodes) were conducted to establish the accuracy of the results. The variation of the temperature distribution along the domain centerline from inlet to the outlet was investigated to establish the independence of the temperature distribution for a given number of nodes in the computational domain. The results of the grid independence tests are shown in Figure 16.

The maximum temperature difference along the domain centerline between the cases with 12400 and 24800 nodes was 2.25%. While, the maximum temperature difference

along the domain centerline between the cases with 24800 and 49600 nodes was 0.58%. Therefore, the grid with 24800 nodes was chosen for the current investigation to ensure accuracy of the results with minimum computational time.

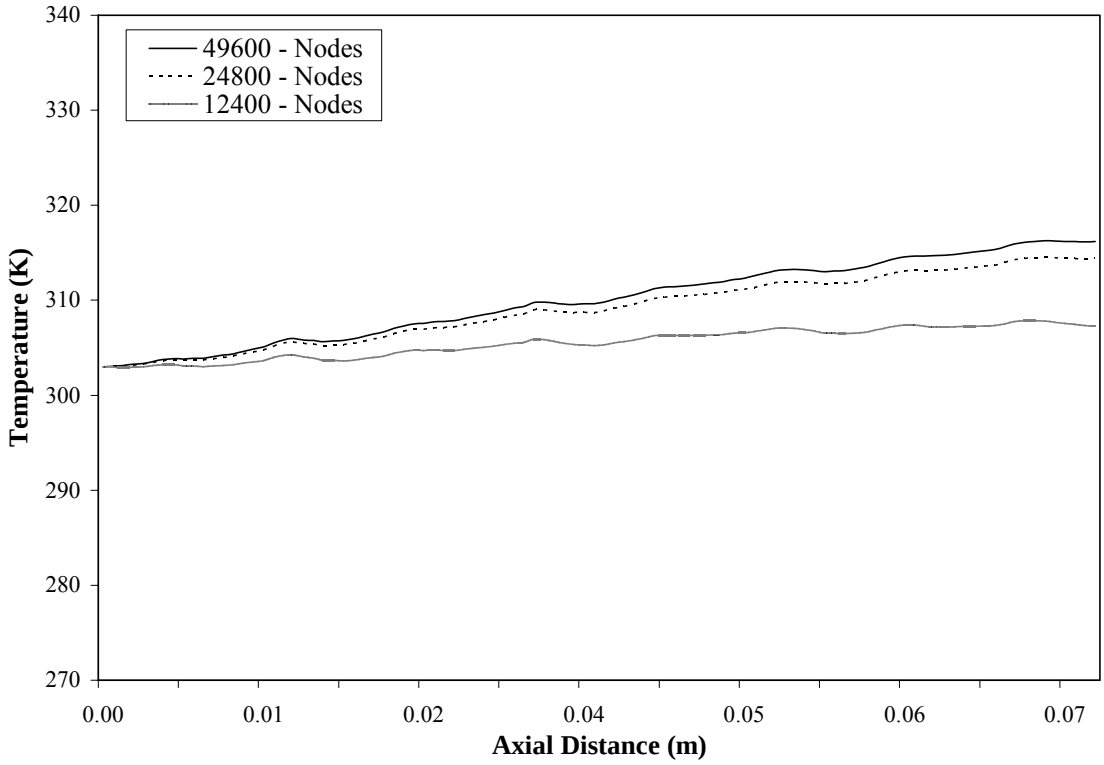

Figure 16. Domain centerline temperature profiles for different grid resolutions for wavy-fin staggered configuration for the transitional range flow (k-ε model)

The RNG k-ε Model

This section describes the grid independency tests taken on plain-fin staggered configuration and wavy-fin staggered configuration using the RNG k-ε model. Tables 6 and 7 show different grid resolutions used for plain-fin staggered and wavy-fin staggered configurations for the RNG k-ε model study.

Table 6. Different grid resolutions for the plain-fin staggered configuration for the transitional range flow (RNG *k*-ε model)

Plain-Fin Staggered Configuration (RNG *k*-ε Model)	Reynolds Number (Re_H)	Number of Nodes
Test 1	2000	11200
Test 2	2000	22400
Test 3	2000	44800

Table 7. Different grid resolutions for the wavy-fin staggered configuration for the transitional range flow (RNG *k*-ε model)

Wavy-Fin Staggered Configuration (RNG *k*-ε Model)	Reynolds Number (Re_H)	Number of Nodes
Test 1	2000	12400
Test 2	2000	24800
Test 3	2000	49600

Plain-Fin Staggered Configuration:

Grid independence tests with three different grid sizes (11200, 22400 and 44800 nodes) were conducted to establish the accuracy of the results. The variation of the temperature distribution along the domain centerline from inlet to the outlet was investigated to establish the independence of the temperature distribution for a given number of nodes in the computational domain. The results of the grid independence tests are shown in Figure 17.

The maximum temperature difference along the domain centerline between the cases with 11200 and 22400 nodes was 2.41%. While, the maximum temperature difference along the domain centerline between the cases with 22400 and 44800 nodes was 0.79%.

Therefore, the grid with 22400 nodes was chosen for the current investigation to ensure accuracy of the results with minimum computational time.

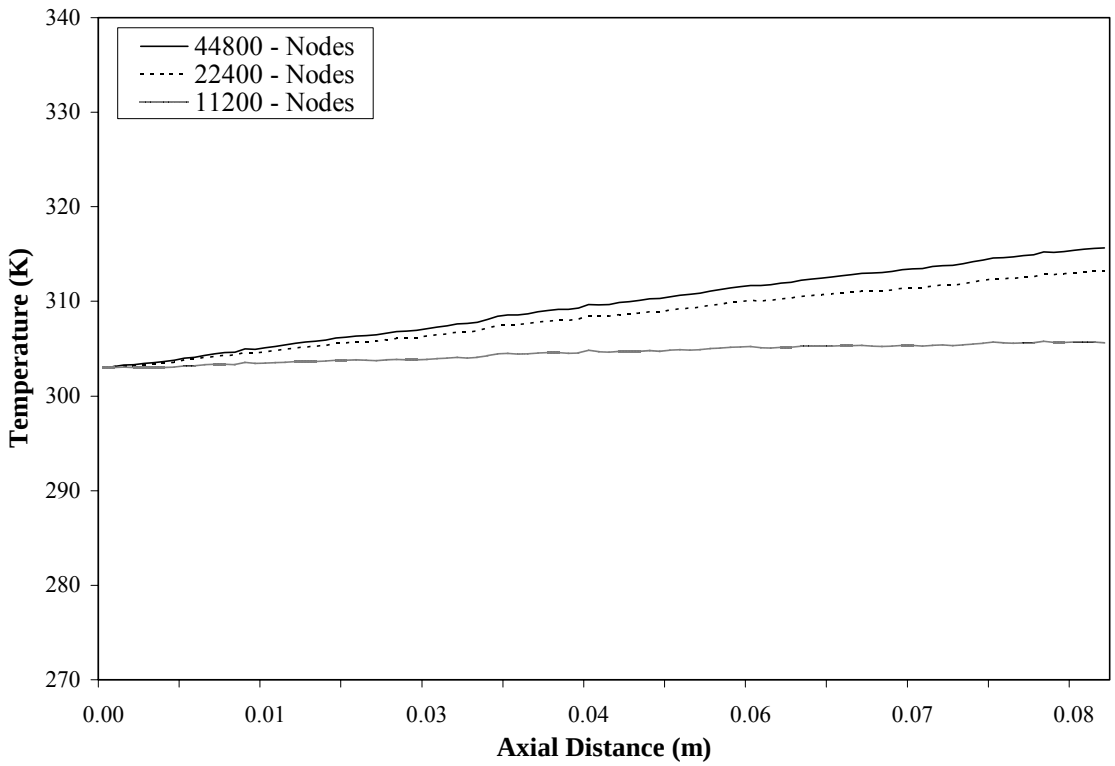

Figure 17. Domain centerline temperature profiles for different grid resolutions for plain-fin staggered configuration for the transitional range flow (RNG *k*-ε model)

Wavy-Fin Staggered Configuration:

Grid independence tests with three different grid sizes (12400, 24800 and 49600 nodes) were conducted to establish the accuracy of the results. The variation of the temperature distribution along the domain centerline from inlet to the outlet was investigated to establish the independence of the temperature distribution for a given number of nodes in the computational domain. The results of the grid independence tests are shown in Figure 18.

The maximum temperature difference along the domain centerline between the cases with 12400 and 24800 nodes was 2.34%. While, the maximum temperature difference along the domain centerline between the cases with 24800 and 49600 nodes was 0.73%. Therefore, the grid with 24800 nodes was chosen for the current investigation to ensure accuracy of the results with minimum computational time.

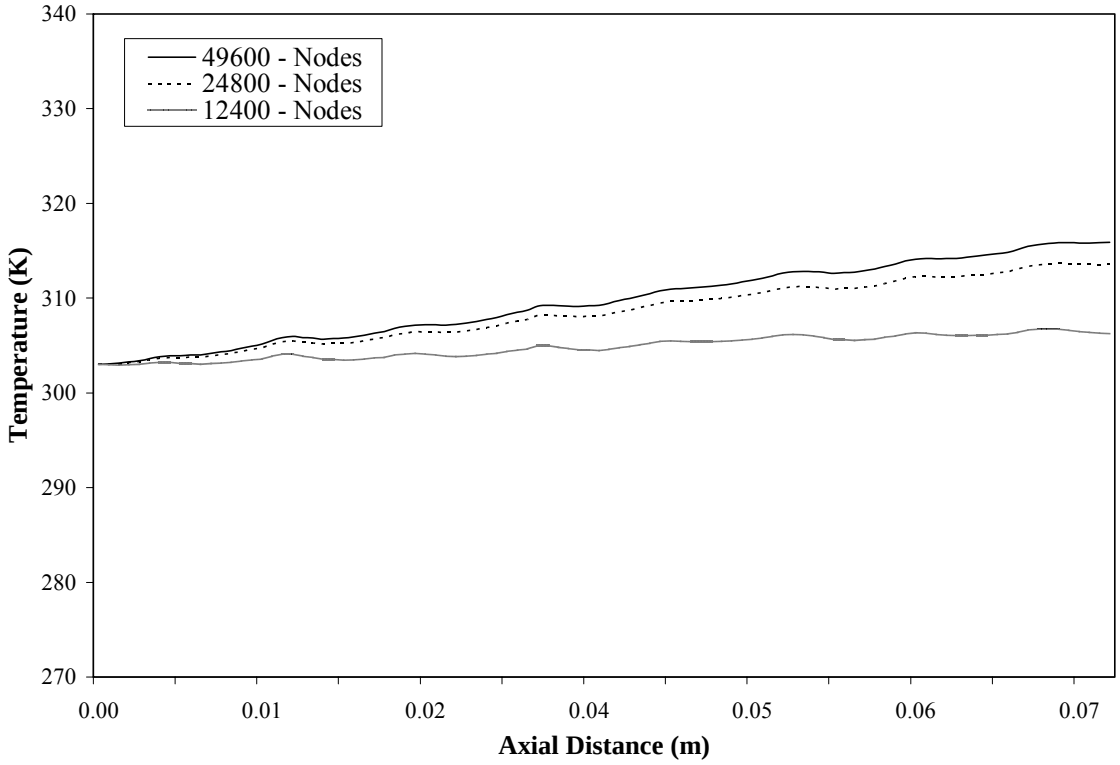

Figure 18. Domain centerline temperature profiles for different grid resolutions for wavy-fin staggered configuration for the transitional range flow (RNG *k*-ε model)

The k-ω Model

This section describes the grid independency tests taken on plain-fin staggered configuration and wavy-fin staggered configuration using the k-ω model. Tables 8 and 9 show different grid resolutions used for plain-fin staggered and wavy-fin staggered configurations for the k-ω model study.

Table 8. Different grid resolutions for the plain-fin staggered configuration for the transitional range flow (k-ω model)

Plain-Fin Staggered Configuration (k-ω Model)	Reynolds Number (Re_H)	Number of Nodes
Test 1	2000	11200
Test 2	2000	22400
Test 3	2000	44800

Table 9. Different grid resolutions for the wavy-fin staggered configuration for the transitional range flow (k-ω model)

Wavy-Fin Staggered Configuration (k-ω Model)	Reynolds Number (Re_H)	Number of Nodes
Test 1	2000	12400
Test 2	2000	24800
Test 3	2000	49600

Plain-Fin Staggered Configuration:

Grid independence tests with three different grid sizes (11200, 22400 and 44800 nodes) were conducted to establish the accuracy of the results. The variation of the temperature distribution along the domain centerline from inlet to the outlet was investigated to establish the independence of the temperature distribution for a given

number of nodes in the computational domain. The results of the grid independence tests are shown in Figure 19.

The maximum temperature difference along the domain centerline between the cases with 11200 and 22400 nodes was 2.22%. While, the maximum temperature difference along the domain centerline between the cases with 22400 and 44800 nodes was 0.52%. Therefore, the grid with 22400 nodes was chosen for the current investigation to ensure accuracy of the results with minimum computational time.

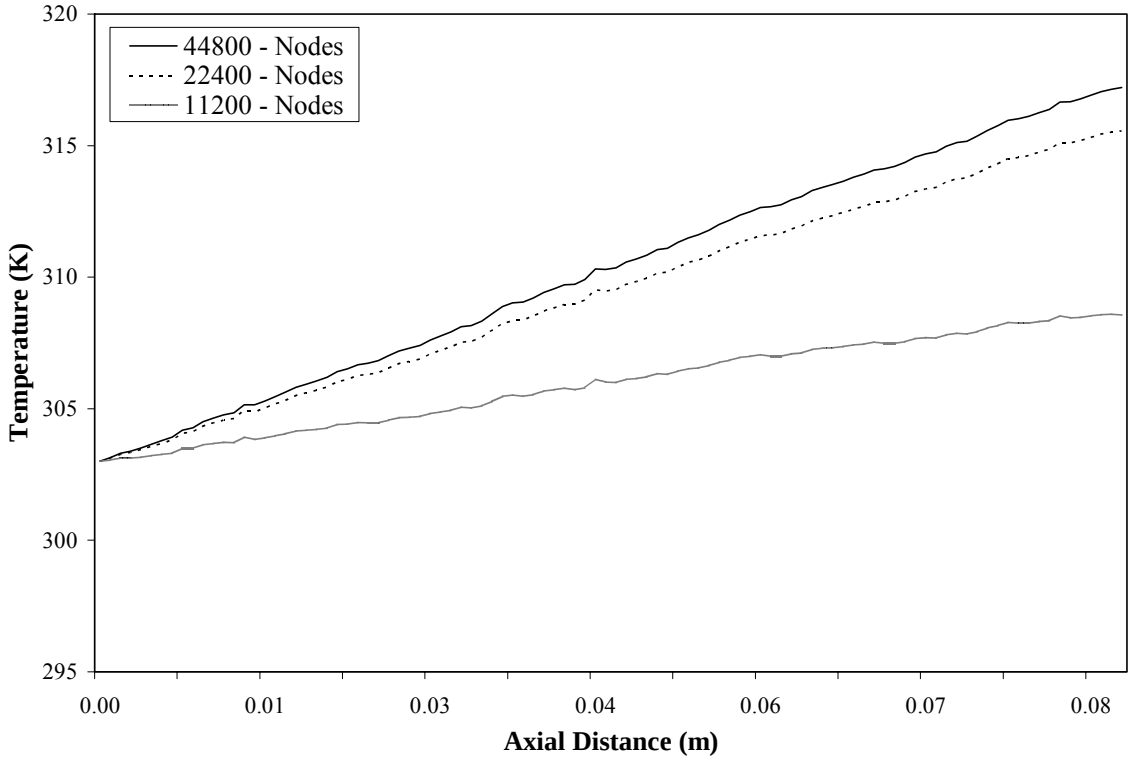

Figure 19. Domain centerline temperature profiles for different grid resolutions for plain-fin staggered configuration for the transitional range flow (k-ω model)

Wavy-Fin Staggered Configuration:

Grid independence tests with three different grid sizes (12400, 24800 and 49600 nodes) were conducted to establish the accuracy of the results. The variation of the temperature distribution along the domain centerline from inlet to the outlet was investigated to establish the independence of the temperature distribution for a given number of nodes in the computational domain. The results of the grid independence tests are shown in Figure 20.

The maximum temperature difference along the domain centerline between the cases with 12400 and 24800 nodes was 2.16%. While, the maximum temperature difference along the domain centerline between the cases with 24800 and 49600 nodes was 0.41%. Therefore, the grid with 24800 nodes was chosen for the current investigation to ensure accuracy of the results with minimum computational time.

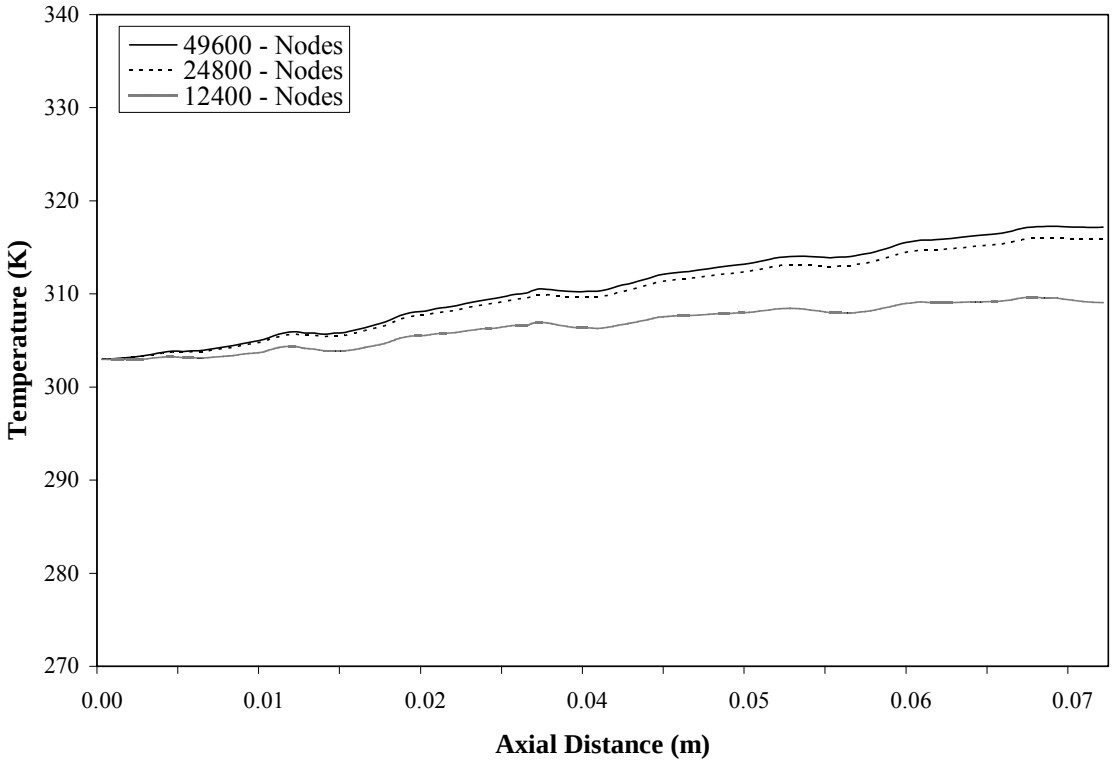

Figure 20. Domain centerline temperature profiles for different grid resolutions for wavy-fin staggered configuration for the transitional range flow (k-ω model)

CHAPTER 6

CODE VALIDATION

The accuracy of present simulation study was validated by comparing the results for plain-fin staggered configuration and wavy-fin staggered configuration with the published experimental results by Wang et al. (1996 and 1997). Once the accuracy of the method used was established, the computations were extended for the cases with plain-fin in-line configuration and wavy-fin in-line configurations as well as for those cases for which no previous studies have been reported.

The validation of the of the numerical simulation presented in this work was done by comparing the published values for the Colburn factor (j) and the friction factor (f) by Wang et al. with the numerical results for both laminar flow range $\left(400 \le \mathrm{Re}_H \le 1200\right)$ and the transitional flow range $\left(1300 \le \mathrm{Re}_H \le 2000\right)$.

The geometrical parameters for the plain-fin staggered configuration and wavy-fin staggered configuration, used by Wang et al. (1996 and 1997) for the experimental studies are shown in Table 10. Same geometrical parameters are used in the current numerical simulation study for the validation of the analysis.

Table 10. Geometrical Parameters for the fin configurations for the Code Validation

	Ll (mm)	Lt (mm)	Fp (mm)	Ft (mm)	D (mm)	Wa (Degrees)	Wh (mm)
Plain Fin Staggered Configuration	22	25.4	3.00	0.13	9.5	-	-
Wavy Fin Staggered Configuration	19.05	25.4	3.53	0.12	9.525	17.5	1.5

Laminar Flow Range

The laminar flow model used for the laminar flow range $(400 \le \mathrm{Re}_H \le 1200)$ gives a fairly close agreement with the experimental results for both plain-fin staggered configuration and the wavy-fin staggered configuration. The error is small at low Reynolds number, starting from $\mathrm{Re}_H = 400$, and error increases towards high Reynolds number. This can be explained as the inability of the laminar model to predict the turbulence in the flow as the Reynolds number increases. The maximum difference between the numerical results and the experimental data was found to be 17%. This simulation validates the current numerical scheme. The overall good agreement with the experimental data gave the confidence about the accuracy of the current numerical method.

Plain-Fin Staggered Configuration:

Figures 21 and 22 show the comparison of the computed values for the Colburn factor (j) and the friction factor (f) with the experimental data of Wang et al. (1996) for the laminar flow range $(400 \le \mathrm{Re}_H \le 1200)$. The agreement between experimental data and computed values is fairly close. The maximum difference between the numerical results and the experimental data for plain-fin staggered configuration was found to be 12%. The percentage error between experimental data and the computed values is small at low Reynolds number and increases with the increase in the Reynolds number for the reason mentioned earlier.

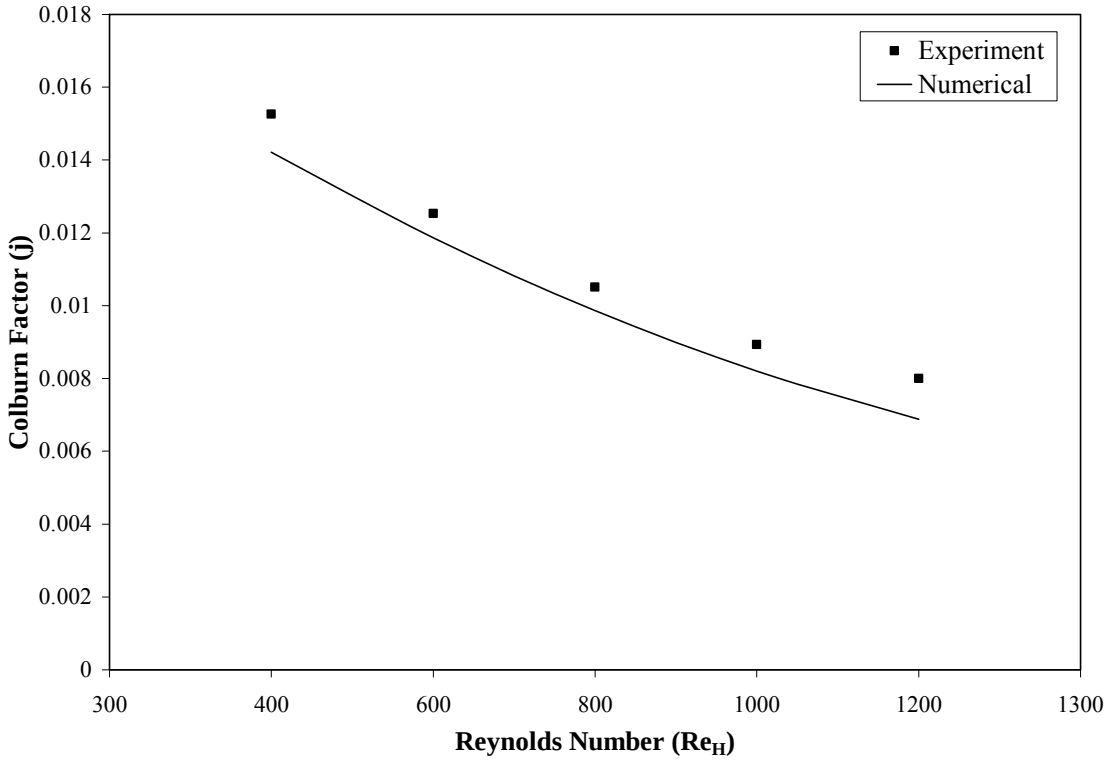

Figure 21. Colburn factor (j) for the plain-fin staggered configuration compared to the experimental data of Wang et al. (1996) for the laminar flow range

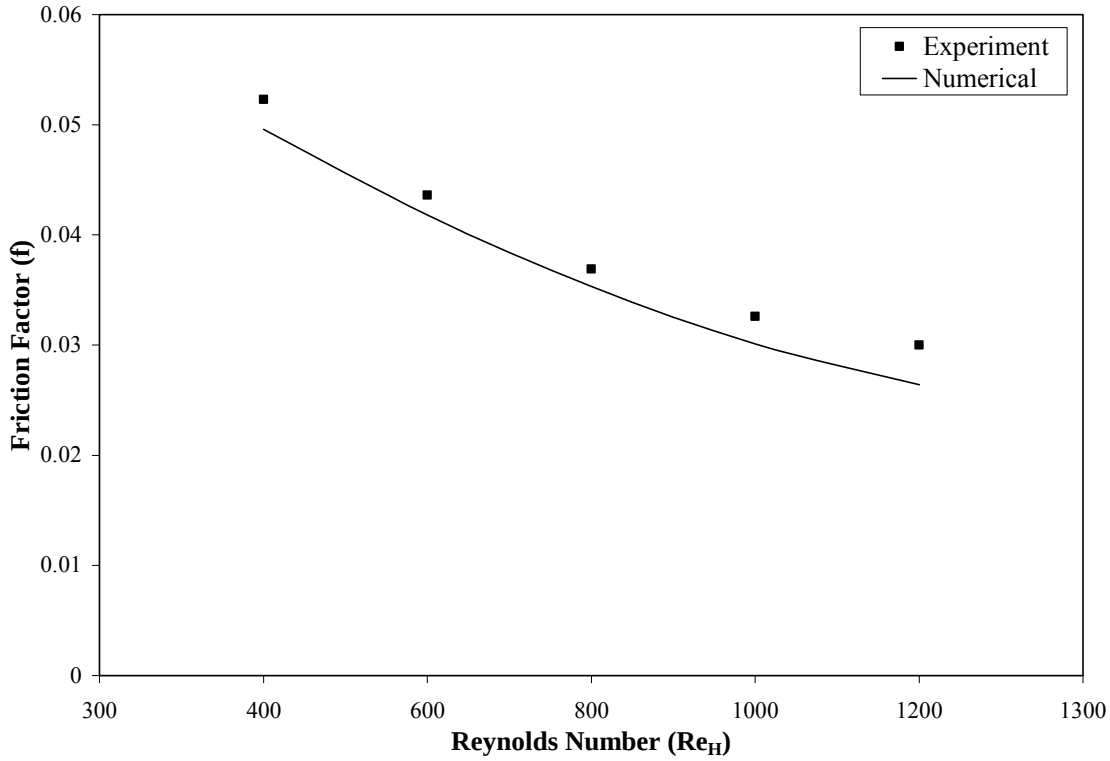

Figure 22. Friction factor (f) for the plain-fin staggered configuration compared to the experimental data of Wang et al. (1996) for the laminar flow range

Wavy-Fin Staggered Configuration:

Figures 23 and 24 show the comparison of the computed values for the Colburn factor (j) and the friction factor (f), with the experimental data of Wang et al. (1997) for the laminar flow range $(400 \le \mathrm{Re}_H \le 1200)$. The agreement between experimental data and computed values is again fairly close. The maximum difference between the numerical results and the experimental data for wavy-fin staggered configuration was found to be 12%. The percentage error between experimental data and the computed values is small at low Reynolds number and increases with the increase in the Reynolds number as seen for the plain-fin staggered configuration.

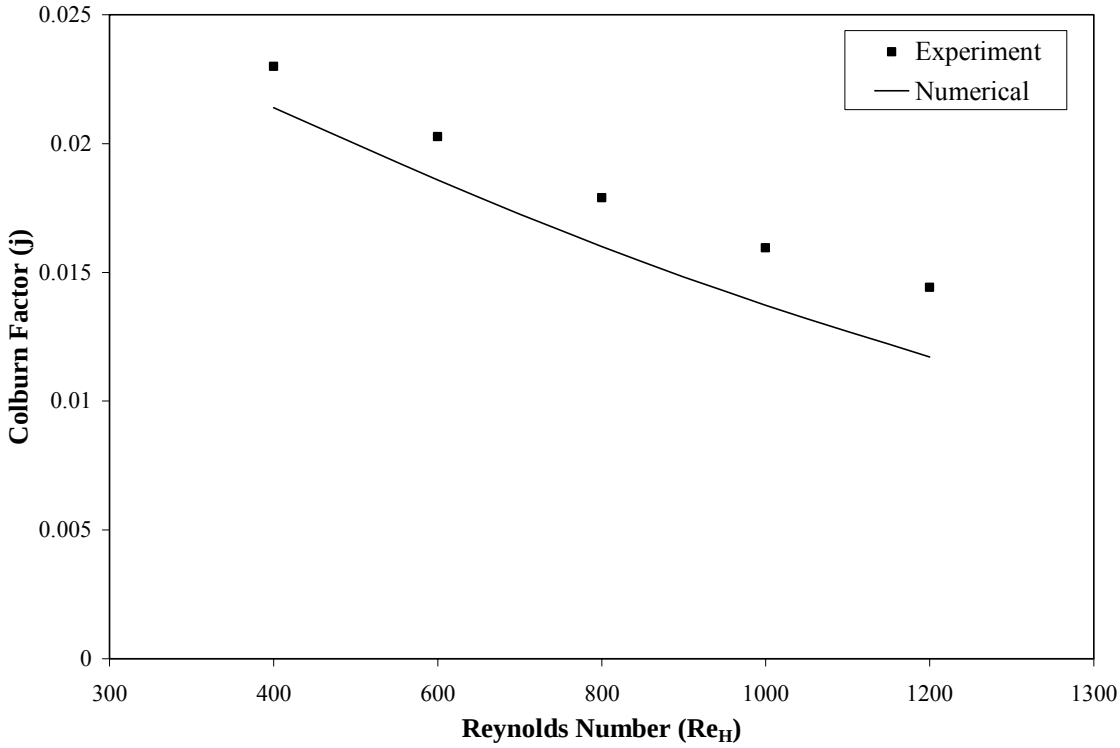

Figure 23. Colburn factor (j) for the wavy-fin staggered configuration compared to the experimental data of Wang et al. (1997) for the laminar flow range

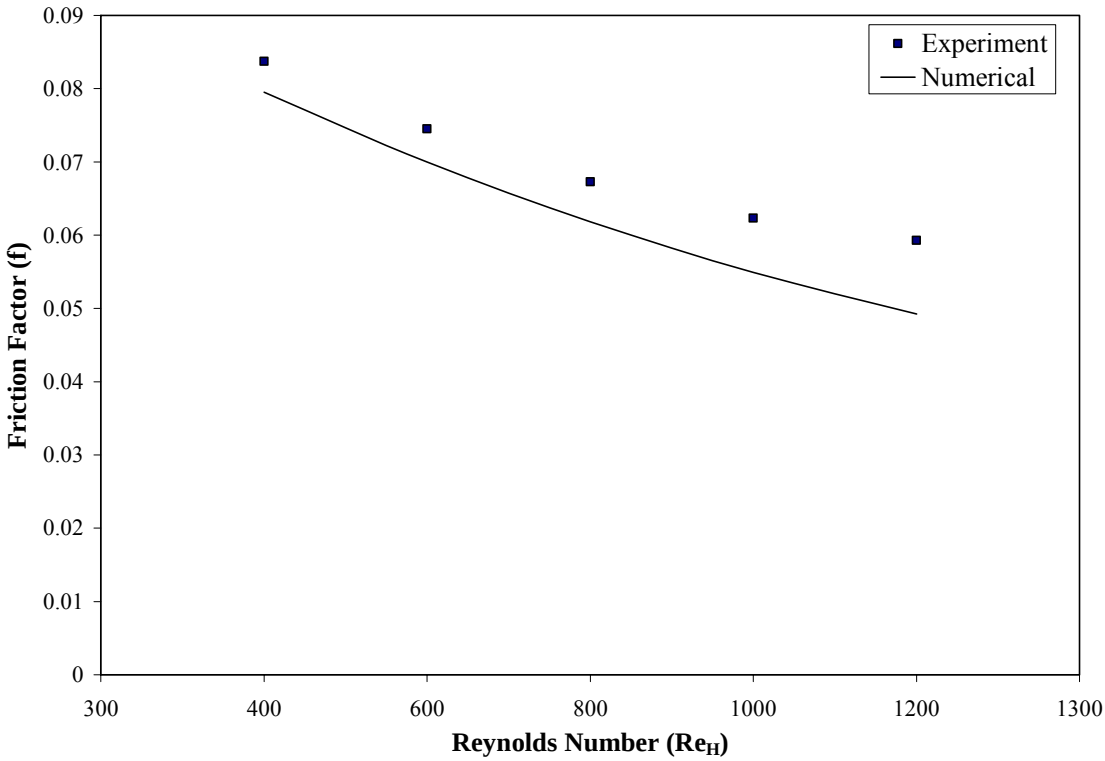

Figure 24. Friction factor (f) for the wavy-fin staggered configuration compared to the experimental data of Wang et al. (1997) for the laminar flow range

Transitional Flow Range

Out of the three turbulence models used to simulate the transitional flow range $(1300 \le \mathrm{Re}_H \le 2000)$ the *k*-ω turbulence model gives a fairly close agreement with the experimental results for both plain-fin staggered configuration and the wavy-fin staggered configuration. The maximum difference between the numerical values and experimental data for the Colburn factor (j) and the friction factor (f) was found to be 8% for the *k*-ω model. On the other hand, the difference between experimental data and numerical results for the Colburn factor (j) and the friction factor (f) for the *k*-ε model and the RNG *k*-ε model was found to be to about 20% and 25% respectively. This

difference in the experimental data and the k-ε based models as compared with the k-ω model is explained in the next section.

Plain-Fin Staggered Configuration:

Figures 25 and 26 show the comparison of the computed values for the Colburn factor (j) and the friction factor (f), with the experimental data of Wang et al. (1996) for the transitional flow range $(1300 \leq \mathrm{Re}_H \leq 2000)$. The agreement between experimental data and computed values for k-ω model are reasonably close. The maximum difference between the numerical results and the experimental data for plain-fin staggered configuration was found to be 7% for the k-ω model. On the other hand, the maximum difference between experimental data and the numerical results are about 25% and 30% for the k-ε model and the RNG k-ε model respectively. The minimum difference between experimental data and the numerical results is 2% for the k-ω model and 11% and 17% for the k-ε model and RNG k-ε model respectively. This difference in the experimental data and the k-ε based models as compared with the k-ω model leads to the conclusion that the k-ω based model is better suited for transitional flows than the k-ε based models.

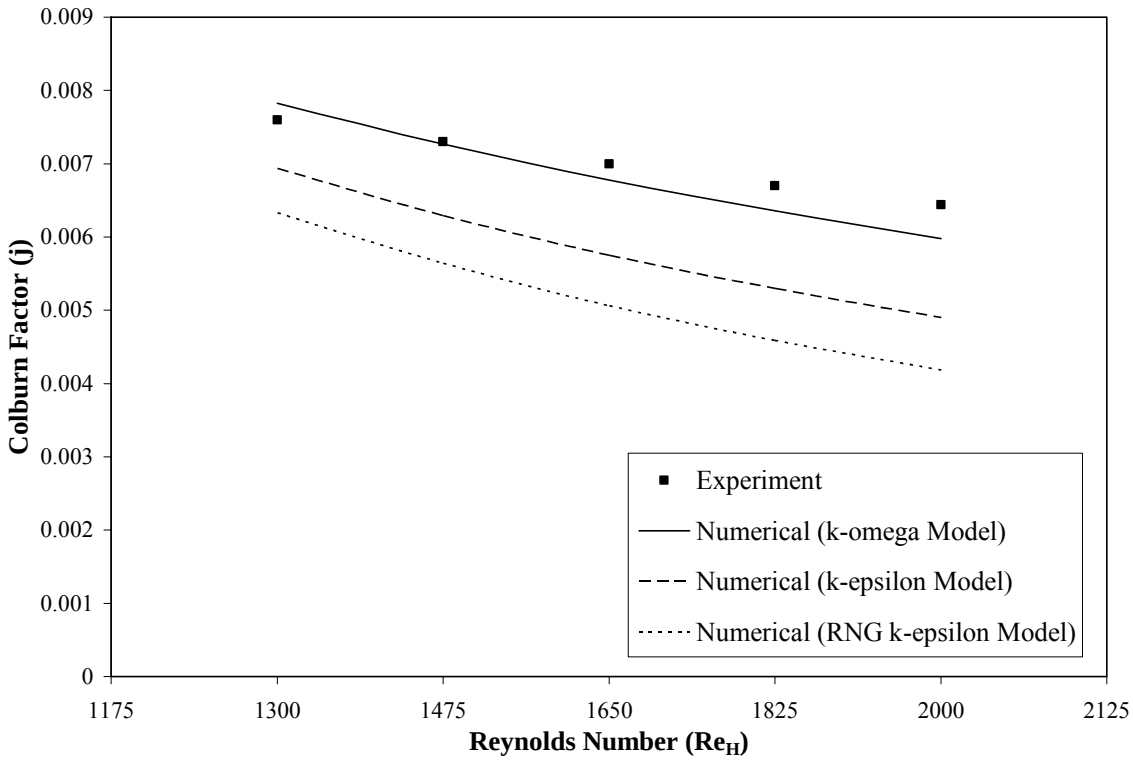

Figure 25. Colburn factor (j) for the plain-fin staggered configuration compared to the experimental data of Wang et al. (1996) for the transitional flow range

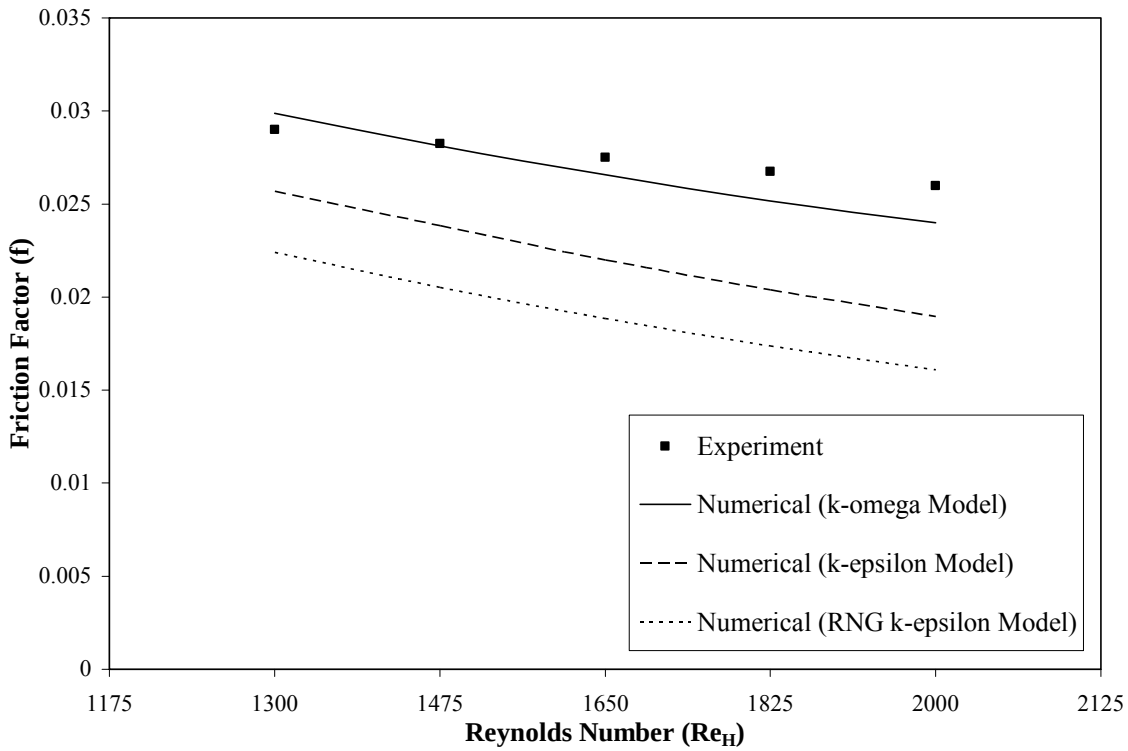

Figure 26. Friction factor (f) for the plain-fin staggered configuration compared to the experimental data of Wang et al. (1996) for the transitional flow range

Wavy-Fin Staggered Configuration:

Figures 27 and 28 show the comparison of the computed values for the Colburn factor (j) and the friction factor (f), with the experimental data of Wang et al. (1997) for the transitional flow range $(1300 \le \mathrm{Re}_H \le 2000)$. The agreement between experimental data and computed values for *k*-ω model are again fairly close. The maximum difference between the numerical results and the experimental data for plain-fin staggered configuration was found to be 9% for the *k*-ω model. On the other hand, the maximum difference between experimental data and the numerical results are about 20% and 25% for the *k*-ε model and the RNG *k*-ε model respectively. The minimum difference between

experimental data and the numerical results is 3% for the *k*-ω model and 15% and 18% for the *k*-ε model and RNG *k*-ε model respectively. This difference in the experimental data and the *k*-ε based models as compared with the *k*-ω model again iterates the postulation that a *k*-ω based model is better suited for transitional flows than the *k*-ε based models.

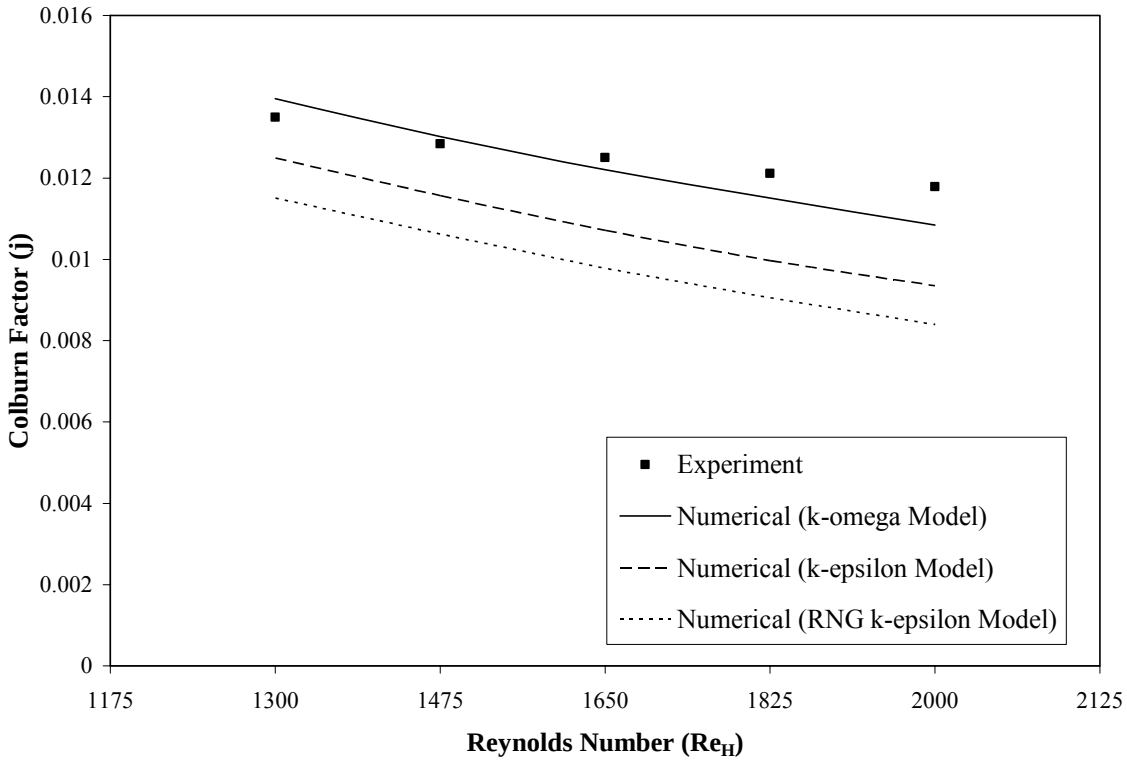

Figure 27. Colburn factor (j) for the wavy-fin staggered configuration compared to the experimental data of Wang et al. (1997) for the transitional flow range

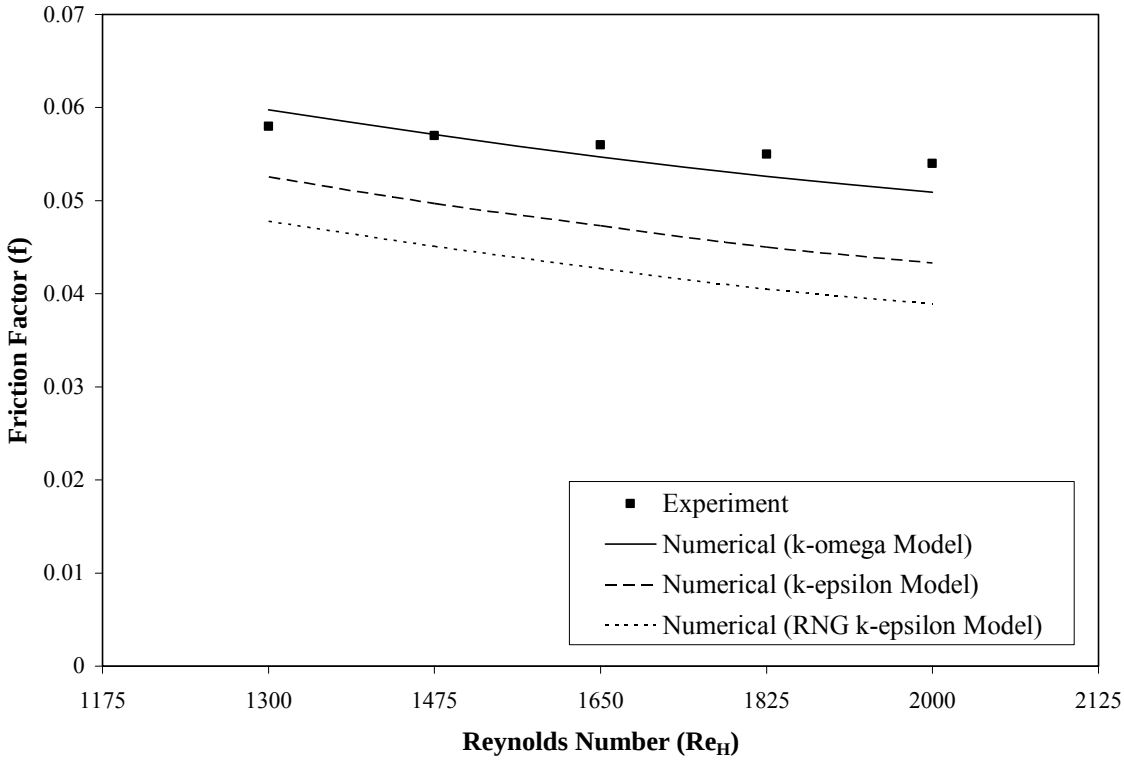

Figure 28. Friction factor (f) for the wavy-fin staggered configuration compared to the experimental data of Wang et al. (1997) for the transitional flow range

Suitability of Turbulence Model for Transitional Flow Representation

The code validation study for the transitional flow range $(1300 \le \mathrm{Re}_H \le 2000)$ leads to the conclusion that the *k*-ω turbulence model would be better suited for this flow range than the *k*-ε based turbulence models. This section explains this behavior for the *k*-ω model and the *k*-ε based models.

The high difference between experimental data and the numerical results for the *k*-ε models might be explained on the basis of the fundamental distinction between the *k*-ε models and the *k*-ω model, based on their near wall treatments.

Two approaches are commonly used to model the flow in the near-wall region are:

(i) The wall-function method and,

(ii) The low-Reynolds-number method

The k-ε based models use the wall-function method for near wall treatment, while the k-ω model uses a blend of low-Reynolds-number method and the wall function method for near wall treatment. For k-ε based models, near wall treatment is always approached by the wall-function method. But in case of k-ω model wall treatment smoothly changes from low-Reynolds number method to the wall-function method as the Reynolds number (Re) of the flow increases.

An important issue in the accurate prediction of industrial turbulent flows is the formulation and the numerical treatment of the equations in regions close to solid walls. The near-wall formulation determines the accuracy of the wall-shear-stress and the wall heat transfer predictions and has an important influence on the development of boundary layers, including the onset of separation.

Near a no-slip wall, there are strong gradients in the dependent variables and viscous effects on the transport processes are large. The representation of these processes within a numerical simulation raises the following problems: (i) how to account for viscous effects at the wall and (ii) how to resolve the rapid variation of flow variables which occurs within the boundary layer region. Two approaches are commonly used to for near-wall region, as mentioned earlier, are: (i) The wall-function method and (ii) The low-Reynolds-number method.

In the wall-function approach, the viscosity affected sublayer region is bridged by employing empirical formulas to provide near-wall boundary conditions for the mean

flow and turbulence transport equations. These formulas connect the wall conditions (e.g. the wall-shear-stress) to the dependent variables at the near-wall grid node which is presumed to lie in the fully-turbulent region of the boundary layer. The major advantage of the wall-function approach is that it conserves valuable computer resources.

An alternative approach to the use of wall-functions is to use a fine-grid analysis in which computations are extended through the viscosity affected sublayer close to the wall. Computer-storage and runtime requirements are usually greater than those of the wall-function approach and care must be taken to ensure good numerical resolution in the near-wall region to capture the rapid variation in variables.

The present numerical study is done for the transitional flow range $(1300 \le \mathrm{Re}_H \le 2000)$, and not for the fully developed turbulent flows. The *k*-ε models have been proven to be stable and numerically robust and has a well established regime of predictive capability for the fully developed turbulent flows. But their applicability is rigid which is mostly suitable for the turbulent flows ($\mathrm{Re} > 10^5$) as demonstrated in a large number of validation studies (Bardina et al. 1980). One of the well known deficiencies of the *k*-ε based models is its inability to handle low turbulent Reynolds number computations (i.e. transitional and laminar flows). When using CFX-5 computational fluid dynamics code, the *k*-ε turbulence models use the scalable wall-function approach for the near wall treatment. This approach has proven to be good for the fully developed turbulent flows. But for the low Reynolds number range complex damping functions need to be added to the *k*-ε models, as well as a highly refined near-wall grid resolution will be required in an attempt to model low turbulent Reynolds

number flow (i.e. transitional and laminar flows). This approach often leads to numerical instability. Some of these difficulties may be avoided by using the k-ω model, making it more appropriate than the k-ε model for low Reynolds number flows, i.e. for the flows which are not fully developed turbulent flows e.g. transitional flows. CFX-5 code uses a different near wall treatment for the k-ω model than the k-ε model. An "automatic" near wall treatment is used in CFX-5 for the k-ω model. This wall treatment for the k-ω model uses a low -Reynolds number wall formulation for Reynolds number less than 10^5 and the wall treatment smoothly changes to the wall function formulation as the Reynolds number increases i.e. goes into the turbulent zone. This feature of the "automatic" wall treatment for the k-ω model is of significant use for modeling the transitional flow zone, where laminar model fails due to inability to handle the unsteadiness of the transitional flow and the k-ε based models fail to resolve the rapid variation of flow variables occurring within the boundary layer region due to wall-function near wall treatment approach.

While the wall-functions method for near wall treatment used by the k-ε based models allow for a consistent grid refinement, thereby conserving valuable computer resources, they are based on physical assumptions which are problematic, especially in flows at lower Reynolds numbers ($Re<10^5$), as the sublayer portion of the boundary layer is neglected in the mass and momentum balance. For flows at low Reynolds numbers, this can cause an error in the displacement thickness of up to 25%. It is therefore desirable to offer a formulation which will automatically switch from wall-functions to a low-Re near wall formulation as the grid is refined. The k-ω model of Wilcox has the

advantage that an analytical expression is known for ω in the viscous sublayer, which can be exploited to achieve this goal. The main idea behind this formulation is to blend the wall value for ω between the logarithmic and the near wall formulation. The flux for the *k*-equation is artificially kept to be zero and the flux in the momentum equation is computed from the velocity profile (For more information on the near wall treatment by the *k*-ε and *k*-ω models as well as mathematical formulation, please refer to Chapter 3: Problem Formulation).

This basic difference in the near wall treatment for the *k*-ε based models and the *k*-ω based models makes the *k*-ω model a better choice for the transitional flow range as is proven by the code validation tests, reported earlier.

CHAPTER 7

RESULTS AND DISCUSSION

The numerical results presented in this chapter were obtained using commercial computational fluid dynamics (CFD) code Ansys CFX-5 (2002). This code offers a wide range of flow analysis models, including laminar model and a number of turbulence models based on the eddy viscosity approach and the Reynolds stress approach. This feature of CFX-5 was particularly useful for the current investigation which ranges from the laminar flow range to the transitional flow range. Accuracy of the current study was tested by comparing the results with the experimental data, reported by Wang et al. (1996 and 1997). Grid independency tests were carried out to ensure that the chosen grid resolution provides accurate results within an acceptable computational time.

Primarily, current research is divided into two parts: (i) laminar flow range $(400 \le \mathrm{Re}_H \le 1200)$ and (ii) transitional flow range $(1300 \le \mathrm{Re}_H \le 2000)$. For the laminar range, four different types of fin configurations were studied in the current investigation. They were plain-fin and wavy-fin staggered and in-lined configurations. First the effect of the number of tube rows for the wavy fin staggered arrangement was investigated in order to optimize the total number of tube rows for such configurations. Similar studies which report the effect of number of tube rows are published by Jang et al. (1996) and Tutar and Akkoca (2004). The current study investigates the effect of number of tube rows on the heat transfer and pressure drop characteristics in further detail. The effect of flow distinction between the plain-fin and the wavy-fin on the heat transfer and pressure drop characteristics was also studied for the laminar flow range.

Furthermore, the effect of geometrical parameters such as longitudinal tube pitch (Ll) and transverse tube pitch (Lt) on the heat transfer and pressure drop characteristics are investigated in the laminar range for the plain-fin staggered and wavy-fin staggered configurations.

For the transitional flow range $(1300 \leq \mathrm{Re}_H \leq 2000)$ three different turbulence models were employed namely k-ε model, RNG k-ε model and the k-ω model. The validity of these turbulence models in the transitional flow range was investigated and the results were compared with each other as well as the laminar model from the point of view of suitability of these models for the stated flow range. Similar study investigating the turbulence models for such applications was reported by Tutar et al. (2001) for only one tube row domain in plain fin configuration. However, a detailed analysis of such turbulence models for the application stated has not been undertaken for the entire four tube row domain either for the plain or the wavy fins. The effects of different geometrical parameters such as fin pitch, wavy angle and wavy height on the heat transfer and pressure drop characteristics are reported by Jang et al. (1997) for the laminar flow range. The current study investigates the effects of theses geometrical parameters on heat transfer and pressure drop characteristics for the transitional flow range.

It is a standard procedure to report the heat transfer and pressure drop characteristics for fin and tube heat exchangers in terms of non-dimensional parameters, Colburn factor (j) and friction factor (f) respectively, as is iterated by Wang et al. (1997), Jang et al. (1997) and Kays and London (1984). Hence the current study also reports these characteristics in terms Colburn factor (j) and friction factor (f).

Flow Distinction

As stated earlier, the current numerical study ranges from laminar flow range $(400 \le \mathrm{Re}_H \le 1200)$ to the transitional flow range $(1300 \le \mathrm{Re}_H \le 2000)$. This flow range is selected for the current study because for the most practical applications the flow remains in either of these flow ranges for the fin-tube heat exchangers as suggested by the experimental studies conducted by Wang et al. (1997) and Jang et al. (1997).

The variation of the Colburn factor (j) and the friction factor (f) against the Reynolds number (Re) for air flow in a circular tube is shown in Figure 29.

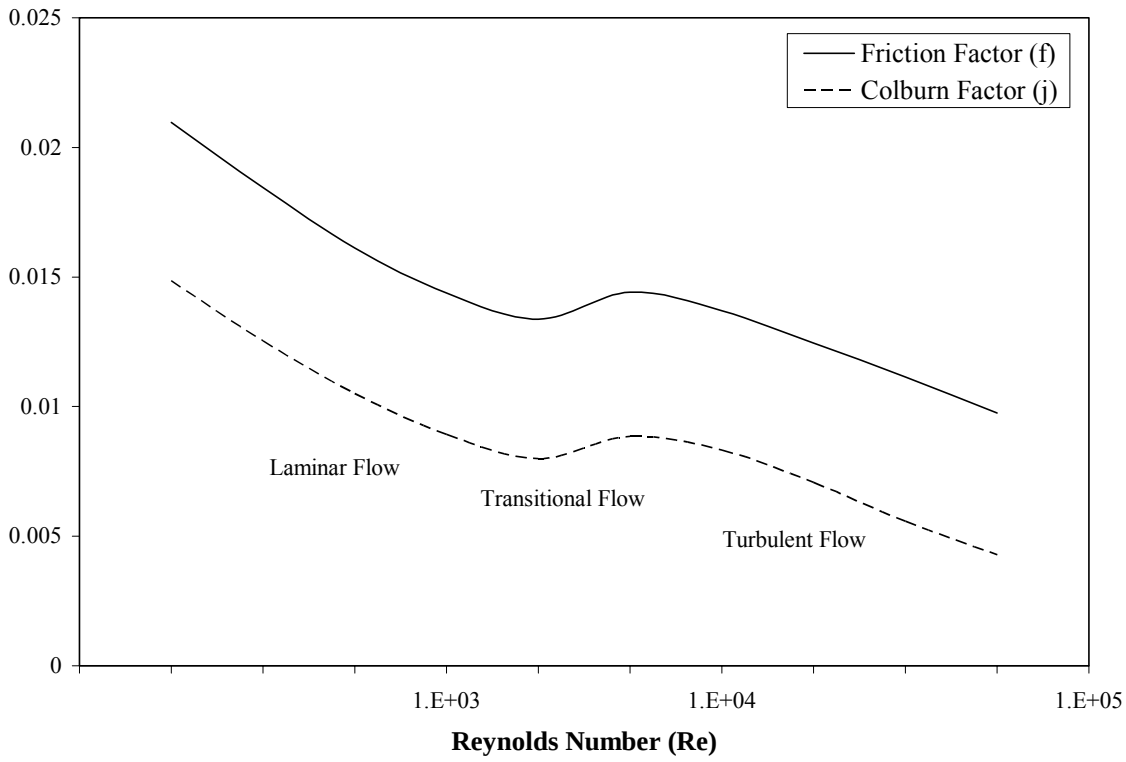

Figure 29. The variation of Colburn factor (f) and the friction factor (f) against Reynolds number (Re) for flow in a circular pipe, Kakac et al. (1981)

The Colburn factor (j) and the friction factor (f) have similar nature in such a case of the circular tube and they are almost parallel. The three flow regimes can be seen from such a plot of variation of the Colburn factor (j) and the friction factor (f) against Reynolds number (Re) for a circular tube. These three flow regions are laminar, transition and turbulent regimes respectively. From this plot of j and f against Re, these three flow regimes are identified based on the slopes of the Colburn factor (j) or the friction factor (f) curves. The Colburn factor (j) and the friction factor (f) curves against the Reynolds number (Re) have one slope in the laminar flow region. The slope of these curves changes and a dip in the Colburn factor (j) and friction factor (f) curves against Re characteristics is observed when the flow transcends from the laminar region into the transition region. This sharp dip in these characteristics is usually a behavior of long continuous flow passages. Generally the interrupted surfaces do not have such a sharp dip in the transition region, but still a change in the slope is observed for the j and f characteristics as the flow passes from laminar to transition range as seen from the experimental studies conducted by Kays and London (1984) for the plain and wavy fin configurations. And again the slope of these j and f variation curves changes when the flow transcends from the transitional regime into the turbulent regime.

The current study defines Reynolds number (Re_H) based on fin spacing (H) and frontal velocity (V_{in}), defined as,

$$\mathrm{Re}_H = \frac{\rho \cdot V_{in} \cdot H}{\mu} \tag{106}$$

Figures 30 and 31 show the Colburn factor (j) against Reynolds number (Re_H) reported by the experimental studies of Wang et al. (1996 and 1997) for the plain-fin and

wavy fin configurations respectively. Wang et al. (1996) defines Reynolds number (Re_D) based on the tube diameter (D) as,

$$\mathrm{Re}_D = \frac{\rho \cdot V_{in} \cdot D}{\mu} \tag{107}$$

The Colburn factors (j) reported in the Figures 30 and 31 are against the converted Reynolds number (Re_H) based on the fin spacing (H). Note the change in slope for the j Vs Re_H curve for both of these figures. The slope changes at around Re_H = 1200. This shows that the flow regime changes from laminar to the transitional regime for these fin configurations at around Re_H = 1200. Once the slope for the Colburn factor (j) changes as the flow transcends into the transitional regime, it remains almost constant for the range of the Reynolds number (Re_H) in the experimental studies of Wang et al. (1997). Since the slope of the Colburn factor (j) variation curve does not change again, it can be concluded that the flow remains in the transitional regime without transcending into the turbulent regime for the range of Reynolds number tested in his experimental studies by Wang et al. (1997). These figures validates the assumption made in the current study that the flow is laminar for the range stated $\left(400 \le \mathrm{Re}_H \le 1200\right)$ for both plain and wavy fin configurations and flow regime is confined to the transitional zone for the range stated $\left(1300 \le \mathrm{Re}_H \le 2000\right)$ for both plain and wavy fin configurations.

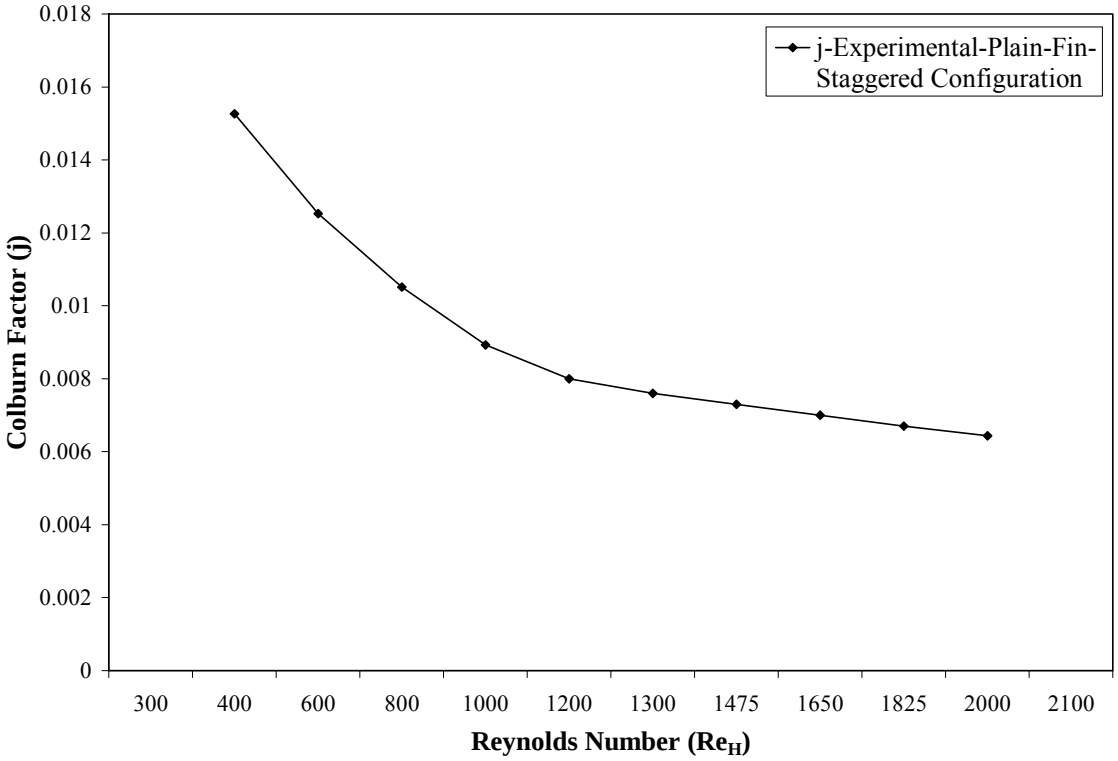

Figure 30. Colburn factor (j) against the Renolds number (ReH) reported by the experimental studies of Wang et al. (1996) for the plain-fin staggered configuration

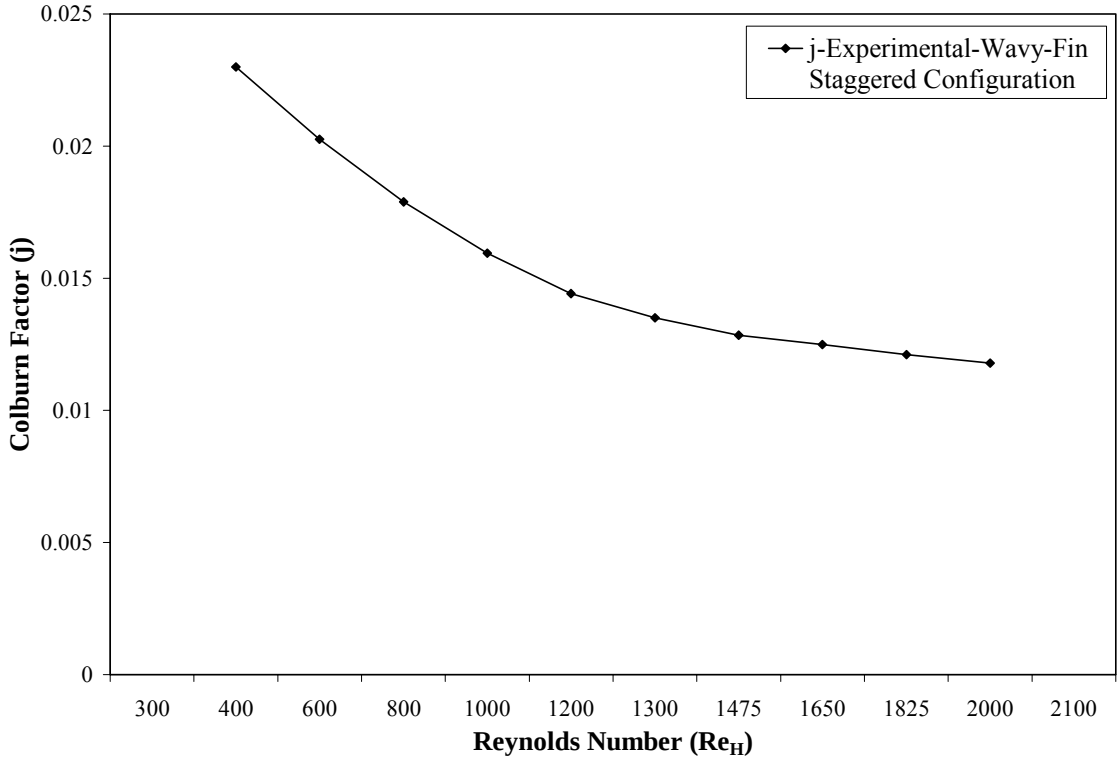

Figure 31. Colburn factor (j) against the Renolds number (ReH) reported by the experimental studies of Wang et al. (1997) for the wavy-fin staggered configuration

Laminar Flow Range

This section describes the results for the current numerical investigation done on the laminar flow range $\left(400 \le \mathrm{Re}_H \le 1200\right)$. Four models are tested in this study, (i) plain-fin staggered configuration (ii) plain-fin in-lined configuration (iii) wavy-fin staggered configuration and (iv) wavy-fin in-lined configuration. Jang et al. (1996) has reported experimental and numerical works that compared staggered and in-lined configurations for the plain-fin. Jang et al. (1997) also compared plain-fin staggered configuration of with wavy-fin staggered configuration for heat transfer and flow friction characteristics. However, a detailed comparative study that investigates difference between heat transfer

and flow friction characteristics for wavy-fin staggered and in-lined configurations is not published. The current numerical investigation also compares these characteristics for the wavy-fin staggered and in-lined configurations with that of plain-fin staggered and in-lined configurations based on their flow structure difference. This section describes the effects of number of tube rows, effects of flow structure difference between plain and wavy fin, effects of longitudinal pitch (Ll) and transverse pitch (Lt) on the heat transfer and flow friction characteristics for these fin configurations.

Effects of Number of Tube Rows

As a first step, the effects of number of tube rows on the heat transfer and flow friction characteristics for the wavy-fin staggered configuration is investigated with the use of 1 to 6 row domain, as shown in Figure 32. Jang et al. (1996) and Tutar and Kakac (2004) have reported that the effect of number of tube rows on the heat transfer and pressure drop characteristics is insignificant as the number of tube rows become more than four for the plain-fin staggered arrangement. The current numerical study is conducted to investigate the effect of number of tube rows for the wavy-fin staggered configuration. Figure 32 shows 1 to 6 tube row domains for the wavy fin staggered configuration used for the current study.

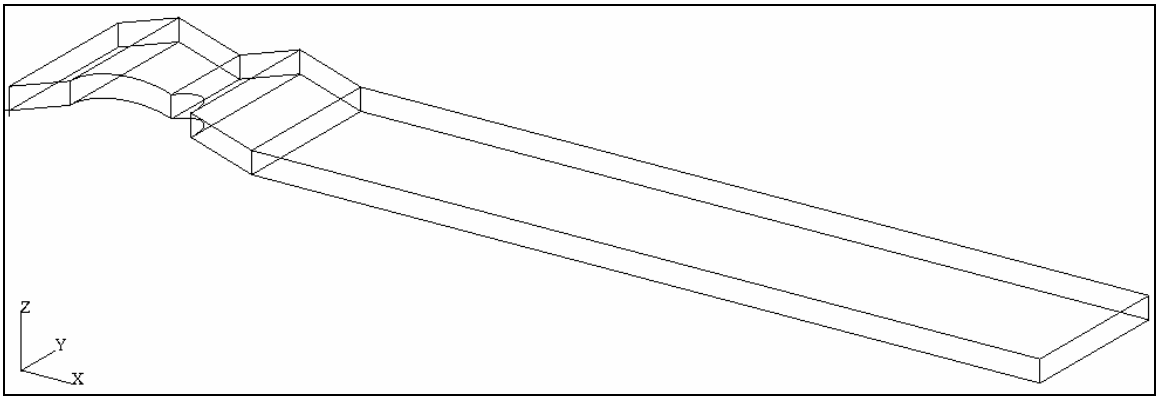

(a)

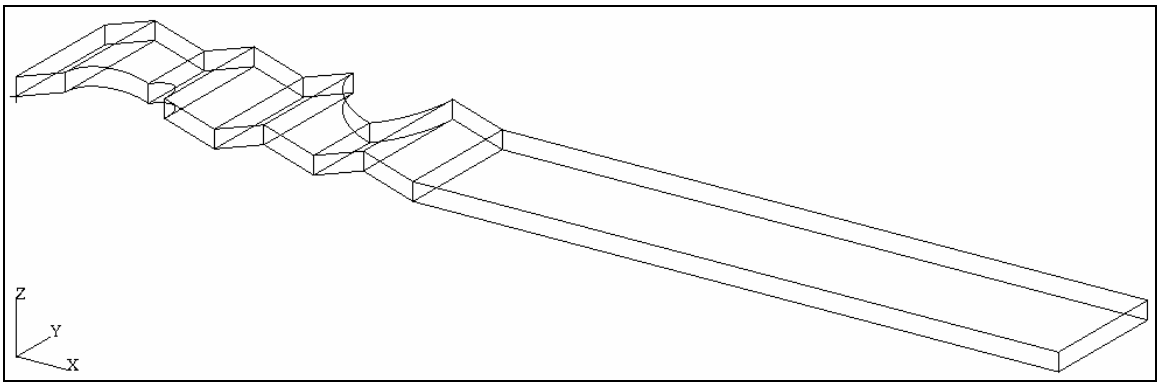

(b)

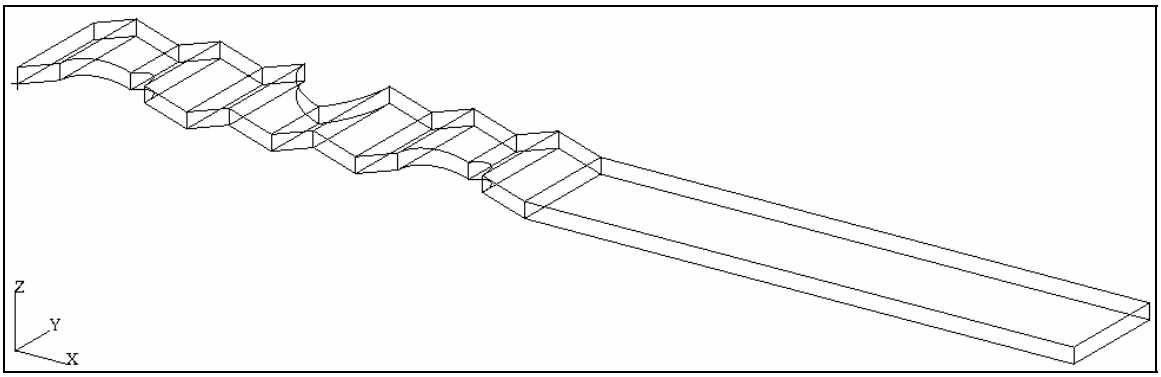

(c)

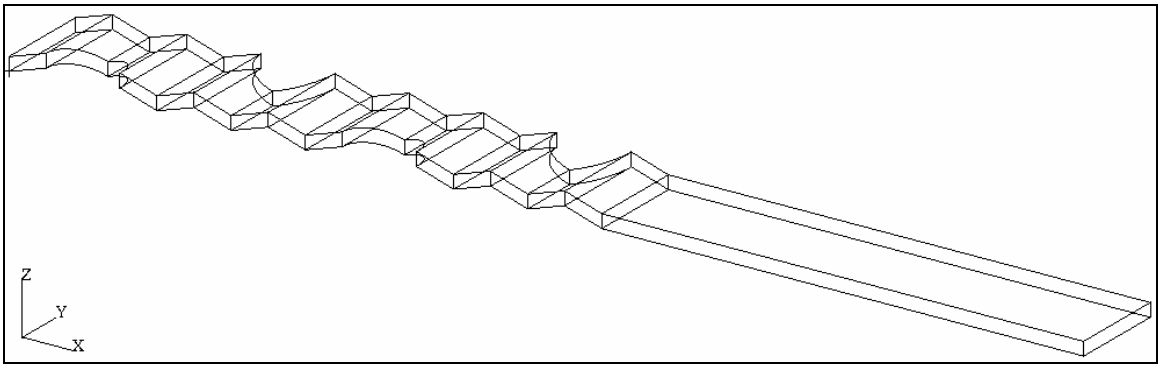

(d)

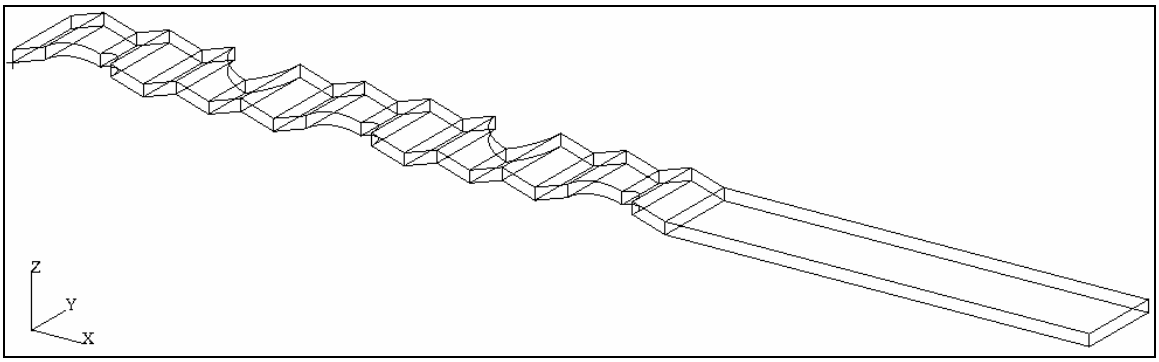

(e)

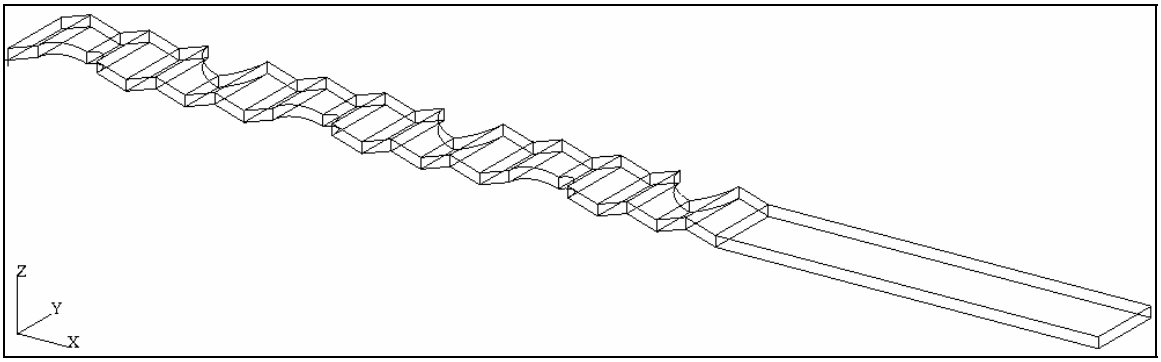

(f)

Figure 32. Computational domains used for the wavy-fin staggered configuration to investigate the effects of the number of tube rows using (a) one (b) two (c) three (d) four (e) five (f) six tube rows

The geometrical parameters used for these domains are shown in Table 11:

Table 11. Geometrical Parameters for the wavy-fin configuration for the effect of tube row numbers study

	Ll (mm)	Lt (mm)	Fp (mm)	Ft (mm)	D (mm)	Wa (Degrees)	Wh (mm)
Wavy Fin Staggered Configuration	19.05	25.4	3.53	0.12	9.525	17.5	1.5

Figure 33 illustrates the variation in the heat transfer coefficient *h*, as a function of the number of tube row for Re_H = 1000 for each individual domain. This heat transfer coefficient *h* is calculated using Equation (63). It is seen that the heat transfer coefficient decreases as the tube row number is increased from 1 to 6 for these six domains. This may be due to the fact that as the number of tube rows increases, the amount of ineffective area that does not take part in the heat transfer also increases. This causes a decrease in the heat transfer coefficient *h*.

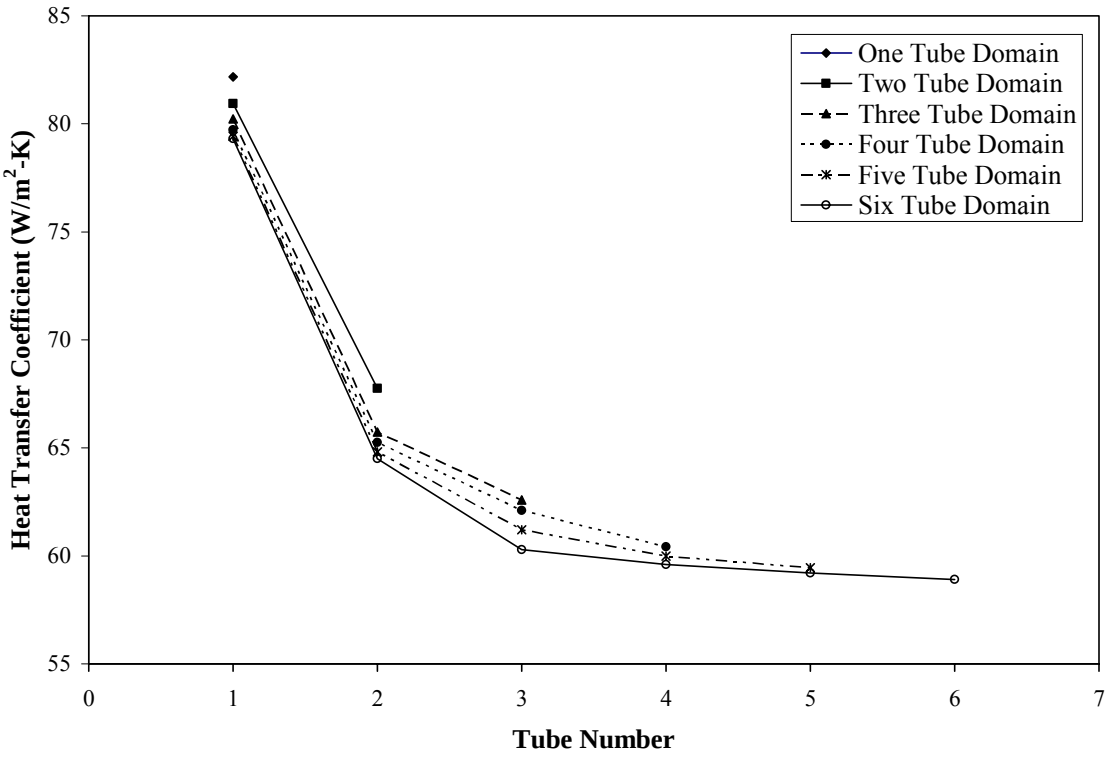

Figure 33. Heat transfer coefficient *h* against the number of tube row for the wavy-fin staggered configuration

Figure 34 illustrates the variation in the average heat transfer coefficient $\bar{h}$, as a function of number of tube row for Re_H = 1000 for these six domains. This heat transfer coefficient $\bar{h}$ is calculated using Equation (66). It can be seen again that the average heat transfer coefficient decreases as the number of tube rows in the domain are increased from 1 to 6.

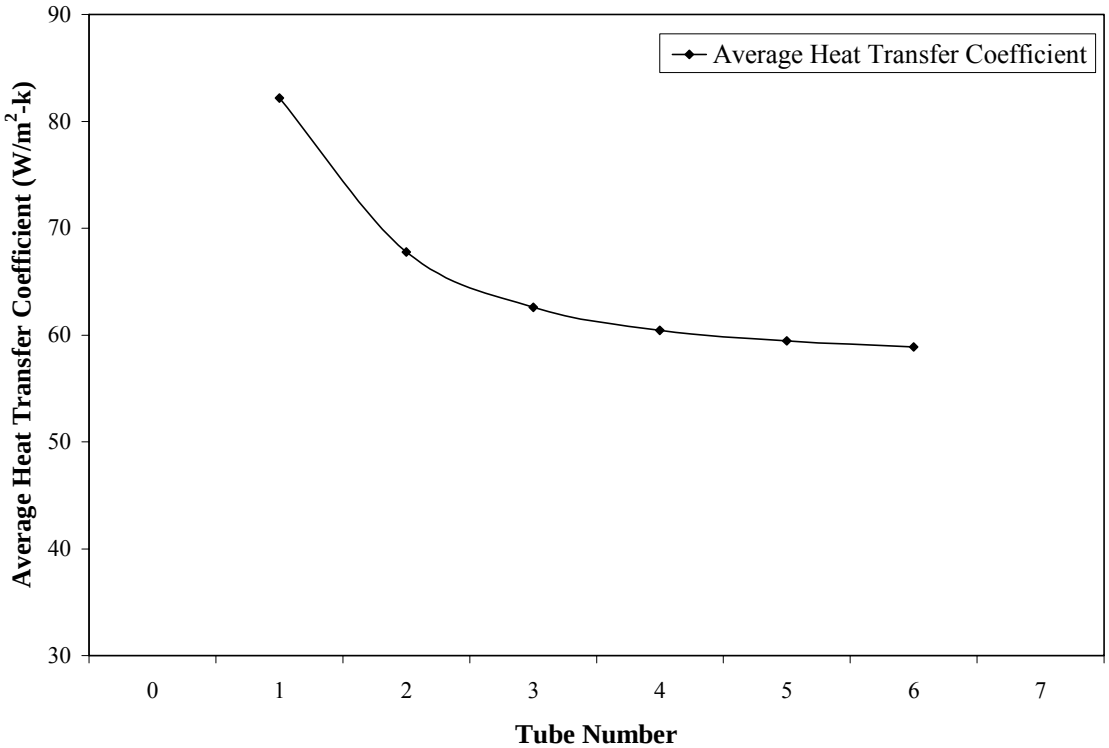

Figure 34. Average heat transfer coefficient $\bar{h}$ against the number of tube row for the wavy-fin staggered configuration

Figure 35 illustrates the variation in the overall heat flux Q (watts), as a function of number of tube row for Re_H = 1000 for these six domains. This heat transfer coefficient Q is calculated using Equation (61). It can be seen that the overall heat flux Q (watts) increases as the number of tube rows in the domain are increased from 1 to 6. However, the slope of this increase is sharp in the beginning and it gradually reduces as the number of rows of tubes increases, as seen from Figure 35. This may be again due to the fact that as the number of rows of tube increases, the amount of ineffective area that does not take part in the heat transfer also increases. This in turn reduces the average heat transfer coefficient $\bar{h}$.

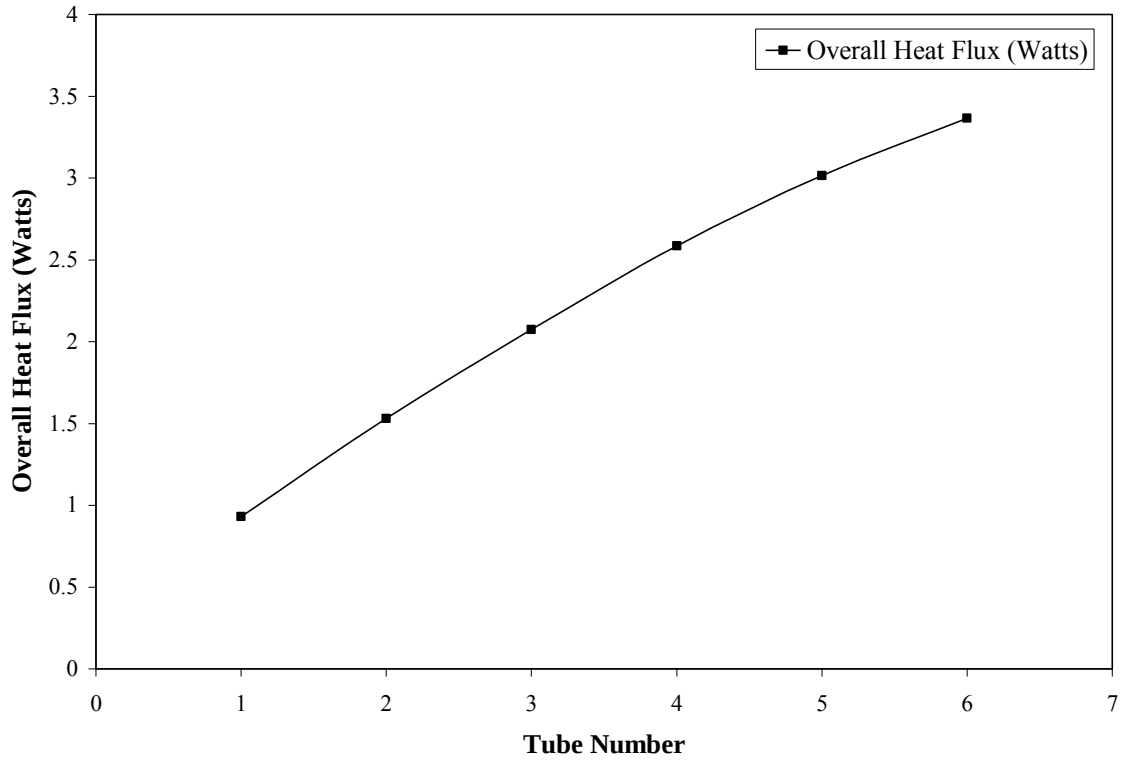

Figure 35. Overall heat flux (Q) against the tube row number for the wavy-fin staggered configuration

Figure 36 illustrates the variation in the overall pressure coefficient $\overline{C_p}$, as a function of number tube row for Re_H = 1000 for these six domains. This heat transfer coefficient $\overline{C_p}$ is calculated using Equation (67). It can be seen that the overall pressure coefficient $\overline{C_p}$ increases as the number of tube rows in the domain are increased from 1 to 6. However, the slope of this increase gradually increases as the number of rows of tubes increases, as seen from Figure 36. This might be due to the fact that the increase in the number of tube rows causes increase in the volume of the domain and the corresponding increase in the flow friction area.

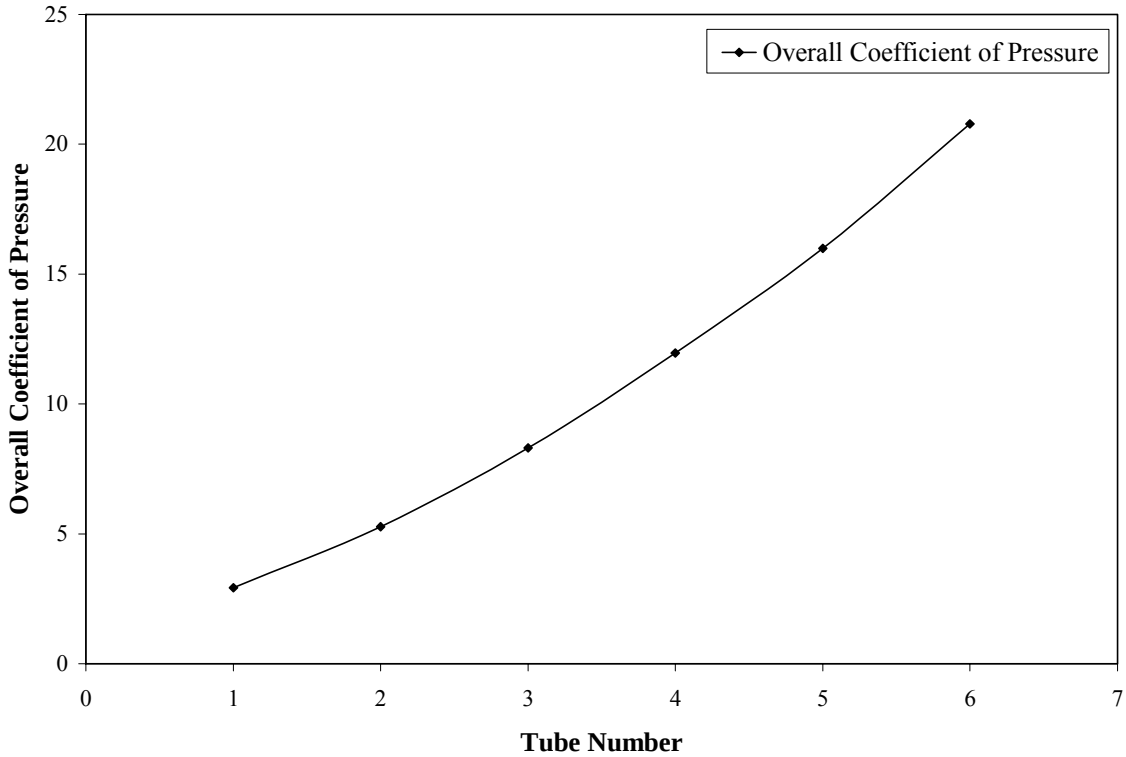

Figure 36. Overall coefficient of pressure ($\overline{C_p}$) against the tube row number for the wavy-fin staggered configuration

Figures 33-36 illustrate that the heat transfer coefficient *h*, the average heat transfer coefficient $\bar{h}$, decreases with the corresponding increase in the overall heat flux Q (watts) as the as the number of rows of tubes in the domain are increased from 1 to 6. However, the pressure penalty also increases as the number of rows of tubes in the domain is increased from 1 to 6. Hence an optimal choice must be selected for the balance between the increase in the heat transfer performance against the increase in the flow friction characteristics. Figures 33 and 34 show that the effect of the number of rows of tubes on the heat transfer coefficient becomes comparatively small when the number of rows of tube is greater than 4. For this reason, 4-row configuration can be regarded as

an optimum multi-row fin-and-tube heat exchanger in terms of row numbers for the wavy-fins. Experimental studies by Wang et al. (1996) and Jang et al. (1996) have already shown that the four tube row configuration is the most optimum choice for the plain-fins. The current numerical investigation shows that four tube row domain will also be an optimum choice and the wavy-fin configuration, hence the rest of the numerical calculations in this investigation have been carried out for the 4-row configuration for both plain and wavy-fins.

Effects of Flow Distinction between Plain-Fin and Wavy-Fin

The fundamental difference between plain-fin and wavy-fin is that plain-fin is flat in nature. Wavy-fin on the other hand is corrugated. The wavy surface can lengthen the path of the airflow and cause better airflow mixing. Consequently, higher heat transfer is expected from the wavy-fin, compared with a plain plate fin surface. This fundamental difference between plain-fin and wavy-fin causes a flow distinction. The flow pattern for plain-fin is relatively simple in nature since flow is straight without any interruptions by the corrugations. The wavy corrugations in case of wavy-fin however, make the flow structure complex. Because of the corrugations, the flow gets re-oriented each time it passes over the corrugation in case of wavy-fin. This flow distinction is examined in detail in this section for both plain and wavy fins, in staggered and in-lined configurations.

The three-dimensional numerical investigation done by Jang et al. (1996) on plain fin staggered and in-lined configurations revealed that the average heat transfer coefficient of staggered arrangement is 15 – 27% higher than that of in-lined arrangement. On the other

hand, the average pressure drop in staggered arrangement is 20 – 25% higher than that of in-lined arrangement for the same geometrical parameters. Experimental studies by Wang et al. (1997) reported the heat transfer and flow friction characteristics for the wavy-fin in staggered and in-lined configurations. However, in these experimental studies by Wang et al., the geometrical parameters for the staggered and in-lined wavy-fin configurations were different. Therefore, a comparative analysis for the wavy-fin in staggered and in-lined configurations for the heat transfer and flow friction characteristics is needed to investigate based on the same geometrical parameters. The current numerical investigation explores this area where a comprehensive comparative analysis is done for the heat transfer and flow friction characteristics for plain and wavy fin in both, staggered and in-lined configurations. The current study is based on the same geometrical parameters for the staggered and in-lined tube layouts of these fins. Furthermore, the current investigation explores the thermal and hydraulic characteristics for the plain and wavy fins in the staggered and in-lined tube layouts, based on the flow structure difference between these two types of fins. The geometrical parameters used for this study are shown in the Table 12. These geometrical parameters are based on the experimental studies by Wang et al. (1996 and 1997).

Table 12. Geometrical Parameters for the fin configurations for the flow structure analysis

	Ll (mm)	Lt (mm)	Fp (mm)	Ft (mm)	D (mm)	Wa (Degrees)	Wh (mm)
Plain Fin Staggered Configuration	19.05	25.4	3.53	0.12	9.525	-	-
Plain Fin In-lined Configuration	19.05	25.4	3.53	0.12	9.525	-	-
Wavy Fin Staggered Configuration	19.05	25.4	3.53	0.12	9.525	17.5	1.5
Plain Fin In-lined Configuration	19.05	25.4	3.53	0.12	9.525	17.5	1.5

As stated earlier, the flow path in case of plain-fin is fairly simple owing to the flat nature of the plain-fin. While the flow path in case of wavy-fin is complex because the flow gets re-oriented each time it passes over a wavy corrugation. These types of flow paths are shown in Figures 37 and 38. As shown in Figure 37 the flow path in case of plain-fin is straight without any interruptions except for the interruption in flow caused by the tubes. On the other hand, it can be seen from Figure 38 that the flow guided by the corrugations for wavy-fin and the flow direction is re-oriented each time the flow passes over a wavy corrugation.

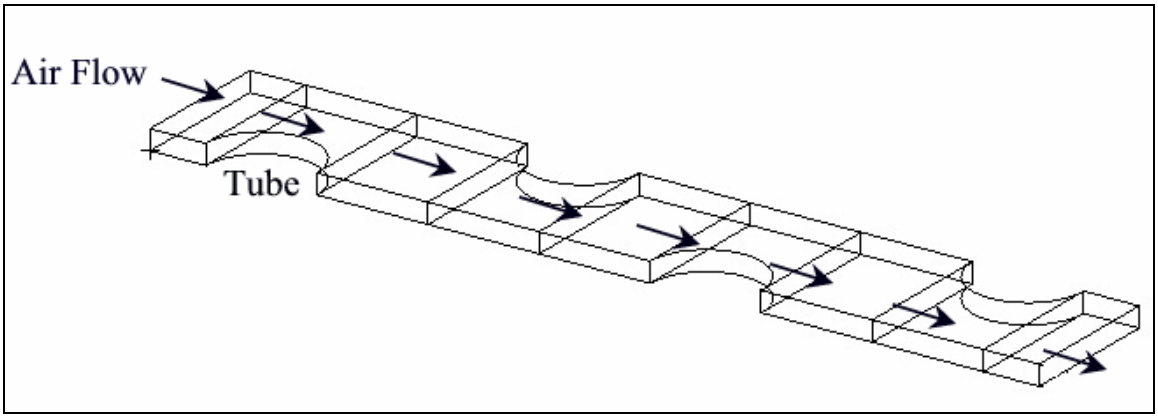

Figure 37. Flow path for the plain-fin staggered configuration

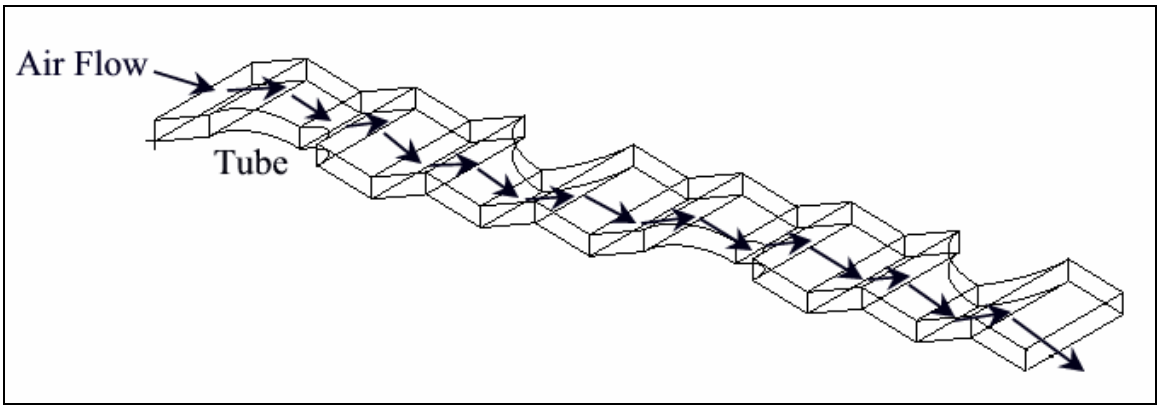

Figure 38. Flow path for the wavy-fin staggered configuration

Figure 39 shows the streamline plot and Figure 40 shows the velocity vectors for the plain-fin staggered configuration taken on the X-Y plane at Z=1.2 mm for Re_H=1000. Since for the plain-fin the flow is fairly straightforward and it gets interrupted only by the tubes, unlike the wavy-fin, a flow recirculation zone is formed in the trailing edge of the tubes and can be seen in Figure 39. Figure 41 shows the enhanced view of the velocity vectors around 2nd tube for the plain-fin staggered configuration. The recirculation zone forming at the trailing edge of the tube can be clearly seen from Figure 41.

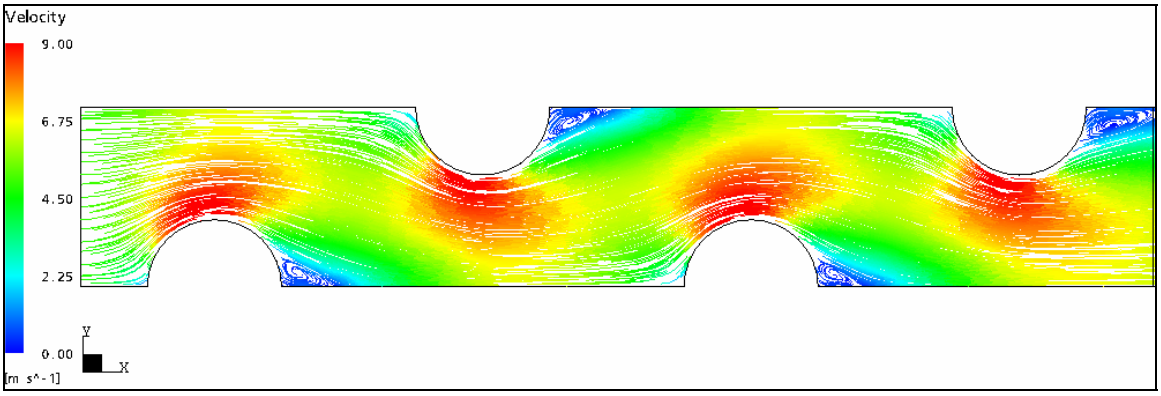

Figure 39. Streamline pattern for the plain-fin staggered configuration

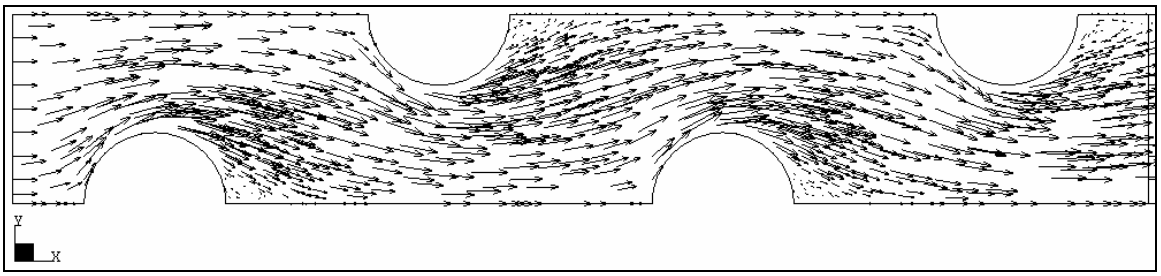

Figure 40. Velocity vectors for the plain-fin staggered configuration

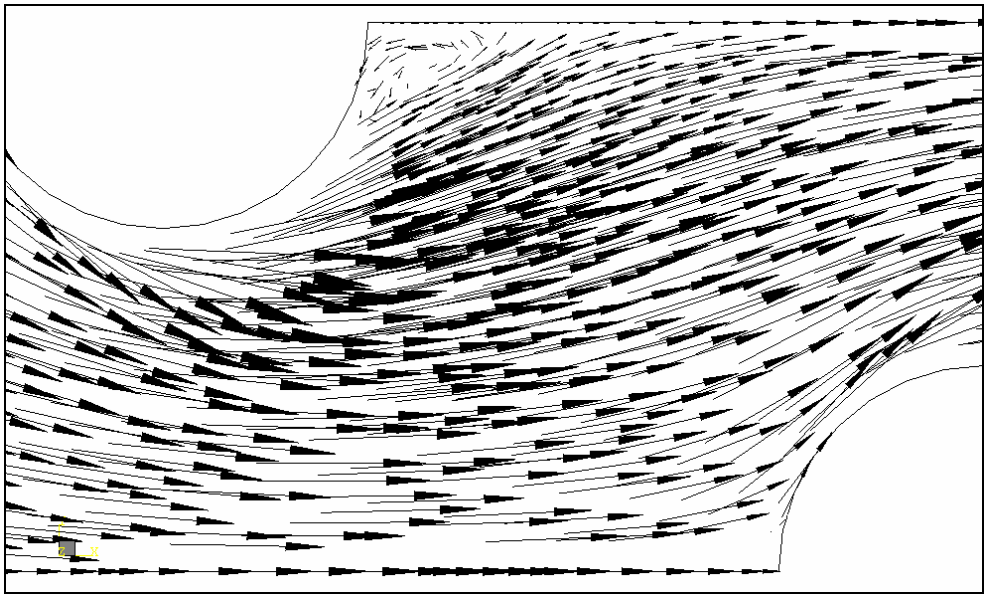

Figure 41. Enhanced view of velocity vectors for plain-fin staggered configuration around 2nd tube

Figure 42 shows the streamline plot and Figure 43 shows the velocity vectors for the plain-fin in-lined configuration taken on the X-Y plane at Z=1.2 mm for Re_H=1000. Again because of the flow interruption by the tubes, a flow recirculation zone is observed in the trailing edge of the tubes as the flow passes over the tubes. However, a distinguishing difference between flow structures for the plain-fin staggered configuration and plain-fin in-lined configuration can be observed from the Figures 39 and 42. For the plain-fin staggered configuration flow interruption takes place on both sides of the domain. Because of this repeated blockage of the flow due to the staggered tube blank on both sides of the domain in case of plain-fin staggered configuration, a smaller recirculation zone is observed in the trailing edge of the tubes. However, in case of plain-fin in-lined arrangement flow is blocked only on one side of the domain due to the in-lined array of the tubes. Since all the tubes for plain-fin in-lined configuration lie on the one side of the domain, flow gets divided into two separate regions as seen from Figure 42. The free flow region, on the upper side of the tubes and the stagnant flow region, in the trailing edge of the tubes. This flow structure results in much larger flow recirculation zone for plain-fin in-lined configuration as compared with plain-fin staggered configuration. Thus in case of plain-fin staggered configuration the flow gets interrupted on both sides of the domain at consistent interval because of the staggered tube layout resulting in smaller recirculation zone in the trailing edge of the tubes as seen from Figure 39. While in case of plain-fin in-lined configuration the flow gets interrupted only on one side of the domain because of the in-lined tube layout resulting in relatively larger recirculation zone in the trailing edge of the tubes and can be seen from Figure 42.

From Figure 42 it can be also seen that for the plain-fin in-lined configuration, the flow separates at the rear portion of a tube and reattaches at the front portion of the following tube to form a larger stationary recirculation region between the two adjacent tubes, resulting in a dead flow zone.

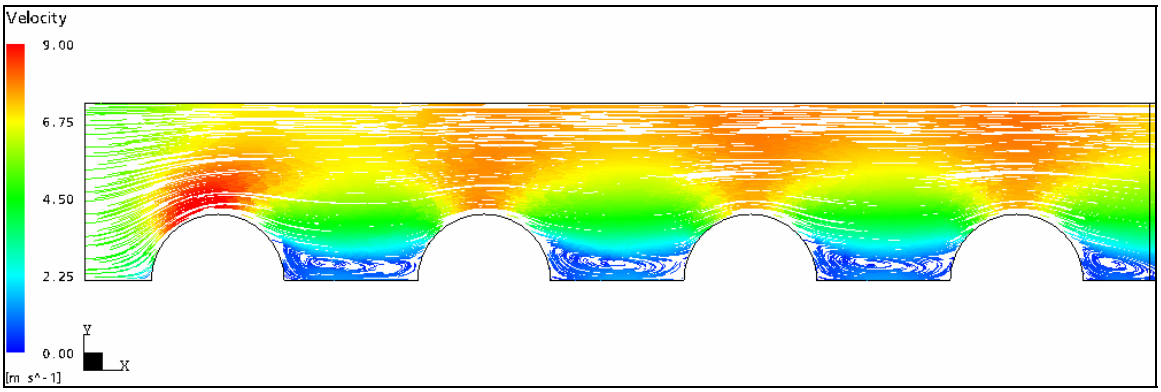

Figure 42. Streamline pattern for the plain-fin in-lined configuration

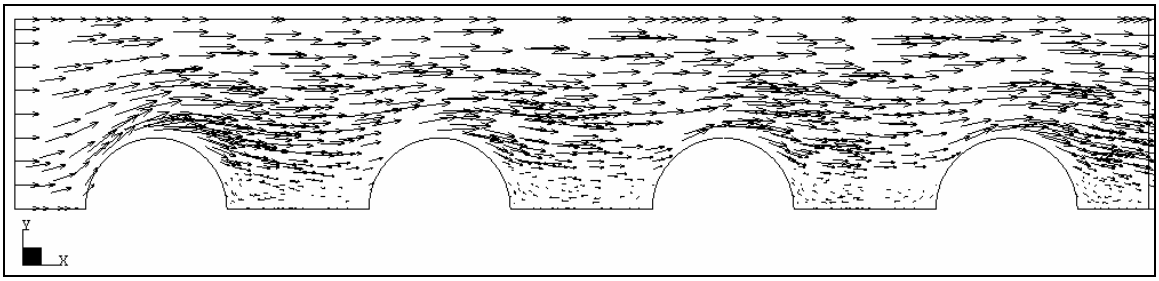

Figure 43. Velocity vectors for the plain-fin in-lined configuration

Figure 44 shows the streamline plot and Figure 45 shows the velocity vectors for the wavy-fin staggered configuration taken on the X-Y plane at Z=1.2 mm for Re_H=1000. The prominent difference between the flow structures for the plain-fin staggered configuration (Figure 39) and the wavy-fin staggered configuration can be easily seen from Figure 44. In case of a wavy-fin, the flow is guided by the fin corrugations and it gets reoriented each time it passes over a wavy corrugation as shown in Figure 38.

Because of this distinctive flow pattern in case of wavy-fin arrangement, no flow recirculation zone is observed in the wake of the tubes.

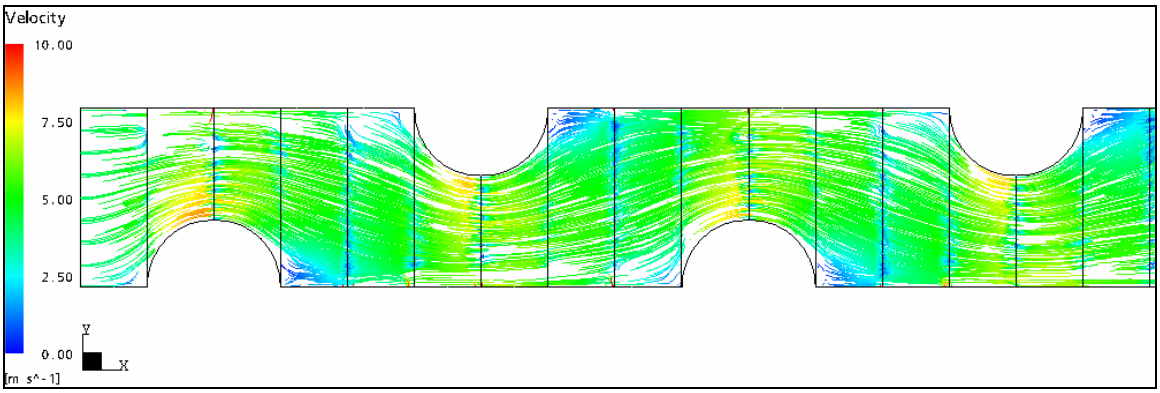

Figure 44. Streamline pattern for the wavy-fin staggered configuration

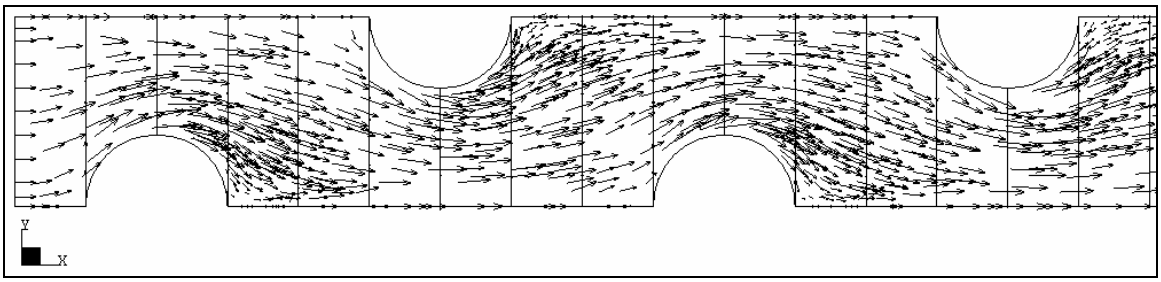

Figure 45. Velocity vectors for the wavy-fin staggered configuration

Figure 46 shows the streamline plot and Figure 47 shows the velocity vectors for the wavy-fin in-lined configuration taken on the X-Y plane at Z=1.2 mm for Re_H=1000. Here again it is observed that the re-orientation of the flow due to fin waviness results in no flow recirculation zones in the trailing edge of the tubes as the flow passes over the tubes. It is worthwhile to reflect on the flow structure difference observed for the plain-fin in-lined configuration (Figure 42) and the flow structure for the wavy-fin in-lined configuration as seen from Figure 46. For plain-fin in-lined arrangement much larger flow recirculation zones were observed in the trailing edge of the tubes as compared with

the plain-fin staggered configuration, because of the difference between staggered and in-lined layout of the tubes. However, in case of wavy-fin such a drastic difference between flow structures for the staggered and in-lined arrangements is not observed because flow is repeatedly reoriented by the fin waviness and unlike the plain-fin counterparts, tubes are not the only blockage to the flow for the wavy-fins.

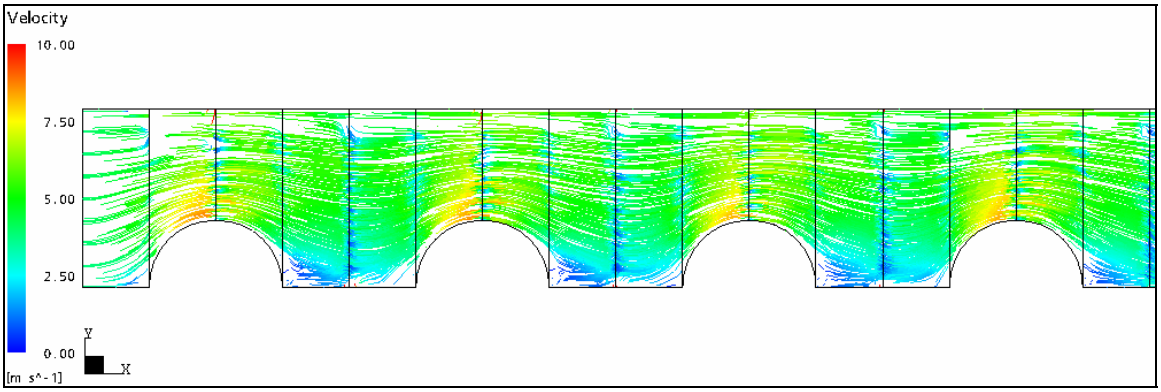

Figure 46. Streamline pattern for the wavy-fin in-lined configuration

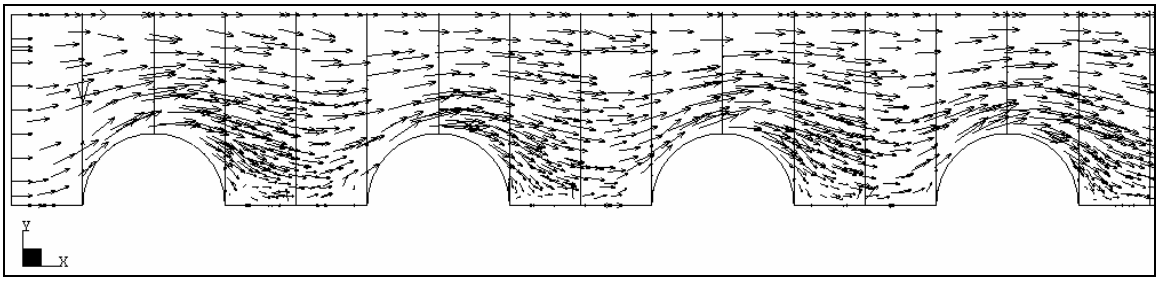

Figure 47. Velocity vectors for the wavy-fin in-lined configuration

Having completed the flow structure analysis, the temperature profiles for these four fin models were investigated. Figures 48, 49, 50 and 51 show the temperature profiles for the plain-fin staggered configuration, plain-fin in-lined configuration, wavy-fin staggered configuration and wavy-fin in-lined configuration respectively. These temperature profiles are illustrated on the X-Y plane at Z=1.2 mm for Re_H=1000. For this analysis the

inlet air temperature was kept at 30^0 C and the fin and the tube surfaces were kept as wall boundary with a constant temperature of 60^0 C. From the flow structure analysis it was found out that much larger flow recirculation zones are observed in the trailing edges of the tubes for plain-fin in-lined arrangement as compared to the plain-fin staggered configuration, while no flow recirculation zones were observed for the wavy-fin staggered and in-lined configurations. The temperature profile study confirms this observation, where it can be seen from Figure 49, that in case of plain-fin in-lined configuration much larger high temperature regions or "warm zones" are observed in the trailing edges of the tubes because of the stagnant recirculation flow zone which stretches between the two adjacent tubes. However, in case of plain-fin staggered configuration, wavy-fin staggered configuration and wavy fin-in-lined configuration, such large "warm zones" are not observed, as seen from Figures 48, 50 and 51, respectively.

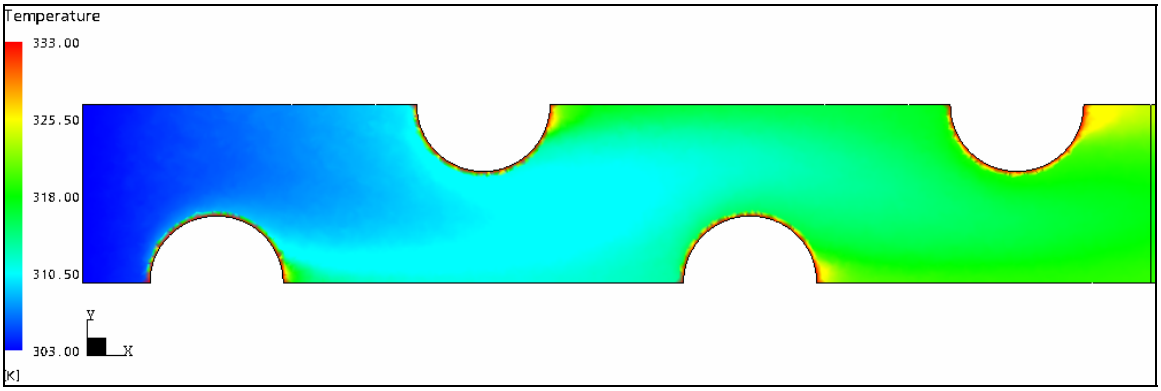

Figure 48. Temperature profile for plain-fin staggered configuration

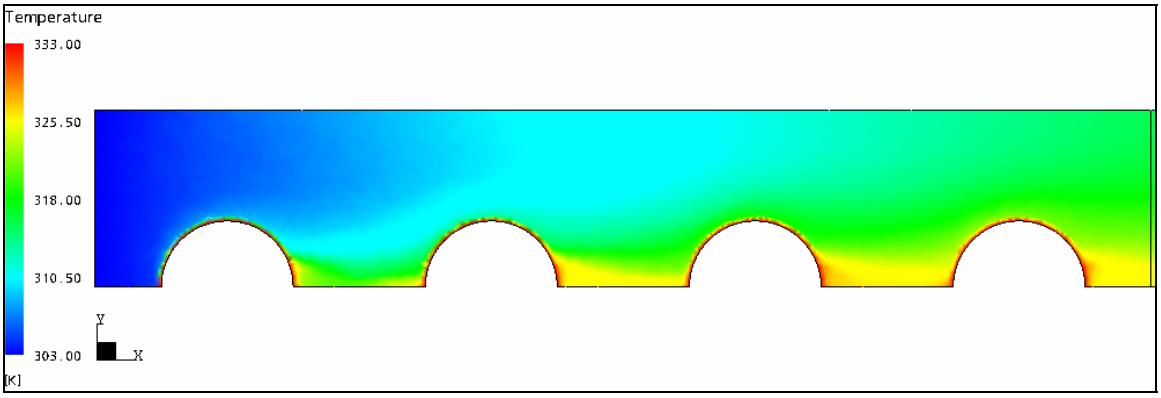

Figure 49. Temperature profile for plain-fin in-lined configuration

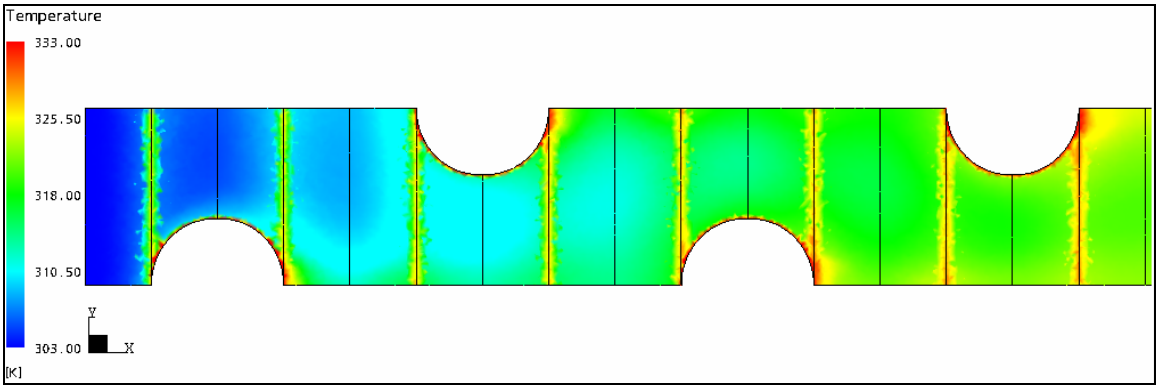

Figure 50. Temperature profile for wavy-fin staggered configuration

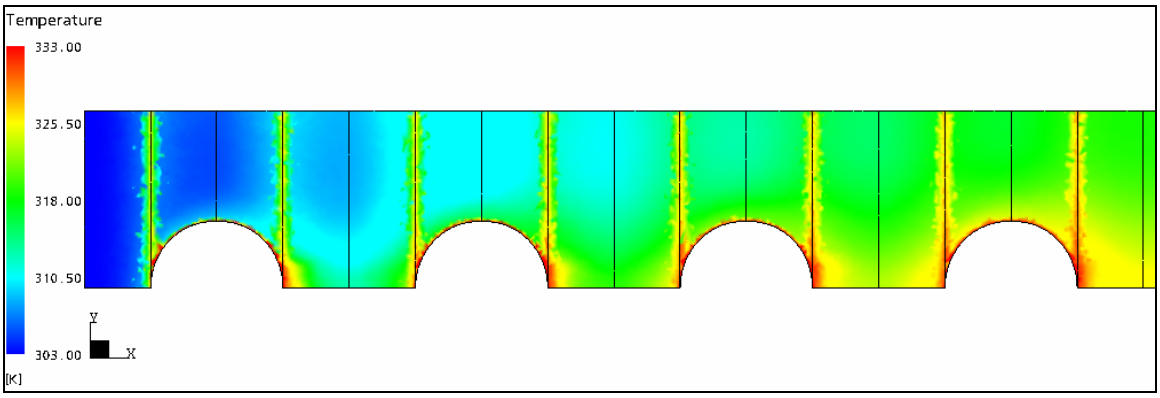

Figure 51. Temperature profile for wavy-fin in-lined configuration

In summary, it can be said that the flow structure for the plain-fin is highlighted by the flow recirculation zones in the trailing edges of the tubes, while flow structure for the wavy-fin configuration is highlighted by the flow reorientation due to fin waviness and as such the absence of the recirculation zones. This difference in the flow structure has a significant effect on the heat transfer and the flow friction characteristics shown by these fin configurations in the staggered and in-lined layouts. The three-dimensional numerical investigation done by Jang et al. (1996) on plain fin staggered and in-lined configurations based on the same geometrical parameters revealed that the average heat transfer coefficient of staggered arrangement is 15 – 27% higher than that of in-lined arrangement, while the average pressure drop of staggered arrangement is 20 – 25% higher than that of in-lined arrangement.

The current numerical study investigates the effect of this flow structure difference for the wavy-fin staggered and in-lined configurations based on same geometrical parameters on the heat transfer and flow friction characteristics. Figure 52 shows the variation of the Colburn factor (j) against the Reynolds number (Re_H), while Figure 53 shows the variation of the friction factor (f) against the Reynolds number (Re_H) for the four fin models under investigation. It can be seen from Figure 52 that the Colburn factor (j) for the wavy-fin staggered arrangement is 7%-11% higher than that of the wavy-fin in-lined arrangement, while the Colburn factor (j) for the plain-fin staggered arrangement is 23%-34% higher than that of the plain-fin in-lined arrangement. Also from Figure 53 it can be observed that the friction factor (f) for the wavy-fin staggered arrangement is 9%-12% higher than that of the wavy-fin in-lined arrangement, while the friction factor (f)

for the plain-fin staggered arrangement is 29%-38% higher than that of the plain-fin in-lined arrangement. Thus it can be concluded that due to the flow structure difference discussed earlier, much higher percentage difference is observed in the heat transfer and the flow friction characteristics for plain-fin staggered configuration when compared to the plain-fin in-lined configuration. On the other hand, a relatively smaller percentage difference is observed for the heat transfer and the flow friction characteristics in case of wavy-fin staggered configuration when compared to the wavy-fin in-lined configuration.

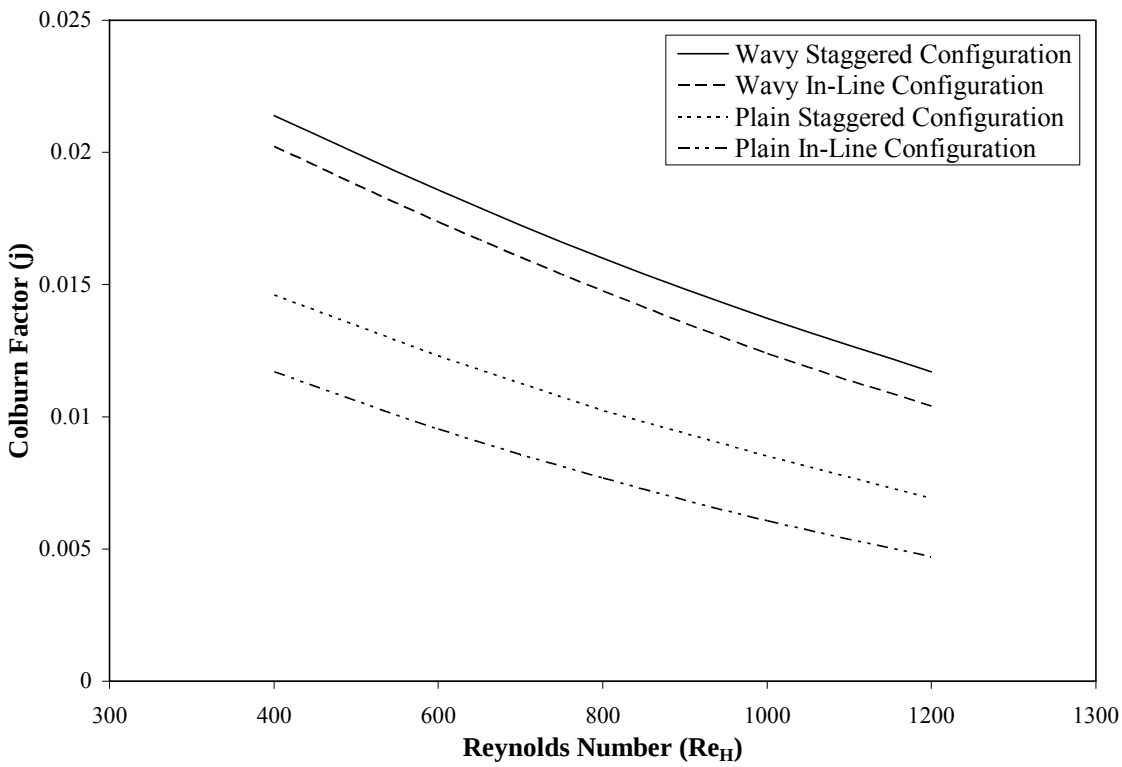

Figure 52. Variation of Colburn factor (j) against Reynolds number (Re_H) for the plain and wavy fin configurations in the staggered and the in-lined layouts

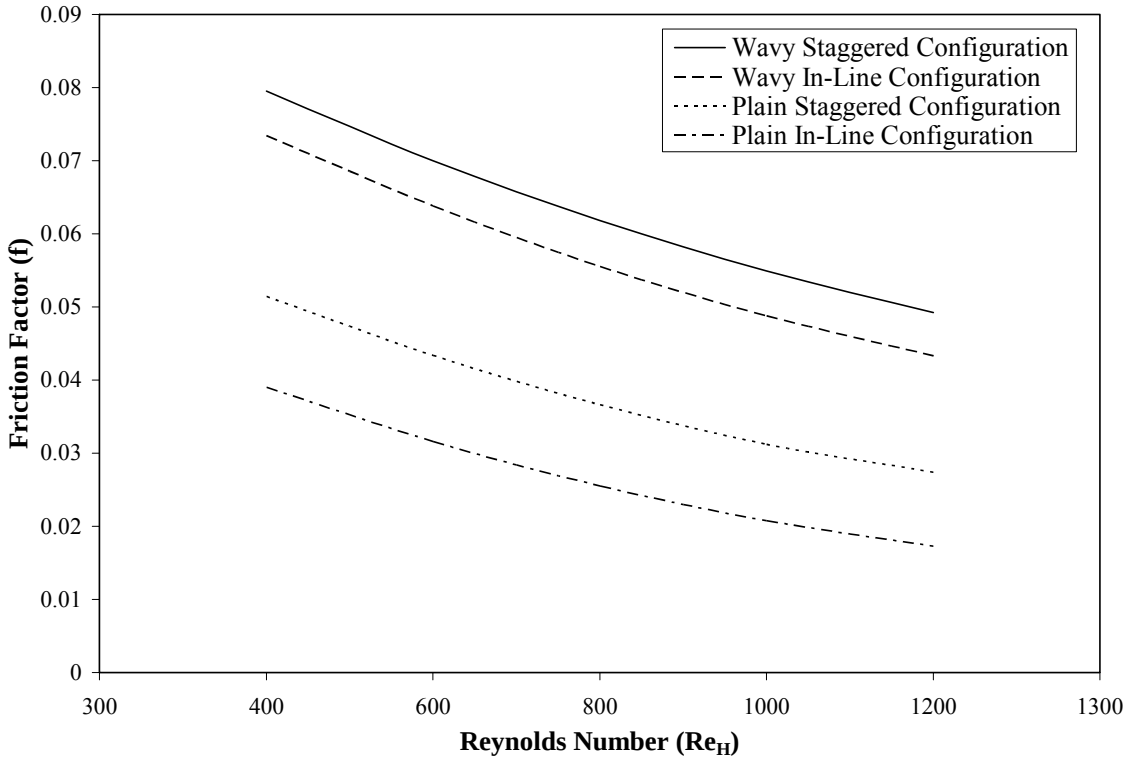

Figure 53. Variation of friction factor (f) against Reynolds number (Re_H) for the plain and wavy fin configurations in the staggered and the in-lined layouts

In case of plain-fin configurations, boundary layer interruption of the flow is caused only by the tubes. Hence, the tube layout is of significant importance for plain-fins from the point of view of heat transfer and pressure drop characteristics. However, for the wavy fins, the flow boundary layer is repeatedly interrupted by the fin waviness as well as the tubes. Hence the tube layout is relatively insignificant for the wavy fin configurations from the point of view of heat transfer and pressure drop characteristics as seen from the flow structure analysis. In case of plain-fin staggered configuration higher heat transfer performance and higher pressure drop is observed as compared to the plain-fin in-lined arrangement because the flow boundary layer is repeatedly interrupted by the

staggered tube layout, thereby causing a better flow mixing as compared to the plain-fin in-lined arrangement. Wavy-fin, on the other hand, does not merely rely on the tube layout for the heat transfer performance. Boundary layer interruption caused by the fin waviness and the flow mixing caused thereby are also important factors in case of wavy-fin staggered and in-lined arrangement, which are independent of the tube layout. This explains the large percentage difference observed for the heat transfer and flow friction characteristics for plain fin staggered and in-lined configurations as compared with the wavy-fin counterparts.

Effects of Longitudinal and Transverse Pitch

Having investigated the effects of the number of tube rows on the heat transfer and pressure drop characteristics for the wavy-fin and the plain-fin, it is concluded that the four tube row domain can be regarded as an optimum multi-row fin-and-tube heat exchanger. The previous numerical investigations by Jang et al. (1996) and Tutar and Kakac (2004) have also concluded that a four row tube configuration is the optimal choice for the balance between the increase in heat transfer performance against the increase in the pressure drop characteristics. However, the effects of the longitudinal and transverse tube pitch on the heat exchanger performance have not been numerically explored. Hence the next logical step in this study was to investigate what effects the longitudinal and transverse pitch has on the heat transfer and pressure drop characteristics for the four tube row domain. The effects of these geometrical parameters on the heat exchanger performance have been investigated for the plain-fin staggered configuration and the wavy-fin staggered configuration over the laminar flow

range $(400 \le \mathrm{Re}_H \le 1200)$. The following section describes the findings of this investigation.

Effects of Longitudinal Pitch

The effects of the change in longitudinal pitch (Ll) on the heat transfer and the pressure drop characteristics for the four tube row domain of the wavy-fin staggered configuration and the plain-fin staggered configuration was studied by running three test cases for each of these fin arrangements. In each case the longitudinal tube pitch (Ll) is changed keeping all other geometrical parameters constant so that the effects of the longitudinal pitch over the heat exchanger performance can be evaluated.

Figures 54, 55 and 56 show the three longitudinal pitch test case domains used for the wavy-fin staggered configurations. Figure 54 shows the wavy- fin staggered configuration domain with longitudinal pitch (Ll) = 19.05 mm. Figure 55 shows the wavy- fin staggered configuration domain with longitudinal pitch (Ll) = 23.8125 mm. While Figure 56 shows the wavy- fin staggered configuration domain with longitudinal pitch (Ll) = 28.575 mm. It should be noted similar three test case domains with consistent increase in the longitudinal tube pitch (Ll) were used for the plain-fin staggered configuration to investigate the effects of longitudinal pitch on the plain-fin heat exchanger performance.

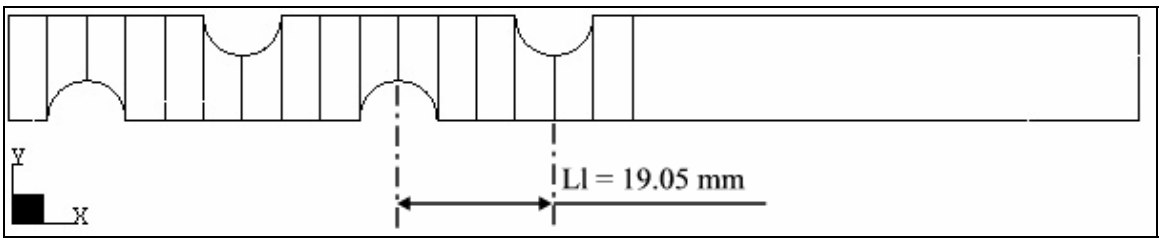

Figure 54. Wavy- fin staggered configuration with longitudinal pitch (Ll) = 19.05 mm

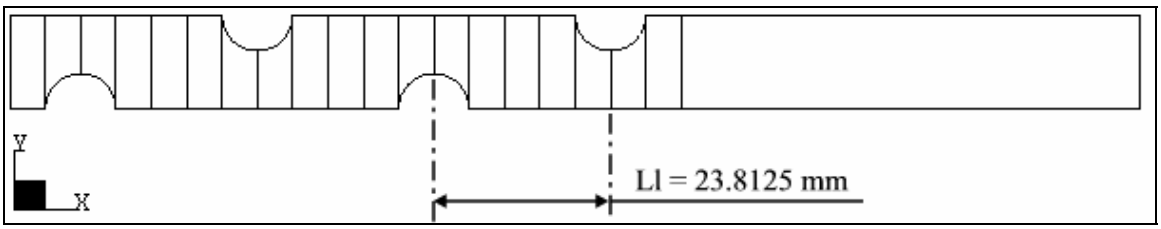

Figure 55. Wavy- fin staggered configuration with longitudinal pitch (Ll) = 23.8125 mm

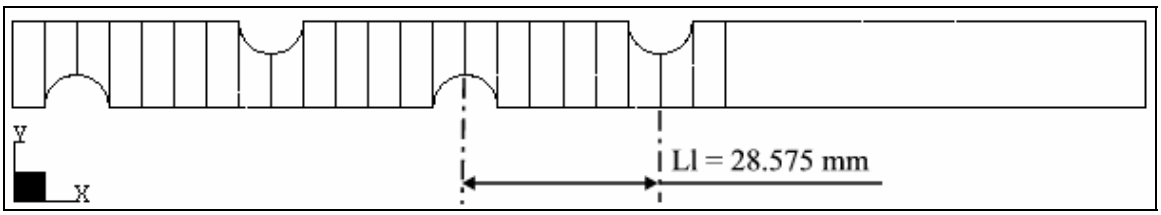

Figure 56. Wavy- fin staggered configuration with longitudinal pitch (Ll) = 28.575 mm

Tables 13 and 14 show the geometrical parameters used for the three longitudinal pitch test cases for plain-fin staggered configuration and wavy-fin staggered configuration respectively. These geometrical parameters are chosen based on the experimental studies by Wang et al. (1996 and 1997).

Table 13. Geometrical Parameters for the plain-fin staggered configuration for the effects of longitudinal pitch (Ll) analysis

Plain Fin Staggered Configuration	Ll (mm)	Lt (mm)	Fp (mm)	Ft (mm)	D (mm)	Wa (Degrees)	Wh (mm)
Test Case 1	**19.05**	25.4	3.53	0.12	9.525	-	-
Test Case 2	**23.8125**	25.4	3.53	0.12	9.525	-	-
Test Case 3	**28.575**	25.4	3.53	0.12	9.525	-	-

Table 14. Geometrical Parameters for the wavy-fin staggered configuration for the effects of longitudinal pitch (Ll) analysis

Wavy Fin Staggered Configuration	Ll (mm)	Lt (mm)	Fp (mm)	Ft (mm)	D (mm)	Wa (Degrees)	Wh (mm)
Test Case 1	**19.05**	25.4	3.53	0.12	9.525	17.5	1.5
Test Case 2	**23.8125**	25.4	3.53	0.12	9.525	17.5	1.5
Test Case 3	**28.575**	25.4	3.53	0.12	9.525	17.5	1.5

<u>Plain-fin Staggered configuration:</u>

The effect of longitudinal tube pitch (Ll) on the heat transfer and pressure drop characteristics for the plain-fin staggered configuration is shown Figures 57, 58 and 59.

Figure 57 shows the variation of the Colburn factor (j) against the Reynolds number (Re_H) for the three longitudinal pitch test cases. It can be seen from Figure 57 that the Colburn factor (j) decreases with the increase in the longitudinal tube pitch (Ll). This observation is contrary to the anticipation that increase in the heat transfer area would also increase in the heat transfer performance. However, this phenomenon can be explained on the fact that lower the longitudinal tube pitch (Ll), more restricted is the flow. Increasing the longitudinal tube pitch causes the flow to be less restricted and decreases the advantage which can be exploited from a better flow mixing achieved from

the obstruction to the flow by the tubes. Thus increase in the longitudinal tube pitch increases the available heat transfer area but decreases the flow mixing. As a result, the average heat transfer coefficient decreases from increasing the longitudinal tube pitch (Ll), since a large amount of ineffective heat transfer may occur that does not take part in the heat transfer.

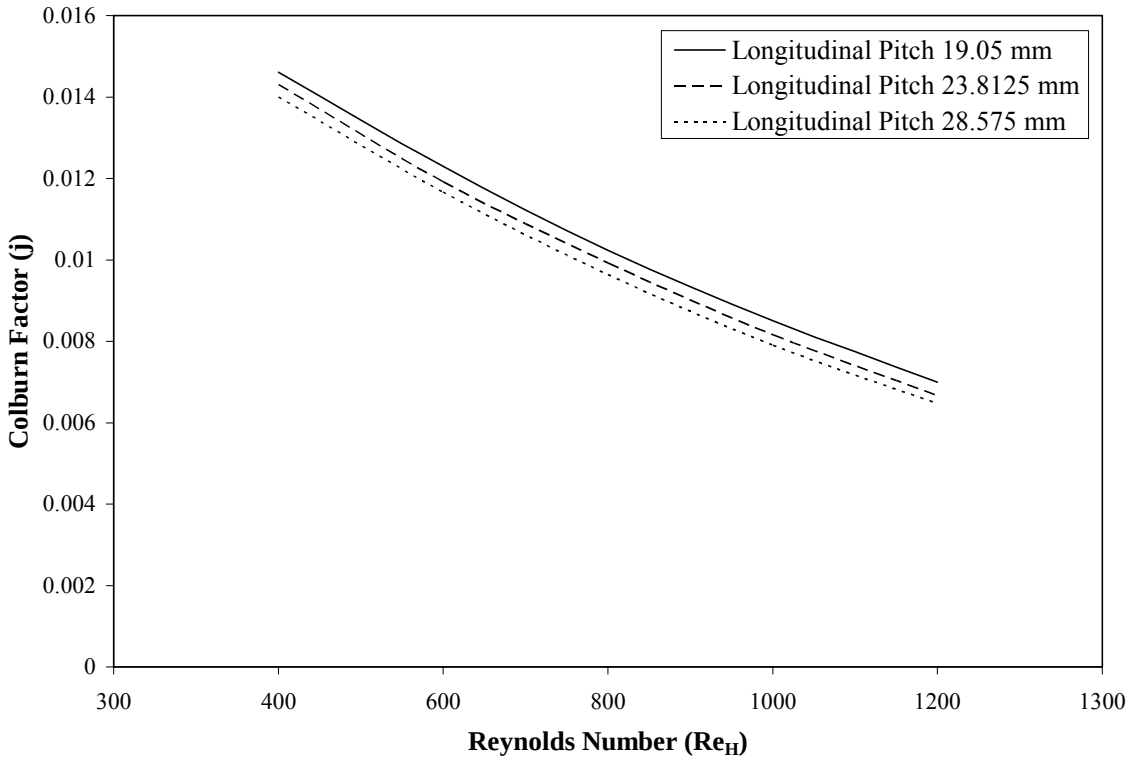

Figure 57. Effect of longitudinal tube pitch (Ll) on the Colburn factor (j) for the plain-fin staggered configuration

Figure 58 shows the variation of the friction factor (f) against the Reynolds number (Re_H) for the three longitudinal pitch (Ll) test cases. It can be seen from Figure 58 that the friction factor (f) decreases with the increase in the longitudinal tube pitch. This observation again contradicts the expectation that increase in the fin surface area would

increase the flow friction characteristics. This phenomenon, again, can be explained on the fact that lower the longitudinal pitch (Ll), more restricted and dense the airflow is, due to the better flow mixing caused by the obstruction to the flow by the tightly spaced tubes. Increasing longitudinal tube pitch, even though increases the fin surface area, the effect is minor when compared with the less restriction to flow caused by the farther spacing of the tubes for the range of the longitudinal tube pitches tested.

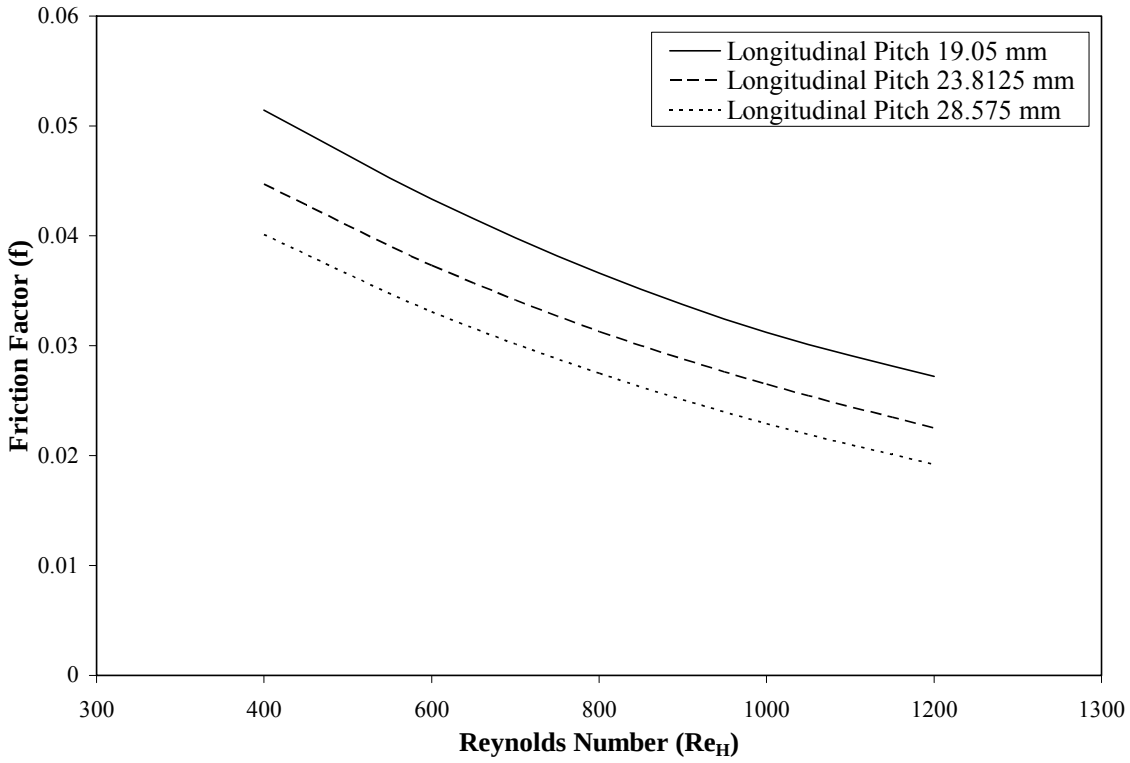

Figure 58. Effect of longitudinal tube pitch (Ll) on the friction factor (f) for the plain-fin staggered configuration

Figure 59 shows the variation of the efficiency index (j/f) against the Reynolds number (Re_H) for the three longitudinal pitch (Ll) test cases. The efficiency of a fin-and-tube heat exchanger depends to a large degree on the fin performance. A good fin

performance requires a very good heat transfer between the fluid and the fin and at the same time a low pressure drop of the flow. These are conflicting parameters. To improve the heat transfer one normally has to pay with higher pressure drop. There are different criteria available to compare fin performances based upon different geometrical aspects. One such criterion is the flow area goodness factor, characterized in this thesis as the efficiency index. The flow area goodness factor is defined by London (1984) as the ratio of the Colburn factor (j) to the friction factor (f), j/f. A surface having a higher j/f factor is "good", because it will require lower free flow area and hence a lower frontal area for the exchanger, as per London (1984). Such a surface would be a best choice for the critical balance between high heat transfer performance and low pressure drop.

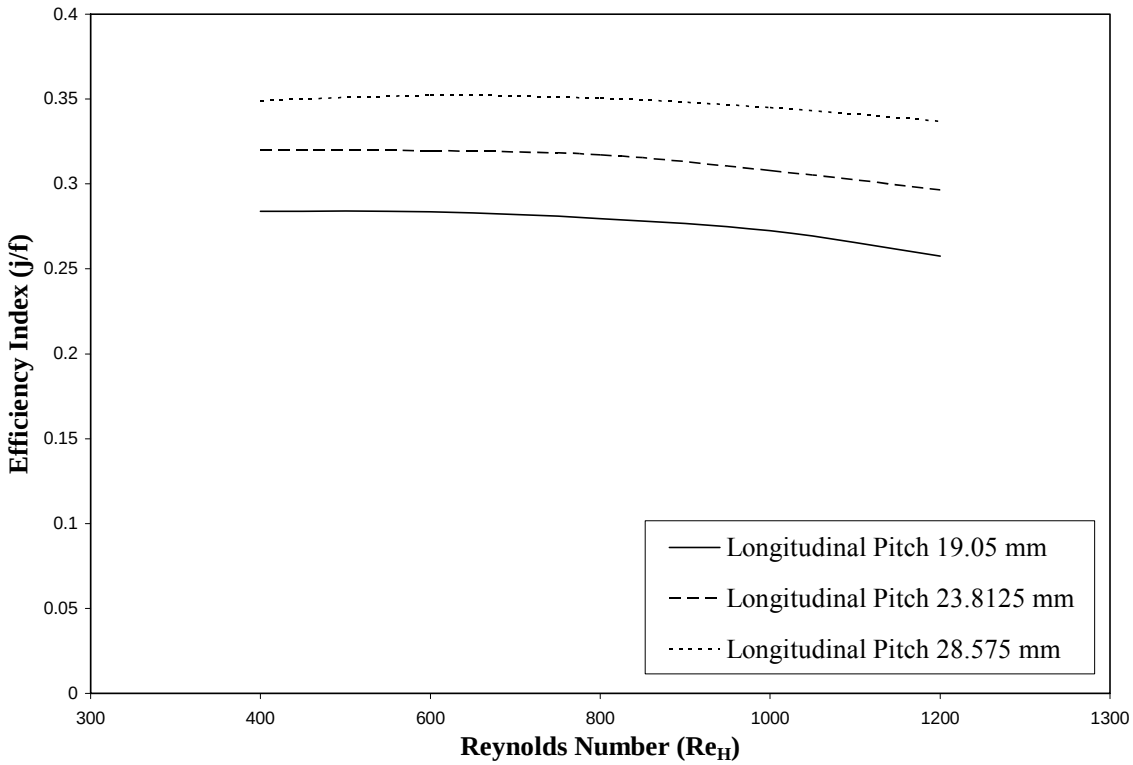

Figure 59. Effect of longitudinal tube pitch (Ll) on the efficiency index (j/f) for the plain-fin staggered configuration

From Figure 59 it can be seen that the efficiency index (j/f) increases with the increase in the longitudinal tube pitch (Ll). This observation indicates that even though the heat transfer performance (j) decreases with the increase the tube longitudinal pitch (Ll), the efficiency for the surface goes up due to the corresponding decrease in the friction factor (f). As seen from the Figures 57 and 58, the Colburn factor (j) and friction factor (f), both decreases with the increase in the longitudinal pitch for the plain-fin staggered configuration. But the percentage decrease in friction factor (f) is higher than the percentage decrease in the Colburn factor (f). This indicates that, as the flow simplifies due to the increase in the longitudinal tube pitch (Ll), the decrease in the pressure drop characteristics (f) is more drastic than the decrease in the heat transfer performance (j). As a result, the efficiency index (j/f) increases with the increase in the tube longitudinal pitch.

Wavy-fin Staggered configuration:

The effect of longitudinal tube pitch (Ll) on the heat transfer and pressure drop characteristics for the wavy-fin staggered configuration is shown in the Figures 60, 61 and 62. Results obtained for the wavy-fin staggered configuration are similar in nature as compared to the plain-fin staggered configuration, even though the percentage differences between the results for these two fin configurations vary, due to the flow distinction reported earlier. As the longitudinal tube pitch (Ll) increases, a higher percentage difference was observed for heat transfer and pressure drop characteristics in

case of the three test cases for plain-fin staggered configuration as compared to the wavy-fin staggered configuration.

Figure 60 shows the variation of the Colburn factor (j) against the Reynolds number (Re_H) for the three longitudinal pitch test cases. It can be seen from Figure 60 that the Colburn factor (j) decreases with the increase in the longitudinal tube pitch (Ll) as seen in case of plain-fin staggered arrangement. This observation again confirms the observation stated before that the increase in the longitudinal tube pitch (Ll) makes the flow more simplistic thereby decreasing the heat transfer performance for the fin-configuration.

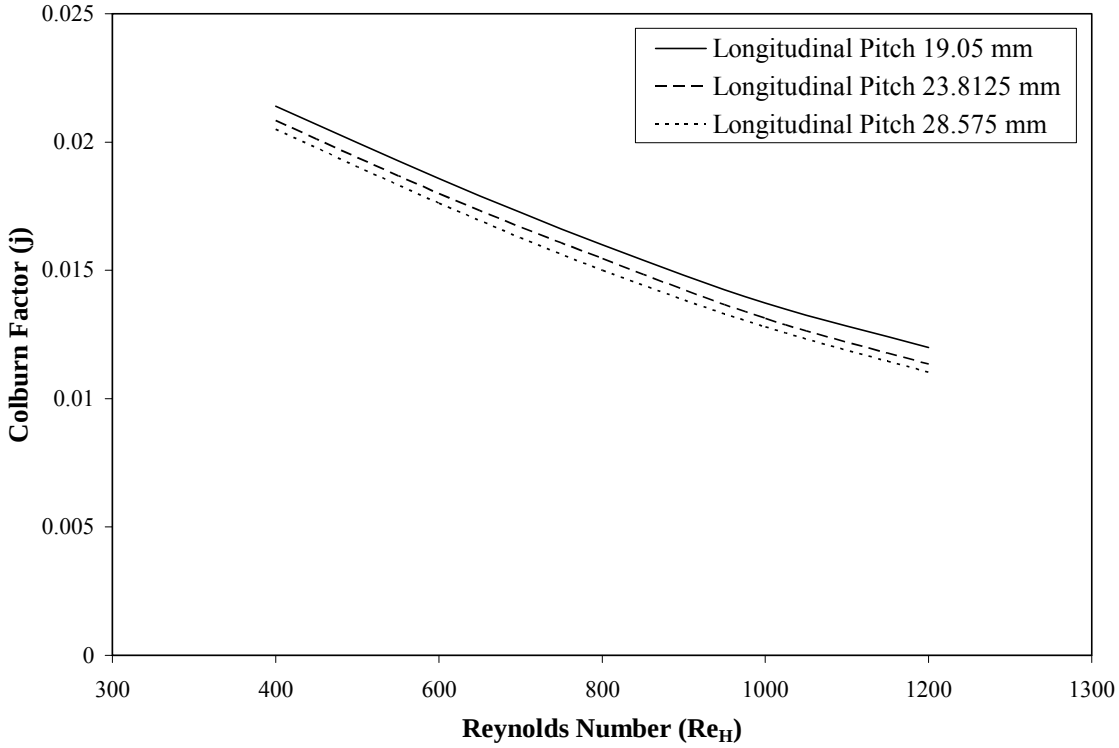

Figure 60. Effect of longitudinal tube pitch (Ll) on the Colburn factor (j) for the wavy-fin staggered configuration

Figure 61 shows the variation of the friction factor (f) against the Reynolds number (Re_H) for the three longitudinal pitch (Ll) test cases. Here again, it can be seen from Figure 61 that the friction factor (f) decreases with the increase in the longitudinal tube pitch as seen in case of plain-fin staggered arrangement. This validates previous observation that the increase in the longitudinal tube pitch decreases the airflow mixing, thereby decreasing the flow friction resistance. Hence the friction factor (f) goes down with the increase in the longitudinal tube pitch (Ll).

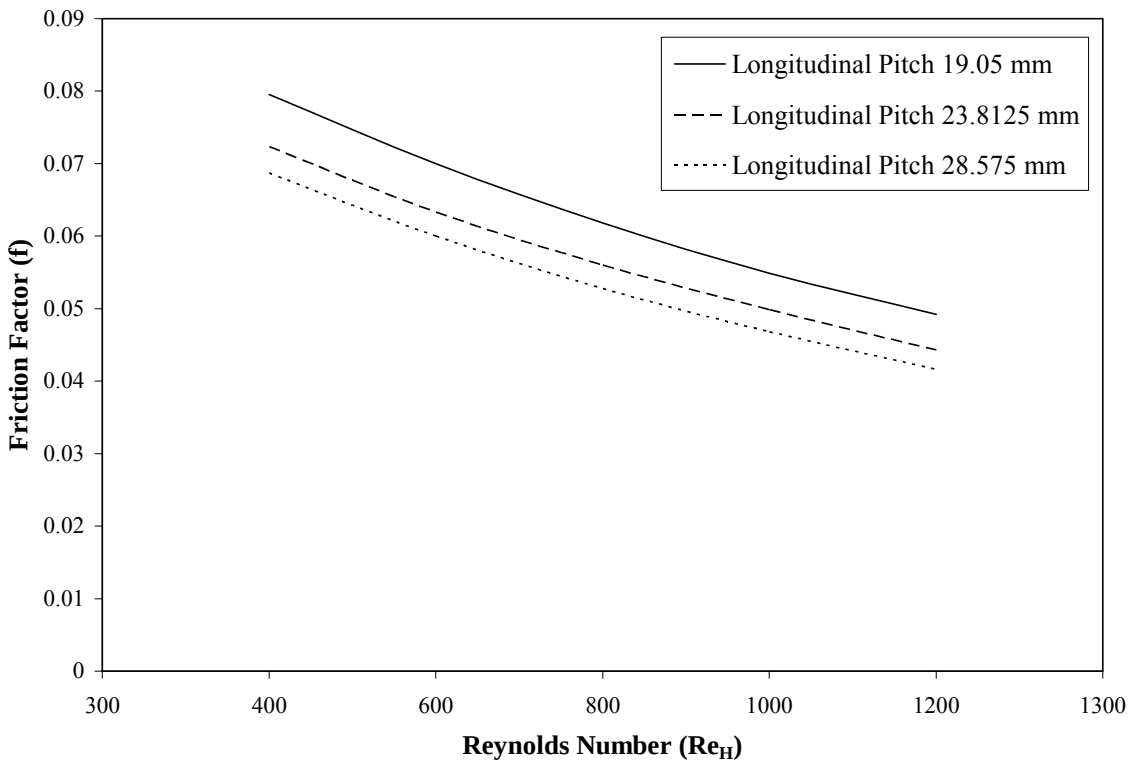

Figure 61. Effect of longitudinal tube pitch (Ll) on the friction factor (f) for the wavy-fin staggered configuration

Figure 62 shows the variation of the efficiency index (j/f) against the Reynolds number (Re_H) for the three longitudinal pitch (Ll) test cases. Once again, it is observed

that the efficiency index (j/f) increases with the increase in the longitudinal tube pitch (Ll), as seen for the plain-fin staggered configuration. This verifies the previous observation that the increase in longitudinal tube pitch (Ll) decreases the friction factor (f) more drastically than decrease in the Colburn factor (j), owing to the flow simplification. As a result efficiency index (j/f) goes up with increase in the longitudinal tube pitch (Ll).

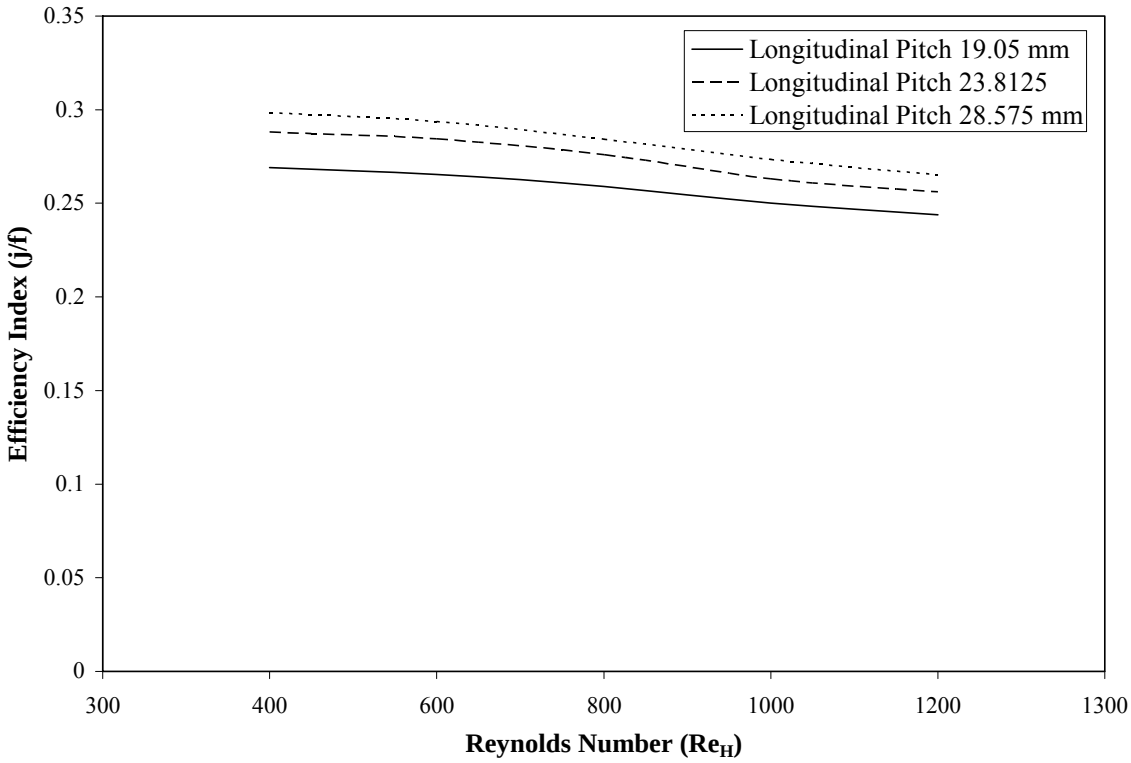

Figure 62. Effect of longitudinal tube pitch (Ll) on the efficiency index (j/f) for the wavy-fin staggered configuration

Effects of Transverse Pitch

After investigating the effects of the longitudinal pitch on the heat exchanger performance next step in this study was to explore the effects of the transverse pitch. The effects of the change in transverse pitch (Lt) on the heat transfer and the pressure drop characteristics for the four tube row domain of the wavy-fin staggered configuration and the plain-fin staggered configuration was studied by running three test cases for each of these fin arrangements. In each case the transverse tube pitch (Lt) is changed keeping all other geometrical parameters constant so that the effects of the longitudinal pitch over the heat exchanger performance can be evaluated.

Figures 63, 64 and 65 show the three transverse pitch test case domains used for the wavy-fin staggered configurations. Note that for this simulation only half of the domain was considered due to the symmetry of the problem. Hence these domain Figures represent half the transverse tube pitch (Lt/2). Figure 63 shows the wavy- fin staggered configuration domain with transverse pitch (Lt) = 25.4 mm. Figure 64 shows the wavy-fin staggered configuration domain with transverse pitch (Lt) = 30.4 mm. While Figure 65 shows the wavy- fin staggered configuration domain with transverse pitch (Lt) = 35.4 mm. Note that similar three test case domains with consistent increase in the transverse tube pitch (Lt) were used for the plain-fin staggered configuration to investigate the effects of transverse pitch on the plain-fin heat exchanger performance.

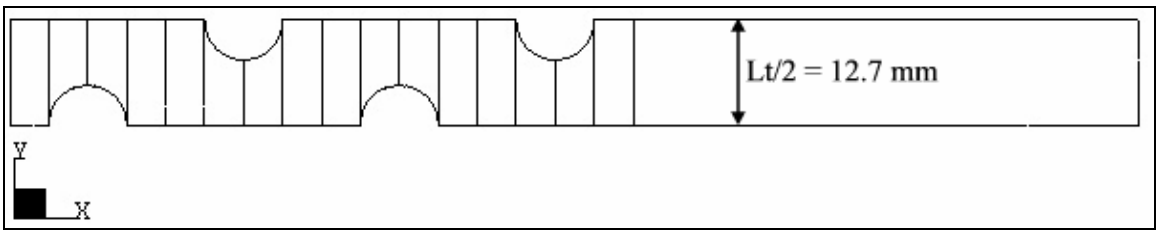

Figure 63. Wavy- fin staggered configuration with transverse pitch (Lt) = 25.4 mm

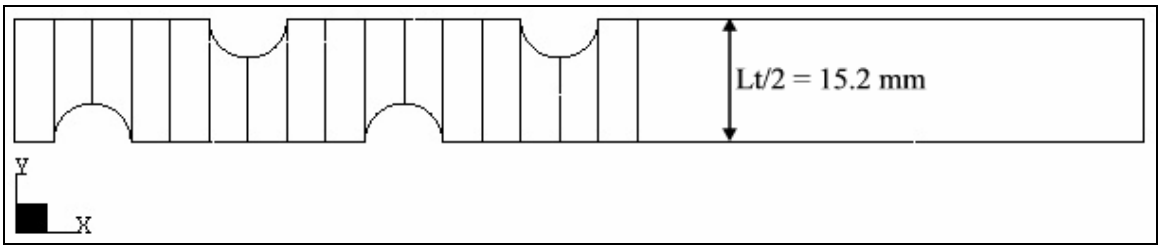

Figure 64. Wavy- fin staggered configuration with transverse pitch (Lt) = 30.4 mm

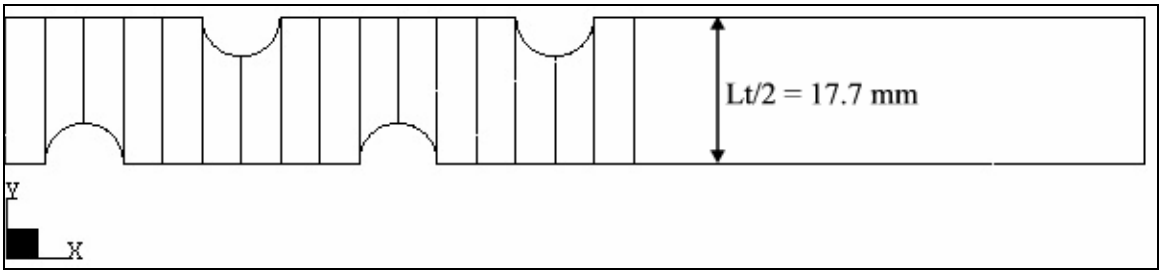

Figure 65. Wavy- fin staggered configuration with transverse pitch (Lt) = 35.4 mm

Tables 15 and 16 show the geometrical parameters used for the three transverse pitch test cases for plain-fin staggered configuration and wavy-fin staggered configuration respectively. These geometrical parameters are chosen based on the experimental studies by Wang et al. (1996 and 1997).

Table 15. Geometrical Parameters for the plain-fin staggered configuration for the effects of transverse pitch (Lt) analysis

Plain Fin Staggered Configuration	Ll (mm)	Lt (mm)	Fp (mm)	Ft (mm)	D (mm)	Wa (Degrees)	Wh (mm)
Test Case 1	19.05	**25.4**	3.53	0.12	9.525	-	-
Test Case 2	19.05	**30.4**	3.53	0.12	9.525	-	-
Test Case 3	19.05	**35.4**	3.53	0.12	9.525	-	-

Table 16. Geometrical Parameters for the wavy-fin staggered configuration for the effects of transverse pitch (Lt) analysis

Wavy Fin Staggered Configuration	Ll (mm)	Lt (mm)	Fp (mm)	Ft (mm)	D (mm)	Wa (Degrees)	Wh (mm)
Test Case 1	19.05	**25.4**	3.53	0.12	9.525	17.5	1.5
Test Case 2	19.05	**30.4**	3.53	0.12	9.525	17.5	1.5
Test Case 3	19.05	**35.4**	3.53	0.12	9.525	17.5	1.5

Plain-fin Staggered configuration:

The effect of transverse tube pitch (Lt) on the heat transfer and pressure drop characteristics for the plain-fin staggered configuration is shown in Figures 66, 67 and 68. Results obtained for the transverse tube pitch (Lt) change are similar in nature as compared with the change in the longitudinal tube pitch (Ll). In the study for the longitudinal tube pitch (Ll) change it was observed that the increase in the longitudinal tube pitch decreases the flow mixing caused by the increased tube spacing, thereby decreasing the flow friction resistance. As a result Colburn factor (j) and friction factor (f) decrease with the increase in the longitudinal tube pitch (Ll). However, the decrease in friction factor (f) was found to be more drastic than the decrease in the Colburn factor (j).

Therefore efficiency index (j/f) increases with the increase in the longitudinal tube pitch (Ll). The current study to investigate the effects of transverse tube pitch (Lt) on the heat transfer and pressure drop characteristics revealed the findings of the similar nature. Increase in the transverse tube pitch (Lt) causes decrease in the flow mixing caused by the increased tube spacing, thereby decreasing the flow friction resistance. As a result Colburn factor (j) and friction factor (f) decrease with the increase in the transverse tube pitch.

Figure 66 shows the variation of the Colburn factor (j) against the Reynolds number (Re_H) for the three transverse pitch (Lt) test cases. It can be seen from Figure 66 that the Colburn factor (j) decreases with the increase in the transverse tube pitch (Lt), verifying the observation stated before that the increase in the transverse tube pitch (Lt) makes the flow more simplistic thereby decreasing the heat transfer performance for the fin-configuration.

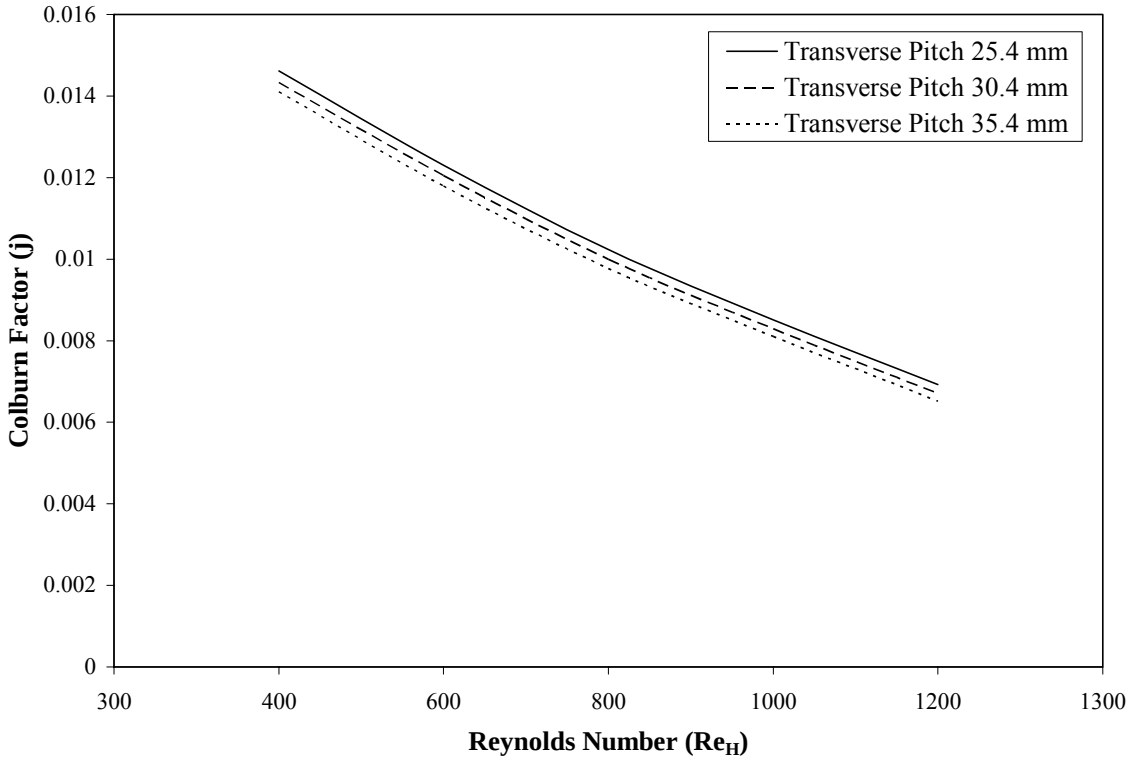

Figure 66. Effect of transverse tube pitch (Lt) on the Colburn factor (j) for the plain-fin staggered configuration

Figure 67 shows the variation of the friction factor (f) against the Reynolds number (Re_H) for the three transverse pitch (Lt) test cases. Here again, it can be seen from Figure 67 that the friction factor (f) decreases with the increase in the transverse tube pitch. This confirms the previous observation that the increase in the transverse tube pitch decreases the flow mixing, thereby decreasing the flow friction resistance. Hence the friction factor (f) goes down with the increase in the transverse tube pitch (Lt).

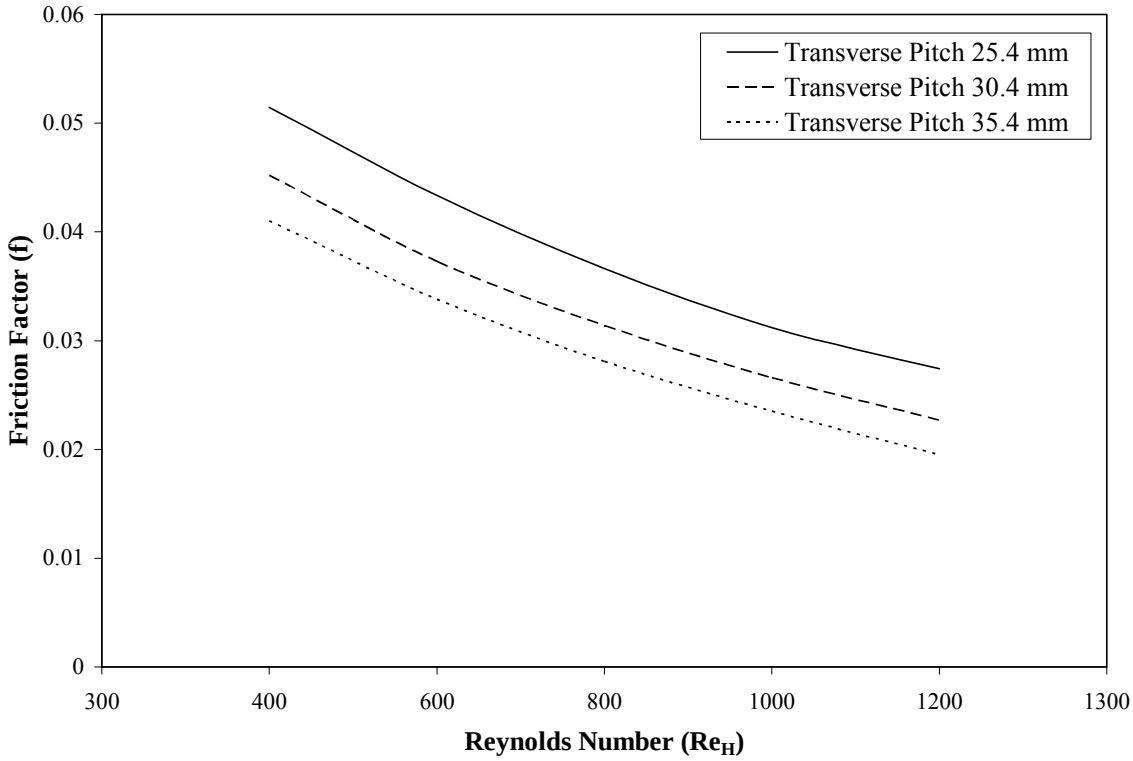

Figure 67. Effect of transverse tube pitch (Lt) on the friction factor (f) for the plain-fin staggered configuration

Figure 68 shows the variation of the efficiency index (j/f) against the Reynolds number (Re_H) for the three transverse pitch (Lt) test cases. Once again, it is observed that the efficiency index (j/f) increases with the increase in the transverse tube pitch (Lt), authenticating the previous statement that the increase in transverse tube pitch (Lt) decreases the friction factor (f) more drastically than decrease in the Colburn factor (j), due to the flow simplification. As a result efficiency index (j/f) goes up with increase in the transverse tube pitch (Lt).

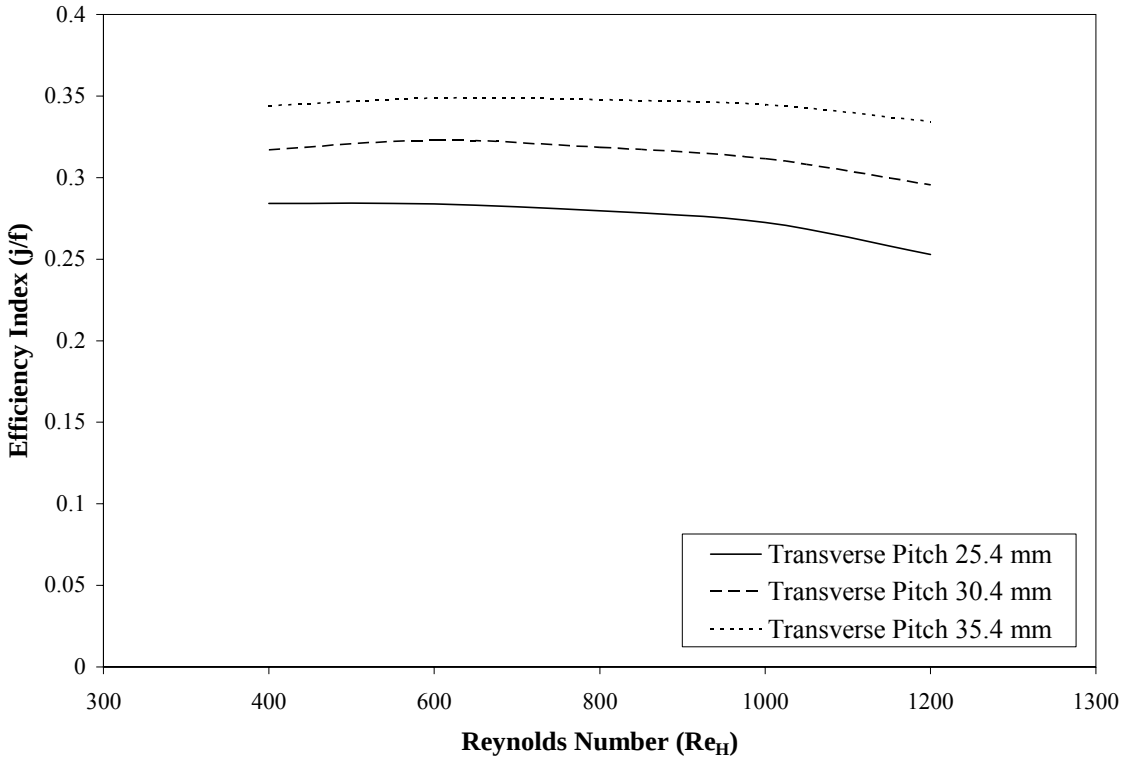

Figure 68. Effect of transverse tube pitch (Lt) on the efficiency index (j/f) for the plain-fin staggered configuration

Wavy-fin Staggered configuration:

The effect of transverse tube pitch (Lt) on the heat transfer and pressure drop characteristics for the wavy-fin staggered configuration is shown in the figures 69, 70 and 71. Results obtained for the wavy-fin staggered configuration are similar in nature as compared to the plain-fin staggered configuration. However, once again the percentage differences between the results for these two fin configurations vary, due to the flow distinction between the plain and wavy fins, explained earlier. As the transverse tube pitch (Lt) increases, a higher percentage difference was observed for heat transfer and

pressure drop characteristics in case of the three test cases for plain-fin staggered configuration as compared to the wavy-fin staggered configuration.

Figure 69 shows the variation of the Colburn factor (j) against the Reynolds number (Re_H) for the three transverse pitch test cases. It can be seen from Figure 69 that the Colburn factor (j) decreases with the increase in the transverse tube pitch (Lt) as seen in case of plain-fin staggered arrangement.

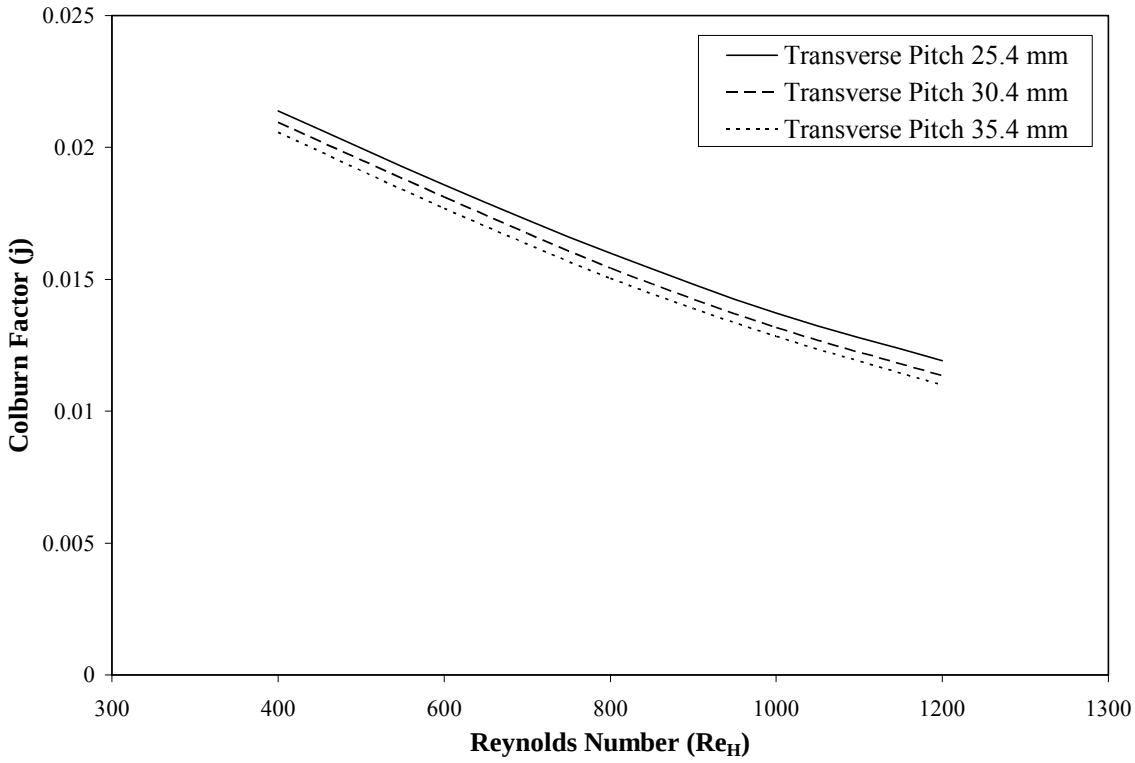

Figure 69. Effect of transverse tube pitch (Lt) on the Colburn factor (j) for the wavy-fin staggered configuration

Figure 70 shows the variation of the friction factor (f) against the Reynolds number (Re_H) for the three transverse pitch (Lt) test cases. It can be seen from Figure 70 that the

friction factor (f) decreases with the increase in the transverse tube pitch as observed in case of plain-fin staggered arrangement.

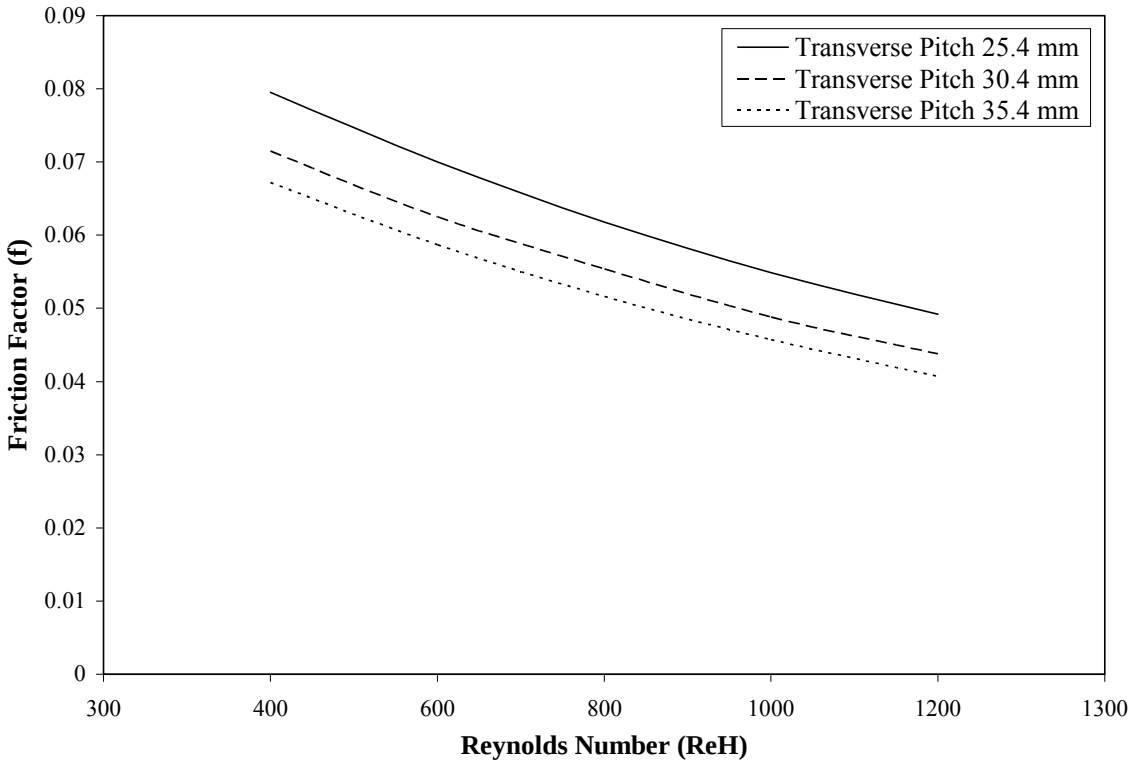

Figure 70. Effect of transverse tube pitch (Lt) on the friction factor (f) for the wavy-fin staggered configuration

Figure 71 shows the variation of the efficiency index (j/f) against the Reynolds number (Re_H) for the three transverse pitch (Lt) test cases. Here again, it can be noted that the efficiency index (j/f) increases with the increase in the transverse tube pitch (Lt), as seen for the plain-fin staggered configuration.

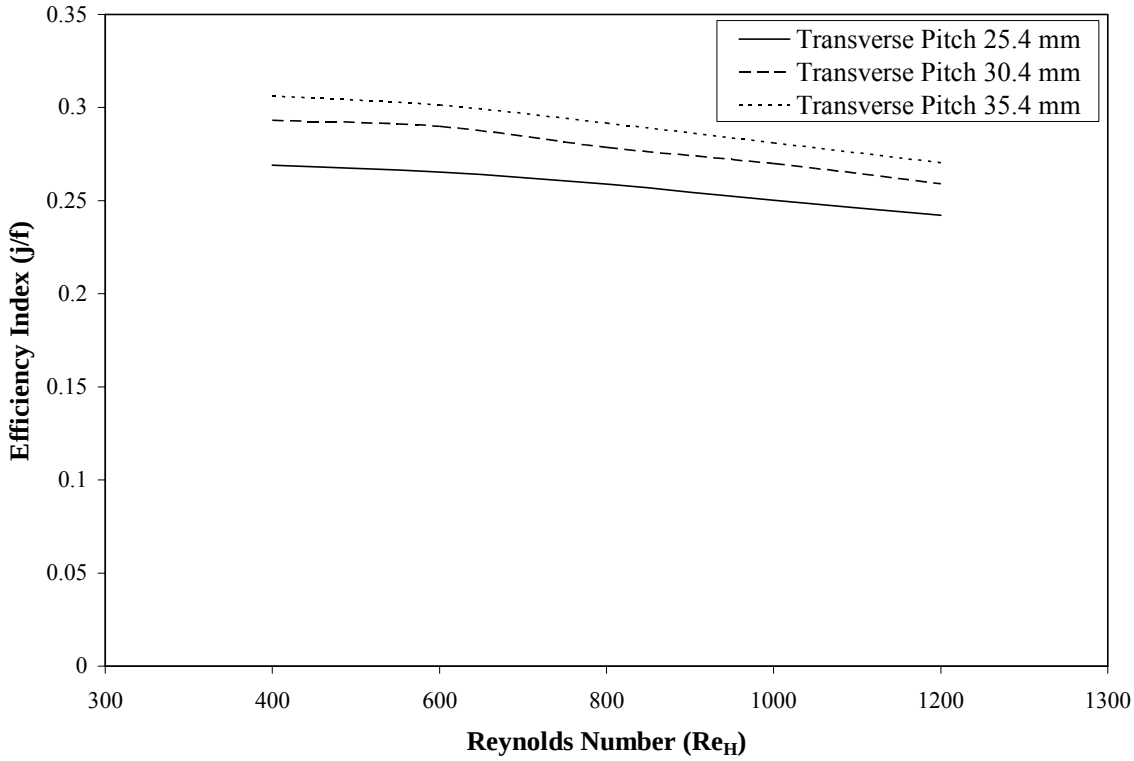

Figure 71. Effect of transverse tube pitch (Lt) on the efficiency index (j/f) for the wavy-fin staggered configuration

Transitional Flow Range

This section describes the results for the current numerical investigation done on the transitional flow range $(1300 \le \mathrm{Re}_H \le 2000)$ for the plain-fin staggered and wavy-fin staggered configurations. In this study three different turbulence models were employed namely *k*-ε model, RNG *k*-ε model and the *k*-ω model. The validity of these turbulence models in the transitional flow range was investigated and the results are compared with each other as well as the laminar model from the point of view of suitability of these models for the transitional flow range for both of these fin configurations. Most of the numerical investigations conducted earlier by researchers like Jang et al (1996 and 1997)

and Romero-Mendez et al. (2000) were limited to the Reynolds number (Re_H) below 1300 for plain-fin and wavy-fin staggered configuration. For these Reynolds numbers (Re_H) below 1300, a laminar model works well, since the flow stays in the laminar flow range. However, the flow distinction section documented earlier shows that when Reynolds number (Re_H) goes above 1300, the flow goes into the transitional region and the flow unsteadiness increases. Therefore a laminar model may not be a suitable approach for investigating the flow beyond Reynolds number (Re_H) 1300, for both plain-fin and wavy-fin configurations. Tutar et al. (2001) conducted a numerical study in which he investigated three turbulence models namely, k-ε model, RNG k-ε model and the large eddy simulation (LES) model for a plain-fin configuration. However, his study was limited to a single tube row domain of a plain-fin which is not representative of real geometries. Also the applicability of the turbulence models is not explored for the transitional flow region, in case of a wavy-fin. The current numerical investigation represents a detailed analysis for the application of the turbulence models as compared with the laminar model for the transitional flow region in case of the plain and the wavy-fin staggered configurations. The flow geometries used in the current study are the realistic four tube row geometries for both plain and wavy fin staggered configurations.

The numerical investigation done by Jang et al. (1996 and 1997) reports the effect of different geometrical parameters such as fin pitch, wavy angle and wavy height on the heat transfer and pressure drop characteristics for the laminar flow range (Re_H<1300) for wavy and plain fin configurations. The current study investigates the effects of these

geometrical parameters on heat transfer and pressure drop characteristics in the transitional flow range $(1300 \le \mathrm{Re}_H \le 2000)$

Comparison of Laminar Model and Turbulence Model for Transitional Flow

A comprehensive comparison between the three turbulence models (*k*-ε, RNG *k*-ε, and *k*-ω model) tested for the transitional flow region for the plain-fin and the wavy-fin staggered configurations was documented in the code validation section. It was found that the numerical results fall within 8% of the experimentally data for the Colburn factor (j) and the friction factor (f) for the *k*-ω model. On the other hand, the difference between experimental data and numerical results for the Colburn factor (j) and the friction factor (f) for the *k*-ε model and the RNG *k*-ε model were found to be about 20% and 25% respectively. The high difference between experimental data and the numerical results for the *k*-ε models was explained on the basis of the fundamental distinction between the *k*-ε models and the *k*-ω model, based on their near wall treatments. This basic difference in the near wall treatment for the *k*-ε based models and the *k*-ω based models showed that the *k*-ω model is a better choice for the transitional flow range modeling for the plain and wavy fin staggered configurations which was proven by the code validation tests.

This section compares the laminar flow model with the turbulence model for simulating the flow in the transitional region for the wavy-fin staggered configuration. This is done because it can be debated that a laminar model can also be used to simulate a transitional flow region for heat transfer and pressure drop characteristics, if a sufficiently

fine grid resolution is used. For this reason the wavy-fin staggered configuration domain was tested in the transitional flow region using the laminar model.

The geometrical parameters used for this wavy-fin staggered configuration are as shown in Table 17:

Table 17. Geometrical Parameters for the wavy-fin staggered configuration for the *k*-ω turbulence and laminar model comparison

	Ll (mm)	Lt (mm)	Fp (mm)	Ft (mm)	D (mm)	Wa (Degrees)	Wh (mm)
Wavy Fin Staggered Configuration	19.05	25.4	3.53	0.12	9.525	17.5	1.5

It is worthwhile to note that a comprehensive grid independency test was carried out for the above mentioned wavy-fin staggered configuration for Reynolds number (Re_H) = 2000 using the laminar flow model as per the grid independency procedure mentioned in the chapter 5. Note that the flow range of interest is the transitional flow range $(1300 \leq Re_H \leq 2000)$ which was simulated using the laminar flow model. A case with highest process parameters (Re_H = 2000) for the transitional flow range, ensured that the grid would be effective for lower values of the process parameters as well. This grid independency test was carried out to ensure that the chosen grid resolution is sufficiently fine for the transitional flow range and also provides accurate results within an acceptable computational time.

Figure 72 shows the variation of the Colburn factor (j) against the Reynolds number (Re_H) for this wavy-fin staggered configuration. Figure 72 compares the laminar model and the *k*-ω model against the experimental data by Wang et al. (1997) over the entire

Reynolds number (Re_H) range including the laminar $(400 \le Re_H \le 1200)$ and the transitional $(1300 \le Re_H \le 2000)$ flow regions. The comparison between laminar model and the *k*-ω turbulence model can be clearly seen from the figure. It was already noted that the laminar model works fairly well in the laminar flow $(400 \le Re_H \le 1200)$ region. However, the laminar model does not work well in the transitional flow range $(1300 \le Re_H \le 2000)$ and is discussed next.

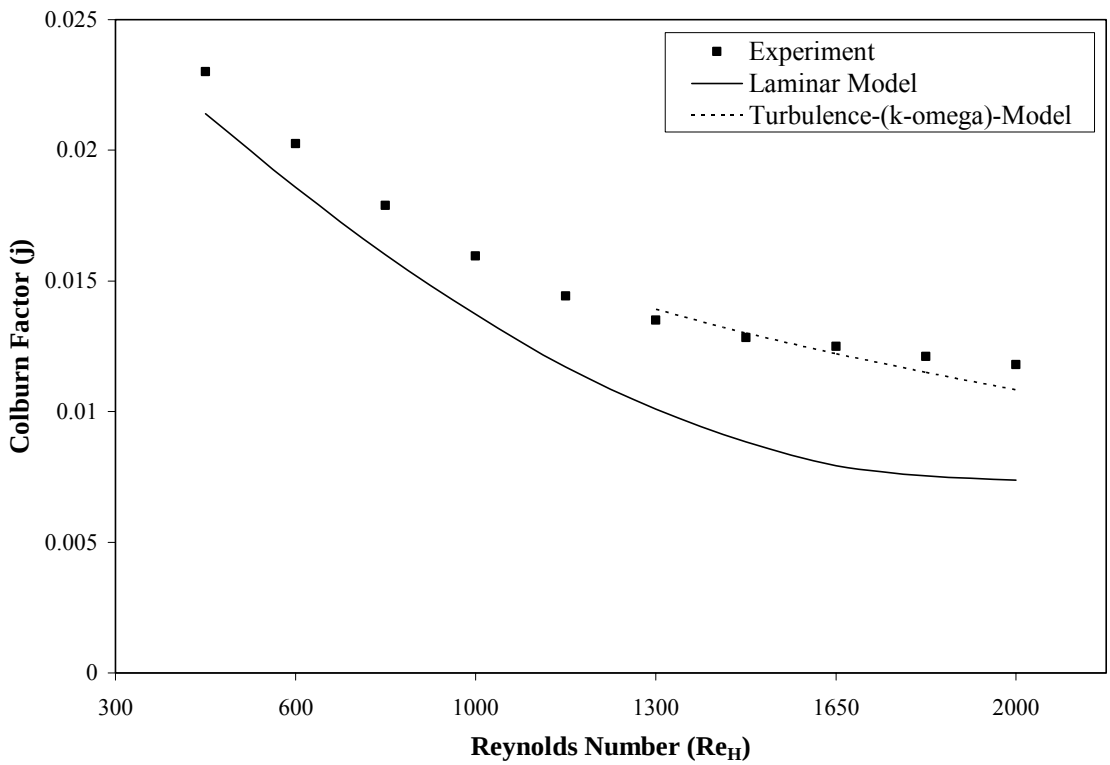

Figure 72. Comparison of the laminar model and the turbulence model with the experimental data by Wang et al. [15] for the wavy-fin staggered configuration

From Figure 72 it is noted that the percentage error for the Colburn factor (j) between the laminar model results and the experimental data for the laminar flow $(400 \le Re_H \le 1200)$ region ranges from 6% at Re_H = 400 to 14% at Re_H=1200 and the

percentage error increases with the Reynolds number (Re_H), since the flow unsteadiness also increases with the increase in Reynolds number. However, when the laminar flow model was tested for the transitional flow region $(1300 \le \mathrm{Re}_H \le 2000)$, it was observed that the percentage error for the Colburn factor (j) between the laminar model results and the experimental data ranges from 16% at Re_H = 1300 to an overwhelming 38% at Re_H=2000 with percentage error increasing with the Reynolds number (Re_H). On the other hand, it can be observed from Figure 72 that for the transitional flow range $(1300 \le \mathrm{Re}_H \le 2000)$, the percentage errors for the Colburn factor (j) between the *k*-ω model results and the experimental data are within 3% and 8% respectively. These observations clearly show that even with the fine grid resolution, the laminar model fails to represent the flow accurately when the flow passes into the transitional flow zone $(1300 \le \mathrm{Re}_H \le 2000)$. Therefore, it can be concluded that a turbulence model is required to accurately represent the flow simulation for the transitional flow range.

This concludes the comprehensive comparative study for the accurate flow representation for the transitional flow region $(1300 \le \mathrm{Re}_H \le 2000)$, using the laminar model and the three turbulence models (*k*-ε, RNG *k*-ε, and *k*-ω model). In summary, it can be said that the fundamental difference in the near wall formulation for the *k*-ε based models and the *k*-ω model makes the *k*-ω model a better choice for the transitional flow range modeling. On the other hand, it is observed from Figure 72 that the laminar model fails to account the flow unsteadiness in the transitional flow range when compared with the *k*-ω model. Thus among the four different models tested, including the three turbulence models (*k*-ε, RNG *k*-ε and *k*-ω) and the laminar model, the *k*-ω turbulence

model turns out to be the most appropriate technique for the transitional flow range modeling. Hence further numerical investigation for the transitional flow region for the plain-fin and wavy-fin configurations is carried out using the *k*-ω turbulence method.

Effects of Fin Pitch

Having established *k*-ω model as the best choice for the transitional flow region, the effects of geometrical parameters on the heat transfer and pressure drop characteristics for the plain-fin and wavy-fin staggered configurations are investigated for this flow range. The first step towards this goal was achieved by testing the effects of fin pitch (Fp) on the heat transfer and flow friction characteristics for plain-fin staggered and wavy-fin staggered configurations for the transitional flow range $(1300 \leq \mathrm{Re}_H \leq 2000)$.

The effects of the change in fin pitch (Fp) on the heat transfer and the pressure drop characteristics for the four tube row domain of the wavy-fin staggered configuration and the plain-fin staggered configuration was studied by running three test cases for each of these fin arrangements. In each case the fin pitch (Fp) is changed keeping all other geometrical parameters constant so that the effects of the longitudinal pitch over the heat exchanger performance can be analyzed.

Figures 73, 74 and 75 show the three fin pitch test case geometries used for the wavy-fin staggered configurations. Note that for this simulation only half of the domain was considered to the symmetry of the problem. Hence these domain figures represent half the fin pitch (Fp/2), with fin as wall boundary condition at the bottom and symmetry boundary condition on the top. It should be noted that the fin thickness is subtracted from the domain, which is Ft = 0.12 mm. Figure 73 shows the wavy- fin staggered

configuration domain with fin pitch (Fp) = 3.53 mm. Figure 74 shows the wavy- fin staggered configuration domain with fin pitch (Fp) = 2.34 mm. While Figure 75 shows the wavy- fin staggered configuration domain with fin pitch (Fp) = 1.69 mm. To clarify the domain used for fin pitch study, Figure 76 shows one such computation domain used in the fin-pitch analysis. The hatched lines in Figure 76 show the computational domain used in the fin-pitch investigation. Owing to the symmetry of the problem, the bottom plane is assigned as a no-slip wall boundary condition, which represents the fin. On the other hand, the top plane is assigned as a symmetry boundary condition.

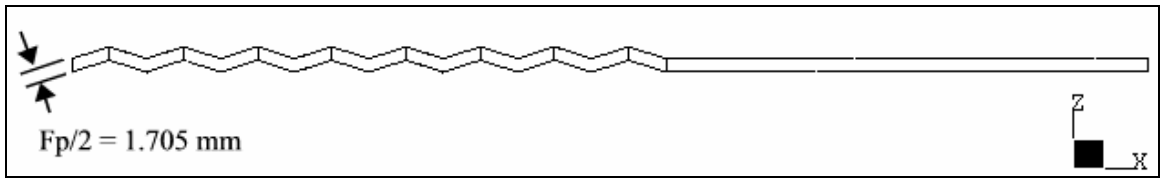

Figure 73. Wavy- fin staggered configuration with fin pitch (Fp) = 3.53 mm

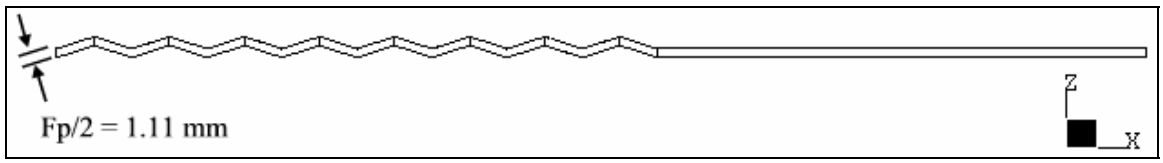

Figure 74. Wavy- fin staggered configuration with fin pitch (Fp) = 2.34 mm

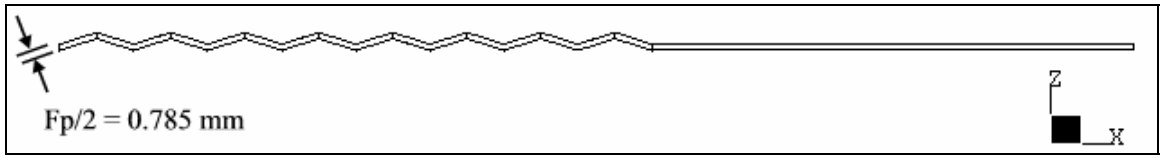

Figure 75. Wavy- fin staggered configuration with fin pitch (Fp) = 1.69 mm

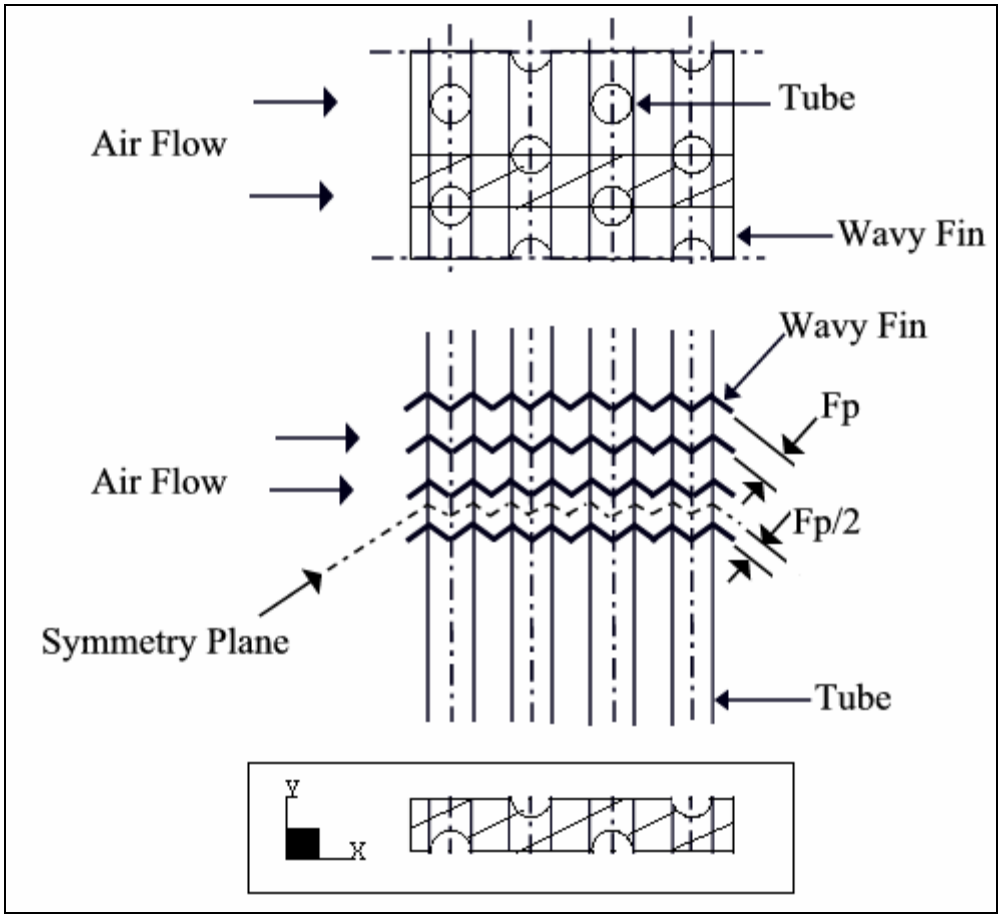

Figure 76. Computational domain used for the fin-pitch analysis

Tables 18 and 19 show the geometrical parameters used for the three fin pitch test cases for plain-fin staggered configuration and wavy-fin staggered configuration respectively.

Table 18. Geometrical Parameters for the plain-fin staggered configuration for the effects of fin pitch (Fp) analysis

Plain Fin Staggered Configuration	Ll (mm)	Lt (mm)	Fp (mm)	Ft (mm)	D (mm)	Wa (Degrees)	Wh (mm)
Test Case 1	19.05	25.4	**3.53**	0.12	9.525	-	-
Test Case 2	19.05	25.4	**2.34**	0.12	9.525	-	-
Test Case 3	19.05	25.4	**1.69**	0.12	9.525	-	-

Table 19. Geometrical Parameters for the wavy-fin staggered configuration for the effects of fin pitch (Fp) analysis

Wavy Fin Staggered Configuration	Ll (mm)	Lt (mm)	Fp (mm)	Ft (mm)	D (mm)	Wa (Degrees)	Wh (mm)
Test Case 1	19.05	25.4	**3.53**	0.12	9.525	17.5	1.5
Test Case 2	19.05	25.4	**2.34**	0.12	9.525	17.5	1.5
Test Case 3	19.05	25.4	**1.69**	0.12	9.525	17.5	1.5

Plain-fin Staggered configuration:

The effect of Fin pitch (Fp) on the heat transfer and pressure drop characteristics for the plain-fin staggered configuration is shown in Figures 77, 78 and 79. The experimental studies done by Elmahdy and Biggs (1979), found that the heat transfer coefficient and friction factor for the plain-fin staggered configuration increased with the increase in the fin spacing for the transitional flow range $(1300 \le \mathrm{Re}_H \le 2000)$. Jang et al. (1996) has reported numerical investigation which explores the effect of fin spacing on the heat exchanger performance. However, his numerical studies were limited to the laminar flow range $(400 \le \mathrm{Re}_H \le 1200)$. The current study attempts to do a numerical investigation for the effects of fin spacing for plain-fin staggered configuration in the transitional flow range using the tested *k*-ω turbulence model.

Figure 77 shows the variation of the Colburn factor (j) against the Reynolds number (Re_H) for the three fin pitch test cases. It can be seen from Figure 77 that the Colburn factor (j) decreases with the decrease in the fin pitch (Fp). This observation can be explained by the fact that keeping the longitudinal tube pitch (Ll) and the transverse tube pitch (Lp) constant, when fin pitch (Fp) is reduced, the flow becomes more streamlined. This flow streamlining caused by reduction in the fin pitch (Fp), simplifies the flow and

hence decreases the turbulence level and the better flow mixing. Also the available heat transfer area from the tube surfaces reduces from decreased fin pitch (Fp) which affects the Colburn factor (j). As a result the Colburn factor (j) decreases with the decrease in the fin pitch (Fp).

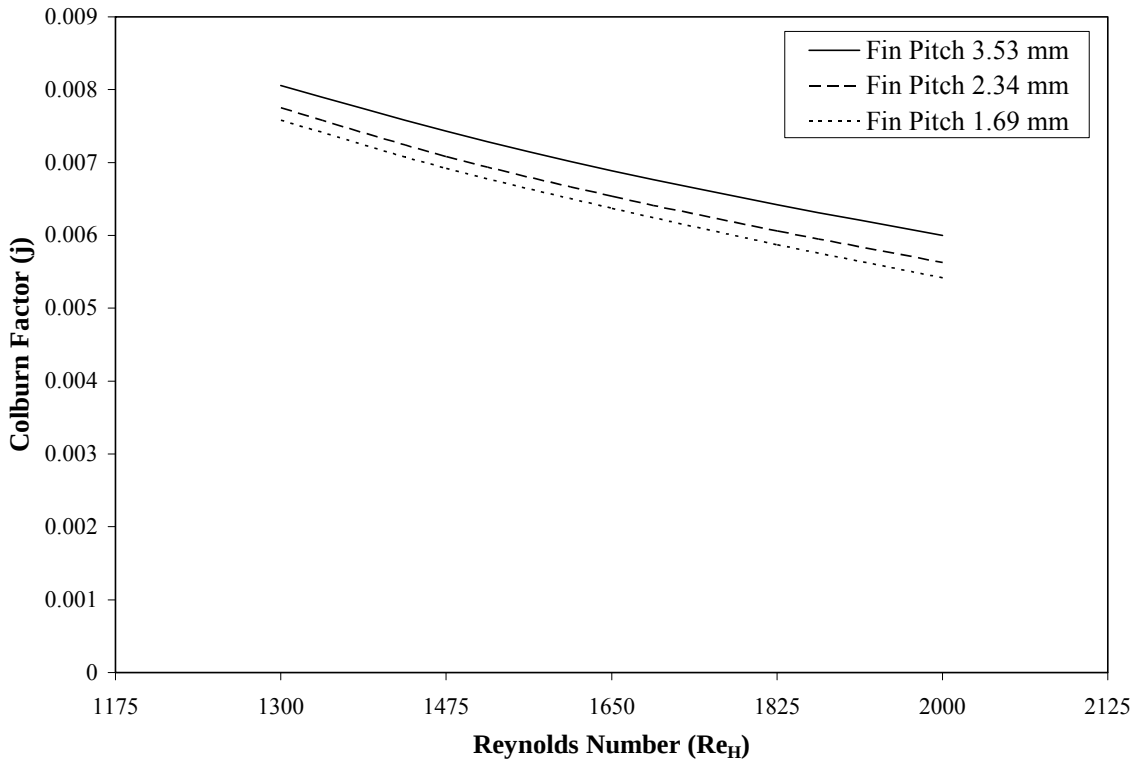

Figure 77. Effect of fin pitch (Fp) on the Colburn factor (j) for the plain-fin staggered configuration

Figure 78 shows the variation of the friction factor (f) against the Reynolds number (Re_H) for the three fin pitch (Ll) test cases. It can be seen from Figure 78 that the friction factor (f) decreases with the decrease in the fin pitch. This observation again can be explained on the basis of the flow streamlining and the flow simplification caused by the reduction of fin pitch. This flow simplification reduces the flow mixing which thereby

reduces the flow friction resistance. Also reduction in the fin pitch (Fp) reduces the tube surface area reducing the flow friction, which certainly has an augmenting effect in reducing the flow friction factor (f).

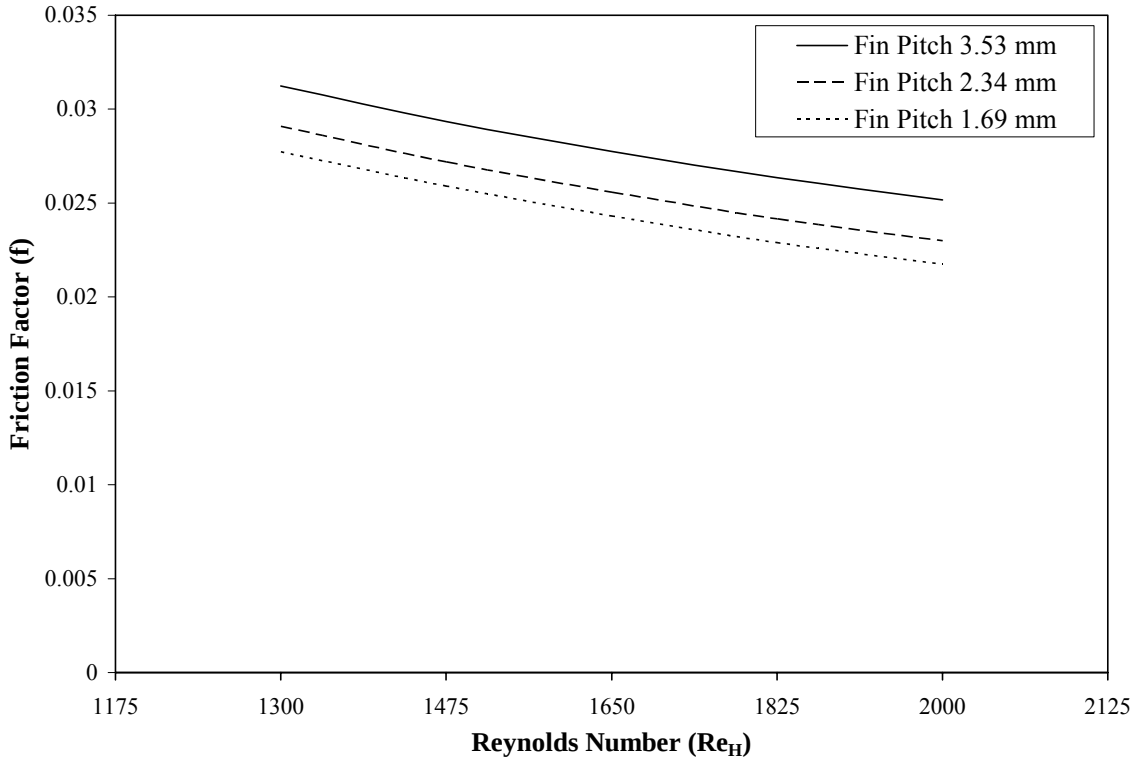

Figure 78. Effect of fin pitch (Fp) on the friction factor (f) for the plain-fin staggered configuration

Figure 79 shows the variation of the efficiency index (j/f) against the Reynolds number (Re_H) for the three fin (Fp) test cases. It can be seen from Figure 79 that the efficiency index (j/f) increases with the decrease in the fin pitch (Fp). This observation suggests that even though the heat-transfer performance (j) decreases with the decrease in the fin pitch (Fp), the efficiency for the surface goes up due to the corresponding decrease in the friction factor (f). As seen from Figures 77 and 78, the Colburn factor (j) and

friction factor (f), both decreases with the decrease in the fin pitch for the plain-fin staggered configuration. However, the percentage decrease in friction factor (f) is higher than the percentage decrease in the Colburn factor (f). This indicates that, as the flow streamlines due to the decrease in the fine pitch (Fp), the decrease in the pressure drop characteristics (f) is more drastic than the decrease in the heat transfer performance (j). As a result, the efficiency index (j/f) increases with the decrease in the fin pitch.

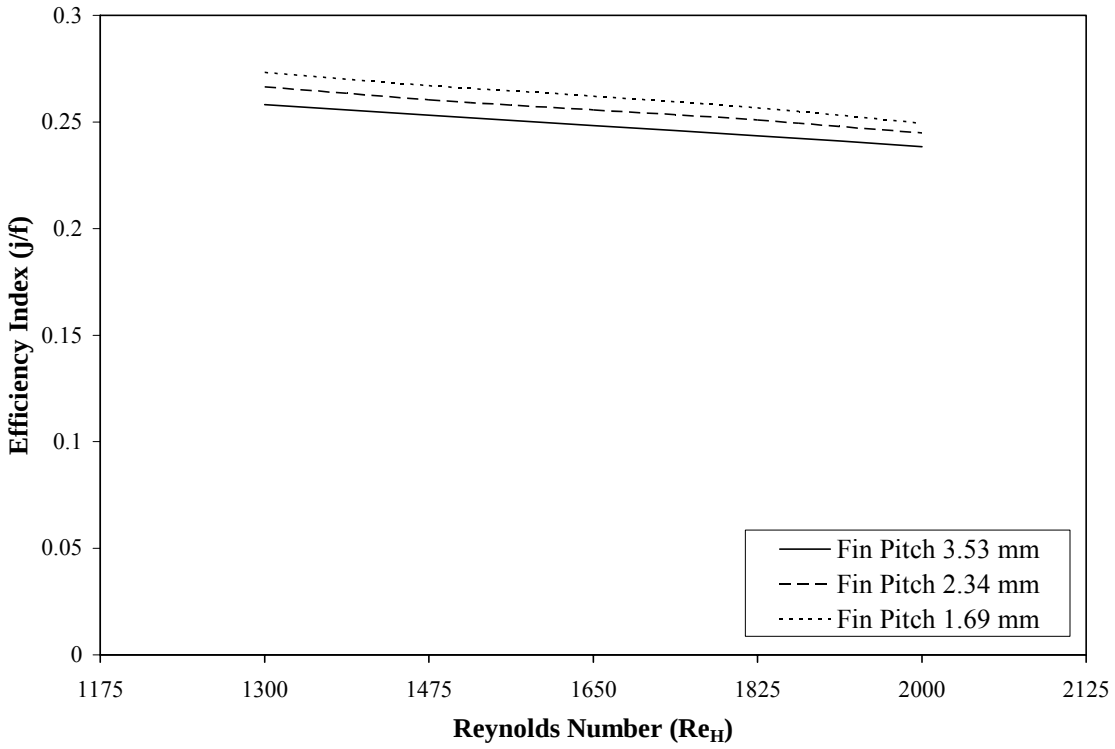

Figure 79. Effect of fin pitch (Fp) on the efficiency index (j/f) for the plain-fin staggered configuration

Wavy-fin Staggered configuration:

The effect of Fin pitch (Fp) on the heat transfer and pressure drop characteristics for the wavy-fin staggered configuration is shown in Figures 80, 81 and 82. Wang et al. (1999) carried out extensive experimental studies to check the effects of fin spacing on heat exchanger performance for the wavy-fin staggered configuration. His experimental studies indicated that heat that the heat transfer coefficient and friction factor for the wavy-fin staggered configuration increases with the increase in the fin spacing for the transitional flow range $(1300 \le \mathrm{Re}_H \le 2000)$, the same trend as the plain-fin staggered arrangement. The numerical investigations reported by Jang et al. (1997) also show the similar effect that heat transfer and pressure drop increases with increase in fin spacing. However, the numerical study by Jang et al. (1997) was limited to the laminar flow range $(400 \le \mathrm{Re}_H \le 1200)$ for the wavy-fin staggered configuration. The present numerical investigation explores the effects of fin spacing for the wavy-fin staggered configuration in the transitional flow region using the *k*-ω turbulence model.

Results obtained for the wavy-fin staggered configuration are similar in nature as compared to the plain-fin staggered configuration, even though the percentage differences between the results for these two fin configurations vary. This is due to the flow distinction elucidated earlier.

Figure 80 shows the variation of the Colburn factor (j) against the Reynolds number (Re_H) for the three fin pitch (Fp) test cases. It can be seen from Figure 80 that the Colburn factor (j) decreases with the decrease in the fin pitch (Fp). The same trend was seen in case of plain-fin staggered arrangement. This observation yet again confirms the

statement before that the decrease in the fin pitch (Fp) streamlines the flow, making the flow more simplistic. This effect plus the reduction in the available tube surface heat transfer area due to decrease in the fin pitch (Fp) causes the reduction in the Colburn factor (j) for the wavy fin-configuration with decrease in fin pitch (Fp).

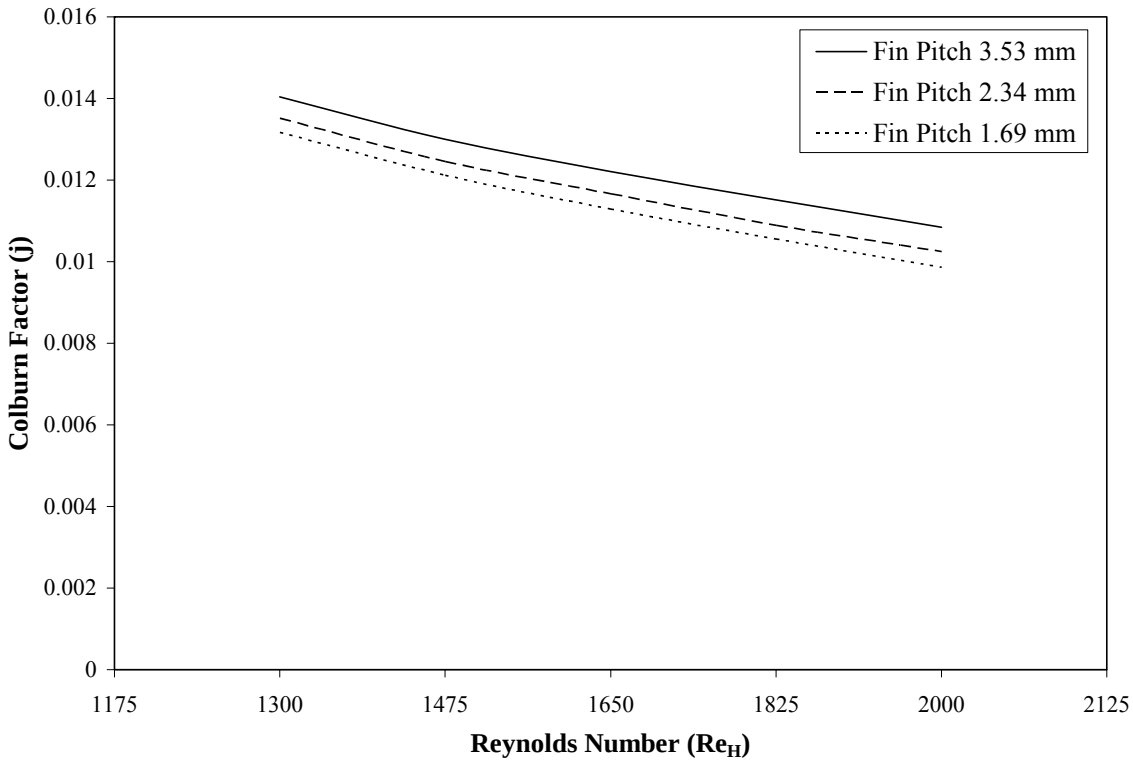

Figure 80. Effect of fin pitch (Fp) on the Colburn factor (j) for the wavy-fin staggered configuration

Figure 81 shows the variation of the friction factor (f) against the Reynolds number (Re_H) for the three fin pitch (Fp) test cases. Here again, it can be seen from Figure 81 that the friction factor (f) decreases with the decrease in the fin pitch as seen in case of plain-fin staggered arrangement. This validates previous speculation that the decrease in the fin pitch decreases the flow mixing by streamlining the flow, thereby decreasing the flow

friction resistance. This effect plus the reduction in the tube surface area due to decrease in the fin pitch (Fp) causes the reduction in the friction factor (f) for the wavy fin-staggered configuration.

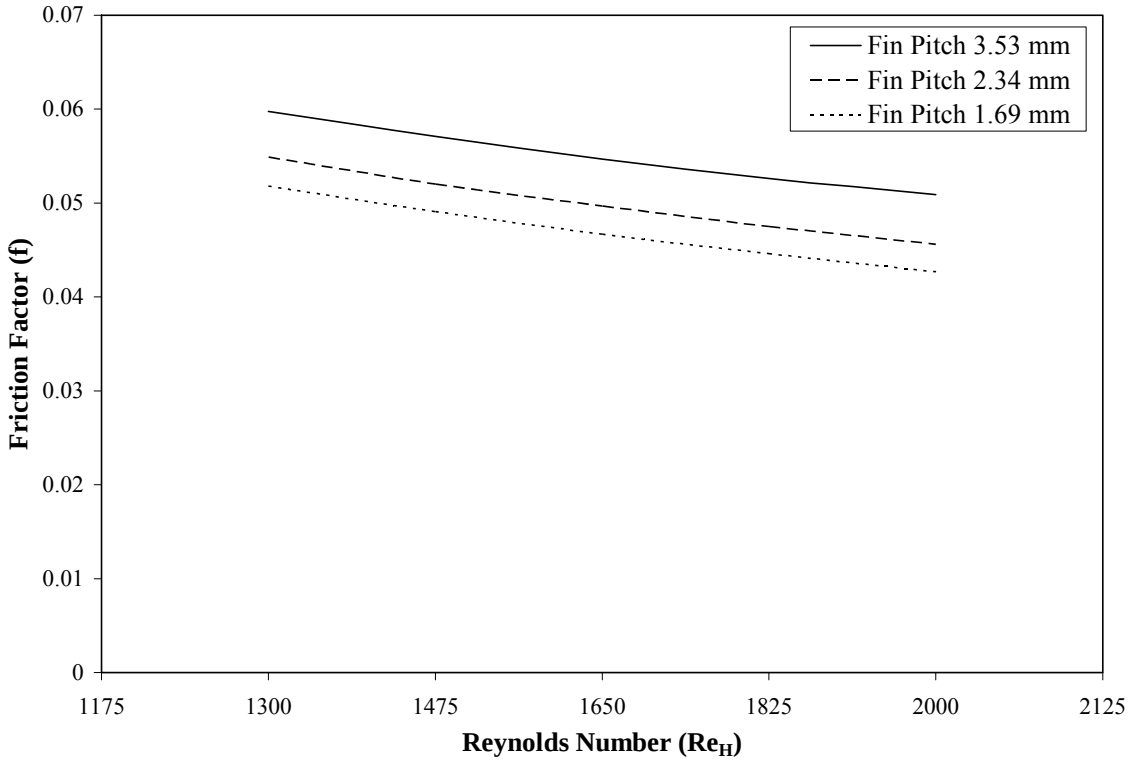

Figure 81. Effect of fin pitch (Fp) on the friction factor (f) for the wavy-fin staggered configuration

Figure 82 shows the variation of the efficiency index (j/f) against the Reynolds number (Re_H) for the three fin pitch (Fp) test cases. Once again, it is observed that the efficiency index (j/f) increases with the decrease in the fin pitch (Fp), as seen for the plain-fin staggered configuration. This verifies the earlier examination that the decrease in fin pitch (Fp) decreases the friction factor (f) more drastically than decrease in the

Colburn factor (j), due to the flow simplification. As a result efficiency index (j/f) goes up with decrease in the fin pitch (Fp).

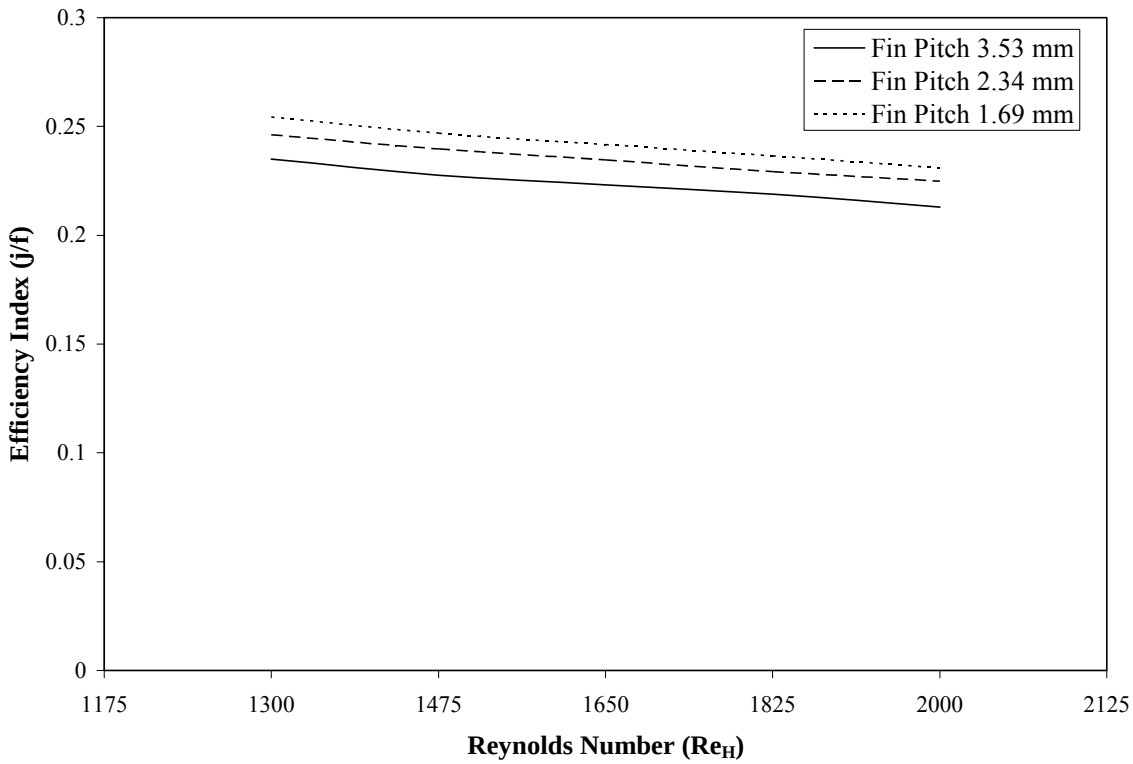

Figure 82. Effect of longitudinal fin pitch (Fp) on the efficiency index (j/f) for the wavy-fin staggered configuration

Effects of Wavy Angle and Wavy Height

After studying the effects of fin pitch (Fp) on the heat exchanger performance, the next step in the current investigation was to explore the effects of wavy angle (Wa) and wavy height (Wh) on the heat transfer and the flow friction characteristics for the transitional flow region in case of wavy-fin staggered configuration. Although the wavy fin-and tube heat exchangers are widely used in industrial products, the literature covering the effects of wavy angle and wavy height on the thermal and hydraulic

performance is limited. Numerical investigation reported by Jang et al. (1997) for the wavy-fin configuration reveals that increase in wavy angle (Wa) and wavy height (Wh) increases the average heat transfer coefficient along with the increase in the pressure drop characteristics. This increase in the thermal and hydraulic characteristics was attributed to the repeated boundary layer interruption as the wavy angle increases. However, the numerical investigation by Jang et al. (1997) was limited to the laminar flow range for the wavy-fin staggered configuration. Equipped with the numerically validated *k*-ω turbulence model, the current study explores the effects of the wavy angle and wavy height on the heat transfer and pressure drop characteristics for the transitional flow region $(1300 \leq \mathrm{Re}_H \leq 2000)$ for the case of wavy-fin staggered configuration.

Effects of Wavy Angle:

The effects of the change in the wavy angle (Wa) on the thermal and the hydraulic characteristics for the four tube row domain of the wavy-fin staggered configuration was investigated by running three test cases. In each case the wavy angle (Wa) is changed keeping all other geometrical parameters constant so that the effects of the longitudinal pitch over the heat exchanger performance can be realized.

Figures 83, 84 and 85 show the three wavy angle test case geometries used for the wavy-fin staggered configurations. Figure 83 shows the wavy- fin staggered configuration domain with wavy angle (Wa) = 8.95^0. Figure 84 shows the wavy- fin staggered configuration domain with wavy angle (Wa) = 17.5^0. While Figure 85 shows the wavy- fin staggered configuration domain with wavy angle (Wa) = 32.21^0.

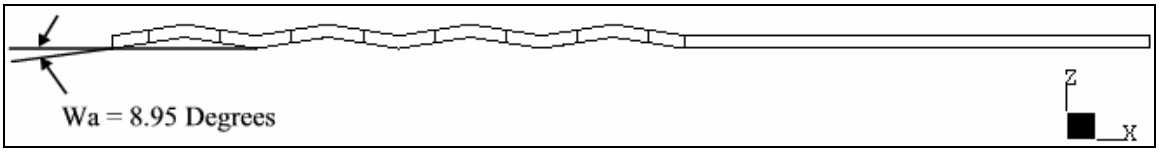

Figure 83. Wavy- fin staggered configuration with wavy angle (Wa) = 8.95^0

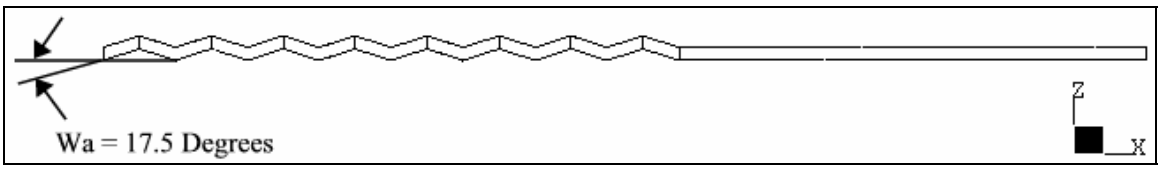

Figure 84. Wavy- fin staggered configuration with wavy angle (Wa) = 17.5^0

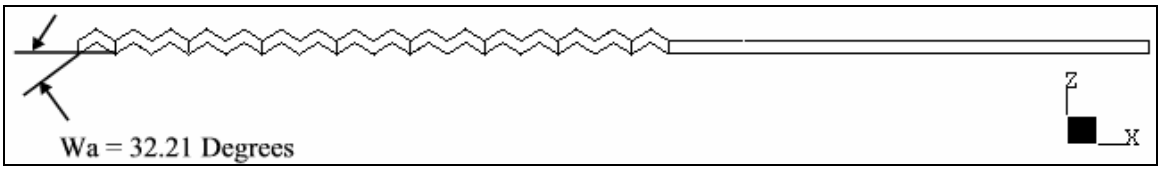

Figure 85. Wavy- fin staggered configuration with wavy angle (Wa) = 32.21^0

Tables 20 shows the geometrical parameters used for the three wavy angle test cases for the wavy-fin staggered configuration.

Table 20. Geometrical Parameters for the wavy-fin staggered configuration for the effects of wavy angle (Wa) analysis

Wavy Fin Staggered Configuration	Ll (mm)	Lt (mm)	Fp (mm)	Ft (mm)	D (mm)	Wa (Degrees)	Wh (mm)
Test Case 1	19.05	25.4	3.53	0.12	9.525	**8.95**	1.5
Test Case 2	19.05	25.4	2.34	0.12	9.525	**17.5**	1.5
Test Case 3	19.05	25.4	1.69	0.12	9.525	**32.21**	1.5

The effect of wavy angle (Wa) on the heat transfer and pressure drop characteristics for this wavy-fin staggered configuration is shown in Figures 86, 87 and 88.

Figure 86 shows the variation of the Colburn factor (j) against the Reynolds number (Re_H) for the three fin pitch test cases. It can be seen from Figure 86 that the Colburn factor (j) increases with the increase in the fin pitch (Fp). This observation can be explained by the fact that keeping the longitudinal tube pitch (Ll) and the transverse tube pitch (Lp) constant, when wavy angle (Wa) is increased, the wavelength of the wavy corrugations decreases. Hence there are more wavy corrugations for a given flow length. As such the boundary layer for the flow is disturbed more repeatedly. This increases flow complexity and better flow mixing. As a result the Colburn factor (j) increases with the increase in the wavy angle (Wa).

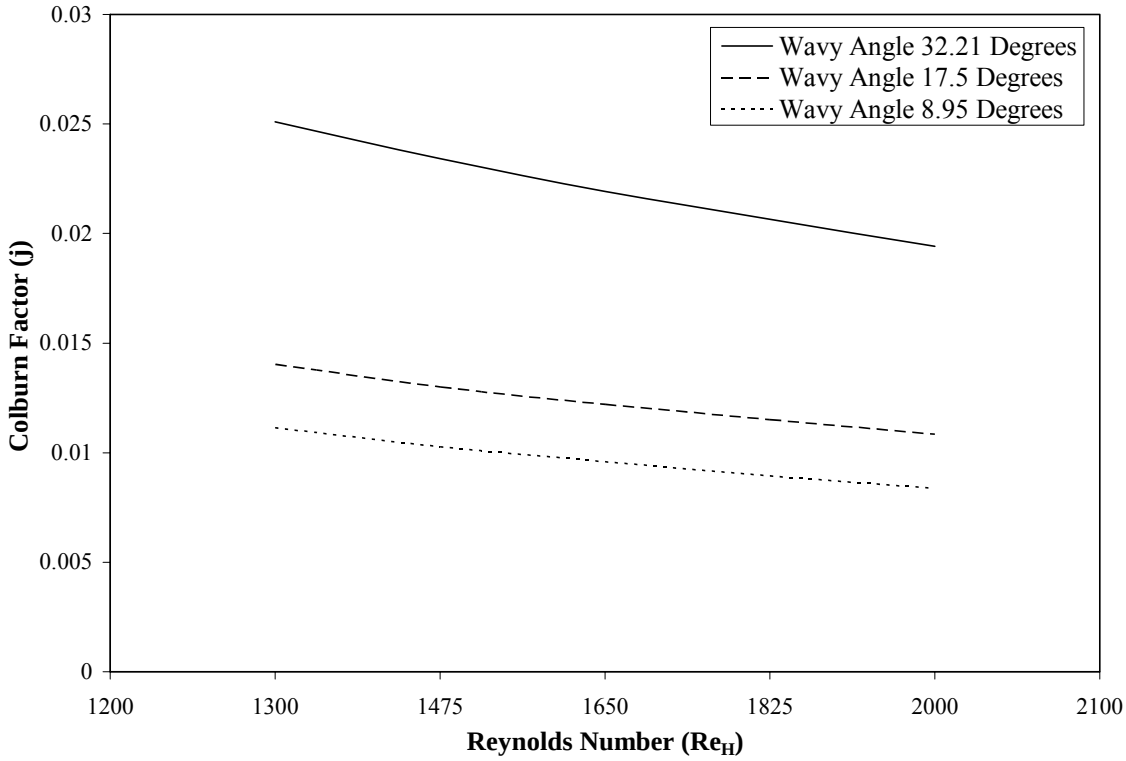

Figure 86. Effect of wavy angle (Wa) on the Colburn factor (j) for the wavy-fin staggered configuration

Figure 87 shows the variation of the friction factor (f) against the Reynolds number (Re_H) for the three wavy angle (Wa) test cases. It can be seen from Figure 87 that the friction factor (f) increases with the increase in the wavy angle. This observation again can be explained on the basis of the more frequent boundary layer interruption for a given flow length as the wavy angle is increased. Thereby the flow mixing and the flow complexities are increased. This in turn causes increase in the flow friction resistance. Hence the friction factor (f) increases with the increase in the wavy angle (Wa).

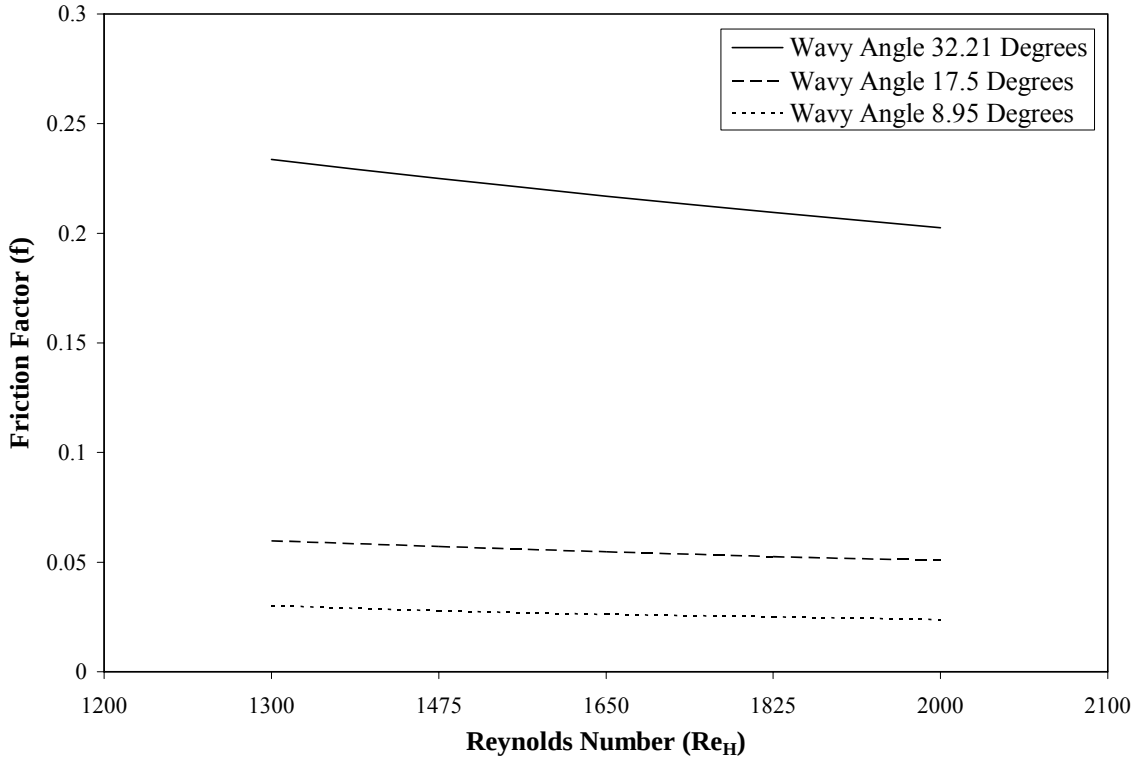

Figure 87. Effect of wavy angle (Wa) on the friction factor (f) for the wavy-fin staggered configuration

Figure 88 shows the variation of the efficiency index (j/f) against the Reynolds number (Re_H) for the three wavy angle (Wa) test cases. It can be seen from Figure 88 that the efficiency index (j/f) increases with the decrease in the wavy angle (Wa). This observation suggests that even though the heat-transfer performance (j) increases with the increase in the wavy angle (Wa), the efficiency for the surface goes down due to the corresponding increase in the friction factor (f). As seen from Figures 86 and 87, the Colburn factor (j) and friction factor (f), both increases with the increase in the wavy angle for the wavy-fin staggered configuration. However, the percentage increase in friction factor (f) is higher than the percentage increase in the Colburn factor (f). This

indicates that, as the flow complicates due to the increase in the wavy angle (Wa), the increase in the pressure drop characteristics (f) is more severe than the increase in the heat transfer performance (j). As a result, the efficiency index (j/f) decreases with the increase in the wavy angle.

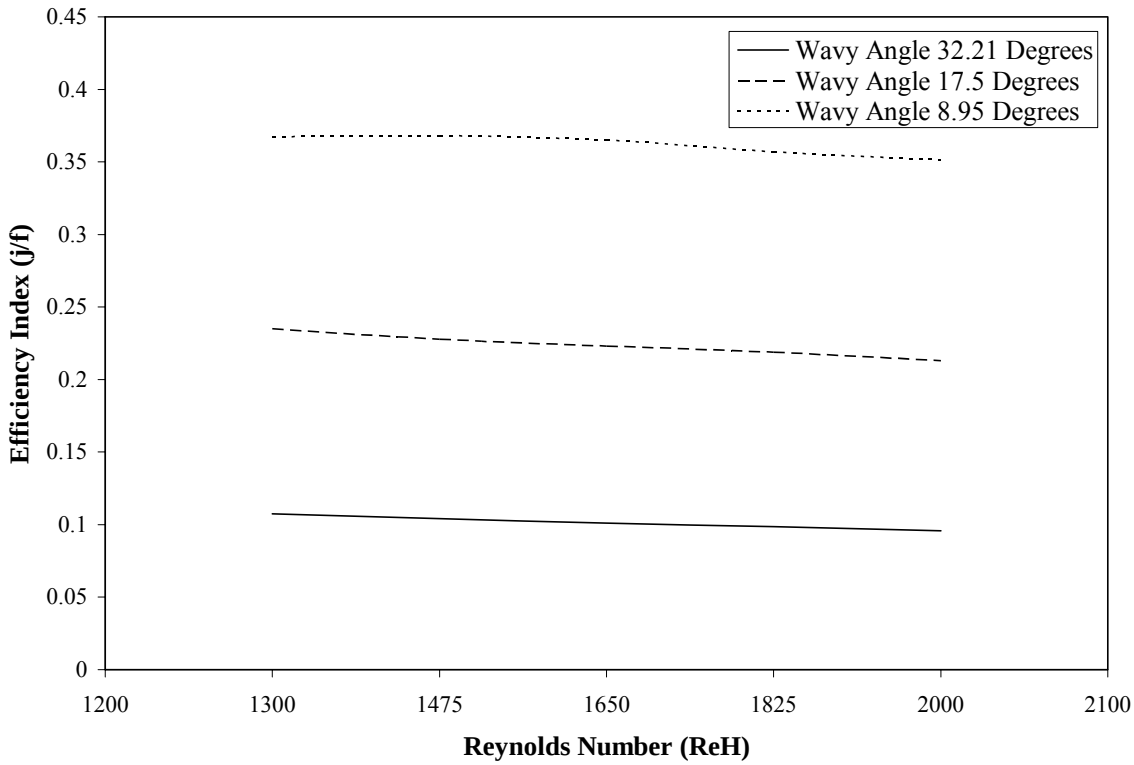

Figure 88. Effect of wavy angle (Wa) on the efficiency index (j/f) for the wavy-fin staggered configuration

Effects of Wavy Height:

The effects of the change in the wavy height (Wh) on the thermal and the hydraulic characteristics for the four tube row domain of the wavy-fin staggered configuration was investigated by running three test cases. In each case the wavy height (Wh) is changed

keeping all other geometrical parameters constant so that the effects of the longitudinal pitch over the heat exchanger performance can be realized.

Figures 89, 90 and 91 show the three wavy angle test case domains used for the wavy-fin staggered configurations. Figure 89 shows the wavy- fin staggered configuration domain with wavy height (Wh) = 0.7508 mm. Figure 90 shows the wavy-fin staggered configuration domain with wavy height (Wh) = 1.5 mm. While Figure 91 shows the wavy- fin staggered configuration domain with wavy height (Wh) = 3.0032 mm.

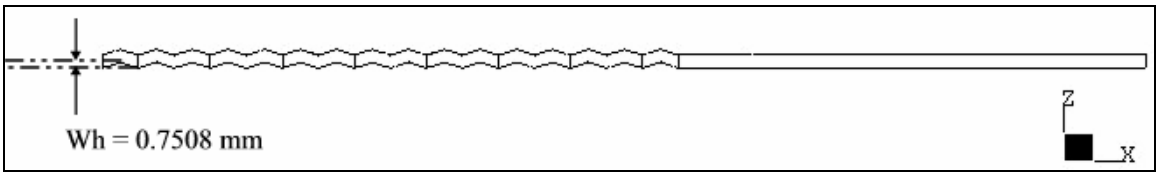

Figure 89. Wavy- fin staggered configuration with wavy height (Wh) = 0.7508 mm

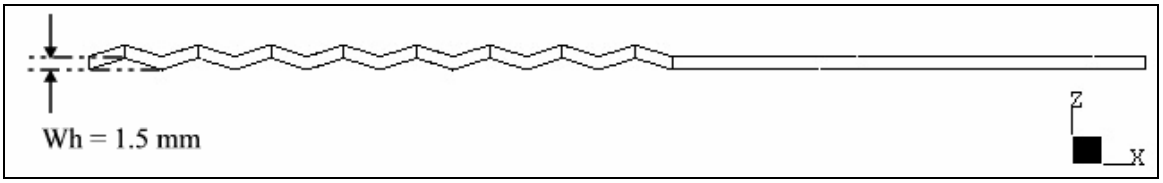

Figure 90. Wavy- fin staggered configuration with wavy height (Wh) = 1.5 mm

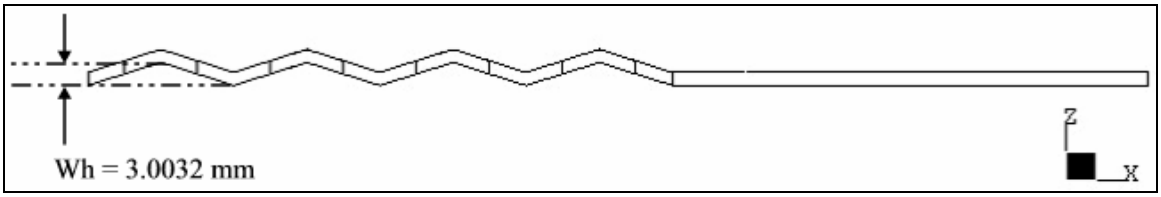

Figure 91. Wavy- fin staggered configuration with wavy height (Wh) = 3.0032 mm

Table 21 shows the geometrical parameters used for the three wavy height test cases for the wavy-fin staggered configuration.

Table 21. Geometrical Parameters for the wavy-fin staggered configuration for the effects of wavy height (Wh) analysis

Wavy Fin Staggered Configuration	Ll (mm)	Lt (mm)	Fp (mm)	Ft (mm)	D (mm)	Wa (Degrees)	Wh (mm)
Test Case 1	19.05	25.4	3.53	0.12	9.525	17.5	**0.7508**
Test Case 2	19.05	25.4	2.34	0.12	9.525	17.5	**1.5**
Test Case 3	19.05	25.4	1.69	0.12	9.525	17.5	**3.0032**

Results obtained for the wavy-fin staggered configuration for the wavy height (Wh) effects are opposite in nature as that of the wavy angle (Wa) effects on the thermal and hydraulic performance.

Figure 92 shows the variation of the Colburn factor (j) against the Reynolds number (Re_H) for the three wavy height (Wh) test cases. It can be seen from Figure 92 that the Colburn factor (j) increases with the decrease in the wavy height (Wh). This observation again shows that the decrease in wavy height (Wh) increases the number of corrugations for a given flow length and as such the flow mixing by complicating the flow. This effect is caused by the more frequent renewal of the boundary layer as wavy height is decreased, since wavelength of wavy corrugations is reduced by decreased wavy height (Wh) for a given flow length. Thus the Colburn factor (j) increases as the wavy height (Wh) is reduced.

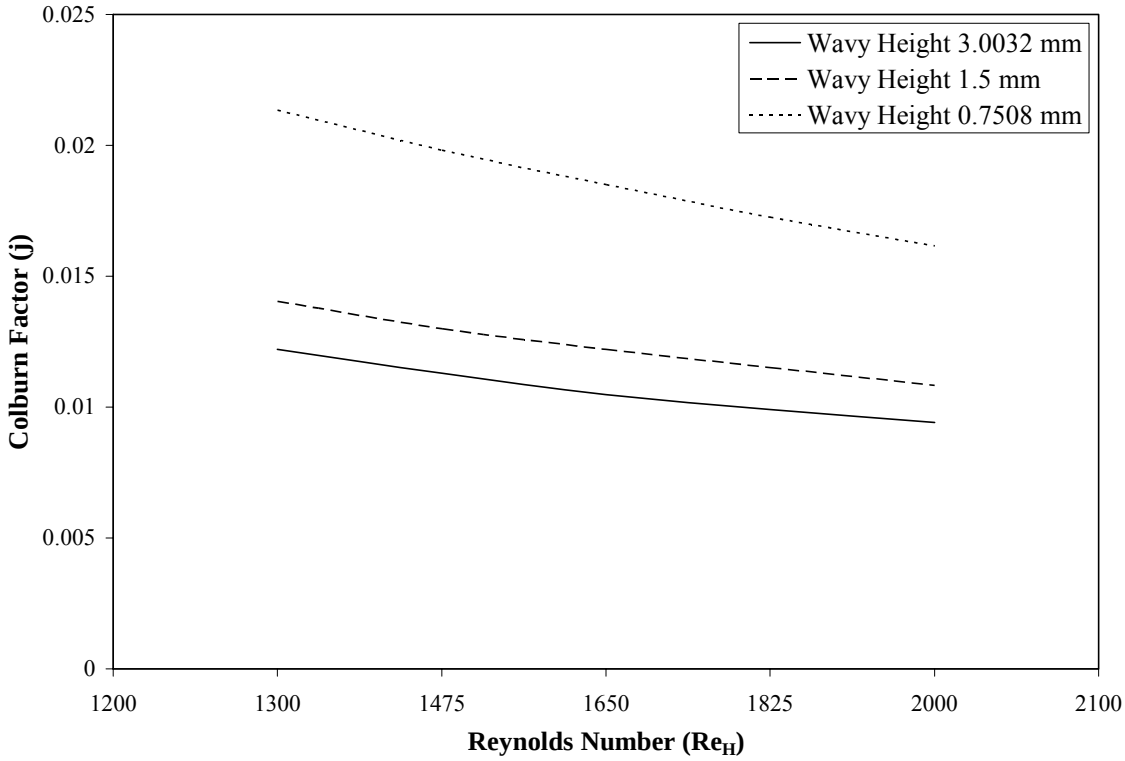

Figure 92. Effect of wavy height (Wh) on the Colburn factor (j) for the wavy-fin staggered configuration

Figure 93 shows the variation of the friction factor (f) against the Reynolds number (Re_H) for the three wavy height (Wh) test cases. Here again, it can be seen from Figure 93 that the friction factor (f) increases with the decrease in the wavy height. This shows that the decrease in the wavy height increases flow complexity, thereby increasing the flow friction resistance. This effect causes the increase in the friction factor (f) for the wavy fin-staggered configuration as the wavy height (Wh) is reduced.

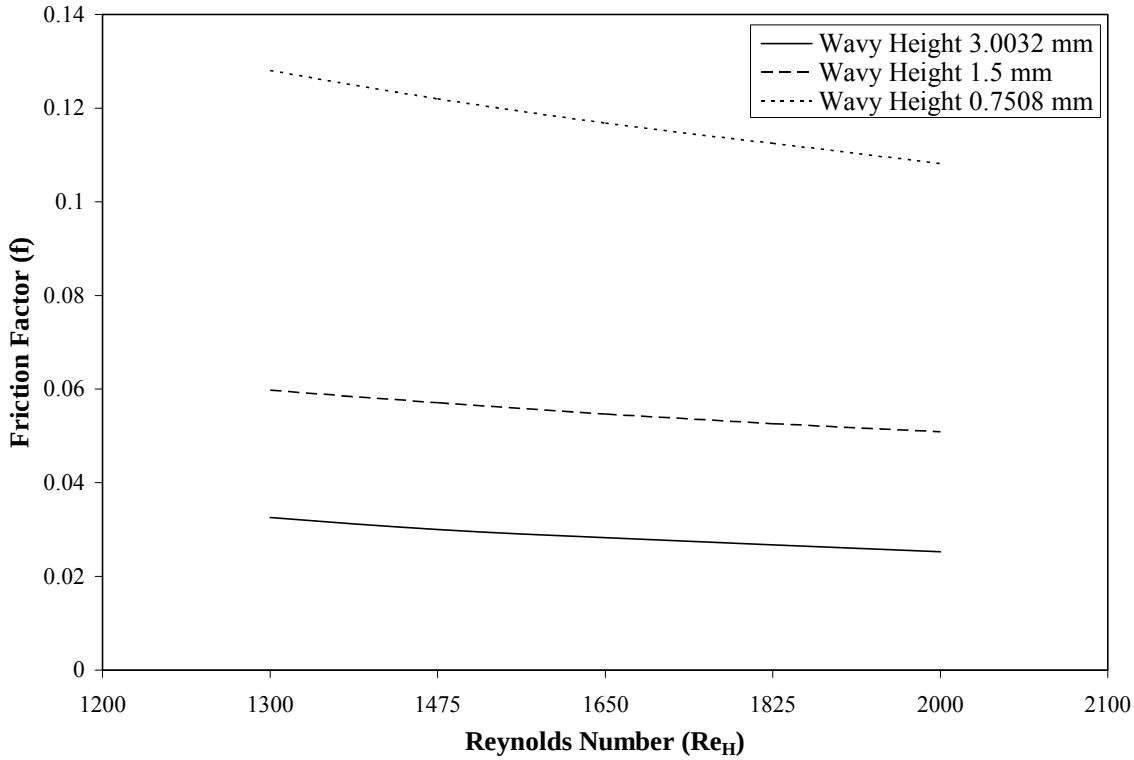

Figure 93. Effect of wavy height (Wh) on the friction factor (f) for the wavy-fin staggered configuration

Figure 94 shows the variation of the efficiency index (j/f) against the Reynolds number (Re_H) for the three wavy height (Wh) test cases. It is observed that the efficiency index (j/f) increases with the increase in the wavy height (Wh). Here again it is seen that the increase in wavy height (Wh) decreases the friction factor (f) more drastically than decrease in the Colburn factor (j), due to the flow simplification. As a result efficiency index (j/f) goes up with decrease in the wavy height (Wh).

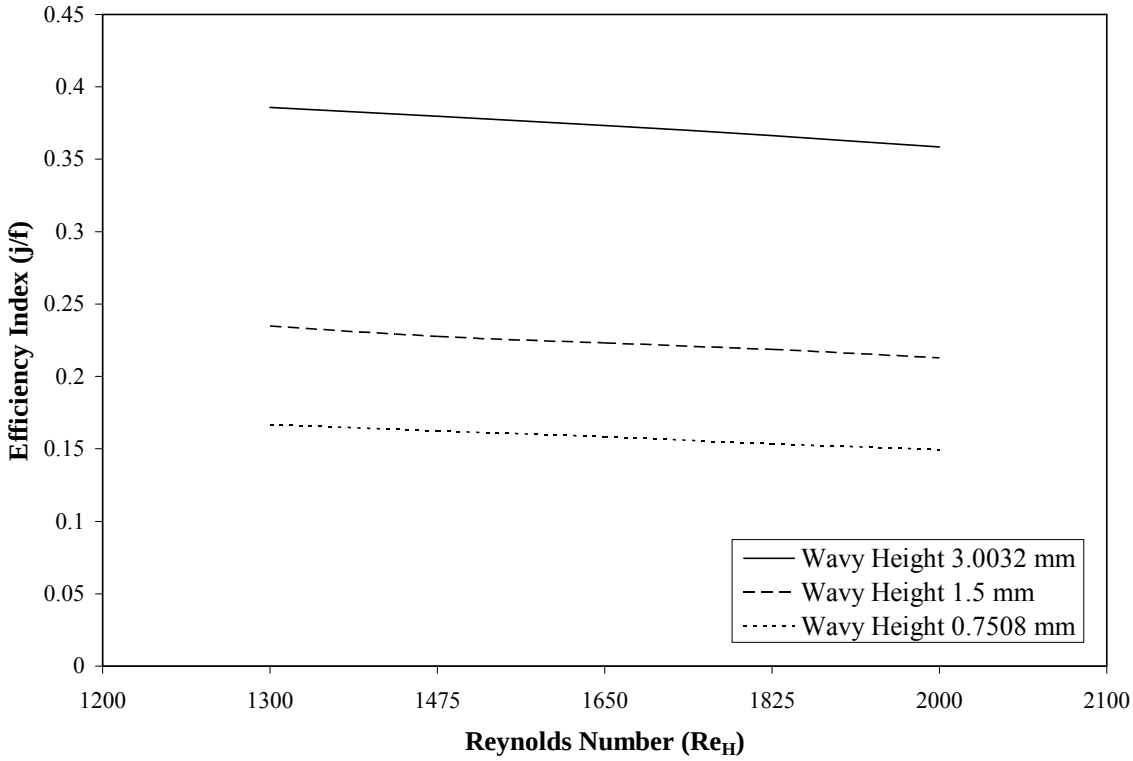

Figure 94. Effect of wavy height (Wh) on the efficiency index (j/f) for the wavy-fin staggered configuration

Fin Analysis

In the present investigation, the boundary condition for the fin is set to be no slip wall boundary condition with a constant temperature (60°C). In the actual working conditions, this approximation is not true due to the fin resistance. There is a temperature variation from the base of the fin to the fin tip. However, the constant temperature wall boundary condition for the fin can be a reasonable approximation, for the geometries investigated in the present study. This can be verified by the close comparisons of the numerical results with the experimental data (Chapter 6: Code Validation). The following fin

analysis is performed to verify the temperature distribution along the fin and to validate the constant temperature approximation made for the fin.

The fin analysis is performed assuming the fin to be an annular fin. The base temperature for the fin is the temperature of the tube surface. The tube surface temperature is assumed to be 60°C in the present study. Figure 95 shows the schematic of the problem.

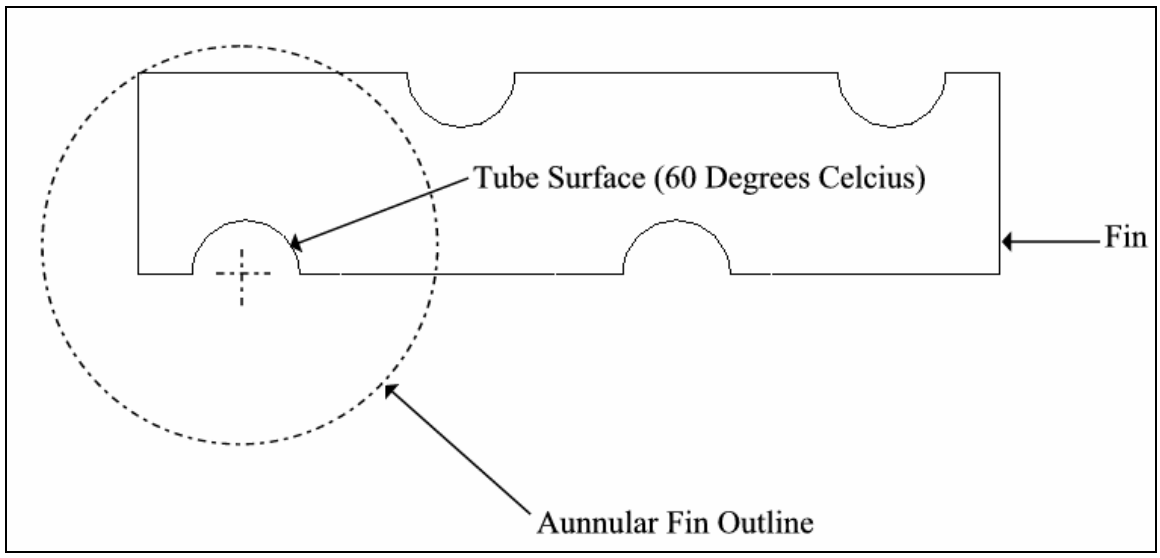

Figure 95. Schematic for the annular fin analysis

For the current fin analysis, one extreme case was considered. A case with highest process parameters ensured that the constant temperature fin approximation would be effective for lower values of the process parameters as well. The current numerical investigation is performed for the laminar $(400 \le \mathrm{Re}_H \le 1200)$ and the transitional $(1300 \le \mathrm{Re}_H \le 2000)$ flow regimes. The extreme case considered in the present fin analysis is for the highest Reynolds number, i.e. $\mathrm{Re}_H = 2000$. Different geometrical parameters were also evaluated in the current numerical investigation. The geometrical

parameters selected for the present fin analysis were also the one for the extreme dimensional case, i.e. transverse tube pitch Lt = 35.4 mm. Figure 96 shows the extreme case considered for the present fin analysis.

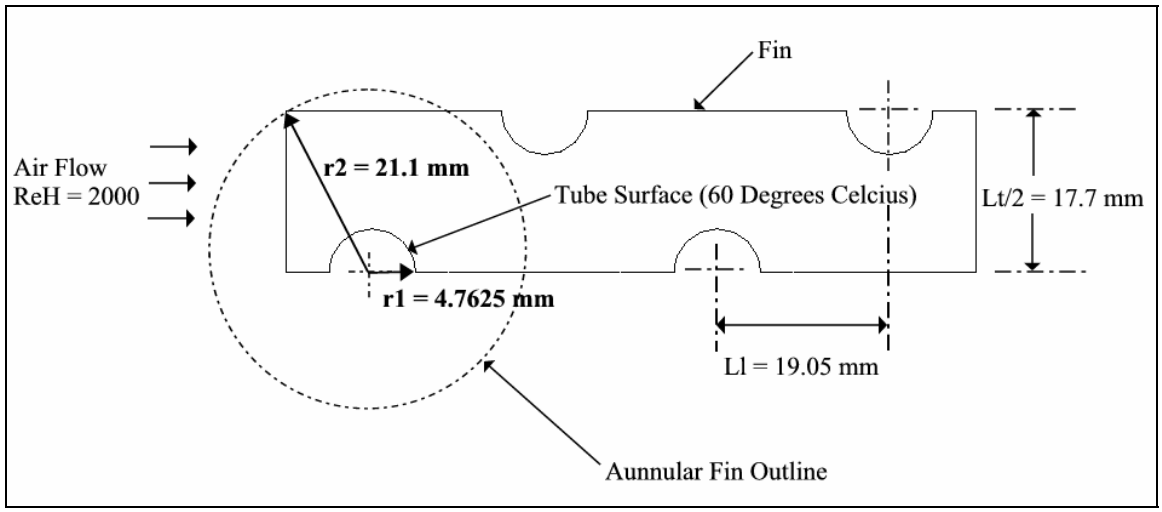

Figure 96. Geometrical parameters for the annular fin

For this case considered in the present fin analysis, r1 is the fin base radius which is 4.7625 mm, r2 is the radius of the fin tip point which is at a distance of 21.1 mm from the center of the tube. The fin is assumed to be made of aluminum with thermal conductivity $\lambda = 200W/m-k$. Fin thickness in the present analysis is Ft = 0.12 mm. The fin base temperature is same as that of the tube surface which is 60°C or 333°K. The inlet air temperature in the present analysis is set to be 30°C or 303°K.

The temperature distribution for an annular fin can be expressed in a general form as follows [Incropera and DeWitt (1996)]:

$$\frac{d^2T}{dr^2} + \frac{1}{r}\frac{dT}{dr} - \frac{2h}{\lambda t}\left(T - T_\infty\right) = 0 \qquad (108)$$

where r is the radial distance from the base of the fin, h is the heat transfer coefficient, λ is the thermal conductivity of the fin, t is the fin thickness and T_∞ is the surrounding temperature.

Defining, $m^2 = \dfrac{2h}{\lambda t}$ (109)

and

$$\theta = T - T_\infty \tag{109}$$

Equation (108) can be written as,

$$\frac{d^2\theta}{dr^2} + \frac{1}{r}\frac{d\theta}{dr} - m^2\theta = 0 \tag{110}$$

Equation (110) is a modified Bessel equation of order zero, and its general solution is of the form,

$$\theta(r) = C_1 I_0(mr) + C_2 K_0(mr) \tag{111}$$

where I_0 and K_0 are modified, zero-order Bessel functions of the first and second kinds, respectively. If the temperature at the base of the fin is known, $\theta(r_1) = \theta_b$, C_1 and C_2 may be evaluated to yield a temperature distribution of the form,

$$\frac{\theta}{\theta_b} = \frac{I_0(mr)K_1(mr_2) + K_0(mr)I_1(mr_2)}{I_0(mr_1)K_1(mr_2) + K_0(mr_1)I_1(mr_2)} \tag{112}$$

Based on Equation (112), the temperature distribution for the annular fin case mentioned earlier, was evaluated. The temperature distribution for this extreme case considered is shown in Figure 97.

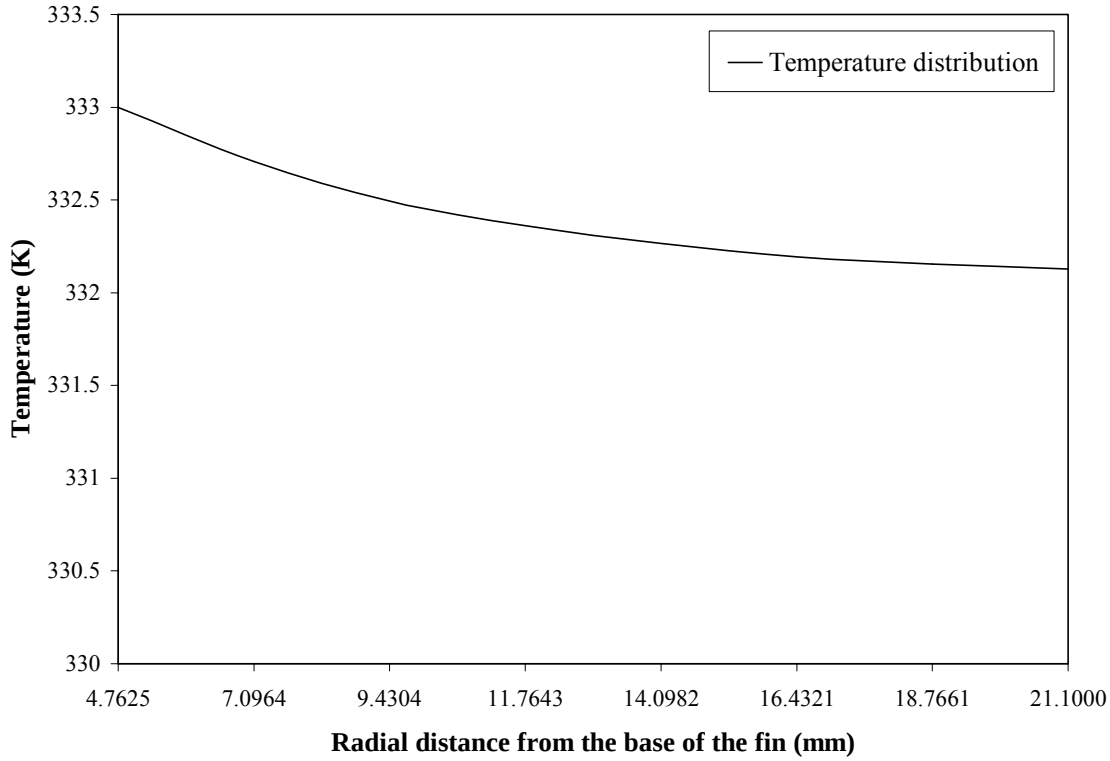

Figure 97. Temperature distribution from fin base to fin tip

Figure 97 shows that the temperature decreases from the base of the fin to the fin tip. The fin base temperature is 333 ^{o}K. The temperature at the fin tip as evaluated from Equation (112) was found to be 332.12 ^{o}K. This analysis shows that the temperature gradient between fin base and fin tip is 0.88 ^{o}K. The inlet air temperature in the present investigation is set to be 303 ^{o}K and the fin is set to be constant temperature (333 ^{o}K) no-slip wall. The temperature gradient (0.88 ^{o}K) found between fin base and the fin tip can be considered negligible when compared with the temperature difference between inlet air flow (303 ^{o}K) and the fin base (333 ^{o}K). Furthermore, the annular fin case considered here is the extreme case of the present investigation, i.e. highest Reynolds number ($\mathrm{Re}_H = 2000$) and the highest transverse tube pitch (Lt = 35.4 mm). Therefore, for all the

other cases investigated in the present study, the temperature gradient between fin base and fin tip would be even smaller. Additionally, the close comparison of the numerical results with the experimental data (Chapter 6: Code Validation) shows that the constant temperature wall boundary condition for the fin can be considered as a reasonable approximation.

Fin Efficiency:

Fins are used to increase the heat transfer from a surface by increasing the effective surface area. However, the fin itself represents a conduction resistance to heat transfer from the original surface. For this reason, there is no assurance that the heat transfer rate will be increased through the use of fins. An assessment of this matter may be made by evaluating the fin effectiveness ε_f. It is defined as the ratio of the fin heat transfer rate to the heat transfer rate that would exist without the fin and is given by,

$$\varepsilon_f = \frac{q_f}{hA_b\theta_b} \tag{113}$$

where q_f is the rate of heat transfer through the fin, h is the convective heat transfer coefficient, A_b is the fin cross-sectional area at the base and θ_b is given as,

$$\theta_b = T_b - T_\infty \tag{114}$$

where T_b is the fin base temperature and T_∞ is the surrounding temperature.

Another measure of fin thermal performance is provided by the fin efficiency η_f. The maximum driving potential for convection is the temperature difference between the base and the surrounding fluid. Hence the maximum rate at which fin could dissipate energy is the rate that would exist if the entire fin surface were at the base temperature.

However, since any fin is characterized by finite conduction resistance, a temperature gradient must exist along the fin. The definition of fin efficiency η_f given by Incropera and DeWitt (1996) is as follows,

$$\eta_f = \frac{q_f}{q_{\max}} = \frac{q_f}{hA_f\theta_b} \tag{115}$$

where q_f is the actual rate of heat transfer through the fin, $q_{\max}$ is the maximum rate of heat transfer through the fin if the entire fin surface were at the base temperature, h is the convective heat transfer coefficient, A_f is the surface area of the fin and θ_b is given as,

$$\theta_b = T_b - T_\infty \tag{116}$$

where T_b is the fin base temperature and T_∞ is the surrounding fluid temperature.

The fin efficiency for the extreme case considered above was calculated based on the Equation (115), given by Incropera and DeWitt (1996) and was found out to be 92%. This high fin efficiency again justifies the constant temperature fin assumption made in the present investigation.

CHAPTER 8

CONCLUSIONS AND RECOMMENDATIONS

The results of the three-dimensional numerical investigation carried out on the plain and wavy fin configurations for the thermal and hydraulic characteristics have been presented in this document. Commercial computational fluid dynamics code CFX-5 was employed to examine the flow structure as well as the heat transfer and pressure drop characteristics of these fin configurations. Accuracy of the code was tested by comparing the obtained results with the experimental data. Furthermore, grid independency tests were carried out to ensure accuracy of the simulations within an acceptable computational time. The present study ranges from the laminar flow range $(400 \le \mathrm{Re}_H \le 1200)$ into the transitional flow range $(1300 \le \mathrm{Re}_H \le 2000)$. The performance of the plain and the wavy fin configurations for the laminar flow range is evaluated using the laminar flow model. On the other hand, the performance for these fin configurations for the transitional flow range was examined by using three turbulence models. In the present study a total of four different fin configurations were evaluated. This includes plain and wavy fin arrangements in the staggered and in-lined layouts. These fin configurations were also investigated with different geometrical parameters namely, longitudinal and transverse tube pitch, fin pitch, wavy angle and wavy height.

Conclusions

Based on the numerical results obtained in this investigation, the following conclusions are made.

1. The flow distinction between the plain fin and the wavy fin was found to have a significant effect on the heat transfer and the flow friction characteristics of these two fin configurations. The flow structure for the plain-fin configuration is marked by the flow recirculation zones found in the trailing edge of the tubes as the flow passes over the tubes. On the other hand, for the wavy-fin configurations no such flow recirculation zones were obtained, since flow is guided by the wavy corrugations and it is repeatedly re-oriented due to the wavy structure of the fin. In case of plain-fin, a much larger flow recirculation zone was seen in between two adjacent tubes for the plain-fin in-lined configuration, since flow is obstructed only on one side of the domain. On the other hand, in case of plain-fin staggered arrangement, smaller recirculation zones were obtained in the trailing edge of the tubes, as the flow is obstructed on the both sides of the domain resulting in a better flow mixing as compared to the plain-fin in-lined configuration. The wavy-fin staggered and in-lined configurations were found to be less dependent on the tube layout for their thermal and hydraulic characteristics, since a better flow mixing is achieved as the flow passes over the wavy corrugations. Hence wavy-fin was also found to show a much larger heat transfer performance as indicated by the higher Colburn factor (j). However, the pressure penalty is also high in comparison with plain-fin counterpart as indicated by the higher friction factor (f).

The flow distinction between the plain and the wavy configurations has a distinguishing effect when these two fin configurations were compared on the basis of their tube layouts. For plain-fin much higher percentage difference for the heat transfer and pressure drop characteristics was obtained between the staggered and the in-lined configurations as compared to its wavy-fin counterpart.

2. Current study reveals that the number of tube rows also plays an important part on the overall heat exchanger performance. The investigation performed for the wavy-fin staggered configuration revealed that the effect of number of tube rows on the heat transfer coefficient diminishes beyond four rows of tubes. The pressure penalty increases as the number of tube rows are increased from 1 to 6, but the overall heat transfer performance does not vary much in comparison as the number of tube rows become more than 4. Therefore, a four row tube configuration may be regarded as optimum choice for the critical balance between the heat transfer performance and the pressure drop.
3. The study on the four tube row domains for the plain and wavy fin staggered configurations revealed that longitudinal (Ll) and transverse (Lt) tube pitches affect the overall heat exchanger performance. It was demonstrated that the increase in the longitudinal and the transverse pitch for the wavy and plain fin staggered configuration causes a decrease in the heat transfer performance because the flow becomes less compact with the increase in the longitudinal and transverse tube pitch. This decrease in the heat transfer performance is also accompanied by the corresponding decrease in the pressure drop characteristics.

The efficiency index (j/f) goes up with the increase in the longitudinal and transverse tube pitch.

4. The transitional flow range $(1300 \le \mathrm{Re}_H \le 2000)$ was investigated with the *k*-ε, the RNG *k*-ε and the *k*-ω turbulence models. After comparing the numerical results for these three turbulence models as well as the laminar model with the experimental data for the Colburn factor (j) and the friction factor (f) in the transitional range, it was evident that the *k*-ω turbulence model is a better choice for the transitional flow range modeling. The better performance of the *k*-ω turbulence model in the transitional flow range was explained on the basis of the better near wall treatment. It appears that the blending of the low-Reynolds number near wall approach and the wall function near wall approach incorporated in the *k*-ω turbulence model makes it a better choice for the transitional flow range regimes.
5. The numerical study performed to investigate the effects of fin pitch (Fp) on the heat exchanger performance for the transitional flow range $(1300 \le \mathrm{Re}_H \le 2000)$ revealed that decrease in the fin pitch has an adverse effect on the heat transfer performance for both plain and wavy fin staggered configurations. From the numerical results, it was concluded that the decrease in the fin pitch (Fp) causes the flow to be more streamlined and takes away the advantage of better flow mixing as the fin spacing is decreased. As a result, heat transfer performance suffers which is evident from the decrease in the Colburn factor (j) values. This decrease in the heat transfer performance is also accompanied by the

corresponding decrease in the pressure drop characteristics which can be seen from the decreasing friction factor (f) values. The efficiency index (j/f) goes up with the decrease in the fin pitch (Fp).

6. The numerical analysis performed to investigate the effects of wavy angle (Wa) and wavy height (Wh) on the overall heat exchanger performance for the transitional flow range $(1300 \le \mathrm{Re}_H \le 2000)$, revealed that the more wavy corrugations for a given flow length, higher is the heat transfer performance accompanied by higher pressure drop. Increasing the wavy angle (Wa) or decreasing the wavy height (Wh), keeping other geometrical parameters constant, increases the number of wavy corrugations for a given flow length. This increases the flow mixing, as the wavy angle (Wa) is increased or wavy height (Wh) is decreased. For an equal wavy height (Wh), both Colburn factor (j) and friction factor (f) are increased as the wavy angle (Wa) is increased. On the other hand, for an equal wavy angle (Wa) they are decreased as the wavy height (Wh) is increased. This observation is reflected by the efficiency index (j/f) as well. The efficiency index (j/f) decreases with the increase in the wavy angle (Wa), while the efficiency index (j/f) increases with the increase in the wavy height (Wh).

Recommendations for future work

Recommendations based on the current numerical investigations are listed next. Possible points of interest in future research may include following:

1. The transitional flow range $(1300 \le \mathrm{Re}_H \le 2000)$ for the plain and wavy fin configurations may be explored using the Reynolds stress turbulence models.

Current study focuses on the suitability of the eddy-viscosity (k-ε, RNG k-ε, and k-ω) turbulence models for the application stated. However, the Reynolds stress turbulence model is based on the transport equations for all components of the Reynolds stress tensor and the dissipation rate. The Reynolds stress model naturally include effects of streamline curvature, sudden changes in the strain rate, secondary flows or buoyancy compared to the turbulence models using the eddy-viscosity approximation. Their general use is limited because of the increased number of additional transport equations which leads to a reduced numerical stability and increased computational effort. However, their suitability for the transitional flow range for these fin configurations should be explored from the point of view of optimization of the heat exchanger performance.

2. Experimental studies by Wang et al. (1996) have shown that in case of plain-fins the flow rage extends from laminar $(400 \le \mathrm{Re}_H \le 1200)$ to the transitional $(1300 \le \mathrm{Re}_H \le 2000)$ and well into the turbulent $(\mathrm{Re}_H > 2000)$ regions. The turbulent flow range in case of plain-fin configurations has not been explored in detail using numerical methods. The suitability of the eddy viscosity and the Reynolds stress turbulence models should be investigated thoroughly for the turbulent flow range for the plain fin configurations.
3. The experimental studies carried out by Guo and Tafti (2003) revealed that there is a strong correlation between the inlet flow angle and the heat exchanger performance for a multi-louvered fin heat exchanger, depending upon the angle of the inlet flow compared with the angle of the louvers. The current numerical

investigation assumes that the inlet flow is normal to the heat exchanger face. This is not the case when heat exchangers are placed in series, when depending on the orientation of the outlet; the flow assumes an angle and will not be normal to the face of downstream exchanger. In many instances, the heat exchanger itself maybe tilted for better condensate drainage. This relation between the inlet flow angle and the heat exchanger performance must be explored in detail, especially for the wavy-fin configurations, where the angle of wavy corrugations increases the complexity of the flow. The current numerical code can be easily modified to explore the effects of the inlet flow angle on the heat exchanger performance.

4. Plain and wavy-fin heat exchangers are also used for cooling of electronic components in the high flying vehicles. Recent advances in vacuum braze technology have allowed construction of high pressure heat exchangers without the problems associated with salt corrosion inherent in dip braze processes. This has allowed the use of liquid coolants such as water and ethylene glycol for construction of high performance heat exchangers with more efficient heat transfer and smaller friction power expenditure. There is a need for an experimental and or numerical study which will evaluate the validity of extending heat transfer rate data correlation to such liquids for the plain and wavy fins. The current numerical set-up can be easily modified to accommodate liquids with different Prandtl numbers for such a study.

REFERENCES CITED

Achaichia, A. and Cowell, T. A., "Heat transfer and pressure drop characteristics of flat tube and louvered plate fin surfaces", Experimental Thermal and Fluid Science, Vol. 1, Number 2, pp. 147-157, April 1988.

Ali, M. M. and Ramadhyani, S., "Experiments on convective heat transfer in corrugated channels", Experimental Heat Transfer, Vol. 5, Number 3, pp. 175-193, 1992.

Amano, R. S., "Numerical study of laminar and turbulent heat transfer in a periodically corrugated wall channel", Journal of Heat Transfer, Transactions ASME, Vol. 107, Number 3, pp. 564-569, August 1985.

Ansys Inc., "CFX-5 Solver and Solver Manual" 1st Edition, 2002.

Asako, Y., and Faghri, M., "Finite-volume solutions for laminar flow and heat transfer in a corrugated duct", Journal of Heat Transfer, Transactions ASME, Vol. 109, Number 3, pp. 627-634, August 1987.

Bardina, J., Ferziger, J. H. and Reynolds, W. C. "Improved subgrid-scale models for large-eddy simulation", AIAA Paper, pp. 1280-1357, 1980.

Bastini, A., Fiebig, M. and Mitra, N. K., "Numerical studies of a compact fin-tube heat exchanger", Proceedings of EUROTHERM Seminar No. 18, Design and Operation of Heat Exchangers, pp. 154-163, Hamburg, Germany, 1991.

Beecher, D. T. and Fagan, T. J., "Effects of fin pattern on the air side heat transfer coefficient in plate finned-tube heat exchangers", ASHRAE Transactions, Vol. 93, Number 2, pp. 1961-1984, 1987.

Brinkman, R., Ramadhyani, S. and Incropera, F. P., "Enhancement of convective heat transfer from small heat sources to liquid coolants using strip fins", Experimental Heat Transfer, Vol. 1, pp. 315-330, 1988.

Eckels, P. W., Rabas, T. J., "Dehumidification: on the correlation of wet and dry transport processes in plate finned-tube heat exchangers", Journal of Heat Transfer, Transactions ASME, Vol. 109, Number 3, pp. 575-582, Aug, 1987.

Elmahdy, A. H. and Biggs, P. F., "Finned tube heat exchanger: Correlation of dry surface heat transfer data", ASHRAE Transactions, Vol. 85, Number 2, pp. 262-273, 1979.

Ergin, S., Ota, M., Yamaguchi, H. and Sakamoto, M., "Numerical study of the effect of interwall spacing on turbulent flow in a corrugated duct", American Society of

Mechanical Engineers, Heat Transfer Division, (Publication) HTD, Vol. 333, Number 2, pp. 47-54, Proceedings of the ASME Heat Transfer Division, 1996.

Fujii, M., Fujii, T. and Nagata, T., "Numerical analysis of laminar flow and heat transfer of air in an in-line tube bank", Numerical Heat Transfer, Vol. 7, Number 1, pp. 89-102, 1984.

Goldstein, L. and Sparrow, J. M. F., "Heat/Mass transfer characteristics for flow in a corrugated wall channel", Journal of Heat Transfer, Transactions ASME, Vol. 99, pp. 187-195, May 1977.

Grotjans, H. and Menter, F. R., "Wall functions for general application CFD codes", ECCOMAS 98 Proceedings of the Fourth European Computational Fluid Dynamics Conference, pp. 1112-1117, 1998.

Guo, D. and Tafti, D. K., "Effect of Inlet Flow Angle on Performance of Multilouvered Fin Heat Exchangers", American Society of Mechanical Engineers, Heat Transfer Division, (Publication) HTD, Vol. 374, Number 1, pp. 103-109, 2003.

Incropera F. P. and Dewitt D. P., "Fundamentals of heat and mass transfer", 4th Edition, John Wiley and Sons, Inc, 1996.

Jang, J. J., Wu, M. C. and Chang, W. J., "Numerical and experimental studies of three-dimensional plate-fin and tube heat exchangers", International Journal of Heat and Mass Transfer, Vol. 39, Number 14, pp. 3057-3066, September 1996.

Kakac, S., Bergles, A. E. and Mayinger, F. "Heat Exchangers: Thermal-Hydraulic Fundamental and Design", 1st Edition, McGraw-Hill, New York, 1981.

Kayansayan, N., "Heat transfer characterization of flat plain fins and round tube heat exchangers", Experimental Thermal and Fluid Science, Vol. 6, Number 3, pp. 263-272, April 1993.

Kays, W. M. and London, A. L., "Compact Heat Exchangers", 3rd Edition, McGraw-Hill, New York, 1984.

Kim, J. Y., and Song, T. H., "Microscopic phenomena and macroscopic evaluation of heat transfer from plate fins/circular tube assembly using naphthalene sublimation technique", International Journal of Heat and Mass Transfer, Vol. 45, Number 16, pp. 3397-3404, May 2002.

Kim, N. H., Youn, B. and Webb, R. L., "Air-side heat transfer and friction correlations for plain fin-and-tube heat exchangers with staggered tube arrangements", Journal of Heat Transfer, Transactions ASME, Vol. 121, Number 3, pp. 662-667, August 1999.

Kim, N. H., Yun, J. H. and Webb, R. L., "Heat transfer and friction correlations for wavy plate fin-and-tube heat exchangers", Journal of Heat Transfer, Transactions ASME, Vol. 119, Number 3, pp. 560-567, August 1997.

Kundu, D., Skeikh, A. H. and Lou, D. Y. S., "Heat transfer in crossflow over cylinders between two parallel plates", Journal of Heat Transfer, Transactions ASME, Vol. 114, Number 3, pp. 558-564, August 1992.

Kundu, D., Skeikh, A. H. and Lou, D. Y. S., "Heat transfer predictions in cross flow over cylinders between two parallel plates", Numerical Heat Transfer: An International Journal of Computation and Methodology; Part A: Applications, Vol. 9, Number 3, pp. 361-377, 1991.

Kundu, D., Skeikh, A. H. and Lou, D. Y. S., "Pressure and heat transfer in cross flow over cylinders between two parallel plates", Numerical Heat Transfer: An International Journal of Computation and Methodology; Part A: Applications, Vol. 9, Number 3, pp. 345-360, 1991.

Launder, B. E. and Massey, T. H., "Numerical prediction of viscous flow and heat transfer in tube banks", Journal of Heat Transfer, Transactions ASME, Vol. 100, Number 4, pp. 565-571, November 1978.

Launder, B. E. and Spalding, D. B. "Numerical computation of turbulent flows", Computer Methods in Applied Mechanics and Engineering, Vol. 3, Number 2, pp. 269-289, March 1974.

McNab, C. M., Atkinson, K. N., Heikal, M. R. and Taylor, N., "Numerical modeling of heat transfer and fluid flow over herringbone corrugated fins" Proceedings of the 11th International Heat Transfer Conference, Kyongiu, Korea, Vol. 6, pp. 119-124, 1996.

McQuiston, F. C. and Tree, D. R. "Heat-transfer and flow- friction data for two fin- tube surfaces", Journal of Heat Transfer, ASME Transactions, Vol. 93, Number 2, pp. 249-250, May 1971.

McQuiston, F.C., "Correlations for heat, mass and momentum transport coefficients for plate-fin-tube heat transfer surfaces with staggered tube", ASHRAE Transactions, Vol. 84, pp. 294-309, 1978.

Mendez, R. R., Sen, M., Yang, K. T. and McClain, R., "Effect of fin spacing on convection in a plate fin and tube heat exchanger", International Journal of Heat and Mass Transfer, Vol. 43, Number 1, pp. 39-51, October 2000.

Menter, F. R., “Two-equation eddy-viscosity turbulence models for engineering applications”, AIAA Journal, Vol. 32, Number 8, pp. 1598-1605, August 1994.

Mirth, D. R. and Ramadhyani, S., “Correlations for predicting the air-side nusselt numbers and friction factors in chilled-water cooling coils”, Experimental Heat Transfer, Vol. 7, Number 2, pp. 143-162, 1994.

Nishimura, T., Yoshino, T. and Kawamura, Y., “Numerical flow analysis of pulsatile flow in a channel with symmetric wavy walls at moderate Reynolds numbers”, Journal of Chemical Engineering of Japan, Vol. 20, Number 5, pp. 479-485, October 1987.

Patel, V. C., Chon, J. T. and Yoon, J. Y., “Laminar flow over wavy walls”, Journal of Fluids Engineering, Transactions of the ASME, Vol. 113, Number 4, pp. 574-578, December 1991.

Patel, V. C., Chon, J. T. and Yoon, J. Y., “Turbulent flow in a channel with a wavy wall”, Journal of Fluids Engineering, Transactions of the ASME, Vol. 113, Number 4, pp. 579-586, December 1991.

Rich, D.G., “Effect of fin spacing on the heat transfer and friction performance of multi-row, smooth plate fin-and-tube heat exchangers”, ASHRAE Transactions, Vol. 79, Number 2, pp. 137-145, 1973.

Rich, D.G., “Effect of the number of tube rows on heat transfer performance of smooth plate fin-and-tube heat exchangers”, ASHRAE Transactions, Vol. 81, Number 1, pp. 307-319, 1975.

Rosman, E. C., Carajilescov, P. and Saboya, F. E. M., “Performance of one- and two-row tube and plate fin heat exchangers”, Journal of Heat Transfer, Transactions ASME, Vol. 106, Number 3, pp. 627-632, August 1984.

Rutledge, J. and Sleicher, C. A., “Direct simulation of turbulent flow and heat transfer in a channel Part II: A Green's function technique for wavy walls”, Communications in Numerical Methods in Engineering, Vol. 10, Number 6, pp. 489-496, June 1994.

Saboya, F.E.M. and Sparrow, E.M., “Experiments on the transfer characteristics of a corrugated fin and tube heat exchanger configuration”, Journal of Heat Transfer, Transactions ASME, Vol. 98, pp. 26-34, February1976.

Saboya, F.E.M. and Sparrow, E.M., “Local and average transfer coefficients for one-row plate fin and tube heat exchanger configurations”, Journal of Heat Transfer, Transactions ASME, Vol. 96, pp. 265-272, August 1974.

Seshimo, Y., and Fujii, M., "Experimental study on the performance of plate fin and tube heat exchangers at low Reynolds numbers", ASME/JSME Thermal Engineering Joint Conference, Vol. 4, pp. 449-454, 1991.

Snyder, B., Li, K. T. and Wirtz, R. A., "Heat transfer enhancement in a serpentine channel", International Journal of Heat and Mass Transfer, Vol. 36, Number 12, pp. 2965-2976, August 1993.

Sparrow, E. M. and Hossfeld, L. M., "Effect of rounding of protruding edges on heat transfer and pressure drop in a duct", International Journal of Heat and Mass Transfer, Vol. 27, Number 10, pp. 1715-1723, October 1984.

Thomas, L. C., "Fundamentals of heat transfer", 1st Edition, Prentice-Hall Inc., 1980.

Tutar, M. and Akkoca, A., "Numerical analysis of fluid flow and heat transfer characteristics in three-dimensional plate fin-and-tube heat exchangers", Numerical Heat Transfer; Part A: Applications, Vol. 46, Number 3, pp. 301-321, August 2004.

Tutar, M., Akkoca, A. and Serdar, O., "A numerical study of heat transfer and fluid flow in a plate fin- and- tube heat exchanger", American Society of Mechanical Engineers, Pressure Vessels and Piping Division (Publication) PVP, Vol. 431, Number 3, pp. 77-84, 2001.

Wang, C. C. and Chi, K. Y., "Heat transfer and friction characteristics of plain fin-and-tube heat exchangers, Part I: New experimental data", International Journal of Heat and Mass Transfer, Vol. 43, Number 15, pp. 2681-2691, April 2000.

Wang, C. C., Chang, Y. J., Hsieh, Y. C. and Lin, Y. T., "Sensible heat and friction characteristics of plate fin-and-tube heat exchangers having plane fins", International Journal of Refrigeration, Vol. 19, Number 4, pp. 223-230, May 1996.

Wang, C. C., Chi, K. Y. and Chang, C. J., "Heat transfer and friction characteristics of plain fin-and-tube heat exchangers, Part II: Correlation", International Journal of Heat and Mass Transfer, Vol. 43, Number 15, pp. 2693-2700, April 2000.

Wang, C. C., Fu, W. L. and Chang, C. T., "Heat transfer and friction characteristics of typical wavy fin-and-tube heat exchangers", Experimental Thermal and Fluid Science, Vol. 14, Number 2, pp. 174-186, February 1997.

Wang, C. C., Hwang, Y. M. and Lin, Y. T., "Empirical correlations for heat transfer and flow friction characteristics of herringbone wavy fin-and-tube heat exchangers", International Journal of Refrigeration, Vol. 25, Number 5, pp. 673-680, August 2002.

Wang, C. C., Lee, W. S. and Sheu, W. J., "A comparative study of compact enhanced fin-and-tube heat exchangers", International Journal of Heat and Mass Transfer, Vol. 44, Number 18, pp. 3565-3573, July 2001.

Wang, C. C., Lin, Y. T., Lee, C. J. and Chang, Y. J., "Investigation of wavy fin-and-tube heat exchangers: A contribution to databank", Experimental Heat Transfer, Vol. 12, Number 1, pp. 73-89, 1999.

Webb, R. L., "Air-side heat transfer correlations for flat and wavy plate fin-and-tube geometries", ASHRAE Transactions, Vol. 90, Number 2, pp. 445-449, 1990.

Wilcox, D. C., "Multi-scale model for turbulent flows", AIAA 24th Aerospace Sciences Meeting, American Institute of Aeronautics and Astronautics, 1986.

Wung, T. S. and Chen, C. J., "Finite analytic solution of convective heat transfer for tube arrays in crossflow: Part I. Flow field analysis", Journal of Heat Transfer, Transactions ASME, Vol. 111, Number 3, pp. 633-640, August 1989.

Wung, T. S. and Chen, C. J., "Finite analytic solution of convective heat transfer for tube arrays in crossflow: Part II. Heat transfer analysis", Journal of Heat Transfer, Transactions ASME, Vol. 111, Number 3, pp. 641-648, August 1989.

Xin, R. C. and Tao, W. Q., "Numerical prediction of laminar flow and heat transfer in wavy channels of uniform cross-sectional area", Numerical Heat Transfer, Vol. 14, Number 4, pp. 465-481, December 1988.

Yamashita, H., Kushida, G. and Izumi, R., "Fluid flow and heat transfer in a plate-fin and tube heat exchanger (Analysis of heat transfer around a square cylinder situated between parallel plates)", Bulletin of the JSME, Vol. 29, Number 258, pp. 4185-4191, December 1986.

Yan, W. M., Sheen, P. J., "Heat transfer and friction characteristics of fin-and-tube heat exchangers", International Journal of Heat and Mass Transfer, Vol. 43, Number 9, pp. 1651-1659, February 2000.

Yang, L. C., Asako, Y., Yamaguchi, Y. and Faghri, M., "Numerical prediction of transitional characteristics of flow and heat transfer in a corrugated duct", ASME Journal of Heat Transfer, Vol. 119, pp. 62-69, 1997.

Yoshii, T., "Transient testing technique for heat exchanger fin surfaces", Journal of the Institution of Telecommunication Engineers, Vol. 1, Number 3, pp. 51-58, 1972.

Yoshii, T., Yamamoto, M. and Otaki, T., "Effects of dropwise condensate on wet surface heat transfer for air cooling oils", Proceedings of 13th International Congress of Refrigeration, pp. 285-292, 1973.

Yuan, Z. X., "Numerical study of periodically turbulent flow and heat transfer in a channel with transverse fin arrays", International Journal of Numerical Methods for Heat and Fluid Flow, Vol. 10, Number 8, pp. 842-861, 2000.

Zdravistch, F., Fletcher, C. A. J. and Behnia, M., "Laminar and turbulent heat transfer predictions in tube banks in cross flow", Proceedings of the International Conference on Fluid and Thermal Energy Conversion, Bali, Indonesia, pp. 12-16, December 1994.